

ABSTRACT

Title of Document: UNDERSTANDING THE ROLE OF HEAT
RECIRCULATION IN ENHANCING THE SPEED OF
PREMIXED LAMINAR FLAMES IN A PARALLEL
PLATE MICRO-COMBUSTOR

Ananthanarayanan Veeraragavan, PhD, 2009

Directed By: Associate Professor, Christopher Cadou,
Aerospace Engineering

This dissertation investigates the role of heat recirculation in enhancing the flame speeds of laminar flames stabilized in a parallel plate reactor by: 1) developing analytical models that account for conjugate heat transfer with the wall and 2) making measurements of temperature profiles in a simulated microcombustor using non-intrusive FTIR spectroscopy from which heat recirculation is inferred. The analytical models have varying degrees of complexity. A simple heat transfer model simulates the flame by incorporating a concentrated heat release function along with constant temperature wall model. The next level model accommodates conjugate heat transfer with the wall along with a built in heat loss model to the environment. The heat transfer models identify the thermal design parameters influencing the temperature profiles and the Nusselt number. The conjugate heat transfer model is coupled with a species transport equation to develop a 2-D model that predicts the flame speed as an eigenvalue of the problem. The flame speed model shows that there are three design parameters (wall thermal conductivity ratio (κ), wall thickness ratio (τ) and external heat loss parameter (Nu_E)) that influence the flame speed. Finally, it is shown that all these three parameters really control the total heat recirculation which is a single valued function of the flame speed and independent of the velocity profile (Plug or

Report Documentation Page		Form Approved OMB No. 0704-0188
Public reporting burden for the collection of information is estimated to average 1 hour per response, including the time for reviewing instructions, searching existing data sources, gathering and maintaining the data needed, and completing and reviewing the collection of information. Send comments regarding this burden estimate or any other aspect of this collection of information, including suggestions for reducing this burden, to Washington Headquarters Services, Directorate for Information Operations and Reports, 1215 Jefferson Davis Highway, Suite 1204, Arlington VA 22202-4302. Respondents should be aware that notwithstanding any other provision of law, no person shall be subject to a penalty for failing to comply with a collection of information if it does not display a currently valid OMB control number.		
1. REPORT DATE 2009	2. REPORT TYPE	3. DATES COVERED 00-00-2009 to 00-00-2009
4. TITLE AND SUBTITLE Understanding the Role of Heat Recirculation in Enhancing the Speed of Premixed Laminar Flames in a Parallel Plate Micro-Combustor		5a. CONTRACT NUMBER
		5b. GRANT NUMBER
		5c. PROGRAM ELEMENT NUMBER
6. AUTHOR(S)	5d. PROJECT NUMBER	
	5e. TASK NUMBER	
	5f. WORK UNIT NUMBER	
7. PERFORMING ORGANIZATION NAME(S) AND ADDRESS(ES) University of Maryland, College Park, College Park, MD, 20742		8. PERFORMING ORGANIZATION REPORT NUMBER
9. SPONSORING/MONITORING AGENCY NAME(S) AND ADDRESS(ES)		10. SPONSOR/MONITOR'S ACRONYM(S)
		11. SPONSOR/MONITOR'S REPORT NUMBER(S)
12. DISTRIBUTION/AVAILABILITY STATEMENT Approved for public release; distribution unlimited		
13. SUPPLEMENTARY NOTES		
14. ABSTRACT <p>This dissertation investigates the role of heat recirculation in enhancing the flame speeds of laminar flames stabilized in a parallel plate reactor by: 1) developing analytical models that account for conjugate heat transfer with the wall and 2) making measurements of temperature profiles in a simulated microcombustor using nonintrusive FTIR spectroscopy from which heat recirculation is inferred. The analytical models have varying degrees of complexity. A simple heat transfer model simulates the flame by incorporating a concentrated heat release function along with constant temperature wall model. The next level model accommodates conjugate heat transfer with the wall along with a built in heat loss model to the environment. The heat transfer models identify the thermal design parameters influencing the temperature profiles and the Nusselt number. The conjugate heat transfer model is coupled with a species transport equation to develop a 2-D model that predicts the flame speed as an eigenvalue of the problem. The flame speed model shows that there are three design parameters (wall thermal conductivity ratio (&#954;), wall thickness ratio (&#964;) and external heat loss parameter (NuE)) that influence the flame speed. Finally, it is shown that all these three parameters really control the total heat recirculation which is a single valued function of the flame speed and independent of the velocity profile (Plug or Poiseuille flow). On the experimental side, a previously developed non-intrusive diagnostic technique based on FTIR spectroscopy of CO2 absorbance is improved by identifying the various limitations (interferences from other species, temperature profile fitting, ? etc) and suggesting improvements to each limitation to make measurements in a silicon walled, simulated microcombustor. Methane/Air and Propane/Air flames were studied for different equivalence ratios and burning velocities. From the temperature profiles it can be seen that increasing the flame speed pushes the flames further up the channel and increases the combustors inner gas and outer wall temperatures (measured using IR thermography). The temperature profiles measured are used to make a 2-D heat recirculation map for the burner as a function of the equivalence ratio and burning velocity. The experimental results are compared to the analytical models predictions which show a linear trend between flame speed and heat recirculation.</p>		

15. SUBJECT TERMS					
16. SECURITY CLASSIFICATION OF:			17. LIMITATION OF ABSTRACT Same as Report (SAR)	18. NUMBER OF PAGES 228	19a. NAME OF RESPONSIBLE PERSON
a. REPORT unclassified	b. ABSTRACT unclassified	c. THIS PAGE unclassified			

Poiseuille flow). On the experimental side, a previously developed non-intrusive diagnostic technique based on FTIR spectroscopy of CO₂ absorbance is improved by identifying the various limitations (interferences from other species, temperature profile fitting, ... etc) and suggesting improvements to each limitation to make measurements in a silicon walled, simulated microcombustor. Methane/Air and Propane/Air flames were studied for different equivalence ratios and burning velocities. From the temperature profiles it can be seen that increasing the flame speed pushes the flames further up the channel and increases the combustors inner gas and outer wall temperatures (measured using IR thermography). The temperature profiles measured are used to make a 2-D heat recirculation map for the burner as a function of the equivalence ratio and burning velocity. The experimental results are compared to the analytical models predictions which show a linear trend between flame speed and heat recirculation.

UNDERSTANDING THE ROLE OF HEAT RECIRCULATION IN ENHANCING
THE SPEED OF PREMIXED LAMINAR FLAMES IN A PARALLEL PLATE
MICRO-COMBUSTOR

By

Ananthanarayanan Veeraragavan

Dissertation submitted to the Faculty of the Graduate School of the
University of Maryland, College Park, in partial fulfillment
of the requirements for the degree of
[Doctor of Philosophy]
[2009]

Advisory Committee:
Professor Christopher Cadou, Chair/Advisor
Professor Gregory Jackson
Professor Andre Marshall
Professor David Akin
Professor Stuart Antman

© Copyright by
[Ananthanarayanan Veeraragavan]
[2009]

Dedication

To Dilip,

You will remain for ever in my heart and memories. I know you're there somewhere to see me achieve this. Thank you.

Acknowledgements

It is hard to be concise and acknowledge the contributions of the various individuals I owe the existence of this dissertation to in a few words. I would start by thanking my advisor Prof. Chris Cadou for his guidance, understanding and pushing to make me achieve my best and beyond. He has motivated me to believe in doing quality work and achieving success through hard work and perseverance. I would also like to acknowledge his keeping my best interest in mind and often encouraging me to apply for the fellowships and honors that I have had the good fortune to win namely: The future faculty fellowship from the Clark School of Engineering and the best Doctoral dissertation award from the Dept. Aerospace Engineering, Univ. Maryland. I thank the other members of my advisory committee (Professors Antman, Marshall, Akin, and Jackson) for their willingness to spare time from their very busy schedules to help me achieve this dream. Special thanks to Dr. Greg Jackson, for teaching me the SOFC code and for always willing to have stimulating conversations on research and beyond. My interactions with Prof. Anderson while being mentored to teach his graduate course *Fundamentals of Aerodynamics* have left me awestruck at this humility and kindness despite being such an immense personality. I thank him for his belief in me and his support.

Next, I would like to remember my friends here at UMD. I thank Scott Heatwole for initiating me into learning the diagnostic technique we developed together, my predecessor Tim Leach for being a mentor and excellent colleague to work and discuss interesting ideas with, my two best friends at work Shyam Menon and Kiran Dellimore with whom I have spent a considerable amount of time in the lab

and beyond (may our Squash club live and flourish beyond our time here!). I would like to also acknowledge my current colleagues (Jon, Dan, Jeff, Erica, Joshua and Daanish) for making the office a fun and engaging place to come to. In the same vein I would like to remember the friendships I have shared with most of my past roommates: Ritesh, Jeeves, Vinit, Patrick, Matze, Peter, Jan, Steffen, Andreas, Nabi, Joerg, Carl, Arthur, Matt and Chris. Special mention must be made of my roommate Nico Zazworka, whose ever bubbling enthusiasm has kept me going and made my home a very inviting place to come back to. I would also like to appreciate and thank my friend Gabby for lending me a listening ear and being supportive.

I cannot have achieved this without the love and support of my dear sister Bhuvana, who has been patient and endearing besides being extremely supportive of my efforts. I would also like to thank my parents (Mr. A. Veeraragavan and Mrs. R. Lakshmi), my uncle Mr. Ganesh Shastri, my aunt Mrs. Jaya Shastri, my aunt Mrs. Shanta Venkatachalam, and my late uncle Brig. L. Venkatachalam and all my cousins and my grandparents and all other members of my family for their support and blessings.

My friends from the past and my friends who will be there for life: Sub, Baa, SK, Bala, CB, Sai, Subash and Shravan all of whom have always been there at any time I needed them, to offer moral support and more. I also thank Sangeeta for her cheerful presence and constant support. I truly miss my dear friend and mentor Dilip, who would have been most happy to see me achieve this, at this time.

Last but not the least I would like to express my sincere thanks to Dr. Mitat Birkan at the AFOSR for supporting and funding for this work.

Table of Contents

Dedication	ii
Acknowledgements	iii
Table of Contents	v
List of Tables	vii
List of Figures	viii
Chapter 1: Introduction	1
1.1. Motivation: Chemical Thrusters for Microsatellites	1
1.1.1. Size Classes of Satellites	1
1.1.2. Missions for Microsatellites	2
1.1.3. Thruster Performance Requirements	3
1.1.4. Available Propulsion Systems	3
1.1.5. Advantages of Chemical Propulsion	6
1.2. Chemical Rockets	6
1.2.1. Thrust Generation	6
1.2.2. Types of propellants	7
1.2.3. Rocket Cycles	10
1.2.4. Principles of Operation	14
1.2.5. Performance Metrics	15
1.3. Scaling of Chemical Thruster Performance with Size:	16
1.3.1. What changes when you miniaturize?	16
1.3.2. Impact of Reduced Scale on Thruster Performance:	21
1.3.3. Key Barriers to Developing Practical Micro-Chemical Thrusters	22
1.3.4. Problem of interest in this thesis	22
1.4. Previous work:	22
1.4.1. Heat Transfer Modeling	23
1.4.2. Combustion	27
1.4.3. Microscale Energy Conversion Technologies:	35
1.4.4. Measurement and Non-intrusive Diagnostic Techniques	46
1.5. Objectives and Approach:	51
Chapter 2: Heat Transfer Analysis	53
2.1. Gas Energy Equation/Heat Release Model	53
2.1.1. Governing Equation	53
2.1.2. Derivation of Jump Conditions across the Flame	55
2.2. Isothermal Wall Boundary Condition	56
2.2.1. Solution	57
2.2.2. Results	58
2.3. Conducting Wall Boundary Condition (Conjugate Heat Transfer)	73
2.3.1. Solution	76
2.3.2. Results	77
Chapter 3: Flame Speed (Eigenvalue) Solution	92
3.1. Governing Equations	92
3.2. Flame Speed Solution	96
3.3. Results	99

3.3.1. Temperature Profiles.....	99
3.3.2. Flame Speed Contours	102
3.3.3. Heat recirculation.....	108
3.4. Practical Applications of the Model:	111
3.4.1. Identifying Design Ranges:.....	111
3.4.2. Temperature Profile Guesses for Non-intrusive Diagnostics:	112
3.3.4. Thrust Calculation.....	115
Chapter 4: Experiment: Theory and Apparatus	118
4.1. Physics of Absorption:.....	118
4.1.1. Qualitative Description of Absorption:.....	118
4.1.2. Review of Absorption Spectroscopy:	122
4.1.3. Gas Temperature Measurement Principle:.....	126
4.2. Experimental Setup:.....	127
4.2.1. Simulated Microcombustor:.....	128
4.2.2. External Optical System:	130
4.2.3. Flow Control System:	132
4.3. Experimental Procedure:.....	133
4.4. Temperature Measurement in the Microburner:	135
4.5. Challenges in Implementation and Remedies:.....	137
4.5.1. Interference from Silicon and CO:.....	137
4.5.2. High Temperature Effects:.....	139
4.5.3. Lack of CO ₂ in pre-flame region	142
4.6. Gas Temperature Uncertainty:.....	143
4.7. Fundamental limitations:	146
4.8. Initial Guess for T fitting parameters:.....	150
4.8.1. Profile Comparisons.....	151
4.8.2. Initial guesses based on analytical model:	159
Chapter 5: Experimental Results	162
5.1. Model Based Temperature Fit:	162
5.2. Comparisons of Temperature Profiles:	170
5.2.1. Constant Equivalence Ratio ϕ	171
5.3. Heat Recirculation and Flame Speed:.....	175
Chapter 6: Findings and Future Work	180
6.1. Key Contributions:.....	180
6.2. Future Work:	182
Appendix A: Solution and Eigenequation	184
Isothermal Wall (Constant Wall Temperature):	185
Conducting Walls (Conjugate Heat Transfer):	186
Appendix B: Orthogonality Condition.....	188
Isothermal Wall (Constant Wall Temperature).....	188
Conjugate Heat Transfer:	189
Appendix C: Evaluation of Coefficients.....	191
Isothermal Wall:.....	191
Conjugate Heat Transfer:	193
Appendix D: Table of Maximum Temperatures.....	197

List of Tables

Table 1-1: Definition and classification of microspacecraft (Adapted from Mueller [1]).....	2
Table 1-2: Performance comparison of different types of microthrusters (Adapted from J.H. Schilling [1]).....	5
Table 1-3: Theoretical performance of typical solid rocket propellant combinations (Adapted from [1]).....	9
Table 1-4: Theoretical performance of typical liquid rocket propellant combinations (adapted from [3]).....	9
Table 1-5: Models for the microthruster operation [51].....	36
Table 2-1: Nusselt number asymptote values for Pre and Post-flame regions for different Pe numbers for H-P flow.....	72
Table 2-2: Nu asymptotes for different operating conditions of the burner.....	90
Table 3-1: Comparison between the analytical model and the 4 th order temperature profile fit for Poiseuille flow ($\kappa = 10$, $\tau = 2$, $Nu_E = 0.0375$).....	114
Table 4-1: Initial guess choices for 4 th order T profile.....	150
Table 5-1: Initial guess for parameters to be supplied to the fitting routine.....	162
Table 5-2: Operating conditions for data collection from the burner.....	170
Table 5-3: Parameters for freely propagating conditions.....	178

List of Figures

Figure 1-1: Schematic sketch of a thrust chamber for a chemical rocket (adapted from [3]).....	7
Figure 1-2: Sketch of solid rocket motor: Lateral view.....	11
Figure 1-3: Liquid Rocket Turbopump Cycles: a) Fuel rich staged combustion cycle; b) Fuel and Oxidizer rich with auxillary pumps; c) Simple expander bleed cycle d) Expander cycle with internal heat exchanger [4].....	12
Figure 1-4: Scale analysis of microscale combustors, a) Cylindrical b) Cuboid.....	17
Figure 1-5: Illustration of flame holding in combustors a) Conventional Scale, b) Microscale.....	18
Figure 1-6: Depiction of the role of the wall in a microcombustor.....	19
Figure 1-7: Contours of Pelcet number as a function of flow velocity (U) and passage height (d) ([14-17]).....	20
Figure 1-8: Nusselt number at the outer surface (Nu_h) as a function of zPe for pipe Poiseuille flow. $h = 2$, $Pe = 5$, $k_s/k_f = 243$ (upright triangles), and $k_s/k_f = 1$ (inverted triangles). The solid and dashed lines correspond, respectively, to cases when axial conduction is accounted for and cases when it is neglected [26].....	25
Figure 1-9: Exchanger efficiency as a function of the wall conductivity [27].....	26
Figure 1-10: Non-adiabatic H_2 -air combustion in a silicon micro-channel; $\Phi = 0.5$, $P = 1$ atm, $h_{env} = 1$ W/m ² K. Solid lines, contours of non-dimensional power density ($\dot{w}_D / \dot{w}_{D,ref}$) as a function of non-dimensional channel height and length. Dashed lines, contours of overall efficiency [40].....	29

Figure 1-11: Critical velocity vs wall thermal conductivity. The lower curve (●) represents stability loss due to insufficient heat generation. The upper curve (■) represents blowout. The shaded region allows stabilized combustion. The experimentally determined laminar flame speed is plotted as a dashed line [41].....	30
Figure 1-12: Plan view of the Swiss roll burner. Platinum catalyst strips were placed as shown when used. Thermocouples 1-7 were located in the exhaust ‘e’ and inlet ‘i’ turns as indicated [15].....	32
Figure 1-13: Quartz heat recirculation reactor (HRR). (a) Catalyst and thermal shields position. (b) Cross-section of the reactor. (c) Flow direction in HRR mode. (d) Schematic of HRR mode: heat flux direction and thermocouple positions [50].....	34
Figure 1-14: The three-dimensional computational mesh used by Kujawa et al. to simulate a micro-nozzle. It was created using Fluent Inc.’s GAMBIT software [52].....	36
Figure 1-15: Pathlines for the 3-D model with isothermal boundary conditions [53].....	37
Figure 1-16: Thrust production in 2D and 3D micro-nozzles for varying expander half-angles from Hitt et al. [53].....	38
Figure 1-17: Comparison of the measured data of nozzles with the prediction [54]...	39
Figure 1-18: Regeneratively cooled MEMS thrust chamber design to produce 15N thrust [55].....	40
Figure 1-19: H ₂ demo engine with conduction-cooled turbine constructed from six silicon wafers [14].....	41
Figure 1-20: Photograph of the mini-rotary engine [56].....	42

Figure 1-21: Piston-cylinder assembly. The piston is on the left and the end plug is on the right [57].....	43
Figure 1-22: Assembly concept for all non-fuel components of the 20W MICSE chemical-to-electrical energy conversion system indicating major system components. System volume is 17.6 cc (20x20x44 mm) and mass is 54 g [59].....	44
Figure 1-23: Base cavity, swing-arm, valve ports, and resulting four chambers (A-D) in the micro internal combustion swing engine (MICSE). The resulting arrangement produces inherent weight and volume efficiencies over conventional linear piston engines, while avoiding the mechanical complexities of rotary Wankel or turbine engines [59].....	45
Figure 1-23: Schematic of a typical thermocouple arrangement for combustion-system measurements [60].....	47
Figure 1-24: Diagram of apparatus [74].....	50
Figure 1-25: Temperature versus downstream distance inferred from CO absorbance spectra [74].....	51
Figure 2-1: Infinitely thin flame stabilized in a channel between two parallel plates.....	54
Figure 2-2: Heat transfer problem in non-dimensional variables for isothermal BC.....	57
Figure 2-3: Representative computational grid.....	59
Figure 2-4: Non-Dimensional 2-D temperature (θ/θ_F) field ($Pe = 1$).....	62

Figure 2-5: Comparison of axial temperature profiles predicted by the analytical model and the CFD simulations for three transverse (y^+) locations; Hagen-Poiseuille Flow. a) $Pe = 1$ and b) $Pe = 5$	63
Figure 2-6: Comparison of transverse temperature profiles predicted by the analytical model and the CFD simulations for three axial (x^+) locations for Hagen-Poiseuille flow. a) $Pe = 1$ and b) $Pe = 5$	64
Figure 2-7: Non-dimensional temperature profile ($\theta_{avg}/\theta_{avg,F}$) in low Pe limit. a) Plug Flow and b) Hagen-Poiseuille Flow.....	65
Figure 2-8: Non-dimensional temperature profile ($\theta_{avg}/\theta_{avg,F}$) for plug and HP flows in the high Pe limit.....	66
Fig. 2-9: Nu number vs. axial distance for different Pe numbers. a) Plug flow, b) Poiseuille Flow.....	69
Fig. 2-10: Nu asymptote as a function of Pe for H-P flow.....	71
Figure 2-11: Half Channel from Centerline to Outer Edge of Structure.....	73
Figure 2-12a: Effect of Changing Pe on the Non-Dimensional Temperature for: (Plug Flow, $\kappa = 10$, $\tau = 2$, $Nu_E = 10$) (i) $Pe = 0.1$, (ii) $Pe = 1$, (iii) $Pe = 5$, (iv) $Pe = 10$ ($Nu_E = 10$, $\tau = 2$, $\kappa = 10$).....	78
Figure 2-12b: Effect of Changing Pe on the Non-Dimensional Temperature for: (Hagen-Poiseuille Flow, $\kappa = 10$, $\tau = 2$, $Nu_E = 10$) (i) $Pe = 0.1$, (ii) $Pe = 1$, (iii) $Pe = 5$, (iv) $Pe = 10$ ($Nu_E = 10$, $\tau = 2$, $\kappa = 10$).....	79
Figure 2-13a: Effect of Changing κ on the Non-Dimensional Temperature for: (Plug Flow, $Nu_E = 10$, $\tau = 2$, $Pe = 5$), (i) $\kappa = 0.1$, (ii) $\kappa = 1$, (iii) $\kappa = 10$, (iv) $\kappa = 100$	81

Figure 2-13b: Effect of Changing κ on the Non-Dimensional Temperature for: (Hagen-Poiseuille Flow, $Nu_E = 10$, $\tau = 2$, $Pe = 5$), (i) $\kappa = 0.1$, (ii) $\kappa = 1$, (iii) $\kappa = 10$, (iv) $\kappa = 100$	82
Figure 2-14a: Effect of Changing τ on the Non-Dimensional Temperature for: (Plug Flow, $Nu_E = 10$, $\kappa = 10$, $Pe = 5$) (i) $\tau = 1.5$, (ii) $\tau = 2$, (iii) $\tau = 3$, (iv) $\tau = 11$	83
Figure 2-14b: Effect of Changing τ on the Non-Dimensional Temperature for: (Hagen- Poiseuille Flow, $Nu_E = 10$, $\kappa = 10$, $Pe = 5$) (i) $\tau = 1.5$, (ii) $\tau = 2$, (iii) $\tau = 3$, (iv) $\tau =$ 11.....	84
Figure 2-15a: Effect of Changing Nu_E on Non-Dimensional Temperature for: (Plug Flow, $\tau = 2$, $\kappa = 10$, $Pe = 5$), (i) $Nu_E = 0.1$, (ii) $Nu_E = 1$, (iii) $Nu_E = 10$, (iv) $Nu_E =$ 100.....	85
Figure 2-15b: Effect of Changing Nu_E on Non-Dimensional Temperature for: (Hagen-Poiseuille Flow, $\tau = 2$, $\kappa = 10$, $Pe = 5$), (i) $Nu_E = 0.1$, (ii) $Nu_E = 1$, (iii) $Nu_E =$ 10, (iv) $Nu_E = 100$	86
Figure 2-16: Axial variation in the Nusselt number for various Pe numbers (Plug flow, $\kappa = 10$, $\tau = 2$, $Nu_E = 10$).....	88
Figure 2-17: Comparison of the axial variation of the Nusselt number in plug versus fully developed flow for two different Pe numbers ($\kappa = 10$, $\tau = 2$, $Nu_E = 10$)......	89
Figure 3-1: Schematic illustration of flame stabilized in a micro-channel.....	93
Figure 3-2: 2-D Non-dimensional temperature plot as a function of the spatial coordinates ($\kappa = 10$, $\tau = 2$, $Nu_E = 0.0375$). a) Plug flow; b) Poiseuille flow.....	100
Figure 3-3: Pre-flame non-dimensional temperature distributions in gas and structure. a) Plug Flow; b) Poiseuille Flow.....	101

Figure 3-4: Post-flame non-dimensional temperature distributions in gas and structure. a) Plug Flow; b) Poiseuille Flow.....	102
Figure 3-5: Flame speed as a function of heat loss <i>Nusselt</i> number ($\kappa = 10$, $\tau = 2$).....	103
Figure 3-6: Flame speed as a function of Heat Recirculation ($\kappa = 10$, $\tau = 2$).....	105
Figure 3-7: Flame Speed as a function of the Heat Loss ($\kappa = 10$, $\tau = 2$).....	106
Figure 3-8: Burning velocity as a function of heat loss to the environment for four wall thermal conductivity ratios ($\tau = 2.0$).....	107
Figure 3-9: Burning velocity as a function of heat loss to the environment for three wall thickness ratios ($\kappa=10$).....	108
Figure 3-10: Burning velocity as a function of the non-dimensional total heat recirculation.....	109
Figure 3-11: Comparison of transverse temperature profiles in the a) Pre-flame and b) Post-flame, for Poiseuille flow ($\kappa = 10$, $\tau = 2$, $Nu_E = 0.0375$).....	113
Figure 3-12: Schematic illustration of a combustor and nozzle unit.....	115
Figure 4-1: a) Vibrational and electronic transitions for a diatomic molecule b) Electromagnetic Spectrum and corresponding transitions [82].....	119
Figure 4-2: Relative populations of the rotational levels of HCl(g) at three different temperatures. (Adapted from [84]).....	120
Figure 4-3: Rotational bands in CH ₄ spectrum.....	121
Figure 4-4: Illustration of CO ₂ stretching and bending modes.....	122
Figure 4-5: Sample hot versus cold CO ₂ spectra, measured at 16 cm ⁻¹ resolution.....	124

Figure 4-6: Schematic diagram of experiment.....	127
Figure 4-7: Simulated micro-combustor mounted on a vertical traverse.....	128
Figure 4-8: External optical arrangement (IR beam path in red).....	130
Figure 4-9: Side view of optical system.....	131
Figure 4-10: Flow Control System.....	132
Figure 4-11: Illustration of discretized beam path with an assumed temperature distribution.....	135
Figure 4-12: Comparison of CO ₂ , CH ₄ (absorption) and Si (% transmittance) spectra.....	136
Figure 4-13: Absorbance spectra of CO ₂ showing the relative influence of each species given as an input to the EM2C program in the spectral region of interest (T = 900 K, Optical Path Length (2 d) = 2.15 mm).....	138
Figure 4-14: Fit of CO ₂ spectra: $\phi = 0.85$, U = 50 cm/s, 2.12 mm wafer spacing, 21 mm downstream from inlet.....	139
Figure 4-15: Percent transmittance of double side polished Si wafer vs. temperature at different wave numbers around the CO ₂ regime (2250 – 2450 cm ⁻¹).....	140
Figure 4-16: Comparison of CO ₂ absorbance spectrum at the same location for seeded and unseeded flows in the pre-flame. $\phi = 0.8$, U = 50 cm/s, z = 12 mm.....	142
Figure 4-17: Plot of centerline temperature as a function of axial distance for three different initial guess values for a flat temperature profile ($\phi = 1.15$, U = 50 cm/s).....	152
Figure 4-18: Plot of temperature as a function of transverse coordinate at four axial locations for four different initial “C” shaped guesses ($\phi = 1.15$, U = 50 cm/s).....	153

Figure 4-19: Plot of centerline and wall temperatures as a function of axial distance for four different initial guess values for a “C” shaped temperature profile ($\phi = 1.15$, $U = 50$ cm/s).....	154
Figure 4-20: Plot of temperature as a function of transverse coordinate at four axial locations for four different initial “C” shaped guesses ($\phi = 1.15$, $U = 50$ cm/s). The dashed lines show the guesses and the solid lines show the converged solutions....	155
Figure 4-21: Plot of EM2C fit to the experimental absorbance as a function of wavenumber at four axial locations for four different initial “C” shaped guesses ($\phi = 1.15$, $U = 50$ cm/s).....	156
Figure 4-22: Plot of centerline and wall temperatures as a function of axial distance for four different initial guess values for a “C” shaped temperature profile ($\phi = 1.15$, $U = 50$ cm/s).....	157
Figure 4-23: Plot of temperature as a function of transverse coordinate at four axial locations for four different initial “C” shaped guesses ($\phi = 1.15$, $U = 50$ cm/s). The dashed lines show the guesses and the solid lines show the converged solutions....	158
Figure 4-24: Plot of EM2C fit to the experimental absorbance as a function of wavenumber at four axial locations for four different initial “C” shaped guesses ($\phi = 1.15$, $U = 50$ cm/s).....	159
Figure 4-25: Transverse temperature profiles in the channel predicted by the analytical model using the Poiseuille flow solution. a) Pre-flame, b) Post-flame....	160
Figure 5-1: Centerline and wall temperatures as a function of downstream distance (CH ₄ /Air, $\phi = 1.15$, $U = 50$ cm/s).....	163

Figure 5-2: Transverse temperature profiles across the channel at select downstream locations (Flame location $x_f = 15$ mm).....	164
Figure 5-3: IR camera image of the burner with the flame stabilized inside (CH_4/Air , $\phi = 1.15$, $U = 50$ cm/s).....	165
Figure 5-4: Comparison of the fit to the experimental data at different axial locations.....	166
Figure 5-5: IR images of the burner at $\phi = 1.0$ for four different burning velocities: a) $U = 55$ cm/s; b) $U = 60$ cm/s; c) $U = 65$ cm/s and d) $U = 70$ cm/s.....	167
Figure 5-6: Absorbance vs Wavenumber ($\phi = 1.0$, $U = 60$ cm/s).....	168
Figure 5-7: 2D temperature distribution in the channel ($\phi = 1.15$, $U = 50$ cm/s) a) pre-flame region; b) Post-flame region.....	169
Figure 5-8: IR images of burner at four different flow velocities (CH_4/Air ; $\phi = 0.85$) a) $U = 40$ cm/s; b) $U = 45$ cm/s; c) $U = 50$ cm/s and d) $U = 55$ cm/s.....	172
Figure 5-9: Average gas and surface temperatures as a function of x for two different velocities for CH_4/Air flame; $\phi = 0.85$	173
Figure 5-10: IR images of burner at two different burning velocities ($\text{C}_3\text{H}_8/\text{Air}$; $\phi = 0.85$) a) $U = 55$ cm/s; b) $U = 60$ cm/s.....	174
Figure 5-11: Average gas and surface temperatures as a function of x for two different velocities for $\text{C}_3\text{H}_8/\text{Air}$ flame; $\phi = 0.85$	175
Figure 5-12: Cartoon sketch of heat fluxes used in calculation of heat recirculation in the burner.....	176
Figure 5-13: Heat Recirculation as a function of ϕ and U for CH_4/Air	177

Figure 5-14: Comparison between model and experiments of non-D heat recirculation
as a function of S_L^* 179

Chapter 1: Introduction

1.1. Motivation: Chemical Thrusters for Microsatellites

Advances in miniaturizing electronics and hence micro-avionics has resulted in the building of nano/pico satellites (satellites of the mass range of 0.1 to 10 Kg). Smaller satellites are appealing for several reasons. Most of the content presented in §1.1 can be found in Micci's book [1], and is summarized and itemized here. First, a constellation of smaller satellites is less subject to single point failures and hence can be more reliable than a single conventional size satellite. Second, having smaller satellites reduces the payload weight and hence the overall mission cost. It is estimated that about 30% of a space mission cost is usually from the launch costs which in turn depends on the mass of the spacecraft. Some examples [1] of microspacecraft are MightySat-1 (U.S. Airforce), SNAP-1 (Surrey Space Centre, England), and Falconsat (U.S. Air Force Academy).

Such small satellites, however, require small propulsion systems. There are a variety of options which include chemical thrusters, electro-thermal thrusters, cold gas thrusters, Hall thrusters, colloid thrusters, other Electric Propulsion etc. Each type has its merits and demerits and the optimum thruster choice ultimately depends on the particular mission. As will be shown towards the end of §1.1, chemical thrusters are especially desirable for missions requiring a high thrust and relatively low propulsion system weight.

1.1.1. Size Classes of Satellites

Microspacecraft can be further subdivided into classes based on their mass, power consumption, dimensions, etc... Table 1-1 provides a commonly adopted sub

classification for small scale satellites. Generally speaking, the number of propulsion systems from which to choose decreases with the size of the microsatellite.

Designation	Mass, kg	Power, W	Dimension, m
Microspacecraft (A/F European definition)	10 – 100	10 – 100	0.3 – 1
Class I microspacecraft (nanosat)	5 – 20	5 – 20	0.2 – 0.4
Class II microspacecraft	1 – 5	1 – 5	0.1 – 0.2
Class III microspacecraft (picosat)	<1	<1	<0.1

Table 1-1: Definition and classification of microspacecraft (Adapted from Mueller [1])

1.1.2. Missions for Microsatellites

Typical missions for microsatellites include:

- 1) Moving from a central distribution point to set up a large-baseline interferometer
(satellites separated by tens or hundreds of km)
- 2) Stationkeeping within the large-baseline interferometer
- 3) Intercepting another satellite from a parking orbit
- 4) Stationkeeping while in the parking orbit
- 5) Attitude control

The next subsection shows that the thrust requirements are different for each of these missions. The mission of interest in this dissertation is a rendezvous/intercept mission which, as we will see, requires a high thrust/weight propulsion system.

1.1.3. Thruster Performance Requirements

Interferometry missions are defined by their tight attitude control requirements. For example, the Laser Interferometer Space Antenna (LISA) mission consists of three small satellites orbiting the earth in a carefully designed formation. The thrust requirements for this mission are in the range of 2 – 20 μN with an allowable variance of 0.1 μN . These numbers are typical of formation type flying missions. Station keeping missions within constellations require a higher thrust of the order of millinewtons. Rendezvous and intercept missions (which is the focus here) are expected to have the highest thrust requirements with ΔV 's of the order of *several thousands of meters per second*. In addition to the thrust requirement, intercept missions also require *high thrust to weight* to enable higher maneuverability owing to the complexity of the orbital transfers required for intercept. Enabling the development of chemical thrusters with such high thrust to weight ratio requirement is the primary focus of this dissertation.

1.1.4. Available Propulsion Systems

Microthrusters can be subdivided into a few broad categories: chemical thrusters (reactive and cold gas), electric propulsion based, and emerging technologies based (MEMS type). Of these, chemical thrusters are most common and include:

- i) Bipropellant (liquid rocket) engines: Fuel and oxidizer stored separately are burned in a combustion chamber to produce hot gases that are expanded out through a nozzle to produce thrust. These are typically used when high thrust is required.

- ii) Monopropellant (solid rocket) thrusters: Similar in concept to bi-propellant engines except that the propellant (usually a solid) contains both fuel and oxidizer. These are often used in initial parts of launch sequences.
- iii) Cold gas thrusters: Thrust is produced by expanding a stored cold gas through a nozzle. These are usually used in low thrust requirement missions (orientation control).
- iv) Hybrid rocket motors: Liquid or gaseous oxidizer is injected into the combustion chamber which contains a solid fuel. The hot gases are expanded through a nozzle to produce thrust.

Examples of electric thrusters include:

- i) Ion engines: The propellant (typically a noble gas) is ionized in a plasma chamber and accelerated through a charged grid to produce thrust.
- ii) Hall thrusters: Similar to the ion engine except that thrust production is enhanced by applying a magnetic field. This generates a Lorentzian force on the ion stream causing the ions to bombard more incoming propellant and increasing ion density.
- iii) Field Emission Electric Propulsion (FEEP): Conceptually the same as Ion and Hall thrusters and differs only in the production of the ions which occurs via field emission from a liquid metal surface with the metal being the propellant.
- iv) Pulsed plasma Thrusters (PPTs): In PPTs, the propellant is first ionized and then electromagnetically accelerated between two parallel electrodes in pulses.
- v) Resistojets: A liquid or gaseous propellant is heated by a heater element and the hot vaporized gas is expanded through a nozzle to achieve thrust.

vi) Colloid Thrusters: An ionic liquid is accelerated electrostatically to produce thrust. If the ionic liquid is HAN, a colloid thruster can be paired with a chemical thruster to make a hybrid thruster system able to produce high thrust for repositioning and small thrust (high Isp) for stationkeeping [2].

Type	I_{sp} , s	Total system efficiency η , %	Mass, kg	Thrust, mN
Cold-gas Thruster	75	95+	0.01	5
Solid Rocket Motor	185	90+	1.6	10^5
Digital MEMS	200	75	0.04	50
Monopropellant (N_2H_4)	220	95+	0.16	100
Bipropellant	290	-	0.55	22000
PPT	800	10	0.40	500
Hall Thruster	1500	35	1	10
FEFP	8000	25	305	800

Table 1-2: Performance comparison of different types of microthrusters (Adapted from J.H. Schilling [1])

Other emerging technologies in the Micro Electro Mechanical Systems (MEMS) area include combining MEMS concepts with one of the above technologies, like for example a MEMS-based FEFP or MEMS-based cold gas thrusters. MEMS-based technologies involve using various chemical etching processes to form miniature versions – usually in Silicon - of the various thrusters discussed above. One simple example are digital thrusters which consist of tiny wells full of monopropellant. Each well can be ignited individually to produce a small impulse bit. It is beyond the scope of this introduction to delve exhaustively into each of these technologies but a good review of these can be found in [1].

1.1.5. Advantages of Chemical Propulsion

Intercept missions require a high ΔV and more specifically a high thrust to weight (T/W) thruster. From table 1-2, it is clear that chemical thrusters have the highest T/W (of the order of 4 and above) and therefore would be the best choice for these missions.

1.2. Chemical Rockets

In the previous section we concluded that chemical propulsion has the advantage of high thrust to weight ratio compared to the other propulsion options. In this section, the thrust production mechanism in chemical rockets is explained briefly for solid and liquid rocket motors along with the relevant engine cycles etc. Consideration is also given to the performance metrics that characterize chemical rockets.

1.2.1. Thrust Generation

Fig 1-1 is a schematic illustration of a chemical rocket. It consists of a combustion chamber coupled to a convergent-divergent (c-d) nozzle. The propellant is burned in the combustion chamber to produce a high temperature gas that is accelerated as it passes through the c-d nozzle to exit the nozzle at a high velocity (U_e). The pressure is highest in the combustion chamber and decreases as the flow accelerates through the nozzle.

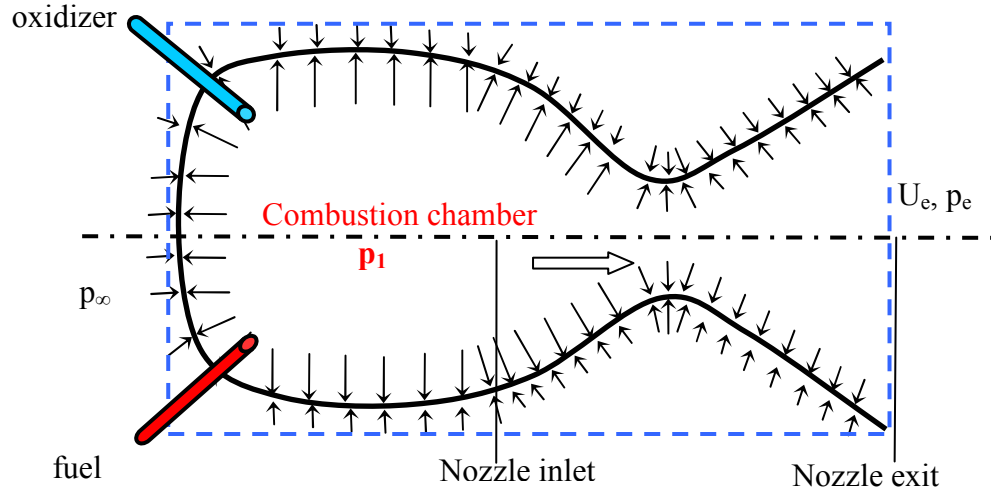


Figure 1-1: Schematic sketch of a thrust chamber for a chemical rocket (adapted from [3])

The thrust can be calculated by performing an integration of forces over the control volume illustrated by the blue dashed lines in the figure. The final expression is given below:

$$T_h = \dot{m} U_e + (p_e - p_\infty) A_e \quad (1-1)$$

T_h is the total thrust produced by the thruster, \dot{m} is the mass flow rate through the thruster, p_e is the exit pressure at the nozzle exit, A_e is the exit area and p_∞ is the ambient pressure (in vacuum this would be close to zero). The equation above shows that for a perfectly expanded nozzle ($p_e = p_\infty$) the thrust is a function of only the exit velocity and the mass flow rate.

1.2.2. Types of propellants

Rocket engines differ from engines used in other vehicles (like cars or airplanes) in that they carry both the fuel and oxidizer on board. This is because they often operate in space where oxygen is not available. Propellants can be broadly categorized into two

types: monopropellants and bipropellants. Monopropellants have both the fuel and oxidizer mixed together (as is the case with solid propellants and some liquid propellants). Bipropellants usually consist of a fuel and an oxidizer stored separately and mixed together in the combustion chamber. In this section we make a slightly different distinction and categorize propellants as either solid or liquid.

i) Solid Propellants: Solid propellants can consist of two or more of the following [ref Sutton]: Oxidizer (Nitrates or perchlorates), Fuel (plastics or metal hydrides), Binders (compounds that combine fuel and oxidizer together in a matrix), Additives (for controlling burning rate), and Inhibitors (to restrict the burning surface). Typically, solid rocket motors form the initial stages of the launch where high thrust is required. A drawback of using solid propellants is that they cannot be stopped once they are ignited. Also, the control of the combustion rate relies on inhibitors and other additives to the propellant mixture. Therefore, combustion control is generally not possible.

Composite solid propellants consist of separate fuel and oxidizer neither of which would burn satisfactorily independently. The oxidizer is usually ground into a small particles and dispersed in a fuel matrix. *Homogenous* propellants are capable of combustion in seclusion. These are often unstable chemicals such as nitroglycerin in which the oxidizer occurs bonded to the fuel. Some typical solid propellants and their properties are listed in table 1–3 below.

Oxidizer	Fuel	ρ (g/cm ³)	$T_{\text{comb.}}$ (K)	c^* (m/s)	M_{wt} (kg/mol)	I_{sp} (s)
Ammonium Nitrate	11% binder and 7% additives	1.51	1282	1209	20.1	192
Ammonium perchlorate 78-66%	polymer binder and 4-20% aluminum	1.69	2816	1590	25.0	262
Ammonium perchlorate 84-88%	12% polymer binder and 4-20% aluminum	1.74	3371	1577	29.3	266

Table 1–3: Theoretical performance of typical solid rocket propellant combinations (Adapted from [1])

Broadly speaking the manufacturing process for composite propellants involves grinding of oxidizer crystals, mixing of appropriate quantities of oxidizer and fuel along with additives and inhibitors (usually in a batch), casting of the grain (into the desired shape) and curing it usually by heating. For homogenous propellants the process involves using a solvent in which the propellant and additives may be added and mixed together and then cast into the desired shape and dried by evaporation of the solvent.

ii) Liquid Propellants: Liquid propellants can be produced as mono or bipropellants. Monopropellant liquids have both the oxidizing agent and the combustible substance together. An example of this would be hydrogen peroxide or hydrazine. Table 1 – 4 gives properties of some common liquid propellants.

Oxidizer	Fuel	Avg. specific gravity	Chamber T (K)	Chamber c^* (cm/s)	M_{wt} (kg/mol)	I_{sp} (s)
Oxygen	Methane	0.81	3526	18355	18.3	296
Oxygen	Hydrogen	0.26	2959	2428	8.9	386
Oxygen	UDMH	0.96	3542	1835	19.8	295
N_2O_4	Hydrazine	1.20	3258	1765	19.5	283
H_2O_2 (90%)	RP-1	1.29	2760	21.7	21.7	297

Table 1-4: Theoretical performance of typical liquid rocket propellant combinations (adapted from [3])

Monopropellants are typically stable at room temperature and pressure but decompose when heated or reacted with a catalyst exothermically to produce hot gases. Bipropellant liquids are those in which the oxidizer is separate from the fuel. Typical examples are liquid hydrogen/oxygen, kerosene/oxygen etc. Liquid propellants are typically used in booster stages and a few second stages. Liquid propellants are more attractive than solid propellants because the combustion process can be controlled and even stopped by varying the propellant flow rates. Liquid propellants also have a higher I_{sp} than solid propellants. The desirable properties for liquid propellants are high specific gravity (or density) for compact storing and high I_{sp} .

1.2.3. Rocket Cycles

Solid and liquid rockets have vastly different cycles of operation. Solid rocket motors have a simpler cycle as compared to liquid rocket motors (discussed next). Solid rocket motors usually consist of a chamber inside which the solid propellant is cast in a given shape (star, cylindrical etc), an igniter (controlled electronically) to ignite the propellant, a cavity to accumulate the hot gases, and a nozzle attached to the chamber through which

the hot combustion gases expand to produce thrust. The chamber is a pressure vessel capable of withstanding large pressures. A typical chamber pressure is ~200 bar.

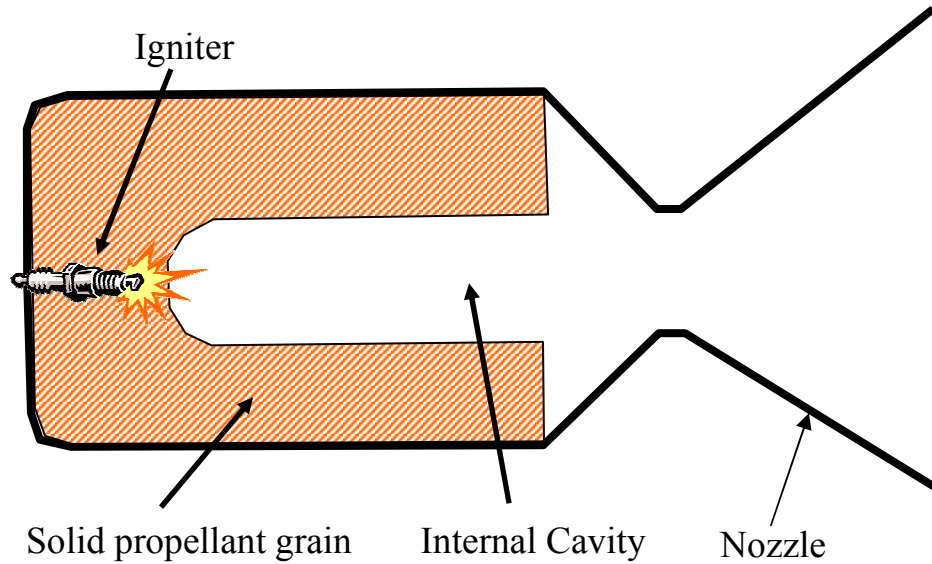


Figure 1-2: Sketch of solid rocket motor: Lateral view.

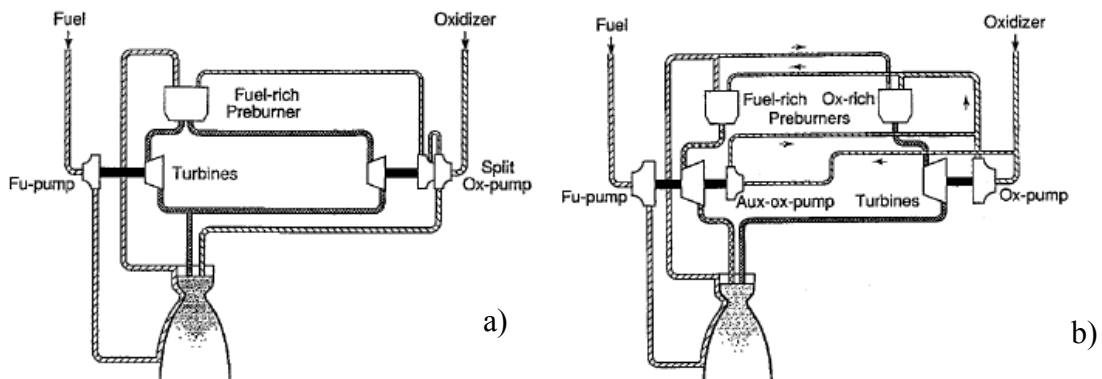
Solid rocket motor cycle can be broken into three time sequence intervals: 1) Ignition time lag: This is the time taken from receiving an electrical signal to the igniter to the actual commencement of ignition, 2) Flame spreading interval: As the name suggests this is the time taken for the flame to spread throughout the burning surface till the grain area is starting to burn and 3) Chamber filling interval: The time required to fill the internal cavity to reach initial equilibrium chamber pressure and flow rate. The burning rates of the solid propellants are usually characterized using the chamber pressure given by a power law as:

$$r = a p^n \quad (1-2)$$

In this expression, r is the rate of burning, p is the chamber pressure and a is an empirical constant dependent on temperature. As discussed previously, typical solid rocket motors

are single-use. Once the propellant is ignited, the combustion process does not stop until the propellant grain is completely burned.

Liquid rocket engines are more complex than solid rocket motors and require a system of pumps (to deliver the fuel and oxidizer to the combustion chamber) and turbines (to drive the pumps). These are usually turbo-pumps that are driven by the exhaust of a separate gas generator which runs fuel rich. There are many different rocket cycles but they all fall into two broad categories: open and closed. In the open cycle, the turbopump exhaust is either expanded separately in its own separate nozzle or added to the main nozzle in the expanding section after the throat. This is a slightly less efficient cycle than the closed cycle in which the turbopump exhaust (which contains unburned fuel) is fed into the combustion chamber to react completely. A few types of open and closed cycles are illustrated in Figure 1-3 and described below. Much more extensive discussions are available elsewhere[4].



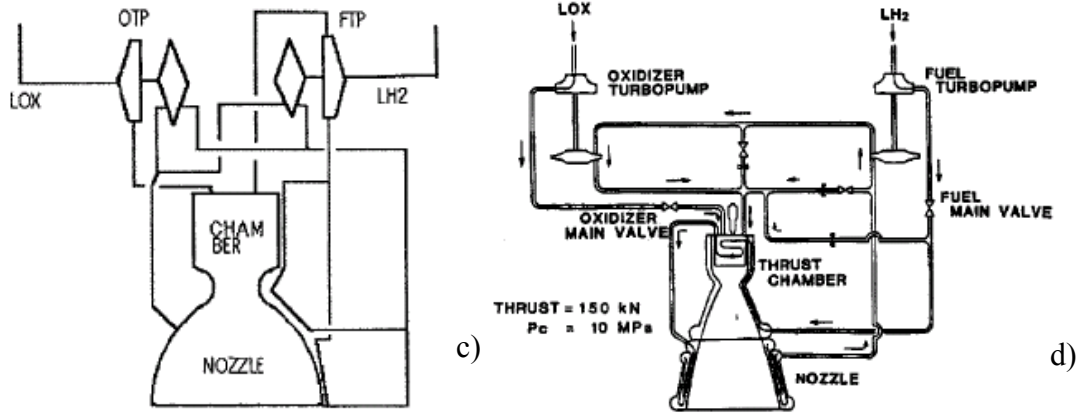


Figure 1-3: Liquid Rocket Turbopump Cycles: a) Fuel rich staged combustion cycle; b) Fuel and Oxidizer rich with auxillary pumps; c) Simple expander bleed cycle d) Expander cycle with internal heat exchanger [4]

i) Staged combustion cycle: This is a closed cycle and in which a pre-burner is employed to generate power to drive the turbines that operate the fuel and oxidizer pumps. Fig. 1-3 a shows a simple staged combustion cycle involving a fuel rich pre-burner which drives two turbines which in turn operate the fuel and oxidizer pumps. Fig 1-3 b shows a more advanced version of this cycle wherein two separate pre-burners are employed (one fuel rich and one oxidizer rich) with an auxiliary pump to deliver fuel/oxidizer to the pre-burners. In both cases the exhaust from the turbines are fed into the combustion chamber and burned to extract all of the remaining energy from it before expanding the flow through the main nozzle.

ii) Expander cycle: Expander cycles are open cycles in which the working fluid (usually liquid H_2) is used to cool the nozzle (see Fig 1-3 c and d). It is vaporized during this process and drives the turbopump which, in turn, pumps the fuel and oxidizer into the combustion chamber. The exhaust from the turbopump is injected into the expander portion of the nozzle to extract some thrust out of it. However, part of the energy in the

working fluid remains untapped as unburned fuel is not combusted. The advantage of expander cycles is their relative simplicity and fewer components (no pre-burner) which assist in lowering the weight. But, their performance is poorer than staged combustion cycles as they not extract the maximum energy from the propellants.

1.2.4. Principles of Operation

So far we have seen some important features of chemical rockets such as thrust production, types of propellants, and operational cycles each in a separate manner. In this subsection it is attempted to present the complete operational principles of a chemical rocket drawing upon the previous three subsections and integrating them. Let us start with a generic liquid rocket, as our motivation is to understand maneuverable chemical thrusters, and sequentially breakdown the entire operational procedure.

i) Mixing of fuel and oxidizer: The starting point in the operation would be to employ turbopumps as described in the liquid rocket cycles and bring fuel and oxidizer from the tanks in which they are stored to the combustion chamber with the desired flow rates to achieve maximum combustion efficiency. Next, the fuel and oxidizer need to mix and mixing length studies in the past (simple Burke-Schumann [5] for gas phase mixing) and more recent liquid impingement and mixing in the presence of turbulence ([6] and [7]) have developed methods to achieve rapid mixing to reach stoichiometric proportions in the shortest possible length.

ii) Ignition and flame propagation: Once the fuel and oxidizer have mixed the next step is to ignite them and achieve a stable combustion front to burn them and extract the energy stored in the chemical bonds of the fuel and oxidizer to produce hot combustion gases. Ignition studies have been undertaken ([8] and [9]), to provide a detailed

understanding of the ignition process. Combustion studies (discussed in literature review) focus more on the understanding of flame propagation once ignition has been achieved. In this dissertation the emphasis will be placed on understanding the processes responsible for enhancing the burning rate and flame stabilization in microscale combustors such as might be used in a small scale chemical thruster

iii) Flow acceleration and Thrust: As seen in the earlier subsection the main thrust producing mechanism in chemical rockets, which is the next step once combustion produces hot gases, is to expand the flow through a c-d nozzle. Micronozzle studies (discussed in literature review) analyze the performance of nozzles as the scale of the device is reduced. Some important considerations involve 3-D effects, boundary layer growth and heat transfer to the nozzles structure from the hot gases.

iv) Cooling: Finally it is required to have a reliable way of cooling the nozzles structure to prevent structural disintegration owing to excessive heating. One way is to extract the thermal energy using a coolant on the outer surface and use that energy to drive turbines as is done in the expander cycles. Another way to cool is by film cooling [10]. Film cooling is done by injecting a coolant fluid along the internal walls of the nozzle parallel to the flow direction. The injected film forms a jacket over a certain finite length and prevents the hot gases from coming in direct contact with the nozzle walls.

1.2.5. Performance Metrics

There are three standard metrics of chemical thruster performance that are worth summarizing in preparation for the next section which discusses performance scaling. The effective exhaust velocity (c) is defined as the average equivalent velocity at which the propellant is ejected from the vehicle. The specific impulse (I_{sp}) is defined as the total

impulse per unit weight of propellant. The characteristic velocity (c^*) is a measure of the combustion efficiency. Equations for these quantities are presented below where A_e is the exhaust exit area, \dot{m} is the total flow rate, p_e is the exhaust pressure, p_∞ is the ambient pressure, and p_t is the combustion chamber pressure.

$$c = U_e + (p_e - p_\infty) A_e / \dot{m} \quad (1-3)$$

$$I_{sp} = \frac{T}{\dot{m} g_0} = c / g_0 \quad (1-4)$$

$$c^* = p_t A_t / \dot{m} \quad (1-5)$$

c is a metric that gives the overall thrust of the combustor per unit flow rate, but it is still a dimensional quantity (dimensions of velocity). In most places, c is replaced with I_{sp} which indicates thrust per unit weight flow rate of fuel. High I_{sp} thrusters can produce higher thrust over short time spans but are usually less efficient than low I_{sp} thrusters. c^* characterizes the burning rate of the propellant and is a characteristic of the combustion efficiency.

1.3. Scaling of Chemical Thruster Performance with Size:

There are several factors that distinguish micro-scale combustion from conventional-scale combustion. These are described in the next three sections along with the potential impact(s) on thruster performance.

1.3.1. What changes when you miniaturize?

- i) Increased Importance of Heat Loss

The energy release in a combustor is proportional to the volume of the device whereas the heat losses are proportional to its surface area. As the scale of the combustor is reduced, the surface area to volume ratio increases as the inverse of the characteristic length scale. This is illustrated for cylindrical and rectangular cuboid combustors in figure 1-4.

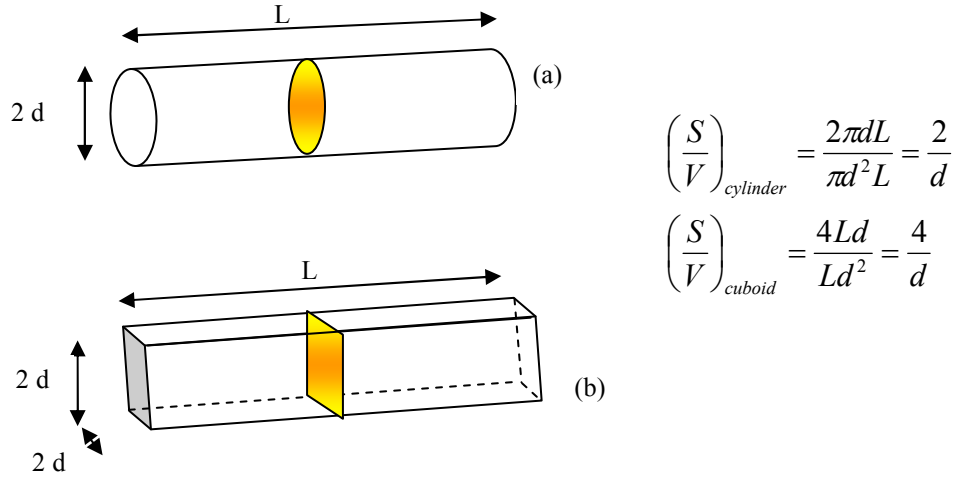


Figure 1-4: Scale analysis of microscale combustors, a) Cylindrical b) Cuboid

Since heat losses scale with surface area, it becomes apparent that the heat losses increase as the scale of the device is reduced.

In early attempts at characterizing combustion in small devices, it was argued that the heat losses would dominate and hence combustion would not be possible below a certain characteristic dimension (“quenching diameter”). The quenching diameter was defined to be that diameter at which the heat losses from the surfaces exceeded the amount of heat released at the flame thus preventing the propagation/stabilization of a flame. Critics of micro-combustion often reference the quenching diameters reported in the classic work of Lewis and Von Elbe [11] (where the concept of quenching diameter was originally proposed) as the smallest possible length scale for combustion. What they fail to

understand is that the quenching diameter is not a fixed property of a fuel-air mixture but rather is a property of a burner that is determined by how easily heat is lost to the environment. Therefore, the quenching diameters observed by Lewis and Von Elbe will be different from those observed by others in different burners. What really matters is the combustion mode and the amount of heat loss to the environment.

ii) Flame Stabilization via Heat Recirculation:

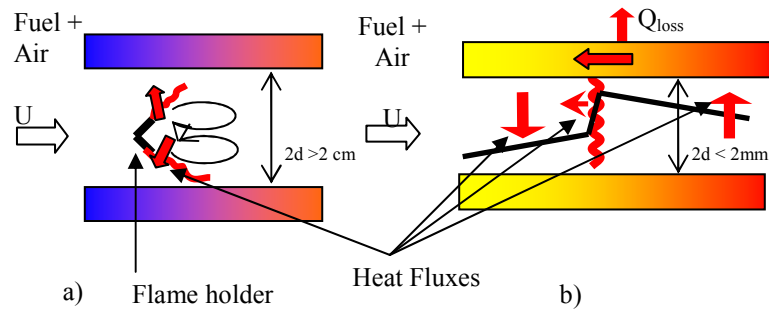


Figure 1-5: Illustration of flame holding in combustors a) Conventional Scale, b) Microscale

Figure 1-5 shows how flames are stabilized in conventional and microscale combustors. In a conventional scale combustor (Fig. 1-5 a), the flame is often stabilized using a flame holder which is essentially a protruding structure in the flow. Recirculation zones form behind it as shown by the circular arrows and provide a mechanism for transferring heat from combustion products to the incoming reactants and causing them to ignite and burn. In microscale combustors (shown in Fig. 1-5 b), the combustor wall assists in pre-heating the incoming mixture. The competition in microscale devices is really between how much of the heat that enters the structure of the combustor is lost to the environment and how much is recirculated.

The thermal resistance of most typical materials used to build combustor devices is several orders of magnitude lower than the gas, and the thermal coupling between the gas and structure is much stronger at the micro-scale. Thus, the wall is expected to play a much more important role in flame stabilization than in conventional-scale systems. Figure 1-6 illustrates the role of the wall in a microcombustor and the competition between axial conduction and heat loss to the environment.

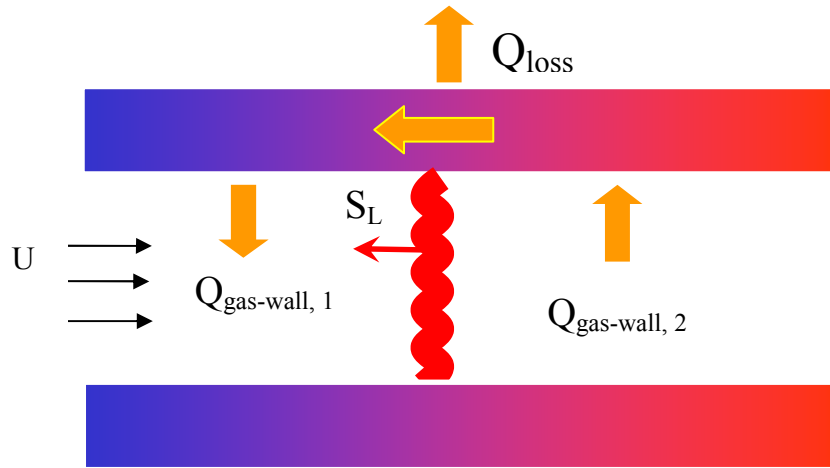


Figure 1-6: Depiction of the role of the wall in a microcombustor

It can be easily verified (from a simple energy balance) that in such small combustors the heat going into the wall from the hot post combustion gases should equal the sum of the heat recirculated back to the pre-flame gases and heat losses. This is shown in the equation below.

$$Q_{gas-wall,2} = Q_{gas-wall,1} + Q_{loss} \quad (1-3)$$

This was the missing piece of information when “quenching diameter” based arguments were used to show flames cannot be stabilized in microscale devices. The heat recirculation actually increases the flame speed which in turn increases the heat release. However, this increased flame speed comes with the cost of flame broadening thus

increasing the length of the combustors and hence increasing the weight. This will be discussed later. This increased rate of heat release is of particular engineering interest if we are able to make use of it to increase a combustor's power density.

iii) Low Peclet Number:

Past research [12] and [13] has concluded that the flow Peclet (Pe) number would be an important parameter for distinguishing micro/mesoscale regimes from the macroscale regime. The Pe number is defined as

$$Pe = Re Pr = \left(\frac{\bar{U}d}{\nu} \right) \left(\frac{\nu}{\alpha} \right) \quad (1-4)$$

where Re is the Reynolds number, Pr is the Prandtl number, α is the thermal diffusion coefficient, ν is the coefficient of viscosity, d is the characteristic length (channel width or diameter of the tube), and \bar{U} is the average flow velocity at the inlet.

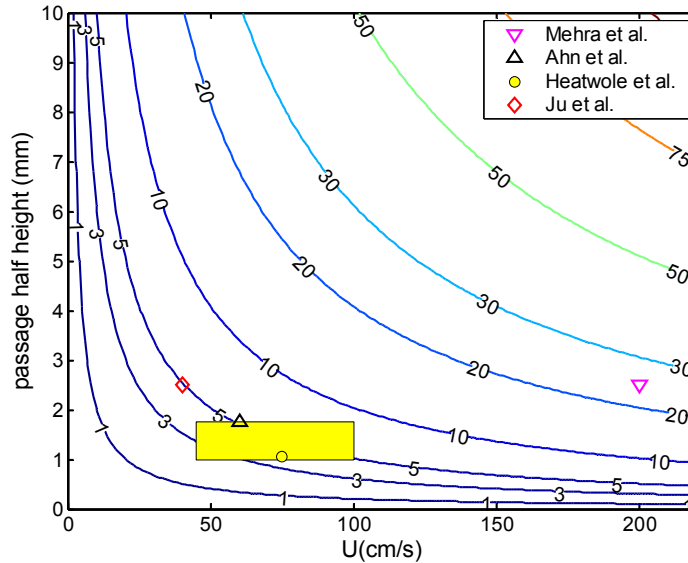


Figure 1-7: Contours of Peclet number as a function of flow velocity (U) and passage height (d) ([14], [15], [16] and [17])

Physically, Pe is the ratio of convective to conductive heat transfer. In large Pe flows, convective heat transfer dominates conductive heat transfer while in low Pe flows the opposite is true. As can be seen from Eq. 1-4, the Pe number includes the effects of the flow velocity and the passage height simultaneously. Another way to think of the Pe is to think of it as the ratio of conductive to convective timescales. Low Pe numbers indicate large convective timescales and therefore have either low flow velocities, small passages, or both. Therefore, in micro-scale devices heat conduction (both axial and transverse) plays an important role in heat transfer.

Figure 1-7 shows contours of Pe as a function of the flow velocity and passage half height. The symbols represent some of the micro/mesoscale devices that have been built [14-17]. These will be discussed later. Based on the figure, it seems reasonable to conclude that $Pe < 30$ would characterize most micro-combustors. For the purposes of our work we assume that Pe numbers below 30 characterize micro/mesoscale devices.

1.3. 2. Impact of Reduced Scale on Thruster Performance:

The concepts introduced in the previous subsections have shown that there are tradeoffs when we attempt to scale down in size. First, the problem with heat loss needs to be addressed if we are to build viable thrusters. Second, flame speed enhancement owing to heat recirculation could be beneficial to increase thrust and could offset increased heat loss. Third, we need to have reliable metrics to show that performance is indeed improved as we scale down. Fourth, we need to have a complete understanding of how the tradeoff between heat losses and heat recirculation occurs and identify the main governing parameters that influence this tradeoff.

1.3.3 Key Barriers to Developing Practical Micro-Chemical Thrusters

Some of the principal problems preventing the realization of high performance microscale thrusters currently are: 1) Very short mixing length requirements 2) Incomplete understanding of combustion process and burning rate control in situations where the wall plays a prominent role 3) Thermal issues related to structure 4) The performance of micro-scale nozzles and 5) Lack of instrumentation to make measurements.

1.3.4. Problem of interest in this thesis

This dissertation will focus on understanding flame propagation in small channels.

1.4. Previous work:

Flame stabilization in a microchannel - contains elements of three broad classes of physical phenomena:

- 1) Heat transfer: It has just been shown that distinguishing aspects of micro-scale combustion are the strength of conjugate heat transfer between gas and wall (thermal coupling), heat transfer from one part of the structure to another, and heat loss to the environment.
- 2) Coupled heat and mass transfer with chemical reaction: Heat and mass transfer processes supply the energy and reactants necessary to initiate and sustain chemical reaction.
- 3) Practical Applications/Limitations: Ultimately, our understanding of flame stabilization at the small-scale must be used to develop and demonstrate practical miniature chemical thrusters.

Apart from these, a fourth related piece is the development of diagnostic techniques suitable for making measurements in small volumes of hot, chemically reacting flows. Therefore, it is important to review previous work in each of these areas in order to characterize the current state of the art and identify the important research challenges.

1.4.1. Heat Transfer Modeling

A simpler view of the microcombustion problem is the heat transfer problem associated with a combustion wave in a duct. This approach is useful because it allows us to investigate heat transfer effects separately. Earlier heat transfer analyses in ducts can be traced back to the classical paper by Graetz [18] that investigated heat transfer to a gas in a duct with isothermal walls. He derived an expression for the Nusselt number (heat transfer number) as a function of the streamwise coordinate. However, Graetz's formulation did not account for the axial conduction of heat through the gas. This was probably because he was developing solutions for heat exchanger configurations where most of the heat transfer occurs between the gas flow and the wall in a direction perpendicular to the flow direction¹. Sellars et al. [19] extended Graetz's work to account for a variety of boundary conditions (constant wall temperature, prescribed wall temperature, and prescribed wall heat flux etc.) in both rectangular and circular ducts. However, axial conduction through the gas was still not included. The focus was on obtaining Nusselt number relations for various duct geometries with different boundary conditions. Following this, analyses by Ebadian and Zhang [20], Michelsen and Villadsen [21], Telles et al. [22], Lahjomri and Oubarra [23] considered the extended Graetzian

¹ Note that the classical theory for flame propagation (discussed in §1.4.2) is based on conduction of heat in the streamwise direction via the gas so this effect is important to include in reacting flows.

problem with axial heat conduction (in the gas) for various wall boundary conditions. The applications were for heat exchangers at either the conventional or micro-scales. A good summary of the work done in this area is given in the book by Kakac [24].

The heat transfer discussed so far focused on heat exchangers which influenced the types of boundary conditions imposed at the walls. In many cases however, heat transfer between the fluid and wall along with heat transfer within the structure of the wall itself are important. Jarosinski [25] analyzed heat transfer between hot combustion products and a cold wall in ‘limit flames’ by developing an analytical model. The author defined ‘limit flames’ as those that are close to being extinguished via excessive heat loss to the wall. The heat transfer between the wall and the fluid was modeled by means of a convective transport term. One of the chief results was the development of a relationship between the Nusselt number (Nu) and the Peclet number for post combustion heat exchange between hot products and the cold wall for plug flow². This analysis was quasi 1-D as the heat transfer between the gas and the wall was modeled based on a convective heat transfer coefficient.

² Chapter 2 provides the Nu as a function of various flow parameters (from our heat transfer models) for parallel plate channels with a premixed laminar flame stabilized inside the channel for both pre and post-flame regions.

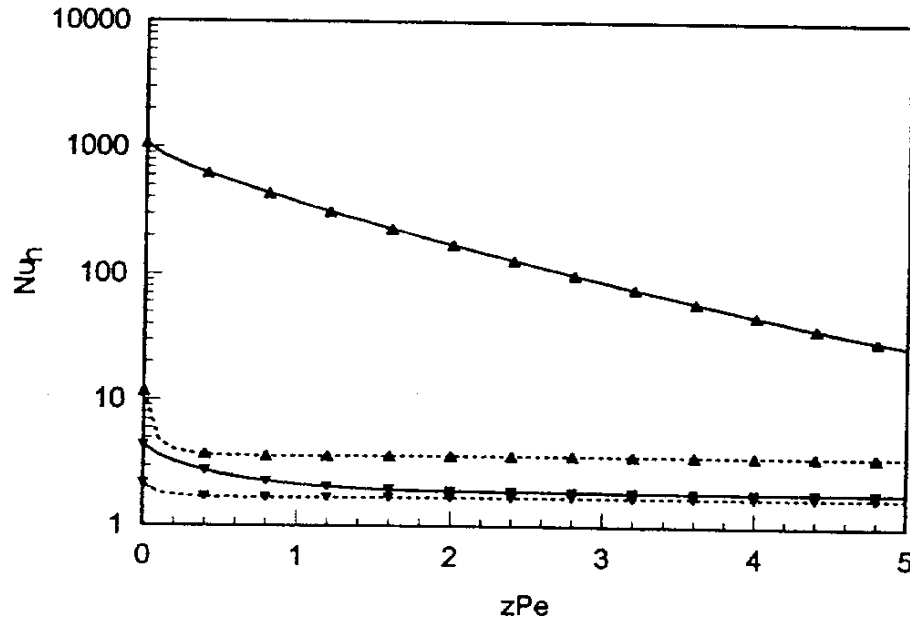


Figure 1-8: Nusselt number at the outer surface (Nu_h) as a function of zPe for pipe Poiseuille flow. $h = 2$, $Pe = 5$, $k_s/k_f = 243$ (upright triangles), and $k_s/k_f = 1$ (inverted triangles). The solid and dashed lines correspond, respectively, to cases when axial conduction is accounted for and cases when it is neglected [26]

Yin and Bau [26] developed an analytical model for heat exchange in small ducts and channels considering plug and Poiseuille flows. They solved the conjugate heat transfer problem by accounting for heat exchange between the wall and the fluid. Two outer wall boundary conditions, constant temperature and constant heat flux, were considered. The governing equations were solved as an eigenfunction expansion in which the coefficients were calculated implicitly. The solution was used to relate the outer boundary Nusselt number to the Peclet (Pe) number and the stream wise coordinate.

Figure 1-8 [31] shows the variation of the outer wall Nu_h as a function of the non-dimensional flow coordinate (zPe). The figure shows that Nu_h depends strongly on the

zPe number for low zPe for conductive walls and that ignoring axial conduction in the wall can give erroneous results. Nu_h tends to a constant value at large zPe values.

More recently Maranzana et al. [27] performed extensive analyses of heat transfer in micro and mini heat exchangers with passage heights of the order of 10 mm to a few mm. They included heat transport via the structure of the heat exchanger and introduced a new non-dimensional number M to indicate the fraction of the total heat transfer that occurred via axial conduction through the walls. This was done in order to emphasize the importance of axial heat transfer through the walls in small scale heat exchangers.

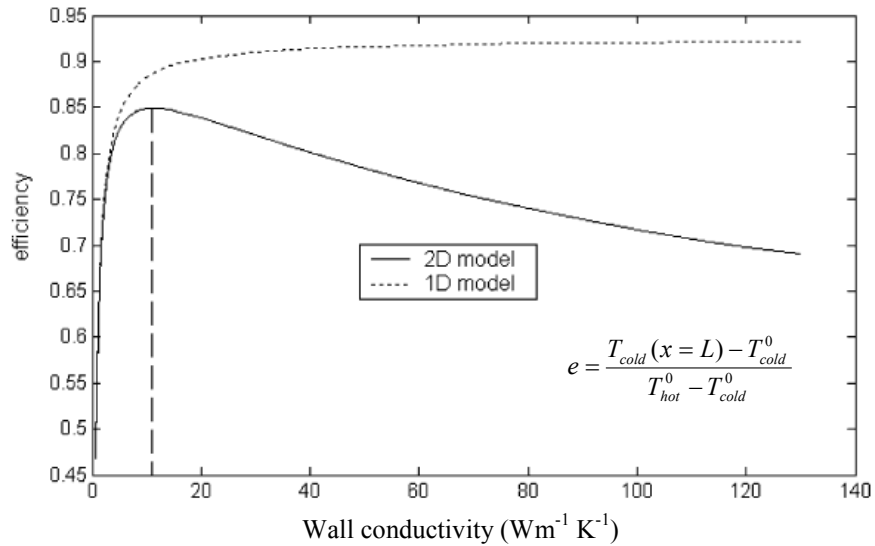


Figure 1-9: Exchanger efficiency as a function of the wall conductivity [27]

Figure 1-9 shows the efficiency as a function of wall thermal conductivity for 1-D (no axial heat conduction) and 2-D (allowing for axial conduction) models. The numerator in the definition of efficiency (e) is the change in temperature of the cold fluid flow as it passes through the length of the heat exchanger and the denominator is the starting point temperature difference between the hot and cold flows. It can be clearly seen that 1-D model over predicts the efficiency. Thus, as we scale down in size it becomes increasingly important to account for the two-dimensionality of the heat transfer process.

Another important consideration is that microcombustors need to be as small as possible. Therefore, flow within them will probably not be fully developed (thermally and or hydrodynamically) and entrance effects are expected to be important. Hsu [28] studied a complex entrance effect problem that accounted for both the transverse non-uniformity in the velocity field and axial conduction in the gas. In 1992 Silva [29] et al. investigated the simultaneous development of 2-D temperature and velocity profiles in a channel formed between two infinitely long parallel plates. They developed a linearization procedure for the velocity and that decoupled the energy equation and solved it using integral transforms. More recent studies (Nield et al. [12]) have focused on thermally developing flow in porous media.

The common thread in all of the heat transfer studies described above is that they start with the classical Graetzian problem and then adapt themselves for the particular problem of interest. Modern extensions to the Graetz problem also usually account for axial conduction in gas and transverse variations in velocity and temperature.

1.4.2. Combustion

i) Conventional Scale:

One of the earliest theories of flame propagation (1883) was that of Mallard and Le Chatelier [30]. It was based on a simplified heat transfer model that accounted for heat transfer from the “hot flame” to the cold reactants via conduction through the gas. In 1941, Zel’dovich [31] showed that there was a minimum radius for tubes below which premixed flames were unable to propagate and extinguished; this got termed as the “quenching diameter”. Following this, Spalding [32] developed a non-adiabatic theory for flame propagation in ducts that accounting for heat loss to the outer environment by

adding a simple loss term to the formulation. He showed that two flame speeds exist for every “condition” (namely mixture composition and heat loss value) and that the higher of the two values was the stable solution. However, his model only accounted for heat loss. No heat recirculation was present, and the predicted flame speeds were always less than the freely propagating flame speed. It is noteworthy that this simple model still managed to capture the qualitative behavior of flame propagation shown by later extensive research (to be described shortly). In the late 1970’s Takeno et al. ([33] and [34]) studied excess enthalpy flames first theoretically and then experimentally (described later). They demonstrated that heat recirculation through a combustor’s structure (in this case a porous medium or a packed bed) was a primary mechanism for stabilizing the flame. “Excess enthalpy flames” were also studied extensively by Weinberg, a good account of which can be found in his text book [35]. He observed that heat recirculation made it possible to get super-adiabatic flames where the flame temperature is significantly higher than the adiabatic flame temperature.

ii) Microscale:

Microscale combustion research is much more recent compared to the classical flame theories and experiments just described. Daou and Matalon (2002) [36] studied the influence of heat loss from the gas to the wall on premixed flames in non-adiabatic channels (i.e. channels that lost heat to the environment via the outer wall). They developed an extinction map that showed that heat losses to the walls could partially or completely extinguish the flame. In 2003, Ronney [37] developed a 1-D model of a heat recirculating burner and showed that heat conduction within the structure is the main process governing flame stabilization. Ju and Choi in 2003 [38] analyzed the role of heat

recirculation by studying oppositely propagating flames in channels sharing a common wall. This enabled them to represent heat transfer through the wall using a quasi 1D model. They showed that two flames were possible and that the higher speed was stable. Cui et al. [39] considered heat loss and showed that the burning rate of flames stabilized in meso/microscale channels no longer depends on the Lewis number.

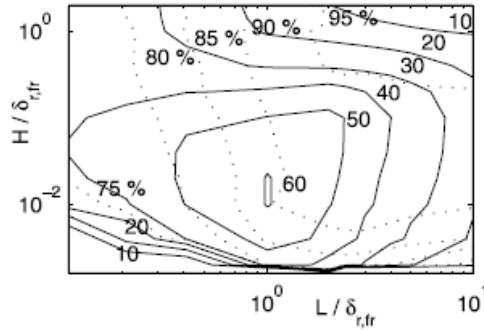


Figure 1-10: Non-adiabatic H₂–air combustion in a silicon micro-channel; $\Phi = 0.5$, $P = 1$ atm, $h_{env} = 1$ W/m² K. Solid lines, contours of non-dimensional power density ($\dot{w}_D / \dot{w}_{D,ref}$) as a function of non-dimensional channel height and length. Dashed lines, contours of overall efficiency [40].

Work by Leach et al. in 2004 [40] has also shown that axial conduction of heat through walls plays a major role in determining micro-combustor performance. They modeled the coupled heat transfer problem between wall and gas using a thermo-electric analogy and solved the resulting heat transfer resistance network. Figure 1-10 is one of their key results, which shows that there is an optimum passage height and length combination for the combustor that gives maximum efficiency along with a high power density.

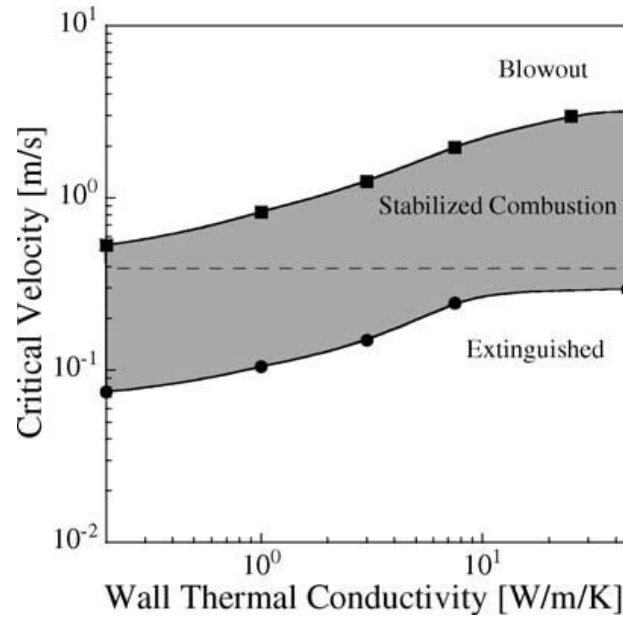


Figure 1-11: Critical velocity vs wall thermal conductivity. The lower curve (●) represents stability loss due to insufficient heat generation. The upper curve (■) represents blowout. The shaded region allows stabilized combustion. The experimentally determined laminar flame speed is plotted as a dashed line [41].

Norton and Vlachos in 2004 [41] developed a 2-D numerical simulation of premixed hydrocarbon flames (Methane/Air and Propane/Air) in micro-channels using *Fluent*. The simulation accounted for conjugate heat transfer via the structure of the combustor and reaction chemistry using a single step model. The heat loss to the outer environment was modeled using Newton's law of cooling via a single heat transfer coefficient that accounted for all the heat losses together. They showed that there exists an optimum thermal conductivity (close to that of common ceramics) that gives the maximum flame speed. This optimum occurs due to the tradeoff between heat loss and heat recirculation. Figure 1-11 shows that the stability limit is broadened when the thermal conductivity of the wall material is increased. Using a simple 1-D numerical model (with full reaction chemistry) of a flame held between two infinitely long plates, Leach and Cadou [42]

showed that axial conduction through the structure and distributed heat transfer between gas and structure causes the reaction zone to broaden and the burning velocity to increase. Schoegl and Ellzey [43] used a semi-analytical model to revisit the problem of two flames propagating in two channels sharing a common wall similar to earlier work by Ju. They studied both co-flow and counterflow configurations where heat conduction through the wall separating the two channels was accounted for. They concluded that the counter-flow configuration was superior to the co-flow configuration in that flammability limits were considerably broader and higher and the flame speeds were higher.

While these model problems are interesting and illuminating, most practical configurations feature a single flame stabilized in a channel that loses heat to the environment. These are more challenging to model because heat recirculation and heat losses occur together and hence cannot be decoupled. In 2007, Barrios et al. [44] developed a numerical model employing two-step chemistry to estimate the quenching diameter in small channels. They concluded that the heat loss and not radical quenching was the primary reason for extinction of flames. More recently Kim (2009) [45] studied flames in conductive tubes assuming that there exists a critical length scale upstream where thermal gradients in the radial direction are insignificant. This allowed the combustor to be split into 1-D and 2-D regions. It was shown that the propagation velocity of the flame depends strongly on parameters such as the velocity profile adopted at the inlet and the pre-heating of the inlet stream. Plug and fully developed flow profiles (termed in their work as “slip” and “no slip”) were examined along with three different temperature heating values. They concluded that the propagation velocity of the flame increased as the inlet temperature was increased (the equivalent of pre-heating by heat

recirculation) and that the effect was more significant for fully developed flow profiles. This implies that the heat transfer is impacted in the pre-flame region based on the choice of the velocity profile.

On the experimental front, early microcombustion work dates back to Kotani and Takeno [46], who studied microcombustion in a stack of ceramic tubes. They showed that heat recirculation through the perforated tubes enhanced flame stability. Churchill [47] in 1989 did further experimental studies that showed that thermally stabilized combustion was possible in small passages. Ahn et al. [15] built and tested a swiss roll combustor and explored the effect of using a platinum catalyst for flame stabilization. Figure 1-12 shows the swiss-roll combustor that was used. They showed that the use of the catalyst increased the stability limits and allowed combustion at very low Re (~ 1) compared to the situation without a catalyst ($Re \sim 40$).

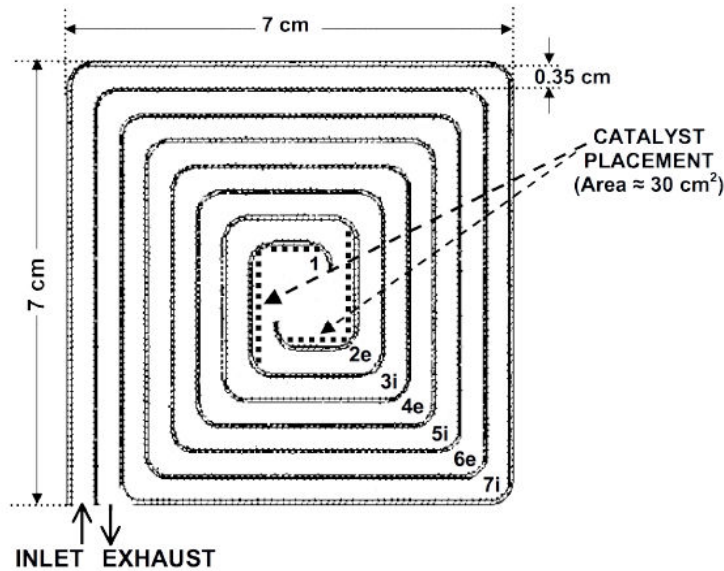


Figure 1-12: Plan view of the Swiss roll burner. Platinum catalyst strips were placed as shown when used. Thermocouples 1-7 were located in the exhaust ‘e’ and inlet ‘i’ turns as indicated [15].

Ronney et al. [48], [49] (2001-2002) have built heat recirculating burners for use with thermoelectric generators. The burners are a ‘Swiss roll’ designs and work by allowing heat to be exchanged between product and reactant streams. The counter-current heat exchanger design greatly reduces heat loss to the environment as most of the surface is exposed to cool reactants and most of the heat goes to preheating rather than being lost to the environment. Heat recirculation also widens the flammability limits of the burner by preheating the incoming reactants. While thermoelectric materials are relatively inefficient in converting heat to electric power, the Swiss roll design has the advantage of high thermal efficiency without the need for moving parts.

Ju and Xu [17] studied the propagation of methane/air and propane/air flames in a tube reactor and measured flame speeds using a high speed camera. They concluded that both fuels had multiple extinction limits and flame regimes and that the flame speed had a non-monotonic dependency on equivalence ratio. They also showed that the channel influenced the type of transition between slow and fast flames.

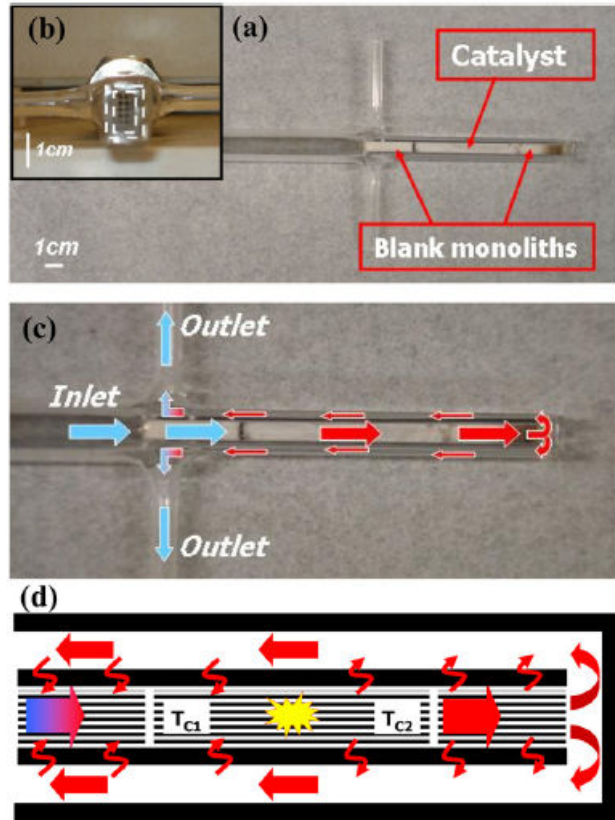


Figure 1-13: Quartz heat recirculation reactor (HRR). (a) Catalyst and thermal shields position. (b) Cross-section of the reactor. (c) Flow direction in HRR mode. (d) Schematic of HRR mode: heat flux direction and thermocouple positions. [50]

Scarpa et al. [50] experimentally studied the effect of heat recirculation on self sustaining catalytic combustion. They burned propane/air mixtures in a quartz reactor (Figure 1-13) with outer tube dimensions of 14.6 mm x 10.6 mm and inner tube dimensions of 10.6 mm x 6.6 mm. The wall thickness of both tubes was 1.3 mm. They compared the results of the heat recirculating reactor (HRR) with a non heat recirculating reactor (NRR) and showed that the flames experienced enhanced stability in the HRR. They also showed that the NRR was operating in the blow out regime and was quenched

owing to insufficient pre-heating. The catalyst widened the stability limits by lowering the critical equivalence.

Taken together, the survey of the heat transfer and combustion literature (both theoretical and experimental) has shown that 2-D heat transfer models which can account for conjugate heat transfer between wall and gas are required.

1.4.3. Microscale Energy Conversion Technologies:

i) Microthrusters

Some of the previous micro-thruster work found in the literature on coupling of heat transfer and combustion suggests that microscale chemical thrusters would be strongly affected by heat loss to the environment. Rudnyi et al [51] proposed that any model for the operation of a microthruster should include an electro-thermal process for ignition, sustained combustion, membrane rupture, and gas dynamics. They developed a strategy for rendering these sub-models computationally tractable and hence practical for system simulation. Table 1-5 shows some of the models they considered in their modeling strategy.

Task	Available models	Modelling strategy
Electro-thermal ignition	1) Coupled Poisson and heat transfer equations, Eqs (1) to (4). 2) Lumped resistor and heat transfer, Eqs (3) and (5). 3) Lumped heat transfer.	The lumped resistor and 3D heat transfer model discretized with the finite element method and followed by a model order reduction.
Ignition and sustained combustion	1) Detailed chemical kinetics. 2) QSHOD. 3) Adiabatic flame temperature.	Experimental ignition temperature as input to the electro-thermal ignition problem, experimental burning rate and flame properties as inputs to gas dynamics.
Membrane rupture	1) Molecular and multiscale simulations. 2) Finite element method. 3) Bulge test theory.	Bulge test model and experiments.
Gas dynamics	1) Direct Simulation Monte-Carlo. 2) Navier-Stokes equations for the reactive flow. 3) Local equilibria hypothesis to treat chemistry. 4) Fixing chemical composition at the flame front. 5) Quasi-1D approximation. 6) Ideal rocket model.	Ideal rocket model followed by empirical corrections.

Table 1-5: Models for the microthruster operation [51]

Kujawa et al. [52] modeled a micro-nozzle geometry numerically using FLUENT in 2-D and 3-D for adiabatic and isothermal walls. Figure 1-14 shows their computational mesh and Figure 1-15 shows path lines associated with the fluid flow.

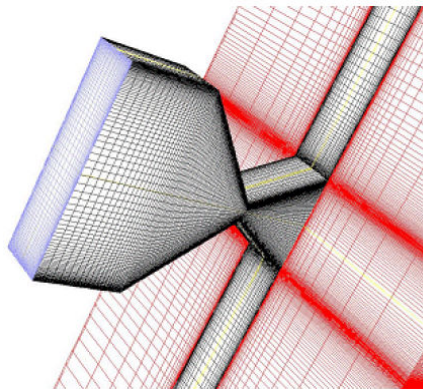


Figure 1-14: The three-dimensional computational mesh used by Kujawa et al. to simulate a micro-nozzle. It was created using Fluent Inc.'s GAMBIT software [52]

Their computations showed that the 2-D model compared well with quasi 1-D simulations. The 3-D simulation results showed that it was important to include conjugate heat transfer when modeling these nozzles.

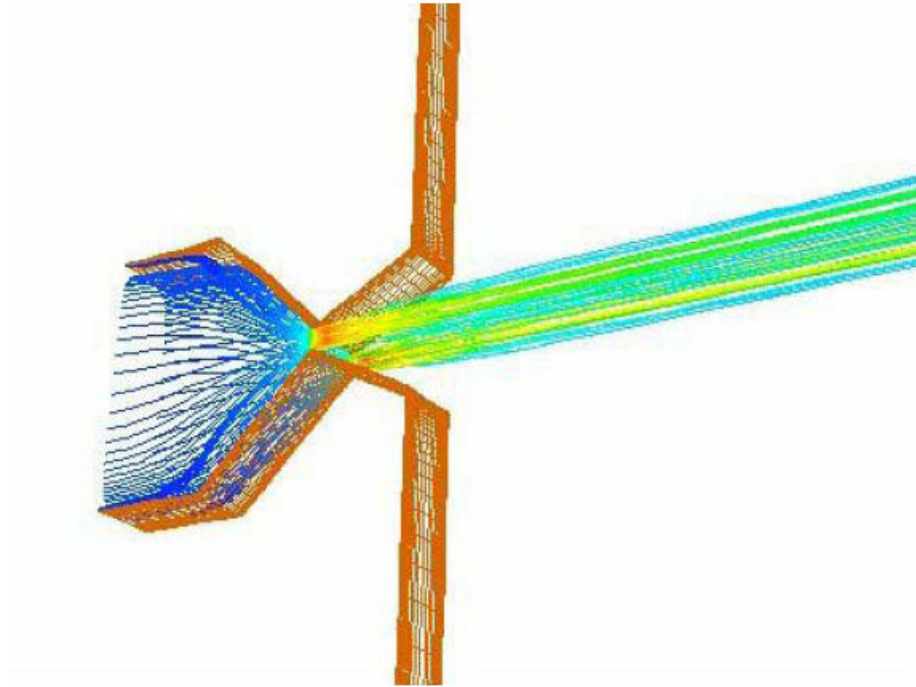


Figure 1-15: Pathlines for the 3-D model with isothermal boundary conditions [53]

More recent work by the same group (Louisos and Hitt) comparing 2-D and 3-D nozzle geometries show that the thrust (Figure 1-16) is significantly over predicted with 2-D models. Therefore, 3-D simulations appear to be required. However, their simulations also indicated that heat loss from the micro-nozzle flow increased the predicted thrust due to Rayleigh acceleration and the corresponding density increase as the flow is cooled. Heat transfer also raised the Mach number in the vicinity of the expander walls. This was helpful because it prevented the subsonic boundary layer from growing large as was predicted by the adiabatic simulations.

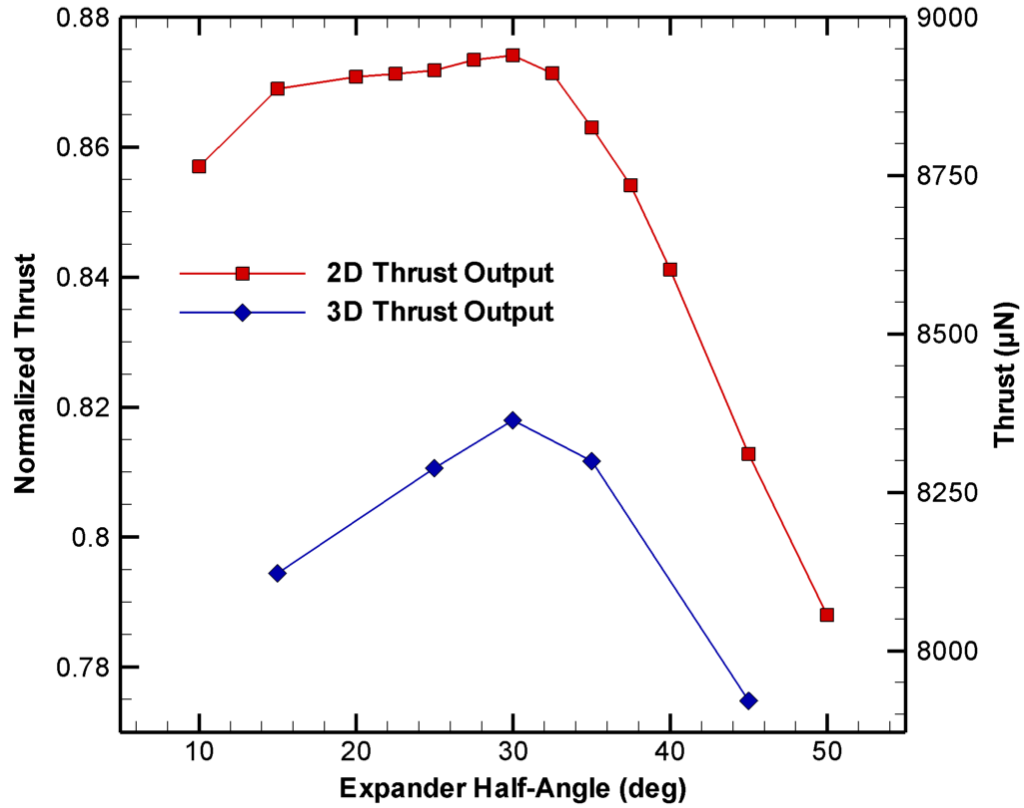


Figure 1-16: Thrust production in 2D and 3D micro-nozzles for varying expander half-angles from Hitt et al. [53].

The 2D thrust was calculated assuming a planar micro-nozzle with depth of $150\mu\text{m}$. The value of the extrapolated 2D thrust is greater than 3D owing to the fact that the 2D simulations do not account for the subsonic layers on the micro-nozzle side-walls. For small half-angles, performance degradation is due to the growth of a large subsonic layer. While, at large expander angles performance degradation is a result of geometric losses. Note that this trade-off results in an optimum expander half-angle of 30° which becomes more pronounced in 3D simulations.

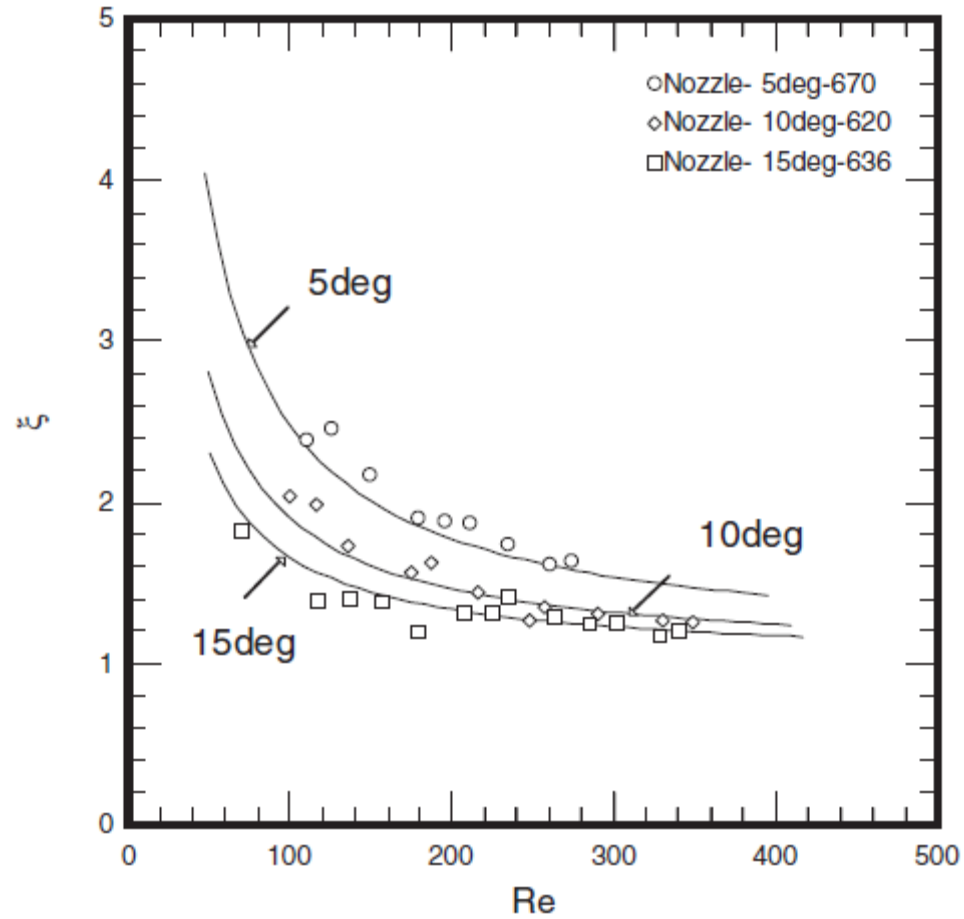


Figure 1-17: Comparison of the measured data of nozzles with the prediction [54]

Yang et al. [54] studied how the pressure loss scaled with Re in micro-diffusers and nozzles by means of a simple model and experiments. Figure 1-17 shows a comparison between their model and experimentally measured pressure loss coefficients as a function of the Re number. Their results indicate that pressure losses are higher at lower Re and reach an asymptote for fairly high Re numbers.

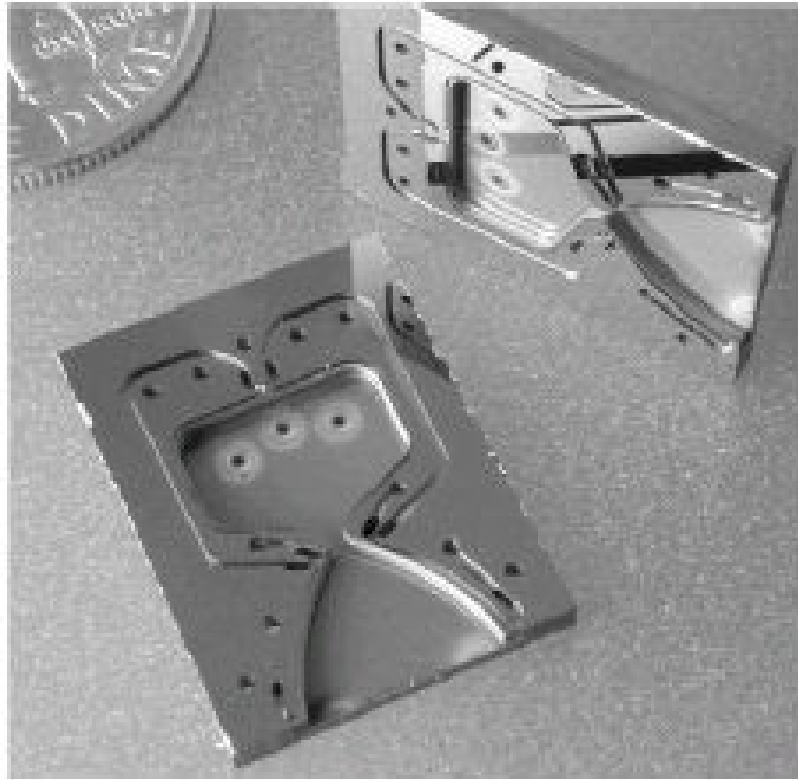


Figure 1-18: Regeneratively cooled MEMS thrust chamber design to produce 15N thrust [55].

A bi-propellant micro-thruster was developed by London (Figure 1-18) at MIT that was based on the combustion of O_2 and CH_4 . In spite of the device's small size, viscous losses did not prevent the generation of about 1 N thrust at a chamber pressure of 12 atmospheres. Continued development is expected to increase the thrust to around 12-15N.

ii) Micro-engines and power technologies:

Next we examine various attempts at building compact power systems based on microcombustion. As discussed previously, interest in microscale heat engines has been driven by the need for battery replacements with higher endurance and miniature propulsion systems for micro Unmanned Air Vehicles (MAVs). More particularly the

focus is on the development of heat engines that consume liquid hydrocarbon fuels in a miniature combustor with dimensions below 1mm.

The seminal program in this area that produced the first micro-engine was the micro gas turbine [14] engine project at MIT. The objective was to microfabricate a gas turbine engine with integral electric generator on a silicon chip. It was intended to produce 10-50W of power.

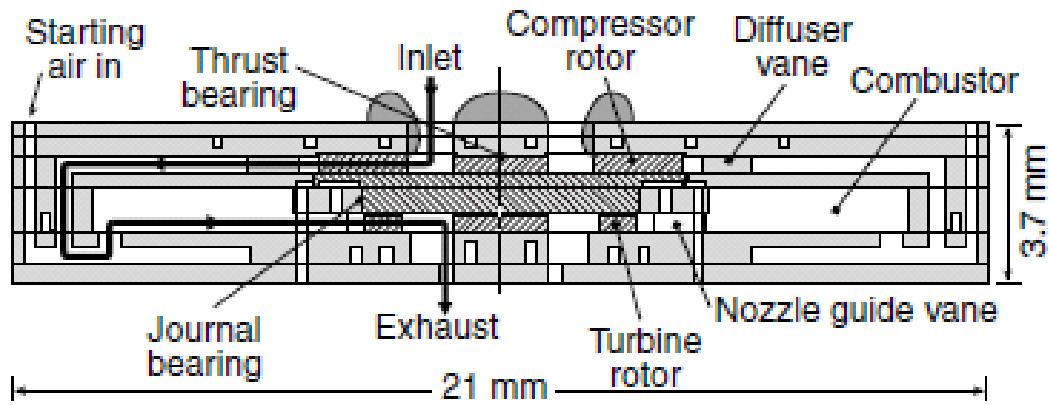


Figure 1-19: H₂ demo engine with conduction-cooled turbine constructed from six silicon wafers [14].

The overall size of the device (shown in Fig. 1-19) is about 2.1 cm x 2.1 cm x 0.38 cm. It is constructed by fusion bonding six etched silicon wafers to form the compressor, turbine, combustor, generator and other flow passages. Individual components of the proposed engine have been demonstrated independently but a complete device has not operated.

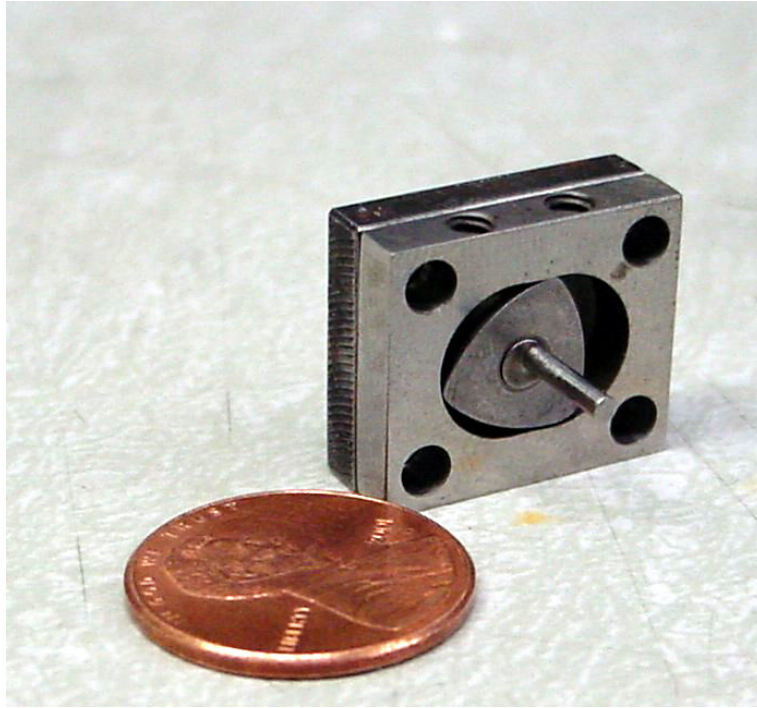


Figure 1-20: Photograph of the mini-rotary engine [56].

Fernandez-Pello and co-workers [56] worked on a small rotary engine (Fig. 1-20) intended to produce $\sim 10\text{-}100$ mW of power. The ‘mini’ version was fabricated using electrodischarge machining (EDM), had a displacement of 0.064 mm^3 , and a rotor of size 1mm. The rotary design has the advantage of simplicity as it eliminates the need for valves. A key aspect of developing any microscale engine is to avoid unnecessary moving parts, sealing or lubrication issues if possible because higher complexity brings with it a greater risk of failure. A ‘micro’ version of the rotary engine that would be manufactured using silicon micromachining was also planned.

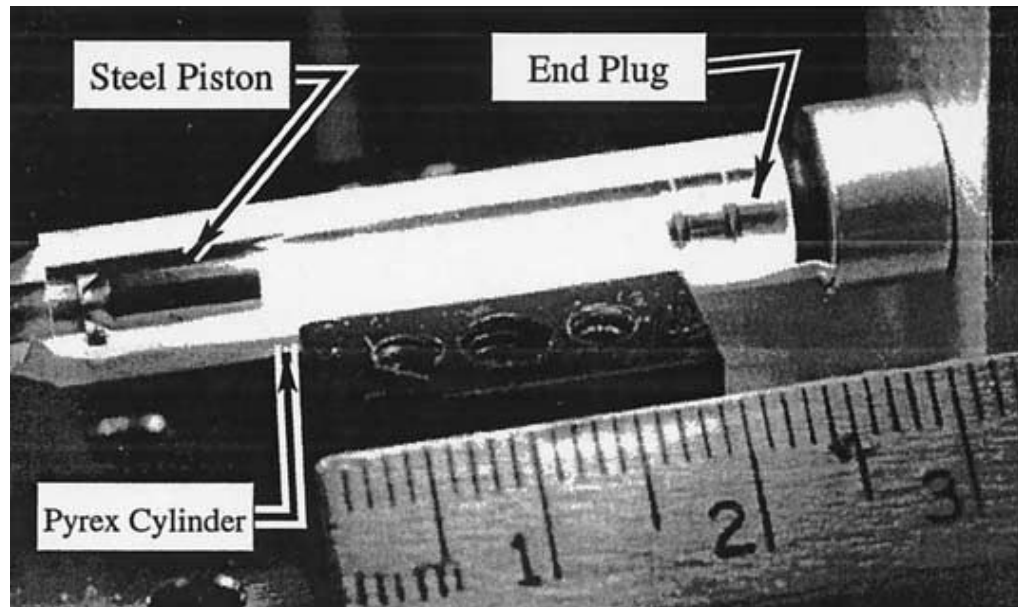


Figure 1-21: Piston-cylinder assembly. The piston is on the left and the end plug is on the right [57].

Aichlmayr and co-workers [57], [58] designed a homogenous charge compression ignition (HCCI) free piston micro-engine (Fig. 1-21, photograph of the actual piston cylinder assembly) capable of producing 10W. HCCI engines differ from conventional compression and spark ignition engines in that they compress premixed fuel and air until it ignites spontaneously. This enables operation at very low overall equivalence ratio which can reduce NO_x . It also eliminates the need (in theory at least) for an external ignition system. This makes the design less complex. The free piston serves as the moving element of a permanent magnet generator

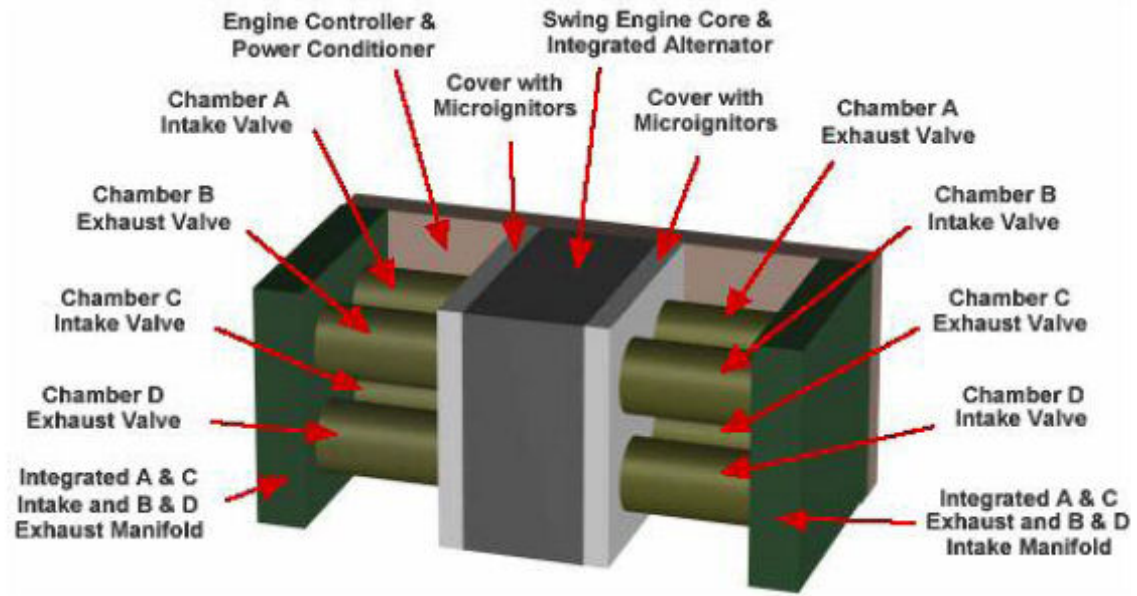


Figure 1-22: Assembly concept for all non-fuel components of the 20W MICSE chemical-to-electrical energy conversion system indicating major system components. System volume is 17.6 cc (20x20x44 mm) and mass is 54 g [59].

Dahm and coworkers have developed an oscillatory rotating free-piston engine called MICSE for Micro Internal Combustion Swing Engine. The engine is intended to produce about 20 W with an overall efficiency of 14 %. Butane is the fuel and the engine is fabricated from steel using wire EDM. The diameter of the swing arm is 16 mm. Fig. 1.18 shows the integrated assembly drawing of the MISCE engine. The overall volume is expected to be 17.6 cc (20x20x44 mm) with a mass of around 54 g.

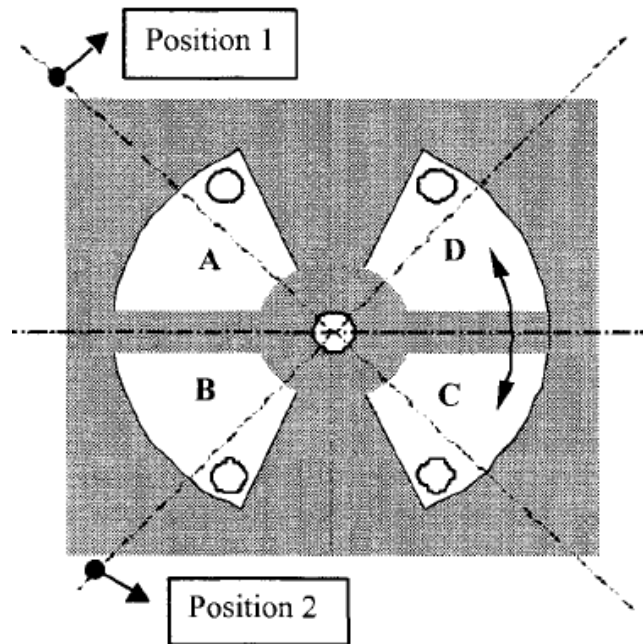


Figure 1-23: Base cavity, swing-arm, valve ports, and resulting four chambers (A-D) in the micro internal combustion swing engine (MICSE). The resulting arrangement produces inherent weight and volume efficiencies over conventional linear piston engines, while avoiding the mechanical complexities of rotary Wankel or turbine engines [59].

Fig. 1-23 shows the swing arm and the valve ports. The mechanical power in the form of the oscillatory motion of the swing engine is converted to electrical power by means of an inductive alternator with either permanent magnets in the swing arm and inductive coils in the cavity base, or by an external shaft-coupled inductive alternator optimized for the rotationally oscillating motion produced by the swing engine. Of all the micro-engines in existence, the swing engine is by far the best developed and the closest to a practical device.

1.4.4. Measurement and Non-intrusive Diagnostic Techniques

Making measurements is an integral part of characterizing performance of devices. Theoretical models and computational results need validation from experimental work, which in turn use various measurement methods and instruments. The more intricate the engineering problem, the more challenging it becomes to make measurements. Microscale combustion devices with their small volumes, high temperatures and chemically reacting environments are extremely challenging to make measurements in. Therefore, there is a need to develop reliable measurement techniques suitable for making temperature, concentration and velocity measurements in these devices. Some of the relevant work in the literature is discussed next.

i) Conventional Scale:

Conventional scale measurement techniques can be both intrusive and non-intrusive. As we will see in the next subsection, microscale combustors require non-intrusive diagnostic techniques owing to the unique challenges of the environment.. One of the simplest temperature measuring devices is a thermocouple. Shaddix [60] developed a heat transfer correction model to improve the accuracy of conventional-scale thermocouple measurements.

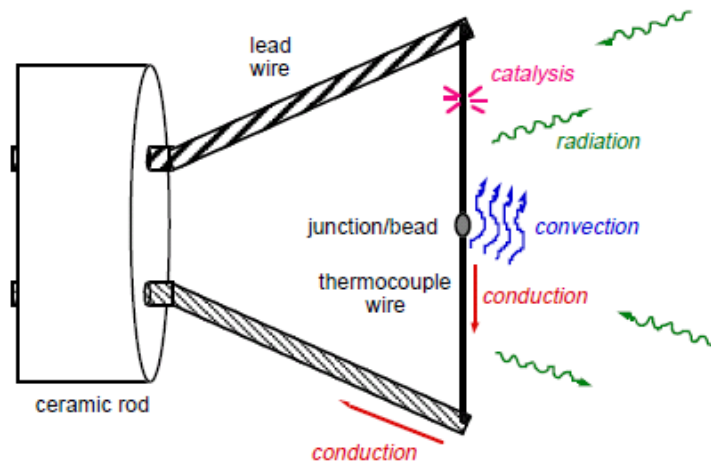


Figure 1-23: Schematic of a typical thermocouple arrangement for combustion-system measurements [60].

Figure 1-23 shows the various heat transfer modes considered by Shaddix [60] from the bead of the thermocouple. His analysis showed that without appropriate corrections, measurement errors could be fairly large. For e.g., the minimum error in temperature measurements due to incorrect modeling of convective losses could be of the order of 50-100 K. It will be significantly higher if all modes of heat transfer are not properly accounted for. Unfortunately, it is not possible to probe micro-scale flows using conventional thermocouples as the diameter of the bead is usually $\sim 1\text{mm}$ which can be greater than the flow passage height.

In applications where it is not feasible to insert a probe because the environment is too hostile – i.e. too hot or oxidizing- or where we do not want to disturb the flow field, non-intrusive techniques become necessary. A variety of non-intrusive methods are available for measuring temperature, composition (species concentration) and velocity fields in conventional scale systems. Particle Image Velocimetry (PIV) is a flow visualization technique in which the flow is seeded with particles which are illuminated

by a laser sheet. Images of the particles at different times are captured using a fast CCD camera and the velocity field is determined by computing the auto course [61].

Transmission Fourier transform infrared (FTIR) spectroscopy is often used to make non-intrusive measurements of species concentration and temperature. It involves passing a beam of light through the sample and measuring molecular absorption as a function of wavenumber using a detector that records the number of photons exiting the sample volume for each wavenumber. In contrast, emission FTIR spectroscopy collects photons that are naturally emitted by the sample. Emission FTIR is often used in combustion measurements since the high temperatures of the combustion environment excite vibrational transitions of most molecules leading to relatively strong emissions that are easy to collect. Emission experiments [62] have the advantage that there is no beam to send through the sample to be collected by a detector. This makes the setup much less complicated, reduces the number of optical components required, and eliminates problems with beam steering. Also, this allows remote sensing measurements of radiative sources at a distance. Jaquot et al. [63] measured temperatures of hot combustion exhaust gases using emission spectroscopy. They used the EM2C narrow band model to infer gas temperature from CO₂ spectra. Measurements of temperatures up to 1100 K have also been made. Bailly et al. [64] used a high resolution spectrometer (0.02 cm⁻¹) to infer gas temperature from CO₂ spectra by only considering the transitions that are excited at high temperatures. The temperatures were obtained with precisions on the order of $\pm 1\%$ for this method.

Transmission FTIR is the most common form of FTIR spectroscopy because the sample does not have to be at the high temperatures needed for emission measurements.

In this technique, a beam is sent through the sample and the molecules absorb light. One particularly relevant investigation to the work presented here is that of Lindner and co-workers [65] who used FTIR measurements to infer gas temperature, CO₂ concentration and combustion efficiency. They used an in-house wide band model with constants obtained from the literature to compute gas temperature and concentrations. Both emission and absorbance measurements were used in this experiment. Koshland et al [66] used in situ transmission FTIR to detect chlorinated hydrocarbons in combustion flows.

While a variety of different types of spectroscopies can be used to measure temperature, all require models for how the spectral features observed depend on temperature. While some models are better than others, often sorting out which is best is not easy. Modest et al. [67] compared the predictions of Hitran [68], Hitemp [69], Radcal [70], and EM2C [71] using an isothermal drop-tube burner and transmission spectroscopy. Their results indicated that the wide band models (Radcal and EM2C) are better able to predict the band structure at higher temperatures (i.e., > 1300K) with EM2C being slightly better than Radcal in this respect.

ii) Microscale:

The combination of small volumes, hot oxidizing environments, and the difficulty of providing optical access have prevented the use of most conventional combustion diagnostic tools at the microscale. As a result, there are far fewer examples of measurements and diagnostic tools in the microscale. Zhang and co-workers [72] developed miniature thermocouples that are micro-fabricated into a combustor's structure. While they could be useful in low temperature reacting flows found in catalytic systems, they are unable to survive at temperatures associated with most gas phase

combustion processes. Breuer [73] took advantage of silicon's transmissivity in the infrared regime to measure velocity using Micro-Particle Image Velocimetry (MPIV). Breuer's technique uses volume illumination and narrow depth of field camera optics to eliminate the need to produce a sheet of light with thickness of a few microns.

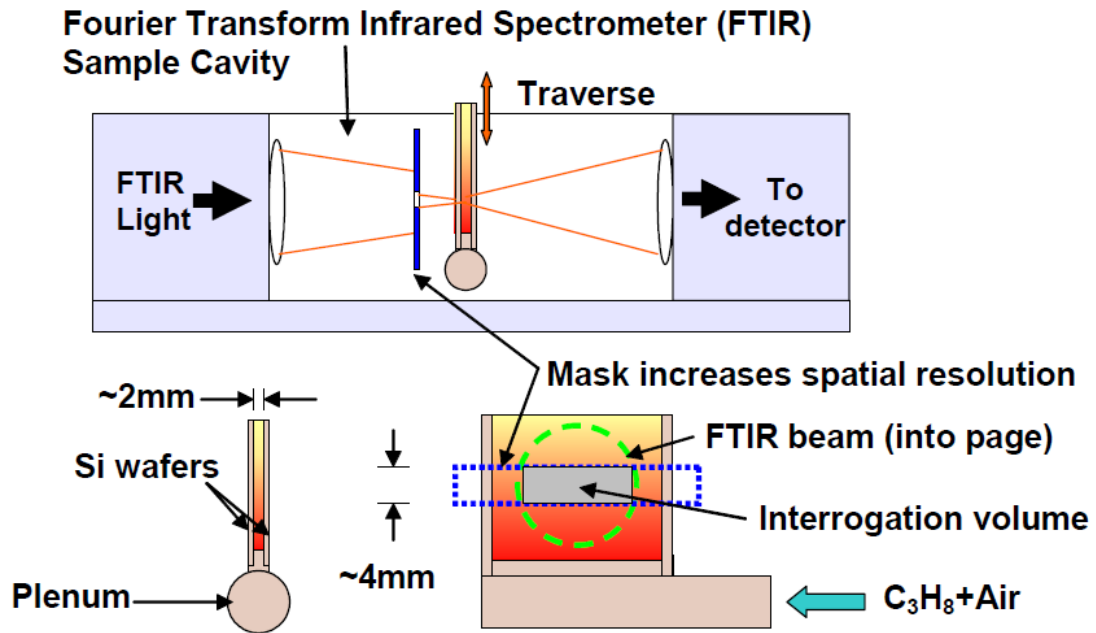


Figure 1-24: Diagram of apparatus [74]

Heatwole et al. [74] demonstrated the feasibility of using silicon's transmissivity in the IR to make absorption measurements using FTIR spectroscopy. The measurements were carried out in the silicon walled microcombustor shown in Fig. 1-24. Concentrations of CO, CO₂ and CH₄ were determined from the integrated absorbance of each molecule's rotational band. Gas temperature was determined from measurements of rotational line strengths and comparison to predictions of the HITRAN database. Unfortunately, the uncertainties in the individual line strengths in the HITRAN database led to unacceptably large uncertainties in temperature (Fig. 1-25).

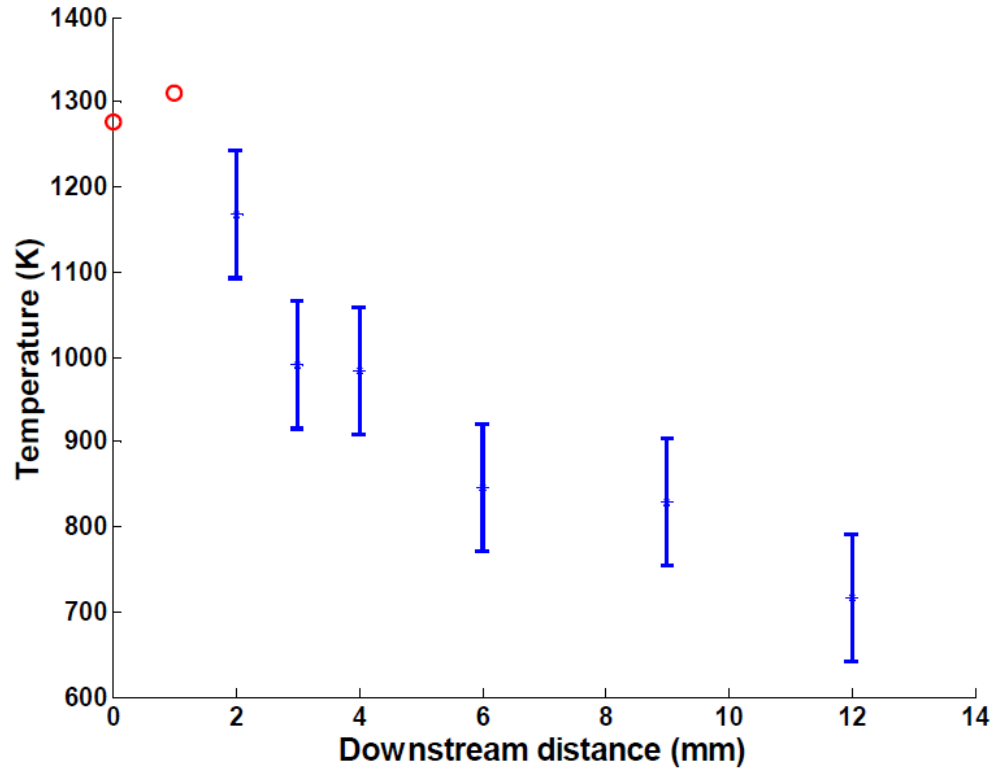


Figure 1-25: Temperature versus downstream distance inferred from CO absorbance spectra. [74]

These problems were overcome by following the procedure suggested by Modest [67] which is to measure absorbance across the entire rotational band and use the EM2C models [71] to infer gas temperature from the shape. This was demonstrated successfully in a microburner [16], [75].

1.5. Objectives and Approach:

The main objectives of this dissertation are to understand the influence of heat recirculation through a combustor's structure on flame stabilization and burning rates in microscale devices, to identify the critical combustor design parameters, and to exploit this understanding to develop high performance microcombustors and thrusters. This will

be accomplished through a combined program of analytical modeling from first principles and experiments in a simulated micro-combustor

The approach is outlined below:

1. Develop 2-D analytical models for heat transfer accounting for heat exchange with the wall. Identify design parameters governing the heat transfer problem and explore the influence of each parameter on the temperature profiles and Nu number for heat exchange between wall and gas.
2. Incorporate a species transport model that accounts for chemical reaction and heat release and incorporate it along with the heat transfer model in order to predict the flame speed. Use the model to identify the main governing parameter controlling the flame speed.
3. Improve the non-intrusive diagnostic technique based on FT-IR spectroscopy developed in previous work [16] to enable measurement of temperature profiles along a line of sight and extend the uncertainty analysis appropriately.
4. Use the diagnostic technique to make detailed temperature measurements at different flow rates (velocities), equivalence ratios, and for different fuels (methane and propane).
5. Use the temperature measurements to compute heat recirculation and compare to the theory predicted by models from approaches 1 and 2.

Chapter 2: Heat Transfer Analysis

In this chapter we look at the heat transfer that occurs for a laminar flame stabilized within a canonical parallel plate reactor. The focus will be on understanding the balance between the different heat transfer mechanisms (convective, diffusive etc) and also to understand the role of the wall as the reactor is scaled down in size. The primary reason for beginning this analysis (initially) was to develop a model with which to obtain approximations for the temperature profiles in the transverse direction in order to make line of sight non-intrusive, FT-IR spectroscopy based temperature measurements by fitting the absorption data with a guess for the temperature profile [76]. This led to the detailed analytical modeling presented in this chapter. The model was built in increasing levels of complexity starting with a simple problem of the wall being at constant temperature and then advancing to conjugate heat transfer with the wall accounting for heat loss to the environment.

2.1. Gas Energy Equation/Heat Release Model

2.1.1. Governing Equation

Figure 2-1 illustrates the basic physical problem. A flame is stabilized in the infinitely channel formed between two parallel plates. Reactants are fed into the channel from the left side at exactly the right velocity (the flame speed) so that the flame position remains fixed in the laboratory reference frame.

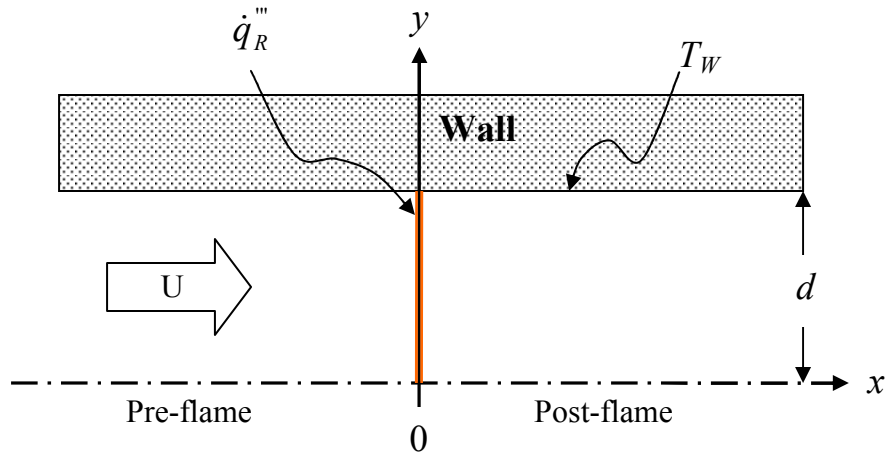


Figure 2-1: Infinitely thin flame stabilized in a channel between two parallel plates

Hot combustion products in the post-flame zone heat the walls of the channel which, in turn, pre-heat the reactants entering the reaction zone. The governing energy equation for the gas (involving gas temperature T_g) in this problem is given in eq. 2-1 below, where the heat release at the flame is represented by a concentrated volumetric heat release function with the zone of heat release assumed to be infinitesimally thin.

$$\rho U(y) C_p \frac{\partial T_g}{\partial x} = k_g \left(\frac{\partial^2 T_g}{\partial x^2} + \frac{\partial^2 T_g}{\partial y^2} \right) + \dot{q}_R''' \frac{\delta(x)}{1/d} \quad (2-1)$$

Where, x is the stream wise coordinate and y is the transverse coordinate. ρ is the density of the gas, C_p is the specific heat capacity, k_g is the thermal conductivity of the gas, $U(y)$ is the velocity profile and \dot{q}_R''' is the volumetric heat release and is assumed constant in the y^+ direction. Only one half of the channel is shown in fig. 2-1 as the problem is expected to be symmetric about the centerline in the absence of body forces.

Eq. 2-1 is re-written in terms of the following non-dimensional variables:

$$\theta = \frac{T_g - T_\infty}{\dot{q}_R''' d^2 / k_g}; x^+ = \frac{x}{d}; y^+ = \frac{y}{d};$$

$$U^+(y^+) = U(y^+) / \bar{U} \quad (2-2)$$

Where

$$\bar{U} = \int_0^l U(y^+) dy^+ = \begin{cases} U; \{U(y^+) = U \text{ (Plug flow)}\} \\ \frac{2}{3} U_{max}; \{U(y^+) = U_{max}(1 - y^{+2}) \text{ (Hagen - Poiseuille flow)}\} \end{cases} \quad (2-3)$$

Note that two velocity profiles across the channel are considered: A uniform velocity distribution (plug flow) and a parabolic distribution (Hägen-Poiseuille flow). The non-dimensional form of the energy equation becomes:

$$Pe U^+(y^+) \frac{\partial \theta}{\partial x^+} = \frac{\partial^2 \theta}{\partial x^{+2}} + \frac{\partial^2 \theta}{\partial y^{+2}} + \delta(x^+) \quad (2-4)$$

In this expression, Pe is the Peclet number - a ratio of convective to conductive heat transfer as discussed in Chapter 1.

$$Pe = Re Pr = \frac{\rho \bar{U} C_p d}{k_g} \quad (2-5)$$

2.1.2. Derivation of Jump Conditions across the Flame

In § 2.1.1 we presented the governing energy equation for the gas. Now let us look a little more closely at the meaning of the concentrated heat release function. At the flame itself we require that the temperatures on both sides of the flame be equal owing to the fact that the heat release function is concentrated and therefore the temperature should be continuous. This leads to the following equation:

$$\theta(0^-, y^+) = \theta(0^+, y^+) \quad (2-6 a)$$

Integrating equation 2-4 over an infinitesimally small volume around the flame as follows

$$\int_{0^-}^{0^+} \left(Pe U^+(y^+) \frac{\partial \theta}{\partial x^+} = \frac{\partial^2 \theta}{\partial x^{+2}} + \frac{\partial^2 \theta}{\partial y^{+2}} + \delta(x^+) \right) dx^+ \quad (2-6 \text{ b})$$

gives the “*jump condition*” across the flame sheet:

$$\left. \frac{\partial \theta}{\partial x^+} \right|_{0^-}^{0^+} = -1 \quad (2-6 \text{ c})$$

Equation 2-6 c can be understood as an energy balance. The energy released at the flame is dissipated via conduction into the pre and post-flame regions. Together equations 2-6 a and c are known as the “jump conditions” [36, 38] across the flame.

2.2. Isothermal Wall Boundary Condition

One of the model problems found in the literature [24] which could be a reasonable representation of a microcombustor is heat transfer in a channel with constant temperature walls. This could be reasonable for a condition where the wall’s thermal conductivity will be several orders of magnitude larger than the gas. Hence, the heat absorbed by the wall might be distributed evenly in a rapid fashion leading to a constant wall temperature. While this is indeed an over simplification of the heat transfer problem, but it serves as a useful starting point for the purpose of comparison with traditional solutions to similar heat transfer problems in channels. With the assumption of the walls being at a uniform temperature (equal to the inlet and exit temperature for the sake of continuity at the exits) and along with the temperature profile in the gas assumed to be symmetric about the centerline we obtain the following boundary conditions:

$$T(\mp \infty, y) = T_\infty \quad (2-7 \text{ a})$$

$$\left. \frac{\partial T}{\partial y} \right|_{y=0} = 0 \quad (2-8 \text{ b})$$

$$T(x,1) = T_w = T_\infty \quad (2-8 \text{ c})$$

Retaining the previous non-dimensionalization (eq. 2-2) the boundary conditions transform to:

$$\theta(\mp\infty, y^+) = 0 \quad (2-9)$$

$$\left. \frac{\partial \theta}{\partial y^+} \right|_{y^+=0} = 0 \quad (2-10)$$

$$\theta(x^+, 1) = 0 \quad (2-11)$$

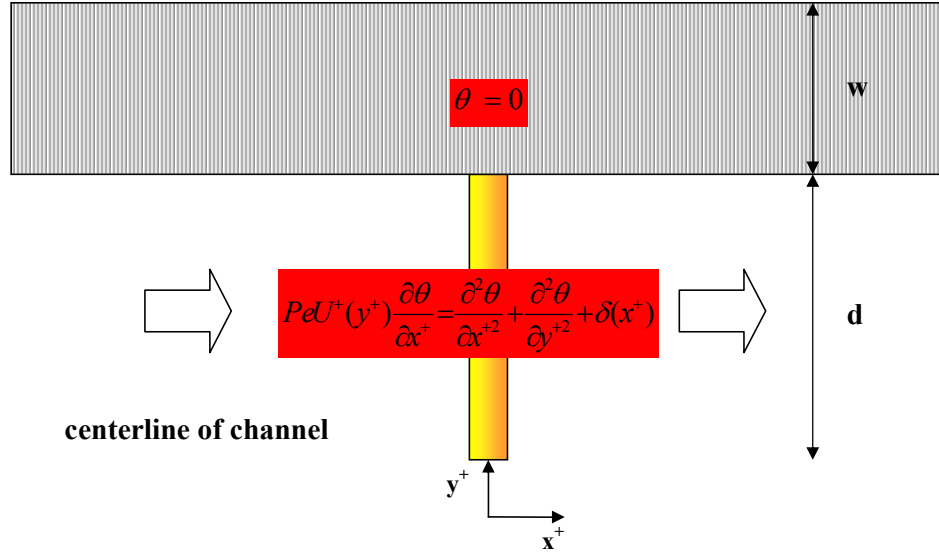


Figure 2-2: Heat transfer problem in non-dimensional variables for isothermal BC.

2.2.1. Solution

Figure 2-2 illustrates the flame stabilization in an isothermal channel problem. It shows the governing equation and the wall boundary condition cast in non-dimensional terms. We seek a separation of variables solution for the temperature field in the non-dimensional streamwise and spanwise coordinate directions x^+ and y^+ respectively. Thus,

$$\theta_g(x^+, y^+) = X(x^+)Y(y^+) \quad (2-12)$$

The details of the mathematical steps involved in obtaining the solution are presented in Appendix A and can also be found in [77]. The resulting solution is given below:

$$\theta(x^+, y^+) = \begin{cases} \sum_{m=1}^{\infty} A_m \exp(\lambda_m x^+) \phi(\lambda_m, y^+); x^+ < 0 \text{ (pre-flame)} \\ \sum_{m=1}^{\infty} B_m \exp(-\beta_m x^+) \psi(\beta_m, y^+); x^+ > 0 \text{ (post-flame)} \end{cases} \quad (2-13)$$

The mathematical procedure adopted to obtain A_n and B_n in closed form (eqs. 2-14 and 2-15) is presented in Appendices B and C. While the solution procedure is unique, it is not our main focus and is hence it is presented in the appendix.

$$A_n = \frac{\int_0^1 \phi_n dy^+}{\int_0^1 (-PeU^+(y^+) + 2\lambda_n) \phi_n^2 dy^+} \quad (2-14)$$

$$B_n = \frac{\int_0^1 \psi_n dy^+}{\int_0^1 (PeU^+(y^+) + 2\beta_n) \psi_n^2 dy^+} \quad (2-15)$$

2.2.2. Results

i) Comparisson to CFD:

The predictions of the analytical model for Hagen-Poiseuille flow were validated via comparison to two-dimensional CFD simulations.

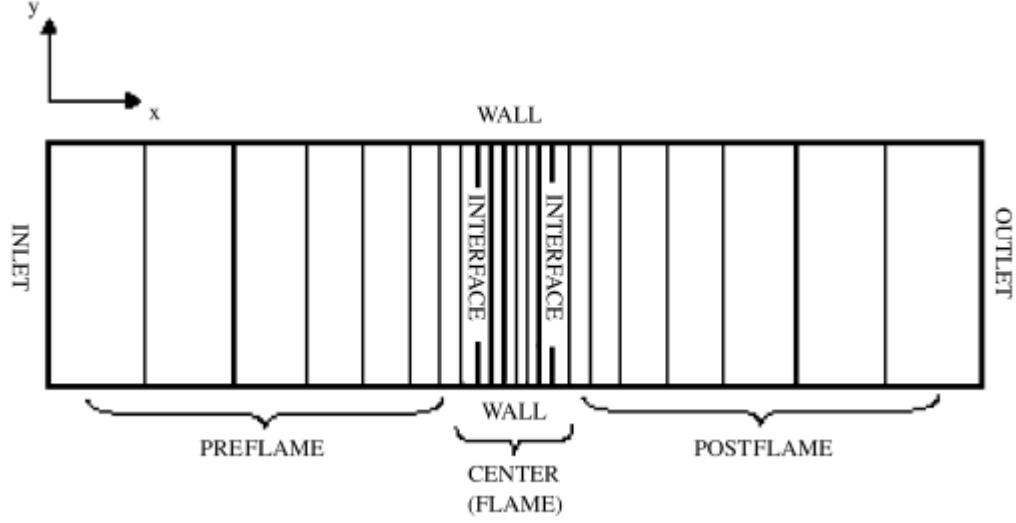


Figure 2-3: Representative computational grid

A commercial CFD package by ESI U.S. R&D Inc., CFD-ACE+ [78] was used to solve the 2D steady, incompressible Navier-Stokes [79] equations (eqs. 2-17 and 2-18) and the energy equation [80] (eq. 2-16), on a structured computational grid based on the geometry illustrated in Fig. 2-3. The details of the grid will be presented shortly.

$$\nabla \cdot (\rho \bar{V} h_0) = \nabla \cdot (k_{eff} \nabla T) + \left[\frac{\partial (u \tau_{xx})}{\partial x} + \frac{\partial (u \tau_{yx})}{\partial y} \right] + \left[\frac{\partial (v \tau_{xy})}{\partial x} + \frac{\partial (v \tau_{yy})}{\partial y} \right] \quad (2-16)$$

$$\nabla (\rho \bar{V} u) = -\frac{\partial P}{\partial x} + \left(\frac{\partial \tau_{xx}}{\partial x} + \frac{\partial \tau_{yx}}{\partial y} \right) \quad (2-17)$$

$$\nabla (\rho \bar{V} v) = -\frac{\partial P}{\partial y} + \left(\frac{\partial \tau_{xy}}{\partial x} + \frac{\partial \tau_{yy}}{\partial y} \right) \quad (2-18)$$

In Eq. 2-16, k_{eff} is the thermal conductivity of the gas, T is the absolute temperature, u and v are the x-component and y-component velocities, ρ is the density, P is the static pressure, and τ is the viscous stress. h_0 is the stagnation enthalpy which is defined as:

$$h_0 = i + \frac{p}{\rho} + \frac{1}{2}(u^2 + v^2) \quad (2-19)$$

where i is the internal energy. Eqs. 2-16 through 2-19 were solved subject to boundary and initial conditions equivalent to those applied to develop the analytical model.

The computational grid breaks into 3 domains as illustrated in Fig. 2-3, a 100mm long pre-flame domain bounded by the inlet plane at the left, solid walls at the top and bottom, and a fluid interface at the right; a 0.1mm long flame domain bounded by fluid interfaces at the left and right and solid walls at the top and bottom; and a 100mm long post-flame region with a fluid interface on the left, a fluid outlet on the right, and solid walls at the top and bottom. The structured grid is 5mm x 200.1mm and contains 24,745 cells. It is coarsest at the inlet and outlet and most refined in the center (where the flame is located) in order to ensure that streamwise temperature gradients are adequately resolved.

The minimum number of cells required to provide an accurate solution was determined by performing a grid convergence test for a Peclet number case ($Pe = 10$) based on the maximum centerline flow velocity, U_{max} , and peak flame zone temperature, T_{max} . It was found that further refining a grid of 17,400 cells causes U_{max} and T_{max} to change by less than 0.1%. Therefore, this resolution appears to be adequate.

The boundary conditions at the inlet are 500 K gas temperature and a fully developed parabolic velocity profile ($u_{mean} = 0.02175$ m/s for $Pe=1$ and $u_{mean} = 0.2175$ m/s for $Pe=10$) associated with Hagen-Poiseuille flow. No slip is enforced at the walls. Heat transfer is allowed between the walls and the fluid but the walls are assumed to be isothermal at 500K. The pressure at the exit boundary is 1 atm. The flame is represented as a constant volumetric heat source of 8.5×10^7 W/m³ located in the center domain. This value was identified by trial and error as the one that produced equal gas temperatures at the inlet and outlet of the concentrated heat source volume that represents the flame. This

was necessary in order to ensure that the boundary conditions used to develop the analytical solution (i.e. that the pre and post-flame temperatures be equal at the flame) were properly represented. The fluid density, specific heat, and thermal conductivity of the gas were 0.706 kg/m^3 , 1029 J/kgK and 0.0395 W/mK respectively in all of the simulations. All cells in the computational domain were initialized to the mean flow conditions at the inlet. The Peclet number was varied from 1 to 10 by changing the flow velocity.

Gradients were computed using a blended quasi-second order spatial differencing scheme with 90% upwinding and 10% backwards Euler. The pressure, velocity, and enthalpy were found using a conjugate-gradient-squared (CGS) solver with preconditioning. A numerical simulation was considered converged when the L_2 norm of all residuals was reduced to at least 1.0×10^{-7} . Once a converged solution was obtained, the temperature distribution was exported to CFD-VIEW where the centerline and local temperature profiles were extracted. All simulations were performed using a Dell x86-based PC with dual 3391 MHz, Model 3 Stepping 4 Intel processors and 2 GB of RAM.

Figure 2-4 shows a typical temperature field computed using the analytical solution for the HP flow situation. It shows, appropriately, that the gas temperature peaks at the flame location ($x^+=0$) and decreases as one moves upstream, downstream, or to the walls.

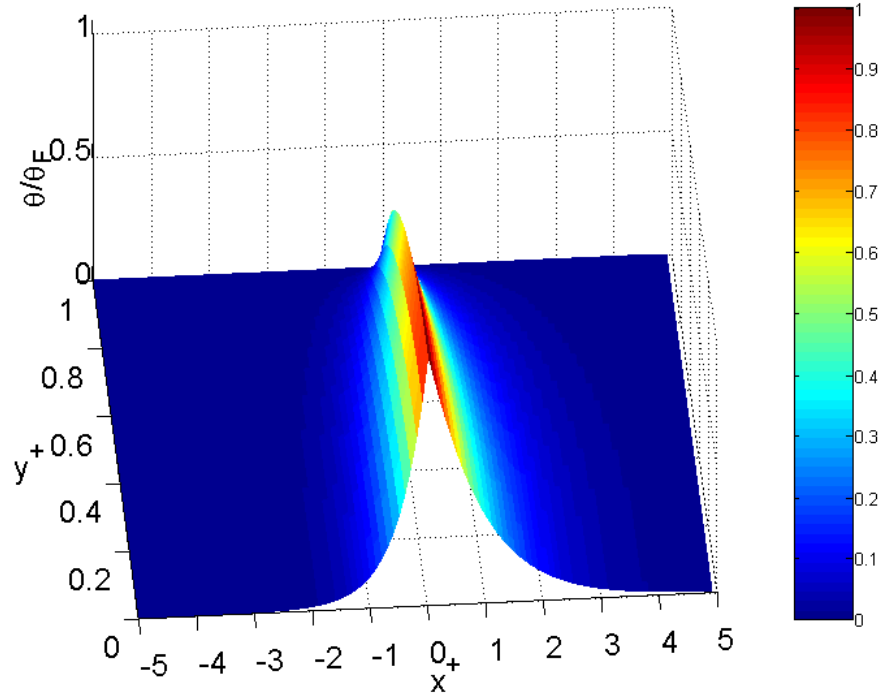
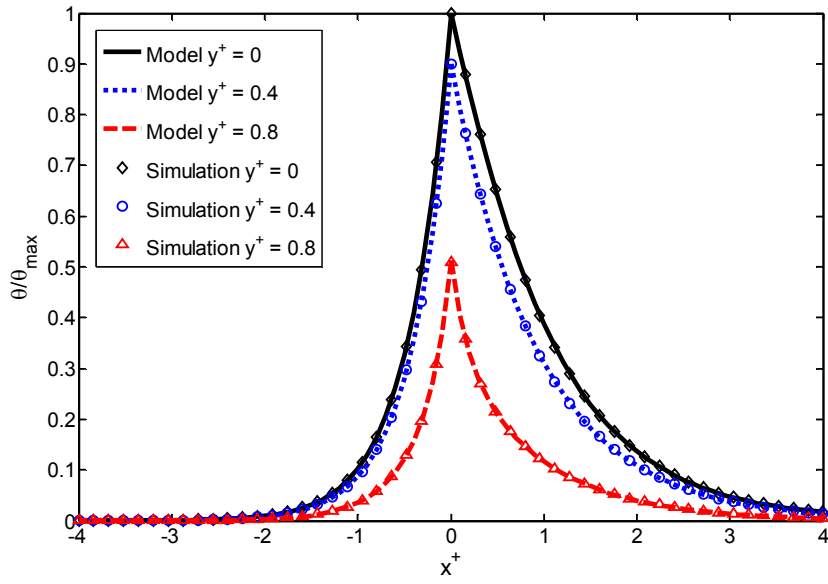
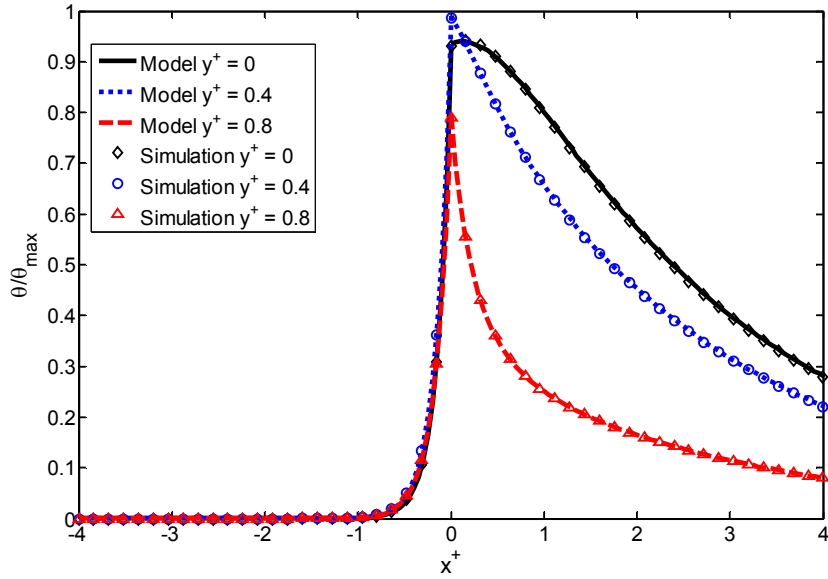


Figure 2-4: Non-Dimensional 2-D temperature (θ/θ_F) field ($Pe = 1$).

Figs. 2-5 and 2-6 compare the analytical and CFD solutions. Fig. 2-5 shows axial temperature profiles at 3 different vertical positions in the channel ($y^+ = 0, 0.4, 0.8$) for two Peclet numbers ($Pe = 1$ and 5). These Pe numbers were chosen because the flow velocities and dimensions generally associated with micro-combustors and burners (our interest here) lead to Pe in the range of 1 to 10. In contrast, Pe associated with conventional scale devices are usually > 35 .



(a)



(b)

Figure 2-5: Comparison of axial temperature profiles predicted by the analytical model and the CFD simulations for three transverse (y^+) locations; Hagen-Poiseuille Flow. a) $Pe = 1$ and b) $Pe = 5$

Figure 2-6 shows transverse temperature profiles at $Pe = 1$ and $Pe = 5$. The maximum difference between the analytical model and the numerical solution is less than 5% over

the entire domain for both Pe numbers indicating that the analytical solution is valid. Interestingly, the peak gas temperature does not necessarily occur along the channel center line as is seen in Figs. 2-6b and 2-7b. The reasons for this and the effect on the Nusselt number will be discussed later.

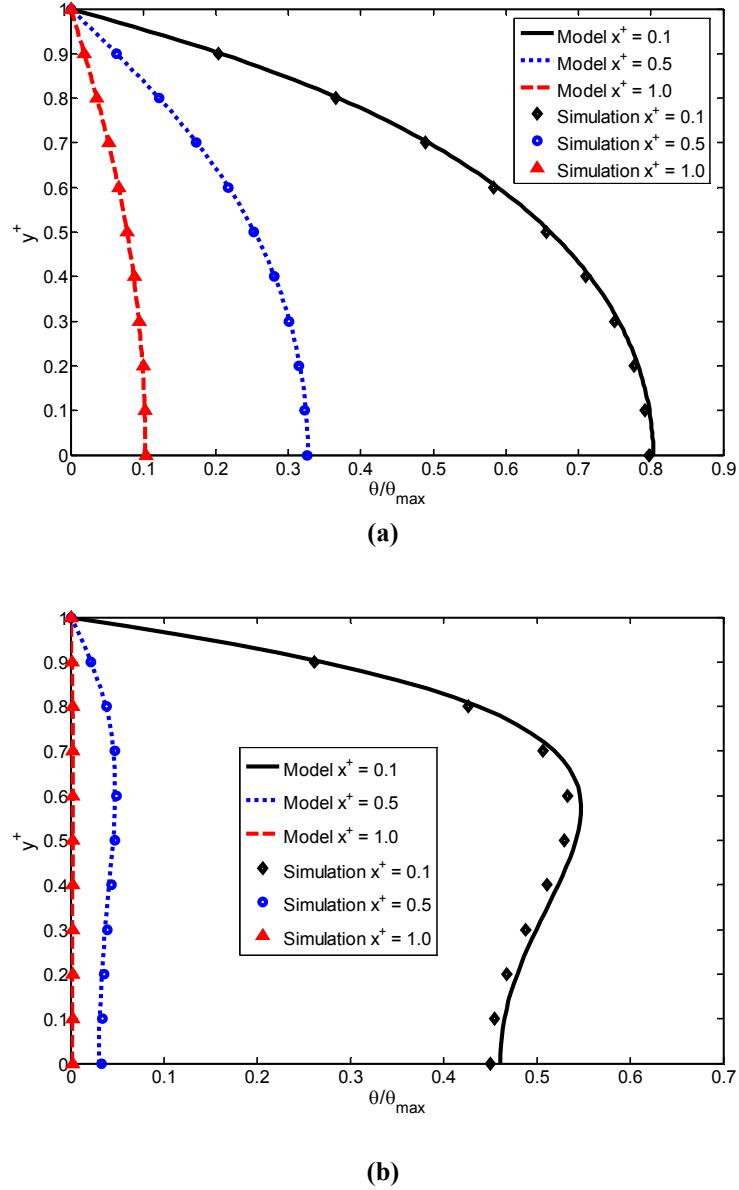
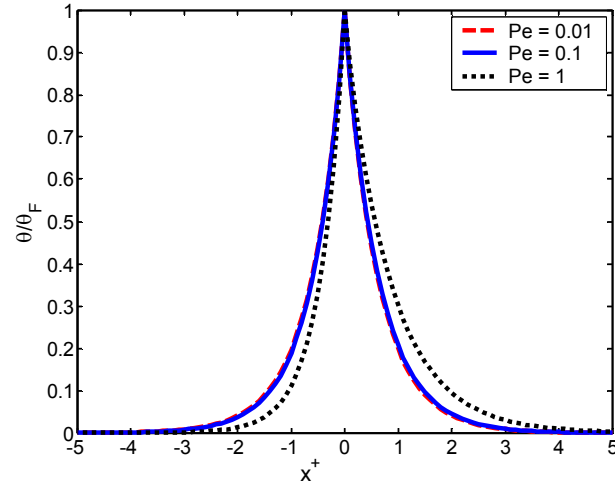


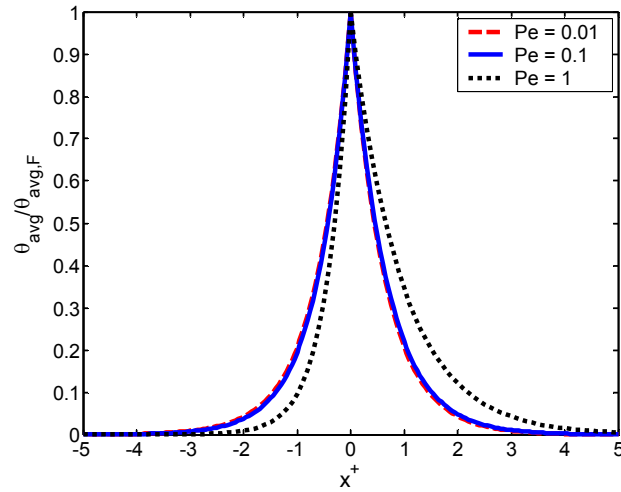
Figure 2-6: Comparison of transverse temperature profiles predicted by the analytical model and the CFD simulations for three axial (x^+) locations for Hagen-Poiseuille flow. a) $Pe = 1$ and b) $Pe = 5$

ii) Low Pe number:

Fig. 2-7 shows the ratio of the average non-dimensional temperature across the channel (in the transverse or y^+ direction) to the non-dimensional flame temperature as a function of axial position in the channel when the Peclet number is relatively small.



(a)



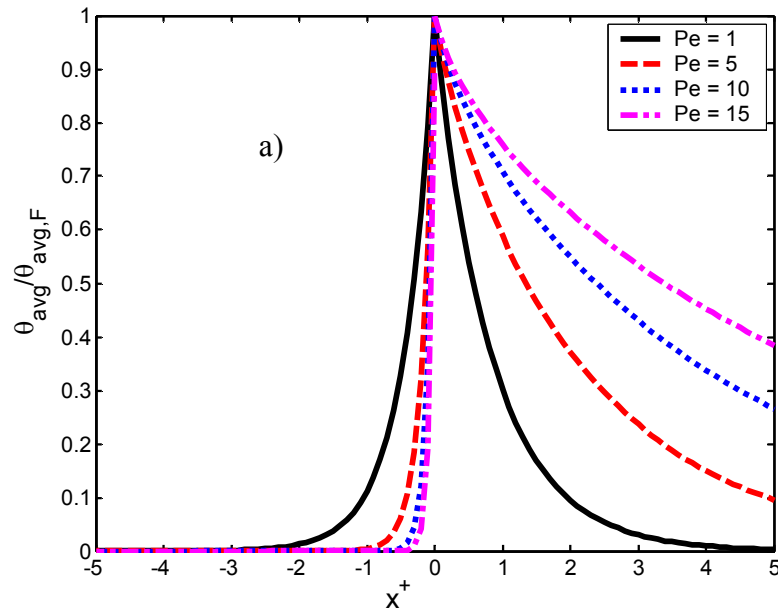
(b)

Figure 2-7: Non-dimensional temperature profile ($\theta_{avg}/\theta_{avg,F}$) in low Pe limit. a) Plug Flow and b) Hagen-Poiseuille Flow

The mean temperature profile is symmetric about the reaction zone and insensitive to flow velocity, velocity profile, or channel height at low Pe because the convective transport term in Eq. 2-4 is small in comparison to the conduction terms.

c) Moderate Pe number:

Fig. 2-8 shows the ratio of the average temperature across the channel (in the transverse or y^+ direction) to the non-dimensional flame temperature as a function of axial position in the channel for moderate values of the Peclet number. In both the plug and Hagen-Poiseuille flow cases, increasing the Peclet number causes the axial temperature distribution to become more asymmetric about the flame (heat release) zone. The asymmetry arises because the effect of the convective term is different in the pre and post-flame regions.



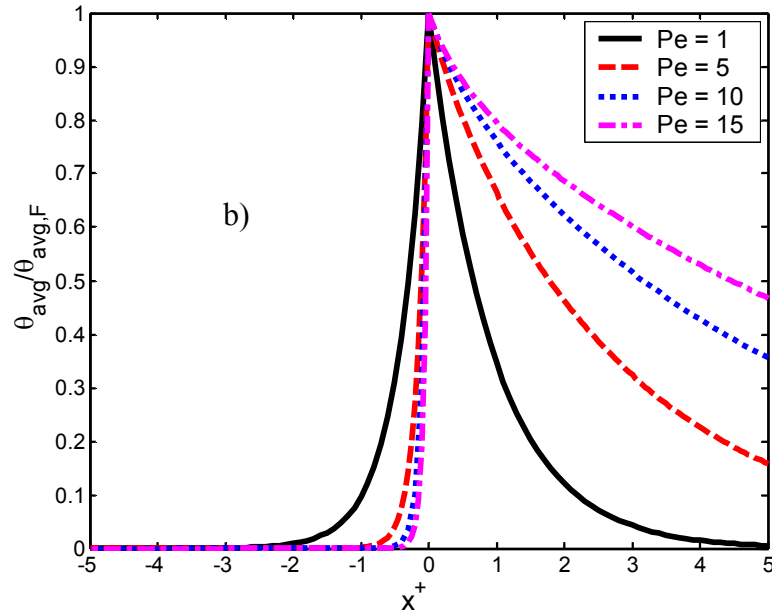


Figure 2-8: Non-dimensional temperature profile ($\theta_{\text{avg}}/\theta_{\text{avg},F}$) for plug and HP flows in the high Pe limit.

To see this, return to equation 2-4 and consider two positions both a distance δ from the flame but located in the pre and post-flame regions respectively. In the post-flame region, $\partial\theta/\partial x^+ < 0$ which means that the convective term acts with (ie. in the same direction or tends to augment) the axial diffusive term ($\partial^2\theta/\partial x^{+2}$). This leads to a net increase in axial thermal transport and a temperature increase over the zero velocity case at the arbitrary location $x^+ = \delta$ in the post-flame. In the pre-flame region however, $\partial\theta/\partial x^+ > 0$ and the convective term acts against the axial diffusive term leading to a net temperature decrease at $x^+ = -\delta$. Increasing the Peclet number increases the level of distortion by increasing the difference between axial diffusive and convective processes in the pre and post-flame regions. This effect distorts axial temperature profiles in both the plug and Hagen-Poiseuille flow cases.

In the Poiseuille flow case, however, the velocity profile causes the importance of the convective term relative to the axial diffusive term to decrease as one moves away from the channel center line. In the post-flame, this just reduces the augmentation of the axial thermal transport and the maximum temperature still occurs at the channel center and decreases as one moves toward the wall. In the pre-flame, however, the convective term acts against the axial diffusive term. The reduction in the net thermal transport in the axial direction is greatest at the centerline and decreases as one moves toward the wall. This means that the peak in the transverse temperature profile does not occur at the channel center – as it does in the post-flame – but at some intermediate point between the center and the wall as shown in fig. 2-7b. Increasing the Peclet number drives the peak temperature farther from the channel center line and closer to the walls. For $Pe > 30$, the flame is essentially a discontinuity, the problem is mostly one-dimensional, and a two-dimensional solution is not required.

iii) Nusselt number:

The Nusselt number is defined as the ratio of the convective heat flux to the conductive heat flux. It is usually written in terms of a heat transfer coefficient h , the thermal conductivity of the gas k , and a characteristic length scale for heat transfer which in this case is taken to be the hydraulic diameter (d_c):

$$Nu = \frac{h d_c}{k} \quad (2-20)$$

The exact solution for the temperature profile can be used to compute an overall Nusselt number for the problem as well as to develop a correlation for the variation of the Nusselt number with downstream distance. The latter is useful in one-dimensional numerical simulations of reacting flow with multi-step gas phase chemistry [20] where a

computationally efficient method for incorporating two-dimensional heat transfer effects is required. The local heat transfer coefficient is given by:

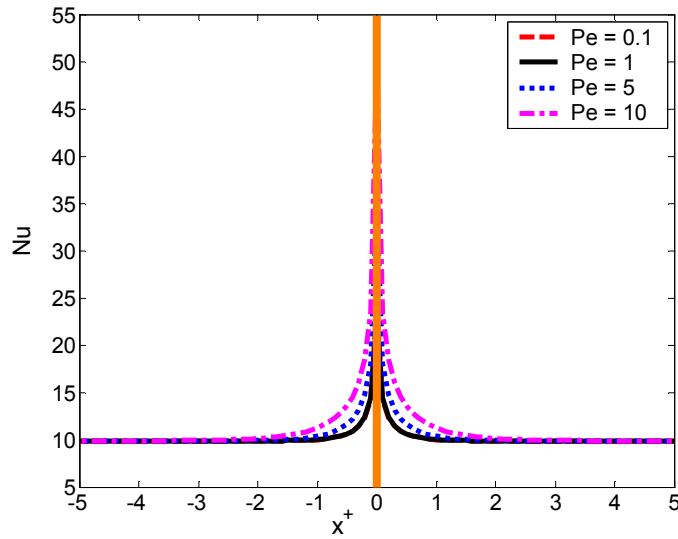
$$h_{x^+} = -\frac{k}{d} \frac{\left(\frac{\partial \theta}{\partial y^+} \right) \Big|_{y^+=1}}{\theta_{avg}} \quad (2-21)$$

Inserting Eq. 2-21 into Eq. 2-20 and assuming a two-dimensional planar passage ($d_c = 4d$) gives:

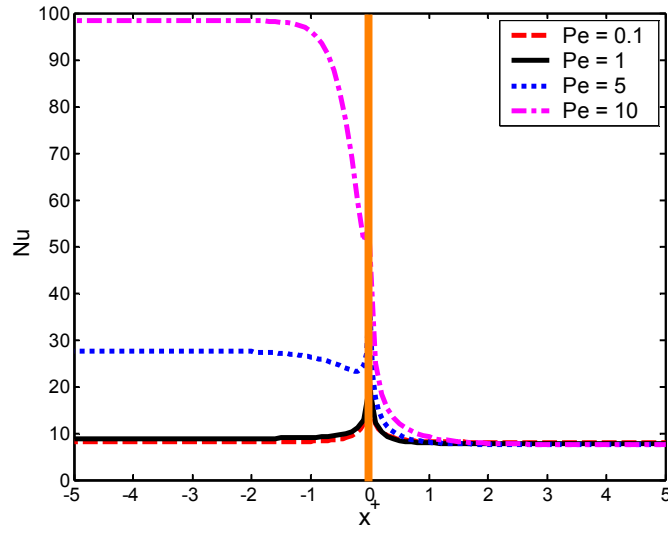
$$Nu_{x^+} = -4 \frac{\left(\frac{\partial \theta}{\partial y^+} \right) \Big|_{y^+=1}}{\theta_{avg}} \quad (2-22)$$

In this expression, θ_{avg} is the mean temperature of the flow:

$$\theta_{avg}(x^+) = \frac{\int_0^1 U(y^+) \theta(x^+, y^+) dy^+}{\int_0^1 U(y^+) dy^+} \quad (2-23)$$



(a)



(b)

Fig. 2-9: Nu number vs. axial distance for different Pe numbers. a) Plug flow, b) Poiseuille Flow

Fig. 2-9 shows the variation of Nusselt number with downstream distance for a range of Pe numbers. In plug flow, the Nusselt number peaks at the flame and rapidly decreases to the value π^2 as x^+ goes to $\pm\infty$. This is consistent with other solutions for heat transfer between parallel plates at constant temperature [24]. In Hagen-Poiseuille flow, however, the situation is quite different. While the solution also asymptotes to π^2 as x^+ goes to ∞ , it asymptotes to different values (that depend on the Peclet number) as x^+ goes to $-\infty$. This curious behavior in the pre-flame is another consequence of the effect of the velocity profile on the competition between convection and axial conduction in the pre-flame region: Increasing the Peclet number moves the peak in the transverse temperature profile closer to the wall. This increases the Nusselt number by increasing the temperature gradient at the wall. The Nusselt number approaches a constant far upstream because the

temperature gradient at the wall goes to zero at the same rate as the mean temperature goes to zero.

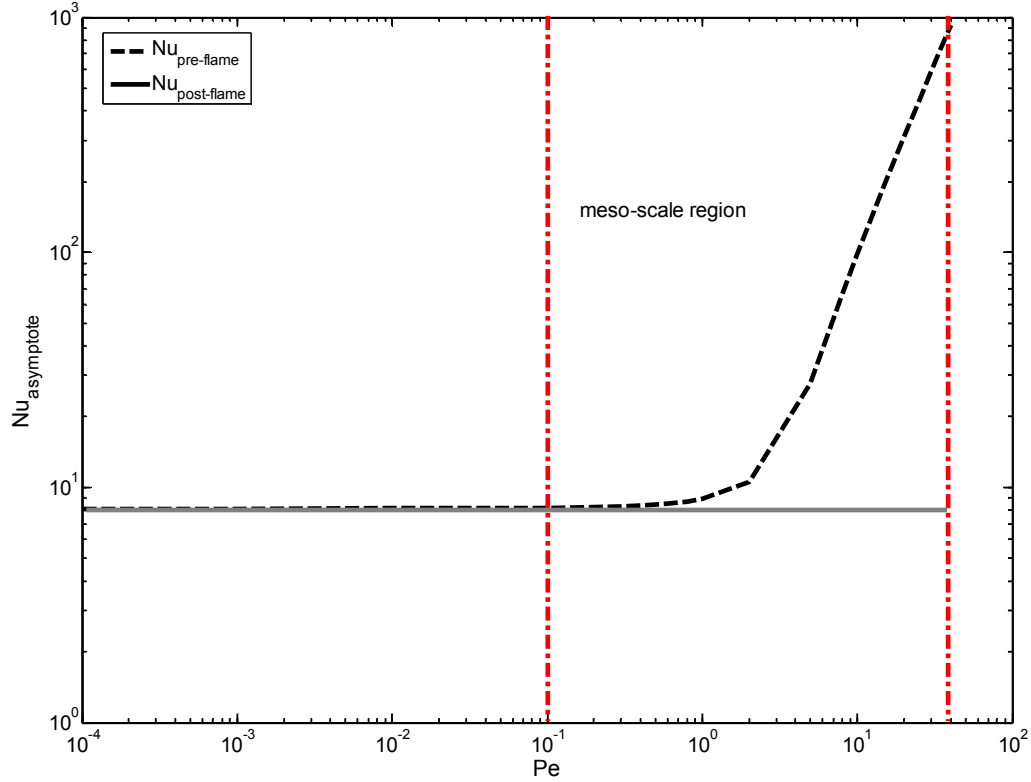


Fig. 2-10: Nu asymptote as a function of Pe for H-P flow

Fig. 2-10 shows that while the Nusselt number in the post-flame is a constant that is independent of Peclet number, it is not a constant in the pre-flame when the Peclet number is of order 1 or greater; the horizontal gray line shows the asymptotic value for Nu from traditional heat transfer analysis for channel flow with constant wall temperature. This result is important because currently accepted practice in the simulation of reacting flows in micro-combustors is to choose a single Nusselt number to represent gas-wall heat transfer over the entire computational domain. Given that pre-heating of the mixture by the structure in the pre-flame region is a critical aspect of micro-combustor

performance [40], and that the potential variation in pre-flame Nusselt number is large (up to 3 orders of magnitude for even an over simplified isothermal wall assumption), it is clear that incorporating this effect will be important in future simulations. Table 2-1 gives the asymptote values of the pre and post-flame Nusselt numbers for different values of Pe for H-P flow. These values may be used in future simulations that model constant wall temperature combustors after estimating the Pe number for the application. The values in the table show that the Nusselt number increases rapidly in the pre-flame region beyond a Peclet number of 1. This makes sense since the flow becomes essentially one-dimensional at $Pe > 30$.

Pe	Nu_{pre}	Nu_{post}
0.0001	8.11747	8.11737
0.001	8.11793	8.11692
0.01	8.12246	8.11244
0.1	8.16984	8.06952
1	8.90686	7.79088
5	27.6355	7.56931
8	66.4142	7.55258
10	98.3997	7.54842
15	193.776	7.54418
20	308.596	7.54267
25	440.381	7.54196
30	587.348	7.54158

Table 2-1: Nusselt number asymptote values for Pre and Post-flame regions for different Pe numbers for H-P flow.

2.3. Conducting Wall Boundary Condition (Conjugate Heat Transfer)

In § 2.2 we assumed the wall temperature was uniform throughout the combustor. While this simplified the solution, and could be realistic in some situations, generally it is not physically realistic. Therefore, let us revisit the problem when the wall temperature is not specified. Fig. 2-11 shows the energy equations that need to be considered both in the gas and the structure. Again, the figure only shows one half of the channel as the problem is assumed to be symmetric.

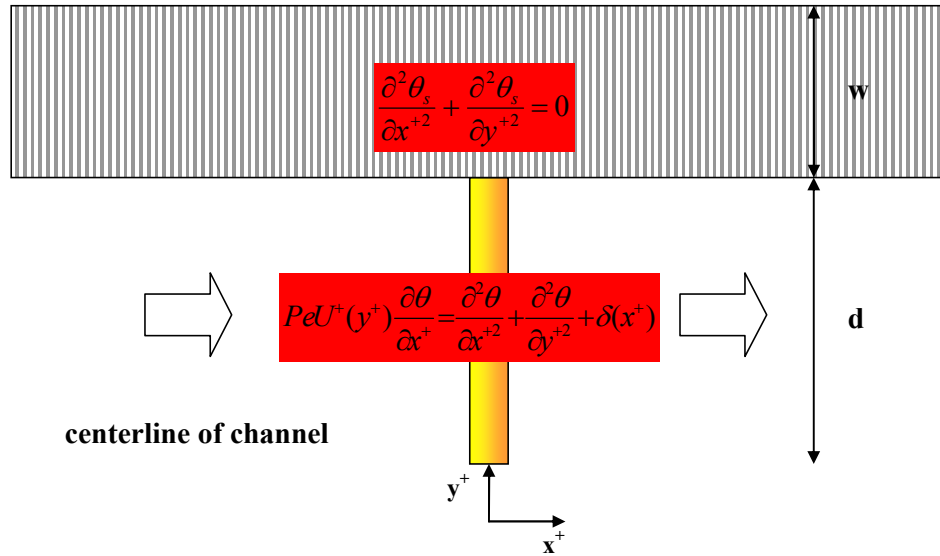


Figure 2-11: Half Channel from Centerline to Outer Edge of Structure.

The energy equations for the gas and structure in non-dimensional form are given by:

$$PeU^+(y^+) \frac{\partial \theta_g}{\partial x^+} = \frac{\partial^2 \theta_g}{\partial x^{+2}} + \frac{\partial^2 \theta_g}{\partial y^{+2}} + \delta(x^+) \quad (2-24)$$

$$\frac{\partial^2 \theta_s}{\partial x^{+2}} + \frac{\partial^2 \theta_s}{\partial y^{+2}} = 0 \quad (2-25)$$

The subscripts g and s stand for gas and structure respectively, where δ is the Dirac delta function. This implies that all of the heat release occurs at the infinitesimally thin flame location ($x^+ = 0$). This is commonly known as the “flame sheet” assumption. The non-dimensionalizations for the temperature, spatial coordinates, and velocity are the same as for the previous problem (see eq. 2-2) but two new non-dimensional parameters κ , and τ are added to account for the thermal conductivity and thickness of the wall (structure).

$$\theta_{g,s} = \frac{T_{g,s} - T_\infty}{\dot{q}_R'' d / k_g}; x^+ = \frac{x}{d}; y^+ = \frac{y}{d}$$

$$\kappa = \frac{k_s}{k_g}; \tau = \frac{w+d}{d}; U^+(y^+) = U(y^+)/\bar{U}$$
(2-26)

Where

$$\bar{U} = \int_0^1 U(y^+) dy^+ \quad (2-27)$$

The Peclet number is defined as before (eq. 2-5). The first two boundary conditions on the gas are the same as before (eqs. 2-9 and 2-10):

$$\theta_g(\mp\infty, y^+) = 0 \quad (2-28a)$$

$$\left. \frac{\partial \theta_g}{\partial y^+} \right|_{y^+=0} = 0 \quad (2-28b)$$

The gas temperature equals the ambient temperature at the ends of the channel (eq. 2-28a) which is equivalent to assuming that the ambient temperatures are the same at the channel inlet and exit and the temperature field is symmetric about the center line (2-28b).

Now that the structure is conductive, it is no longer isothermal and additional boundary conditions are required. The structure temperature is assumed to go to the environment temperature at +/- infinity. Therefore:

$$\theta_s(\mp\infty, y^+) = 0 \quad (2-28c)$$

The structure also loses heat to the environment. This is represented by specifying a Nusselt number for heat transfer from the outer wall to the environment:

$$-\left. \frac{\partial \theta_s}{\partial y} \right|_{y=\tau} = \frac{Nu_E \theta_s(\tau)}{\kappa} \quad (2-28d)$$

The Nusselt number for heat loss to the environment is given by:

$$Nu_E = \frac{h_E d}{k_g} \quad (2-29)$$

This heat loss model is based on Newton's law for cooling [78]. Setting the heat transfer coefficient (h_E) equal to zero gives the adiabatic outer wall condition. Setting $h_E > 0$ incorporates heat loss to the environment. Finally, continuity of temperature and heat flux at the gas-structure interface requires:

$$\theta_g(x^+, 1) = \theta_s(x^+, 1) \quad (2-30a)$$

$$\left. \frac{\partial \theta_g}{\partial y^+} \right|_{y^+=1} = \kappa \left. \frac{\partial \theta_s}{\partial y^+} \right|_{y^+=1} \quad (2-30b)$$

Here κ is the structure to gas thermal conductivity ratio. As before, we require that the temperature on both sides of the flame match but the gradients do not match because of the heat production at the flame. Integrating over an infinitesimally small volume around the flame gives the “*jump conditions*”:

$$\theta_s(0^-, y^+) = \theta_s(0^+, y^+) \quad (2-31a)$$

$$\left. \frac{\partial \theta_g}{\partial x^+} \right|_{0^-}^{0^+} = -1 \quad (2-31b)$$

Temperatures in the structure must also match at the flame location but integrating over a similar volume gives no discontinuity in the structure temperature because there is no heat production in the structure.

$$\theta_s(0^-, y^+) = \theta_s(0^+, y^+) \quad (2-32a)$$

$$\left. \frac{\partial \theta_s}{\partial x^+} \right|_{0^-}^{0^+} = 0 \quad (2-32b)$$

2.3.1. Solution

The solution to the governing equations is obtained by using the same separation of variables procedure used in the first problem and described in Appendix A except that there is now are now two solutions: one for the gas and one for the structure. As before, we choose ϕ as the pre-flame solution and ψ as the post-flame solution. The corresponding eigenvalues in the two regions are given by λ and β respectively.

$$\theta_g(x^+, y^+) = \begin{cases} \sum_{n=1}^{\infty} A_n \exp(\lambda_n x^+) \phi_g(\lambda_n, y^+); x^+ < 0 \\ \sum_{n=1}^{\infty} B_n \exp(-\beta_n x^+) \psi_g(\beta_n, y^+); x^+ > 0 \end{cases} \quad (2-33)$$

$$\theta_s(x^+, y^+) = \begin{cases} \sum_{n=1}^{\infty} A_n \exp(\lambda_n x^+) \phi_s(\lambda_n, y^+); x^+ < 0 \\ \sum_{n=1}^{\infty} B_n \exp(-\beta_n x^+) \psi_s(\beta_n, y^+); x^+ > 0 \end{cases} \quad (2-34)$$

Where,

$$A_n = \frac{\int_0^1 \phi_{g,n} dy^+}{\left(\int_0^1 (-PeU^+(y^+) + 2\lambda_n) \phi_{g,n}^2 dy^+ + \int_1^\tau 2\lambda_n \kappa \phi_{s,n}^2 dy^+ \right)} \quad (2-37)$$

$$B_n = \frac{\int_0^1 \psi_{g,n} dy^+}{\left(\int_0^1 (PeU^+(y^+) + 2\beta_n) \psi_{g,n}^2 dy^+ + \int_1^\tau 2\beta_n \kappa \psi_{s,n}^2 dy^+ \right)} \quad (2-38)$$

2.3.2. Results

In §2.2, the 2D solution for a flame stabilized in a constant wall temperature channel showed that the Peclet number was the only parameter influencing the temperature profiles. In the conjugate heat transfer problem considered here, four parameters now govern the temperature distribution because the wall conducts heat axially and transversely. These are: the Peclet number (Pe), the ratio of thermal conductivities between wall and gas (κ), the geometric ratio of cross sectional areas for conduction (τ), and the heat loss coefficient to the outer environment (Nu_E). The influence of each parameter is explored below.

i) Effect of Pe

The Pe number as discussed previously is the ratio of convective to conductive heat transfer. Large Pe numbers are associated with large passage heights, large flow velocities or a suitable combination of the two. Peclet numbers less than 30 are representative of the micro or meso-scale flow regimes usually associated with miniaturized power applications.

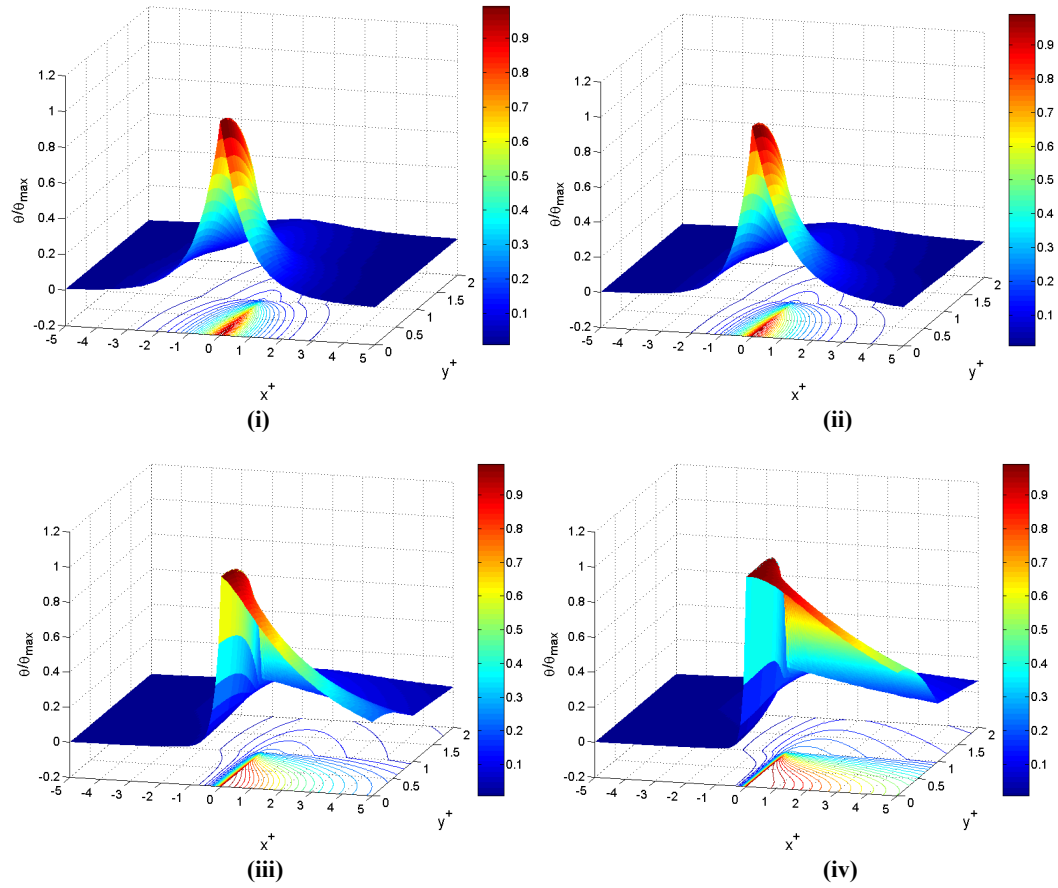
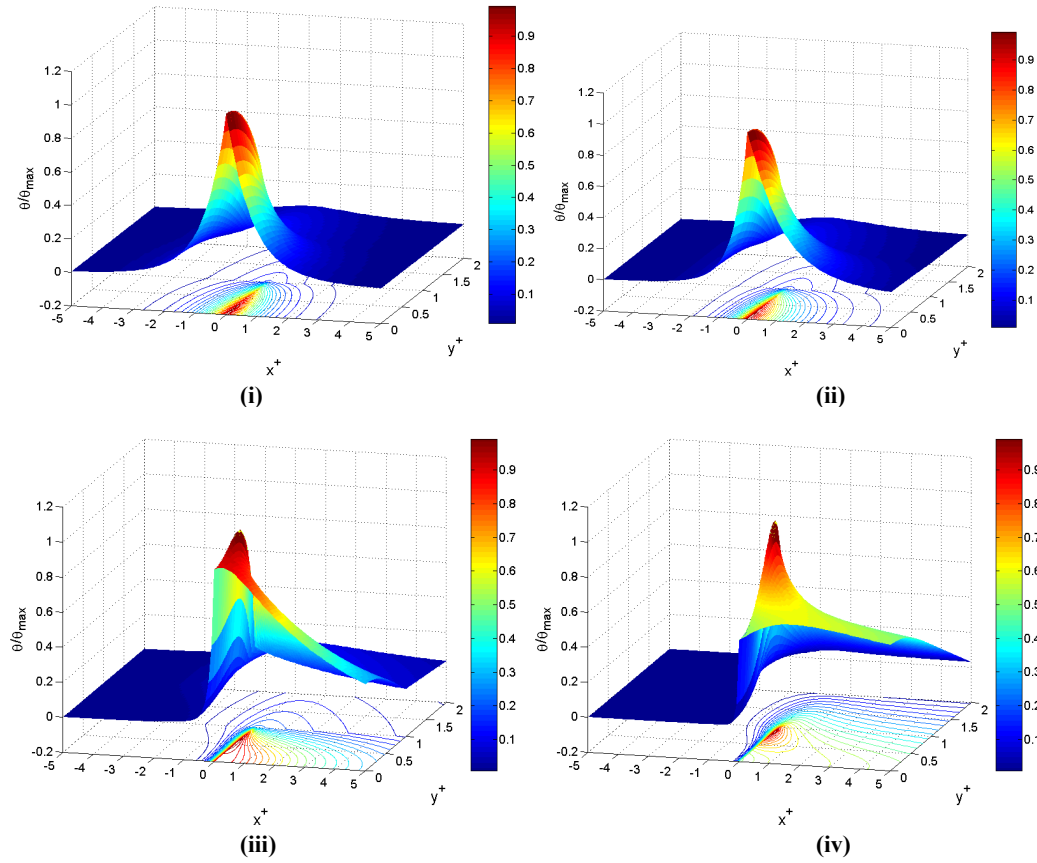


Figure 2-12a: Effect of Changing Pe on the Non-Dimensional Temperature for:
(Plug Flow, $\kappa = 10$, $\tau = 2$, $Nu_E = 10$)
(i) $Pe = 0.1$, (ii) $Pe = 1$, (iii) $Pe = 5$, (iv) $Pe = 10$

Fig. 2-12a shows non-dimensional temperature distributions in the gas and structure associated with four values of the Peclet number lying in the sub meso-scale regime. The velocity profile is uniform (plug flow) and the values of the other governing parameters are held constant.



**Figure 2-12b: Effect of Changing Pe on the Non-Dimensional Temperature for:
(Hagen-Poiseuille Flow, $\kappa = 10$, $\tau = 2$, $Nu_E = 10$)
(i) $Pe = 0.1$, (ii) $Pe = 1$, (iii) $Pe = 5$, (iv) $Pe = 10$**

Fig. 2-12b shows the non-dimensional temperature distributions for plane Poiseuille flow. Figures 12-12a and 12-12b show a significant range of behaviors. At low Pe , the temperature fields are spread out and the structure temperature is relatively uniform. As the Peclet number is increased, convective heat transfer becomes more important and structural heat conduction is not able to smooth out the temperature distribution in the structure as effectively. At the same time, the temperature field in the channel becomes more 1D (ie. less variation in the y^+ direction). Therefore, the model shows that it is

important to consider 2D effects when designing micro and mesoscale combustors that operate at small Pe .

The temperature contours plotted in the X-Y plane below the figure illustrate how heat is transported through the microcombustor. Since heat flux is the negative of the product of the temperature gradient and thermal conductivity, heat flows in a direction perpendicular to the contour lines. The fact that the axial components of the pre-flame temperature gradients in both the gas and structure increase with increasing Pe suggest that more heat recirculation is required to stabilize the flame as the flow velocity is increased. The chief difference between the plug and Poiseuille flow cases is the location of the peak temperature. For plug flow, the peak occurs along the centerline while for Poiseuille flow, the peak occurs between the channel center and the wall interface. The consequences of this will be discussed in more detail later.

ii) Effect of κ

Another important parameter governing the development of the gas and structure temperature distributions is the ratio of the thermal conductivity of the structure to that of the gas (κ). This parameter determines the preferred heat conduction path as intuition tells us that if the structure is a few orders of magnitude more conductive, then the heat transfer path of least resistance could be through the structure. Figs. 2-13a and b show that at constant Pe , increasing κ decreases temperature gradients in the structure. In practice, it is hard to find materials whose thermal conductivities are much less than the gas (air + fuel) although $\kappa \approx 1$ is possible if the structural material is a solgel.

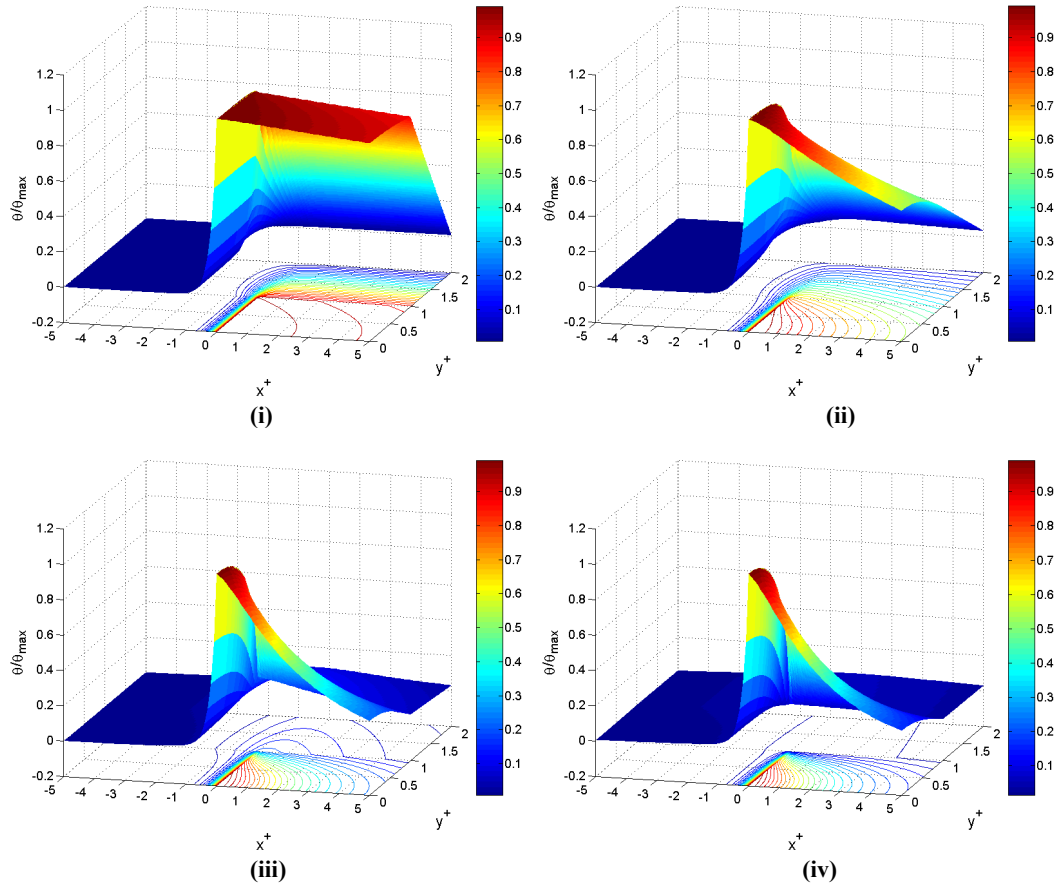


Figure 2-13a: Effect of Changing κ on the Non-Dimensional Temperature for:
(Plug Flow, $Nu_E = 10$, $\tau = 2$, $Pe = 5$),
(i) $\kappa = 0.1$, (ii) $\kappa = 1$, (iii) $\kappa = 10$, (iv) $\kappa = 100$

Even when κ is only moderately large ($\kappa=10$), Fig. 2-13 shows that temperature gradients in the structure are reduced significantly. In the non-adiabatic case, the structure temperature is also reduced as the heat entering the structure from the hot gases near the flame gets conducted more efficiently to the incoming reactants and the environment. Again, the chief difference between Figs. 2-13 a and b is the occurrence of the peak temperature at a different location from the centerline in the case of of HP

flow.

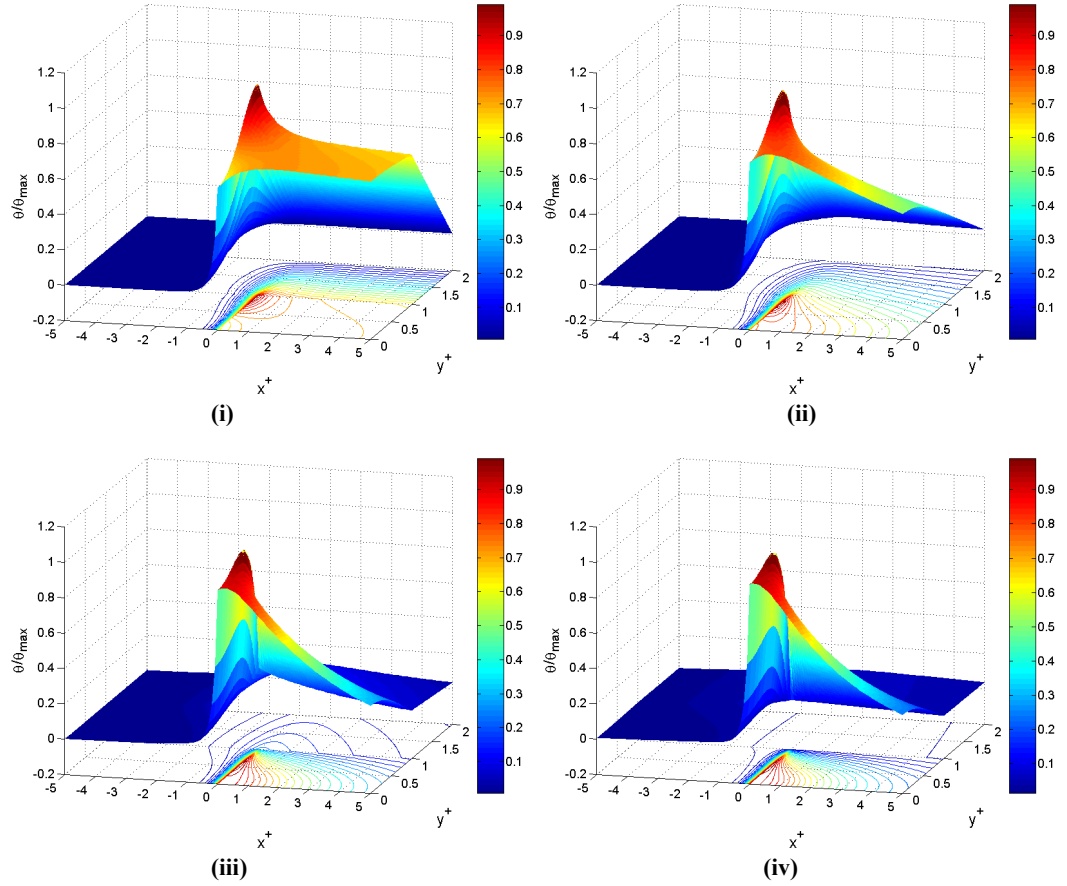


Figure 2-13b: Effect of Changing κ on the Non-Dimensional Temperature for:
(Hagen-Poiseuille Flow, $Nu_E = 10$, $\tau = 2$, $Pe = 5$),
(i) $\kappa = 0.1$, (ii) $\kappa = 1$, (iii) $\kappa = 10$, (iv) $\kappa = 100$

iii) Effect of τ

Figs. 2-14a and b show that while increasing the wall thickness also enables greater heat conduction through the wall and hence enhanced thermal interaction between gas and structure, changing the wall thickness is not equivalent to changing the thermal conductivity of the wall.

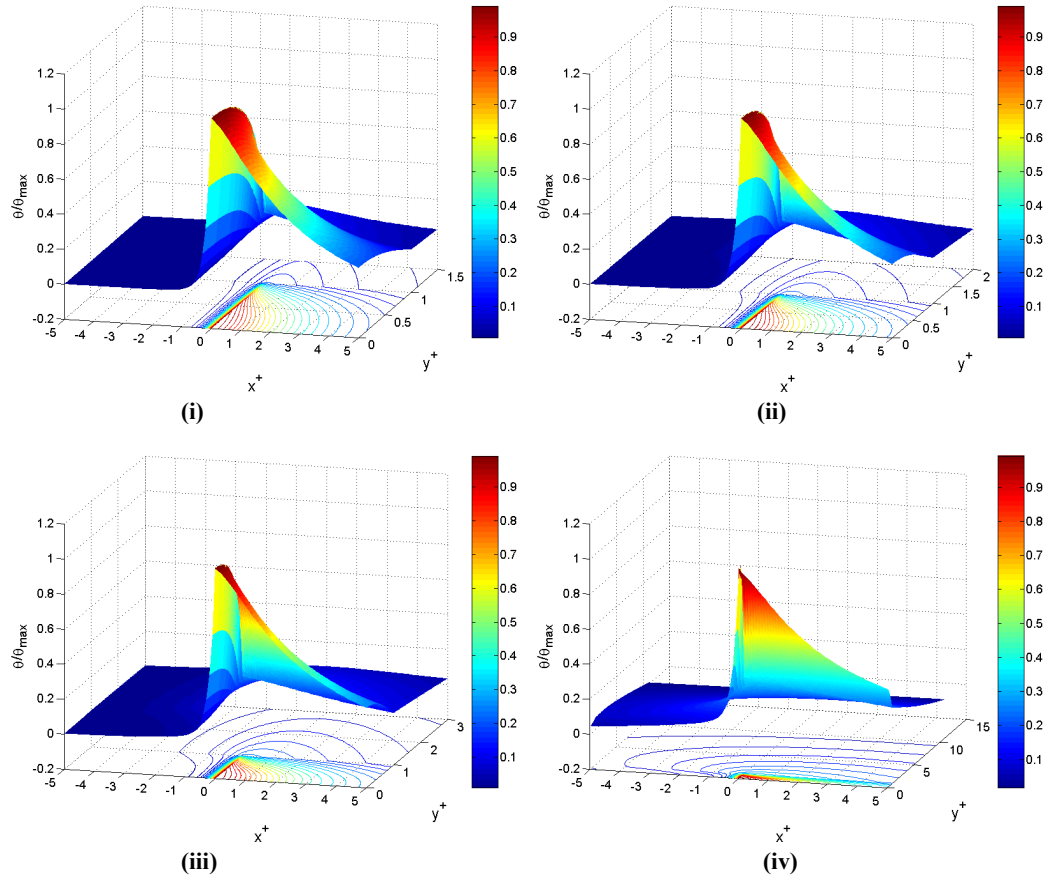


Figure 2-14a: Effect of Changing τ on the Non-Dimensional Temperature for:

(Plug Flow, $Nu_E = 10$, $\kappa = 10$, $Pe = 5$)

(i) $\tau = 1.5$, (ii) $\tau = 2$, (iii) $\tau = 3$, (iv) $\tau = 11$

This is because of the two-dimensional nature of the problem: Thicker walls reduce the temperature gradient between the inner and outer walls with the result that less heat gets lost to the environment and more heat gets transported axially and recirculated.

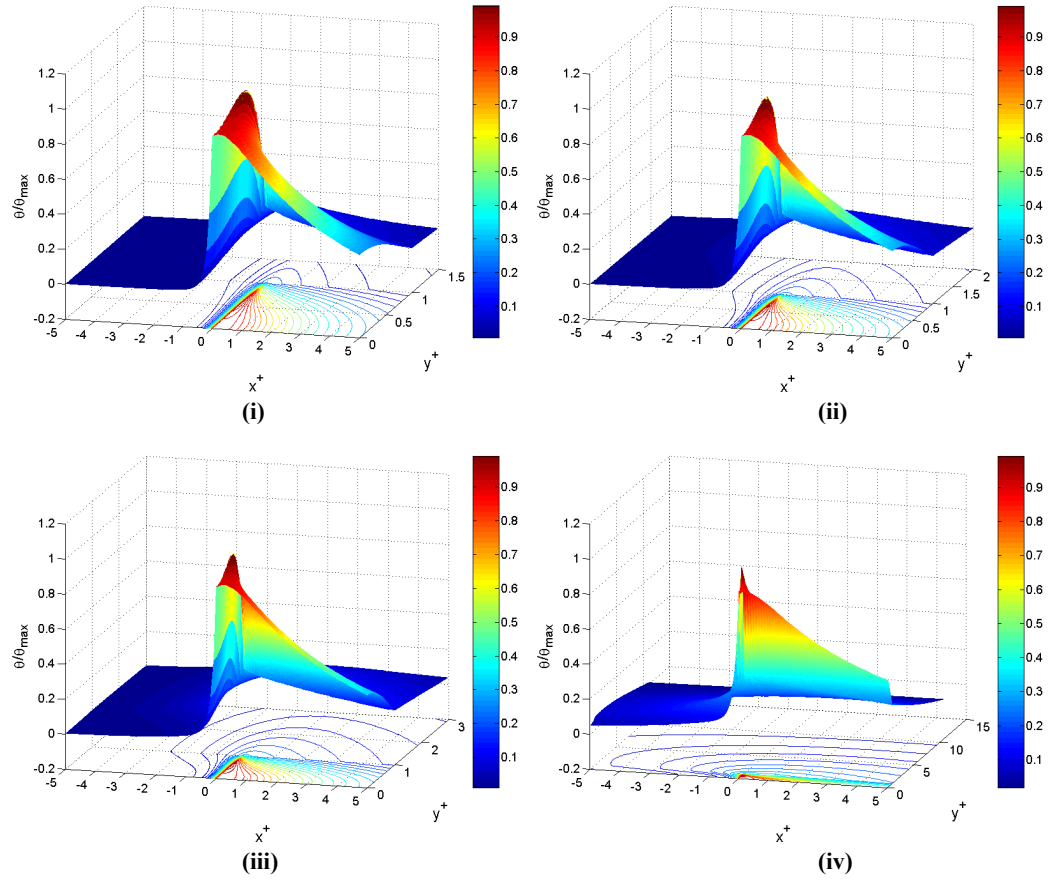


Figure 2-14b: Effect of Changing τ on the Non-Dimensional Temperature for:
(Hagen-Poiseuille Flow, $Nu_E = 10$, $\kappa = 10$, $Pe = 5$)
(i) $\tau = 1.5$, (ii) $\tau = 2$, (iii) $\tau = 3$, (iv) $\tau = 11$

iv) Effect of Nu_E

The final important parameter governing temperature distributions in micro and mesoscale channels is heat loss to the environment. Prior work has shown that the balance between the heat loss to the environment and the heat recirculated upstream via the combustor's structure determines the feasibility of achieving continuous and stable chemical reaction [41].

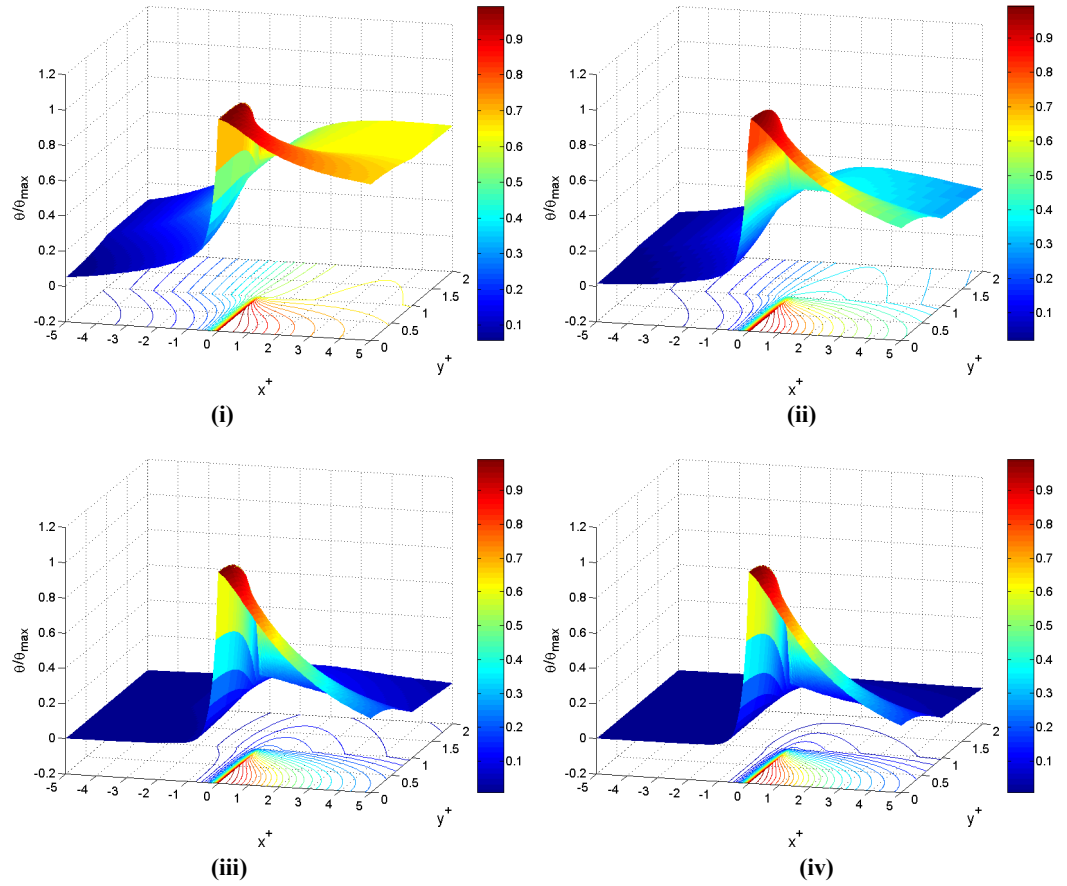


Figure 2-15a: Effect of Changing Nu_E on Non-Dimensional Temperature for:
(Plug Flow, $\tau = 2$, $\kappa = 10$, $Pe = 5$),
(i) $Nu_E = 0.1$, (ii) $Nu_E = 1$, (iii) $Nu_E = 10$, (iv) $Nu_E = 100$

Figs. 2-15a and b show non-dimensional temperature distributions in a micro-channel for different heat losses to the environment described using the Nusselt number (Nu_E). As Nu_E is decreased (or heat loss is reduced), the structure's temperature increases, the thermal interaction between gas and structure is enhanced in the pre-flame region and two-dimensional effects become more important. While operation at low Nu_E is advantageous from the point of view of power system thermodynamics, the figure shows that low Nusselt number operation also leads to steep temperature gradients in the wall which could lead to thermal degradation of the structure material.

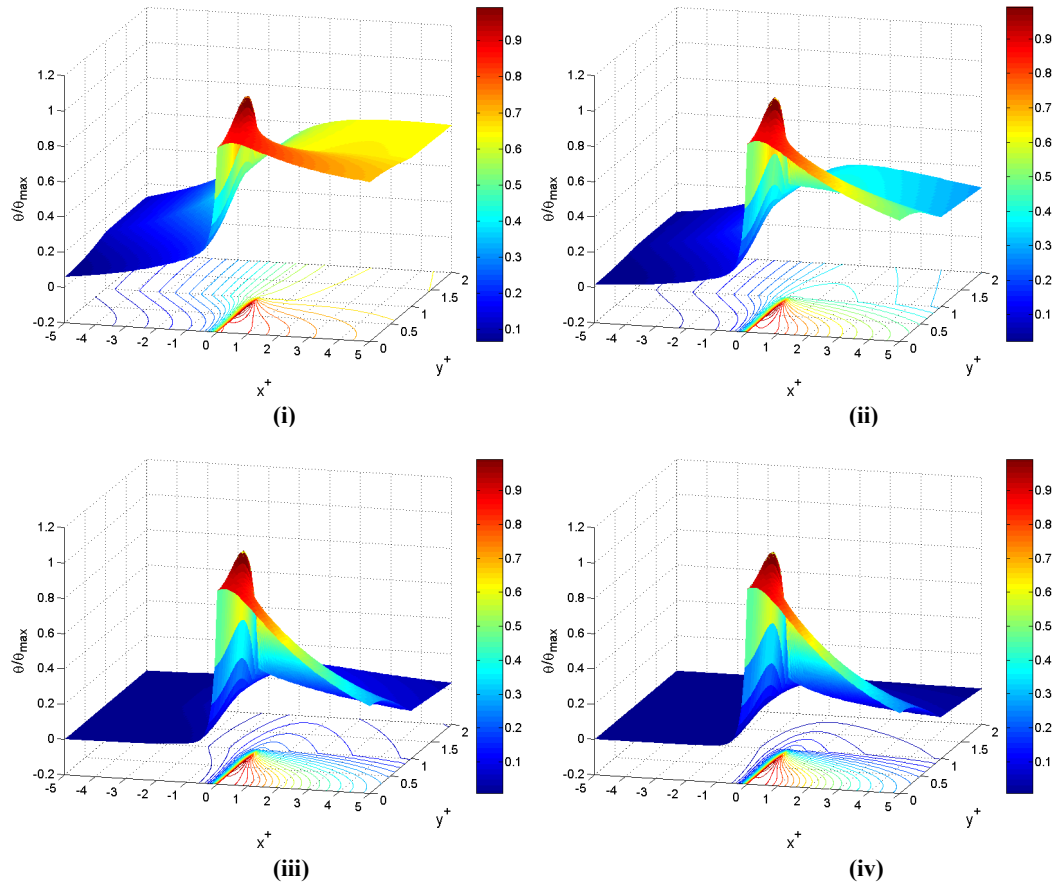


Figure 2-15b: Effect of Changing Nu_E on Non-Dimensional Temperature for:
(Hagen-Poiseuille Flow, $\tau = 2$, $\kappa = 10$, $Pe = 5$)
(i) $Nu_E = 0.1$, (ii) $Nu_E = 1$, (iii) $Nu_E = 10$, (iv) $Nu_E = 100$

v) Nu between structure and gas:

The solution developed here can also be used to develop an analytical expression for the Nusselt number associated with heat transfer between the gas and the structure³. Such an expression is useful for gaining further insight into the heat transfer processes occurring in micro-combustors as well as for developers of numerical simulations with

³ This is an important difference with the previous quasi-1D representation requiring the prescription of a Nu number.

multi-step chemistry that need to save computational time by incorporating 1D heat transfer models. The Nusselt number based on the hydraulic diameter (4 d) is given by:

$$Nu_{x^+} = -4 \frac{\left(\frac{\partial \theta_g}{\partial y^+} \right) \Big|_{y^+=1}}{\bar{\theta}_g - \theta_{g,s,y^+=1}} \quad (2-39)$$

where,

$$\bar{\theta}_g(x^+) = \frac{\int_0^1 U(y^+) \theta_g(x^+, y^+) dy^+}{\int_0^1 U(y^+) dy^+} \quad (2-40)$$

As noted in the problem formulation, there are three modes of heat transport in this problem: convection arising from the gas flow, conduction through the gas, and conduction through the structure. All influence the gas temperature profiles and so all effects are considered simultaneously in the present work. The influence of these various modes of heat transfer can be tracked by monitoring the Nu between the gas and the wall.

Fig. 2-16 shows that the axial variation in Nu is a strong function of the Peclet number. At low Pe ($Pe \sim 0.1$), convective heat transfer between the gas and the wall and conduction through the structure are much smaller than axial conduction in the gas. Since the wall is cooler than the gas in both the pre and post-flame regions, heat transfer is always from the gas to the wall indicating that no heat recirculation takes place.

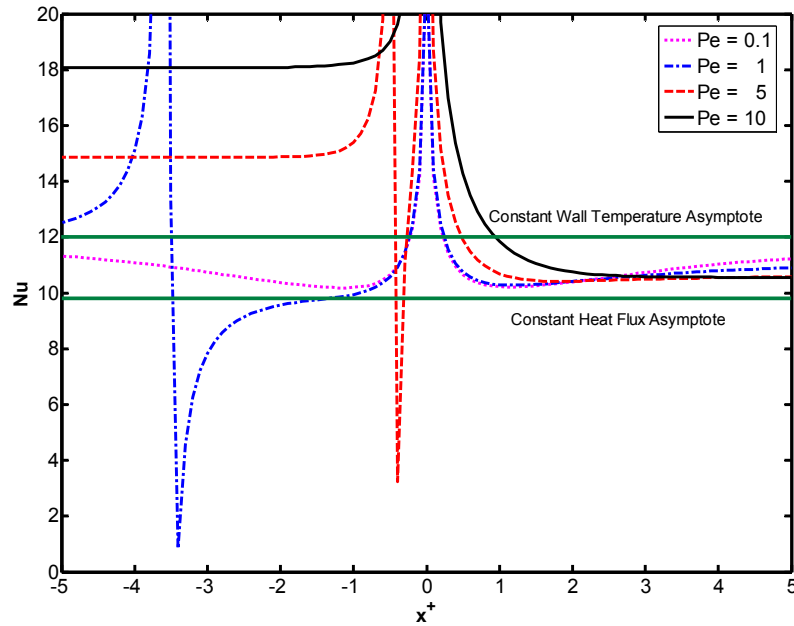


Figure 2-16: Axial variation in the Nusselt number for various Pe numbers.

(Plug flow, $\kappa = 10$, $\tau = 2$, $Nu_E = 10$)

At somewhat higher Peclet numbers, a discontinuity appears at the axial location where the slope of the temperature gradient at the wall changes sign. In the case of $Pe=1$ shown in the figure, this sign change occurs in the $-4 < x^+ < -3$ range. Physically, this means that the gas to the left of the discontinuity is cooler than the wall and hence is being pre-heated. To the right of the discontinuity, the wall is cooler than the gas and conductive heat transfer through the gas from the post-flame to the pre-flame remains the dominant mode of heating. It should be pointed out as an aside that the discontinuity is also present in the low Pe case considered earlier but does not appear in the figure because it occurs at $x^+ < -5$. So, some heat recirculation is still going on but it is very small.

As Pe is increased further, the convective term in Eq. 2-24 drives the discontinuity closer to the flame. At $Pe > 10$, the part of the pre-flame region where axial conduction

through the gas dominates is very small making it difficult to distinguish between the location of the discontinuity and the flame location. At this point, effectively all of the gas in the pre-flame region is pre-heated by heat recirculation through the structure.

The figure also shows that the asymptotic value of the Nu in the pre-flame changes is a function of Pe number. For comparison, the results of previous heat transfer analyses [24] of forced convective flows in channels with two types of boundary conditions are presented below:

$$\begin{aligned} Nu_{\infty, Plug Flow} &= \begin{cases} 9.87, & \text{Constant Wall } T \\ 12.00, & \text{Constant heatflux} \end{cases} \\ Nu_{\infty, H-P Flow} &= \begin{cases} 7.60, & \text{Constant Wall } T \\ 8.23, & \text{Constant heatflux} \end{cases} \end{aligned} \quad (2-41)$$

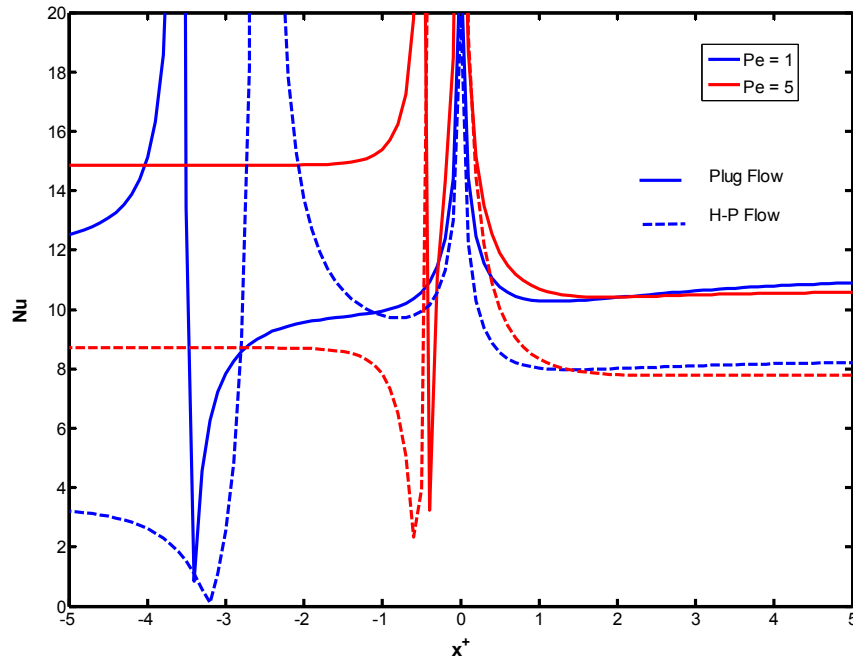


Figure 2-17: Comparison of the axial variation of the Nusselt number in plug versus fully developed flow for two different Pe numbers ($\kappa = 10$, $\tau = 2$, $Nu_E = 10$)

In plug flow, the values of Nu_∞ predicted by the present model lie between the values for the constant wall temperature and constant heat flux cases. This is to be expected as the post-flame region resembles the model problem considered in [24] where hot gas enters the channel and loses heat to the walls. In the pre-flame region, however, the role of the convective heat transfer is different because the axial temperature gradient points in the opposite direction (i.e. has the opposite sign). This leads to the competition between axial and transverse heat transfer discussed earlier. Fig. 2-17 compares the axial variations in Nusselt number for plug and Hagen-Poiseuille (H-P) flows. Both exhibit similar behaviors except that the asymptote values for the H-P flow cases are lower than those of the corresponding plug flow cases.

S. No.	Pe	κ	τ	Nu_E	Nu_∞ (Plug)	Nu_∞ (Plug)	Nu_∞ (HP)	Nu_∞ (HP)
1	1	10	2	10	12.09	11.04	3.38	8.28
2	2	10	2	10	12.77	10.80	7.13	7.96
3	5	10	2	10	14.86	10.61	8.71	7.78
4	10	10	2	10	18.07	10.56	10.12	7.74
5	5	10	2	0.1	13.20	11.93	8.57	8.21
6	5	10	2	1	13.63	11.50	8.67	8.06
7	5	1	2	10	16.24	11.44	7.42	8.04
8	5	0.1	2	10	16.15	11.92	4.75	8.21
9	5	1	2	1	15.74	11.66	8.36	8.12
10	5	10	1.1	10	15.73	10.30	2.72	7.70
11	5	10	3	10	14.04	10.88	8.73	7.86
12	5	10	11	10	12.66	11.62	8.45	8.10

Table 2-2: Nu asymptotes for different operating conditions of the burner

This is because the low speed flow near the wall in the Hagen-Poiseuille case inhibits heat transfer. Table 2-2 gives Nu asymptote values for some ‘typical’ micro/mesoscale

burners. The behaviors of H-P and plug flow are similar in the post-flame region except at low Pe (between 1 and 5) where the H-P asymptote Nu is lower than that predicted by traditional heat transfer analysis. For $Pe \geq 5$ (not shown), the H-P asymptote again falls between the values of heat transfer analysis for constant wall temperature and constant heat flux boundary conditions. As discussed previously, the asymptote value for the *Nusselt* number is quite different in the pre-flame region for both types of flows. This can be seen in Table 2-2 for $Nu_{-\infty}$.

Chapter 3: Flame Speed (Eigenvalue) Solution

In Chapter 2, the conjugate heat transfer model accounting for heat transfer between wall and gas in 2-D for a pre-mixed laminar flame stabilized in a channel was presented along with the analytical solution for two velocity profiles (Plug flow and Poiseuille flow). The chemical reaction term was modeled as a concentrated heat release function, thus enabling the focus to lie on the pure heat transfer problem. This, however, oversimplifies the reaction chemistry and thus makes the Pe number or equivalently the flame speed a user specified parameter. In real flames, the chemical reaction and species transport is connected with the heat transfer and thus the flame speed is set by the interlinking making it an eigenvalue of the problem. Therefore, in this chapter we incorporate the species transport equation with the previously developed conjugate heat transfer model to obtain the flame speed.

3.1. Governing Equations

Figure 3-1 is a schematic diagram of the model problem: a pre-mixed flame stabilized between parallel plates. The problem is made non-dimensional by defining the following variables:

$$\begin{aligned}\theta_{g,s} &= \frac{T_{g,s} - T_{-\infty}}{T_{ad} - T_{-\infty}}; Y_f = \frac{y_f}{y_{f,-\infty}}; x^+ = \frac{x}{d}; y^+ = \frac{y}{d} \\ \kappa &= \frac{k_s}{k_g}; \tau = \frac{w + d}{d}; \\ f(y^+) &= \frac{U(y^+)}{\bar{U}}; S_L = \bar{U}; S_L^* = \frac{S_L}{S_{L,free}}\end{aligned}\tag{3-1}$$

The governing equations are conservation of energy and species in the gas phase:

$$Pe_{free} S_L^* f(y^+) \frac{\partial \theta_g}{\partial x^+} = \frac{\partial^2 \theta_g}{\partial x^{+2}} + \frac{\partial^2 \theta_g}{\partial y^{+2}} + \omega \delta(x^+) \quad (3-2)$$

$$Pe_{free} S_L^* f(y^+) \frac{\partial Y_f}{\partial x^+} = \frac{1}{Le} \left(\frac{\partial^2 Y_f}{\partial x^{+2}} + \frac{\partial^2 Y_f}{\partial y^{+2}} \right) - \omega \delta(x^+) \quad (3-3)$$

where δ is the Dirac delta function and Le is the Lewis number (k_g/α). The treatment of the flame is the same as in Chapter 2 and the use of the delta function implies that all the heat release occurs at the infinitesimally thin flame location ($x^+ = 0$). This is commonly known as the “flame sheet” assumption. The flame is represented as a planar structure with no curvature.

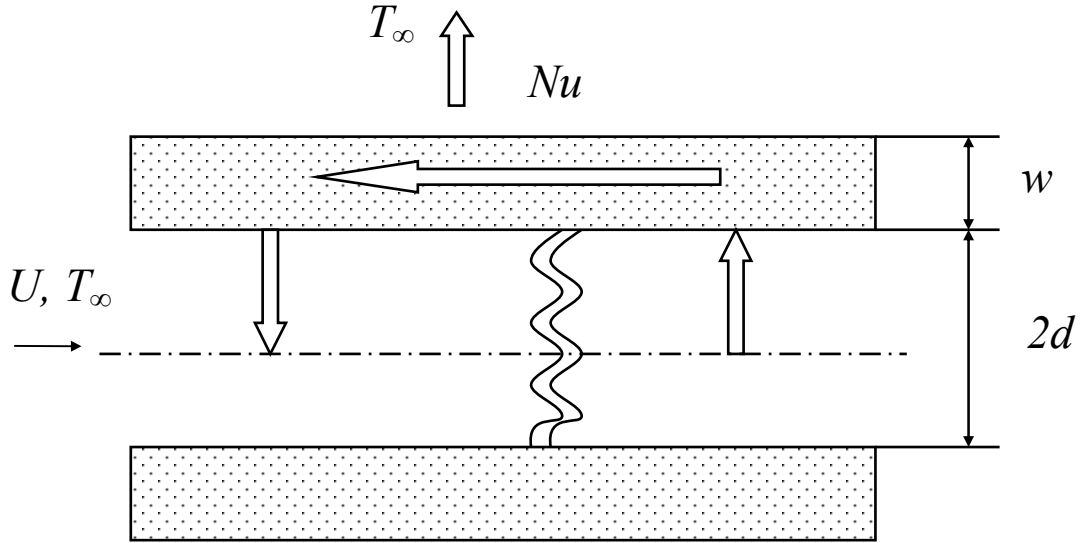


Figure 3-1: Schematic illustration of flame stabilized in a micro-channel.

Of course this is an extremely simplified representation of a two dimensional flame but it is consistent with other research [38 and 43] and, as we will see in the results section, this only affects heat transfer locally in the near vicinity of the flame (from gas to the wall). It does not affect the determination of the eigenvalue (flame speed) which is the

focus of this work. The main difference between the model presented here and that presented in Chapter 2 is the inclusion of the species transport equation (eq. 3-3) which makes the flame speed the eigenvalue of the problem the species equation. The gas phase energy equations are coupled by the reaction term. Conservation of energy in the structure is given by:

$$\frac{\partial^2 \theta_s}{\partial x^{+2}} + \frac{\partial^2 \theta_s}{\partial y^{+2}} = 0 \quad (3-4)$$

The zeroth order chemical reaction term is given by:

$$\omega = \frac{Ze Pe_{free}^2}{2} e^{\frac{Ze(\theta_F - 1)}{1 + \gamma(\theta_F - 1)}} \quad (3-5)$$

Pe_{free} is the ratio of convective to conductive heat transfer based on the freely propagating flame speed $S_{L,free}$ while, Ze and γ are the Zeldovich number and heat release parameter.

These are given by:

$$Pe_{free} = Re Pr = \frac{\rho S_{L,free} Cp d}{k_g}, S_{L,free} = \sqrt{2 A \alpha Ze^{-1} y_{f,\infty}^{-1}} \exp\left(-\frac{T_a}{2 T_{ad}}\right) \\ Ze = \frac{T_a (T_{ad} - T_{-\infty})}{T_{ad}^2}, \gamma = \frac{(T_{ad} - T_{-\infty})}{T_{ad}} \quad (3-6)$$

All temperature gradients are assumed to go to zero at +/- infinity leading to the following boundary conditions on the gas and structure energy equations:

$$\theta_g(\mp\infty, y^+) = 0, \left. \frac{\partial \theta_g}{\partial y^+} \right|_{y^+=0} = 0 \\ \theta_s(\mp\infty, y^+) = 0, -\kappa \left. \frac{\partial \theta_s}{\partial y} \right|_{y=\tau} = Nu_E \theta_s(\tau) \quad (3-7)$$

Nu_E is the Nusselt number for heat transfer from the walls to the outer environment:

$$Nu_E = \frac{h_E d}{k_g} \quad (3-8)$$

If Nu_E is zero, then the walls are adiabatic. The temperature and heat flux must match at the wall-gas interface which leads to the following additional boundary conditions:

$$\theta_g(x^+, 1) = \theta_s(x^+, 1), \quad \left. \frac{\partial \theta_g}{\partial y^+} \right|_{y^+=1} = \kappa \left. \frac{\partial \theta_s}{\partial y^+} \right|_{y^+=1} \quad (3-9)$$

Since the flame is modeled as an infinitely thin sheet of heat release, gas temperatures on both sides of the flame must match but the gradients do not because of the heat production at the flame. Integrating over an infinitesimally small volume around the flame gives the “*jump conditions*” [38, and 81] across the flame.

$$\theta_g(0^-, y^+) = \theta_g(0^+, y^+), \quad \left. \frac{\partial \theta_g}{\partial x^+} \right|_{x=0^-}^{x=0^+} = -\omega \quad (3-10)$$

Similarly, we require that the temperatures in the structure match at the flame location. Integrating over a similar volume gives no discontinuity in the structure temperature because there is no heat production in the structure. The formulation of the energy equations is identical to that in Chapter 2.

$$\theta_s(0^-, y^+) = \theta_s(0^+, y^+), \quad \left. \frac{\partial \theta_s}{\partial x^+} \right|_{x=0^-}^{x=0^+} = 0 \quad (3-11)$$

The boundary conditions for the species equations are:

$$Y_f(-\infty, y^+) = 1, \quad Y_f(\infty, y^+) = 0$$

$$\left. \frac{\partial Y_f}{\partial y^+} \right|_{y^+=0,1} = 0 \quad (3-12)$$

These arise from the fact that at the inlet ($x^+ = -\infty$), the fuel species has not reacted or diffused. At the flame sheet, we assume the fuel reacts completely. Hence, Y_f is zero at the flame location ($x^+ = 0$) and remains so for $x^+ > 0$. At the centerline and at the wall-gas interface, the species gradients go to zero due to the symmetry and non-permeable wall boundary conditions. Integrating the species equation over an infinitesimal volume over the flame gives jump conditions for the species equation.

$$Y_f(0^-, y^+) = Y_f(0^+, y^+) = 0 \quad (3-13 \text{ a})$$

$$\left. \frac{\partial Y_f}{\partial x^+} \right|_{x=0^-} = -Le \, \omega \quad (3-13 \text{ b})$$

Like the temperature gradient, the species gradient at the flame is also set by the reaction rate.

3.2. Flame Speed Solution

Equations 3-1 and 3-2 are solved using separation of variables. The equations are coupled through the temperature and heat flux matching boundary conditions. The solutions for the energy equations are the same as those presented in Chapter two. However, in order to obtain the solutions in the present case, we need to assume an S_L^* . The temperature fields are given by:

$$\theta_g(x^+, y^+) = \begin{cases} \sum_{n=1}^{\infty} A_n \exp(\lambda_n x^+) \phi_g(\lambda_n, y^+); x^+ < 0 \\ \sum_{n=1}^{\infty} B_n \exp(-\beta_n x^+) \psi_g(\beta_n, y^+); x^+ > 0 \end{cases} \quad (3-14)$$

$$\theta_s(x^+, y^+) = \begin{cases} \sum_{n=1}^{\infty} A_n \exp(\lambda_n x^+) \phi_s(\lambda_n, y^+); x^+ < 0 \\ \sum_{n=1}^{\infty} B_n \exp(-\beta_n x^+) \psi_s(\beta_n, y^+); x^+ > 0 \end{cases} \quad (3-15)$$

where

$$A_n = \frac{\omega \int_0^1 \phi_{g,n} dy^+}{\left(\int_0^1 (-Pe_{free} S_L^* f(y^+) + 2\lambda_n) \phi_{g,n}^2 dy^+ + \int_1^{\tau} 2\lambda_n \kappa \phi_{s,n}^2 dy^+ \right)} \quad (3-16)$$

$$B_n = \frac{\omega \int_0^1 \psi_{g,n} dy^+}{\left(\int_0^1 (Pe_{free} S_L^* f(y^+) + 2\beta_n) \psi_{g,n}^2 dy^+ + \int_1^{\tau} 2\beta_n \kappa \psi_{s,n}^2 dy^+ \right)} \quad (3-17)$$

The principal difference from the heat transfer analysis in Chapter 2 is that the flame speed is now an eigenvalue of the problem. A similar separation of variables and application of boundary conditions leads to the following expression for the fuel species distribution:

$$Y_f(x^+, y^+) = \begin{cases} 1 - \sum_{n=1}^{\infty} C_n \exp(\sigma_n x^+) \zeta(\sigma_n, y^+); x^+ < 0 \\ 0; x^+ > 0 \end{cases} \quad (3-18)$$

where

$$C_n = \frac{Le \omega \int_0^1 \zeta_n dy^+}{\int_0^1 (-Pe_{free} Le S_L^* f(y^+) + 2\sigma_n) \zeta_n^2 dy^+} \quad (3-19)$$

The model developed here can accommodate plug flow ($U = \text{constant}$) or fully developed flow profiles. In both cases, the general solution procedure is as follows: 1. Assume a value for S_L^* . 2. Compute the flame temperature θ_F from the solution to the species equation. 3. Compute the flame temperature from the solution to the energy equation. 4. Adjust S_L^* and repeat steps 2 and 3 until they produce the same θ_F .

In the case of plug flow, the solution to the species equation reduces from the series solution to a simple one dimensional form:

$$Y_f(x^+, y^+) = \begin{cases} 1 - \exp(Pe_{free} S_L^* Le x^+); & x^+ < 0 \\ 0; & x^+ > 0 \end{cases} \quad (3-20)$$

Applying Eq. 3-20 to the “jump conditions” for species (Eq. 3-13 b) and substituting for the reaction rate term gives:

$$S_L^* = \frac{Ze Pe_{free}}{2} e^{\frac{Ze(\theta_F - 1)}{1 + \gamma(\theta_F - 1)}} \quad (3-21)$$

Eq. 3-21 relates θ_F to S_L^* (the flame speed/eigenvalue).

Moving on to the energy equation, the flame temperature is defined as the velocity-weighted average temperature across the channel at the flame location ($x^+ = 0$):

$$\theta_F = \int_0^1 f(y^+) \theta_g(0, y^+) dy^+ \quad (3-22)$$

Substituting the solution to the energy equation (Eq. 3-14) into eq. 3-22 gives:

$$\theta_F = \omega \sum_{n=1}^{\infty} \int_0^1 f(y^+) \frac{B_n}{\omega} \psi_g(\lambda_n, y^+) dy^+ \quad (3-23)$$

Note that ω is a known function of θ_F (Eq. 3-5), B_n are given by eq. 3-17, and everything inside the summation in eq. 3-23 can be computed.

In the case of Poiseuille flow, a closed form expression like eq. 3-21 is not obtained but the approach remains the same. Applying eq. 3-13a gives an equation for θ_F which has S_L^* embedded in the terms of the series solution. It is important to note that in both plug and Poiseuille flows, the θ_F obtained from the species equation has no dependency on any of the thermal parameters such as the thermal conductivity ratio, heat loss, or wall thickness ratio. Rather, it corresponds merely to the value required to achieve this particular value of the flame speed from the point of view of the chemical reaction. This fact will be used later in §3.3. Finally, the parameters of the chemical reaction are selected to match experimental conditions in a Methane-Air micro-combustion test burner. E_a is 1.25×10^5 J/mol-K ($T_a = E_a/R_u$), T_{ad} is 2200 K, the inlet temperature is 300 K, Pe_{free} is taken to be 1 and Le is assumed to be 1 for simplicity.

3.3. Results

3.3.1. Temperature Profiles

Figure 3-2 shows a typical non-dimensional temperature field in the burner. Only one half of the channel is shown because of the symmetry of the flow problem. Plots such as these are typical of computational approaches (which can be performed in 2-D) and it is noteworthy that a 2-D analytical model allows us to plot the entire temperature distribution across the domain while keeping the computation time low. This allows us to explore the design space very rapidly and to identify interesting regimes.

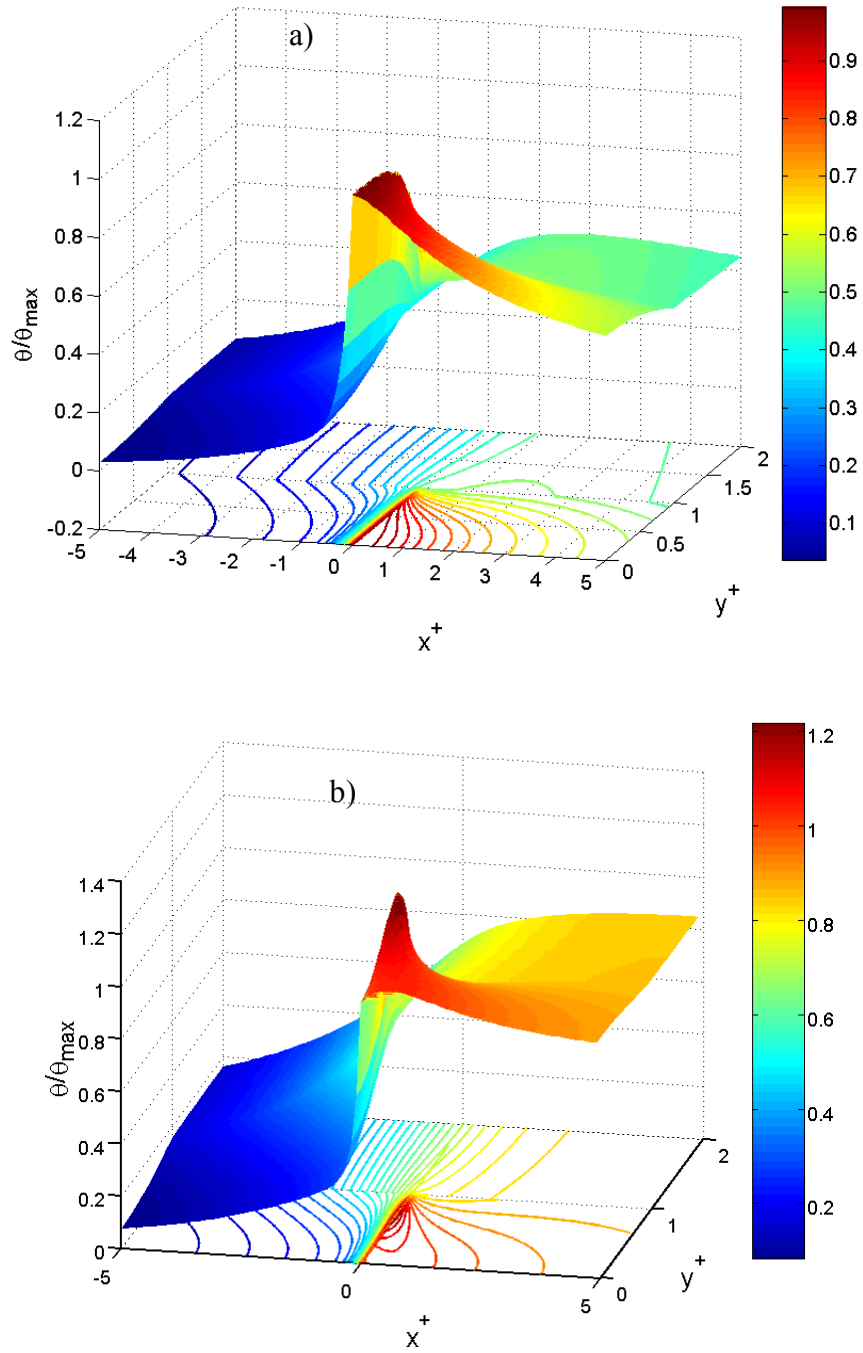


Figure 3-2: 2-D Non-dimensional temperature plot as a function of the spatial coordinates ($\kappa = 10$, $\tau = 2$, $Nu_E = 0.0375$). a) Plug flow; b) Poiseuille flow.

The discontinuity at the gas-structure interface ($\tau = 1$) in Figure 3-2 arises because of the discontinuity in thermal conductivity across the interface. The temperature gradients in

the wall indicate that the wall participates in heat transfer. The temperature contours are plotted in the $z = 0$ plane below. The heat fluxes are normal to these constant temperature contours at every point. Thus we can observe that the wall has thermal gradients that allow both axial and transverse conduction of heat. There is also a difference in the shape of the temperature distribution between the Plug and Poiseuille flow cases - the latter having a more top hat like shape. This is the result of the competition between convective transport and conductive transport of heat in the governing equations as was discussed in Chapter 2. Figure 3-3 shows non-dimensional temperature profiles in the gas and structure at various axial stations in the pre flame region for the same operating conditions as in Fig. 3-2.

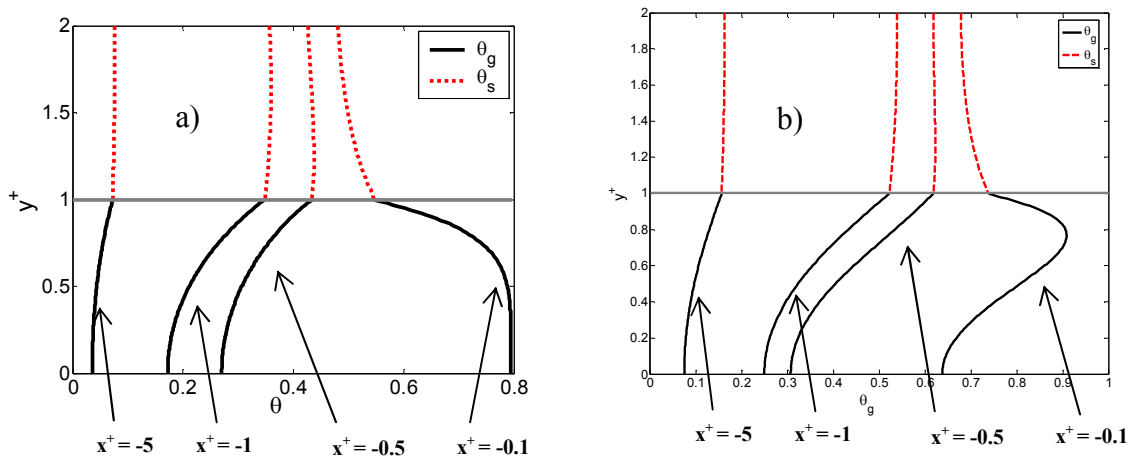


Figure 3-3: Pre-flame non-dimensional temperature distributions in gas and structure. a) Plug Flow; b) Poiseuille Flow

Far upstream of the flame, the gas temperature increases from the channel centerline to the wall indicating that the wall is pre-heating the incoming mixture. Near the flame, however, the trend reverses: the peak gas temperature occurs in the center of the channel because direct conduction through the gas is the most efficient path for transferring heat

from the flame. The structure temperature is highest at the flame location and decreases in the decreasing x^+ direction because of heat loss to the environment. The temperature profiles are shallower in the structure because its thermal conductivity is much greater than the gas.

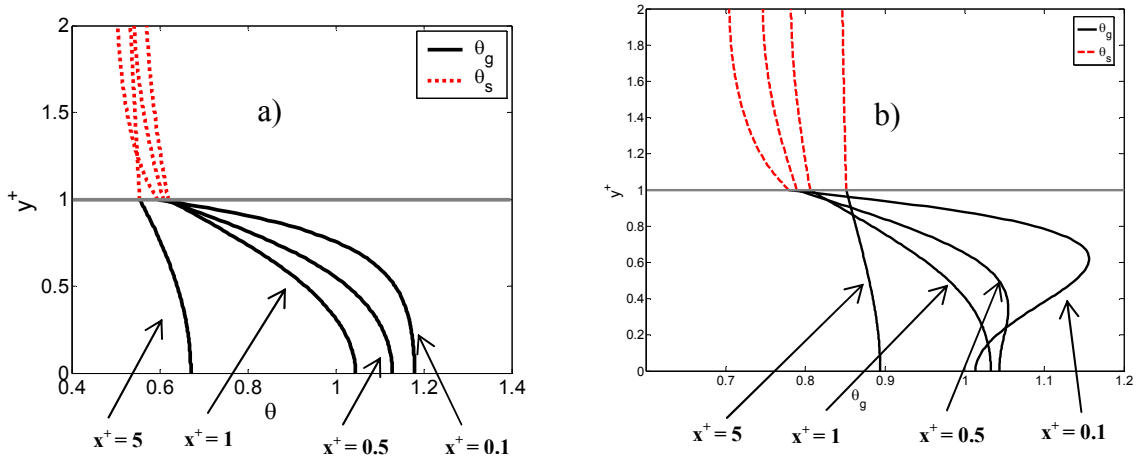


Figure 3-4: Post-flame non-dimensional temperature distributions in gas and structure. a) Plug Flow; b) Poiseuille Flow

Figure 3-4 shows temperature profiles downstream of the flame for the same operating conditions as in Figures 3-2 and 3-3. The peak temperatures remain in the center of the channel for Plug flow indicating that heat is always being transferred from the hot, post combustion gas to the structure. For Poiseuille flow we see the same off center temperature peak present in the pure heat transfer models developed in Chapter 2.

3.3.2. Flame Speed Contours

Figure 3-5 shows the non-dimensional laminar flame speed as a function of the *Nusselt* number for heat loss to the environment (Nu_E) for fixed κ and τ . The backward ‘C’ shaped contour shows that two flame speeds are possible as long as the Nusselt

number is low enough. This is consistent with Spalding's [32] concept of multiple flame speeds and with the quenching and blowoff modes observed by Ronney [37].

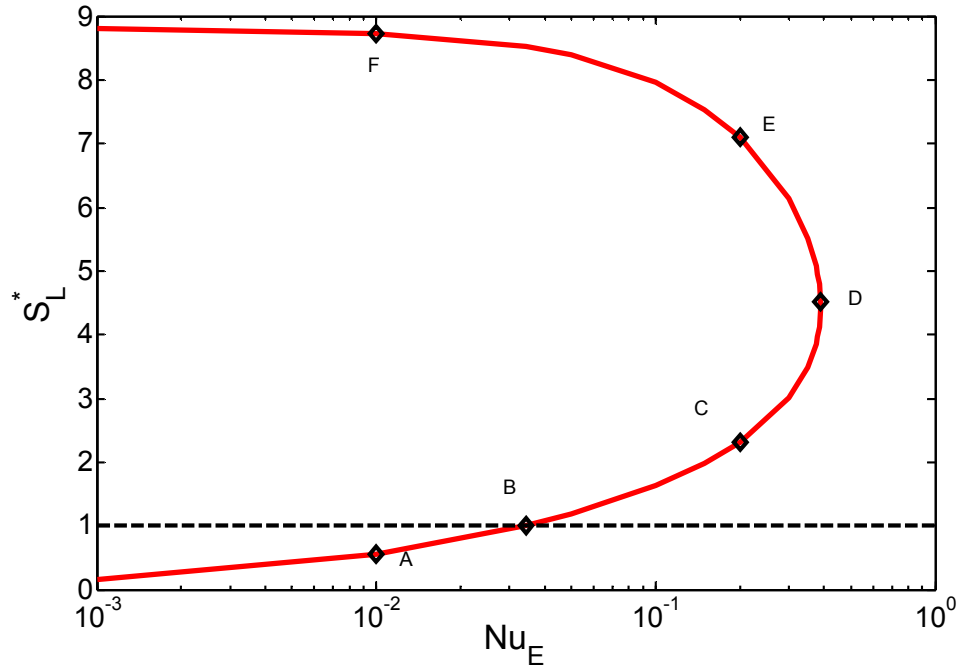


Figure 3-5: Flame speed as a function of heat loss *Nusselt* number ($\kappa = 10$, $\tau = 2$)

The figure shows that for this particular combustor design ($\kappa=10$ and $\tau=2$), wall conduction can increase the flame speed by almost a factor of 10 if the walls are well insulated. Since most structural materials have thermal conductivities that are at least 50 times larger than combustion gases, much higher flame speeds appear to be possible in other systems. The upper and lower solutions meet at the extinction Nusselt number (point D) which represents the maximum heat loss that can be tolerated before the flame is extinguished. Only the upper solution is stable for reasons that will be explained later.

Additional insight can be gained by computing the heat recirculation through the gas and structure at points A-F on figure 3-5. The total heat recirculation is defined as follows:

$$H_{Recirc}^* = \frac{H_{Recirc}}{H_{Recirc,free}} = \frac{k_g \left(\int_0^d \frac{\partial T_g(0,y)}{\partial x} y + \int_{-\infty}^0 \frac{\partial T_g(x,d)}{\partial y} dx \right)}{k_g \frac{\partial T_g(0)}{\partial x}} \quad (3-24)$$

The first term in the numerator accounts for the heat recirculation that occurs via conduction through the gas. The second term in the numerator accounts for the heat recirculation via the wall. The heat recirculation is made non-dimensional by dividing the numerator by the heat conducted via the gas for a freely propagating flame. Re-writing eq. 3-24 in terms of the non-dimensional parameters defined in eq. 3-1 gives:

$$\begin{aligned} H_{Recirc}^* &= H_{Recirc,gas}^* + H_{Recirc,structure}^* \\ &= \frac{1}{Pe_{free}} \left(\int_0^1 \frac{\partial \theta_g(0^-, y^+)}{\partial x^+} dy^+ + \int_{-\infty}^0 \frac{\partial \theta_g(x^+, 1)}{\partial y^+} dx^+ \right) \end{aligned} \quad (3-25)$$

The horizontal axis of figure 3-6 shows the relative contributions of heat recirculation via the structure and the gas for each of the points marked in fig. 3-5 while the vertical axis shows the non-dimensional flame speed at these points. It shows that increasing the total heat recirculation increases the flame speed.

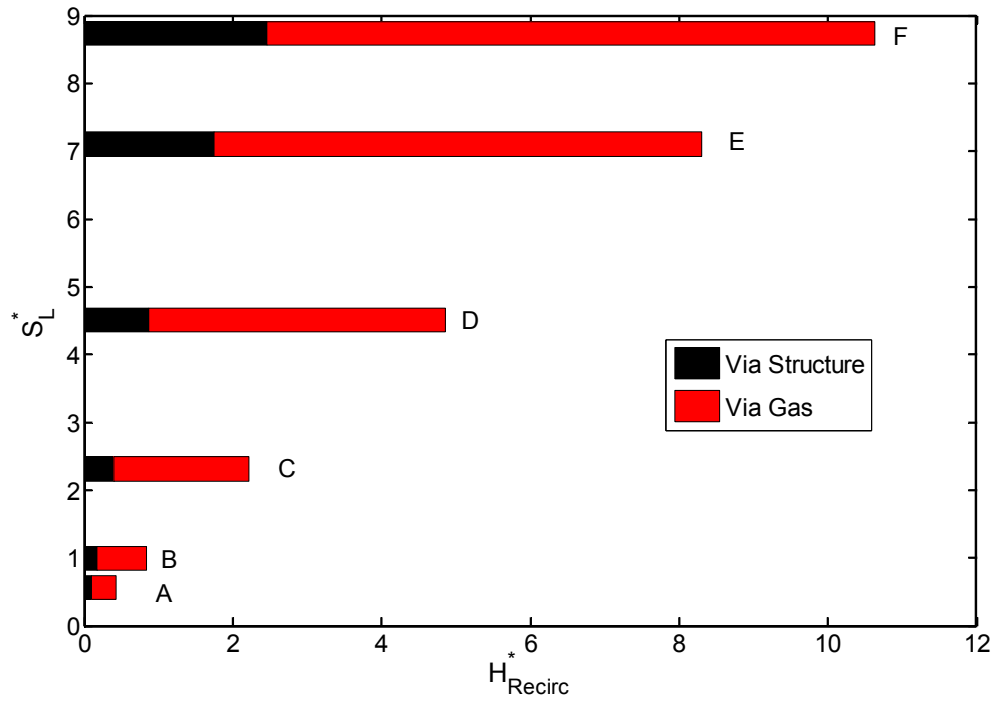


Figure 3-6: Flame speed as a function of Heat Recirculation ($\kappa = 10$, $\tau = 2$)

The fraction of the heat recirculation that occurs via the structure also increases as the flame speed increases. This confirms that heat recirculation through the structure plays an important role in increasing flame speed. Figure 3-7 shows the corresponding heat loss in the pre-flame region to the outer environment. The maximum heat loss occurs at the extinction point (point D).

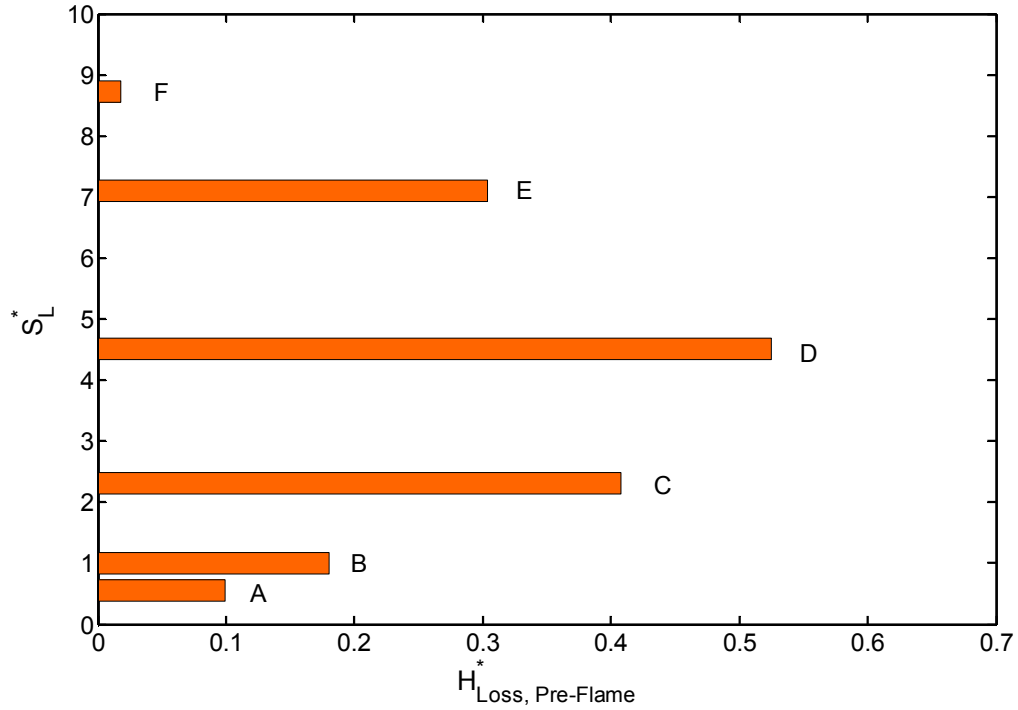


Figure 3-7: Flame Speed as a function of the Heat Loss ($\kappa = 10$, $\tau = 2$).

We are now in a position to understand why only the upper branch of the S_L vs Nu_E curve corresponds to stable flames. Consider first a flame stabilized in the channel. It would be located somewhere along the contour. Now let us perturb the flame by increasing the heat loss (Nu_E) instantaneously by a small amount. We would expect the increased heat loss to decrease the heat recirculated back via the structure instantaneously. This should cause the flame speed to decrease. If the flame starts on the upper branch, increasing the heat loss does indeed drive the flame speed lower and the new stability point can lie on the contour. This is consistent with our observation that decreasing the heat recirculation decreases the flame speed and it will be possible to establish a new equilibrium. If the flame starts on the lower branch however, increasing the heat loss would require that the new equilibrium point have a higher flame speed (in order to lie on the contour). This is inconsistent with our observation that decreasing the

heat recirculation decreases the flame speed and it will not be possible to establish a new equilibrium. Therefore, this flame is unstable.

Having considered the flame speed contour for a particular combustor in detail, we now consider the effects of changing the combustor design by changing τ and κ . Figure 3-8 shows the effect of changing the thermal conductivity ratio for a fixed value of the wall thickness ratio ($\tau = 2$).

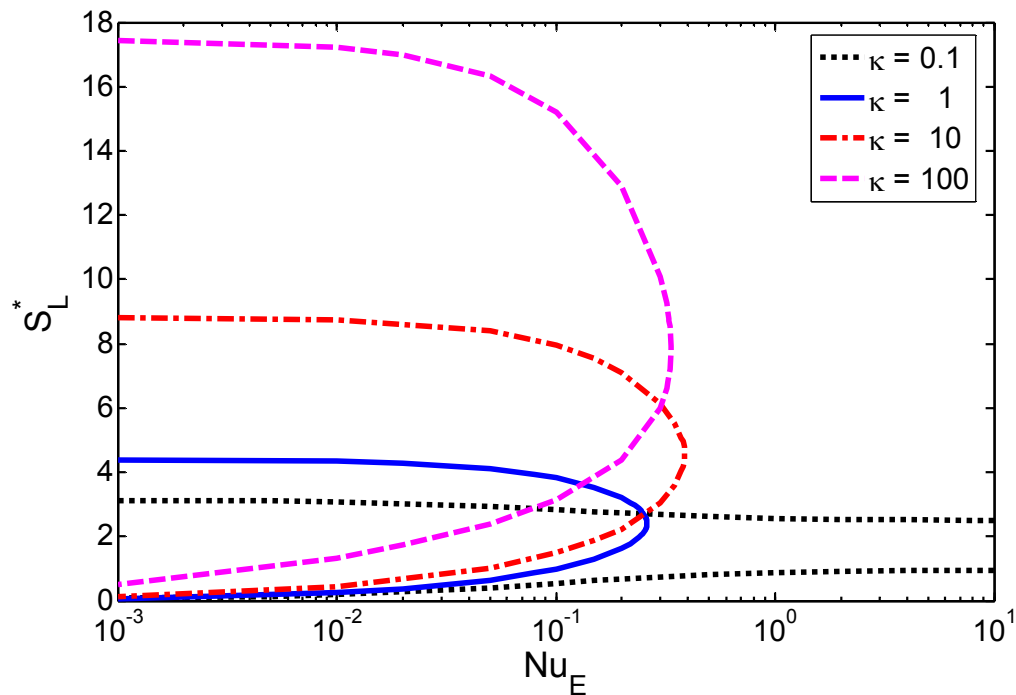


Figure 3-8: Burning velocity as a function of heat loss to the environment for four wall thermal conductivity ratios ($\tau = 2.0$).

As before, Nu_E equal zero corresponds to an adiabatic wall and the point of infinite slope on each curve corresponds to the Nusselt number for extinction. Increasing the thermal conductivity of the structure decreases the Nusselt number associated with extinction but increases the magnitude of the flame speed enhancement by permitting more heat recirculation through the structure. Even when the wall is less conductive than the gas (a

very unlikely situation in practice), enhanced flame speeds are still possible because of the additional heat recirculation through the structure.

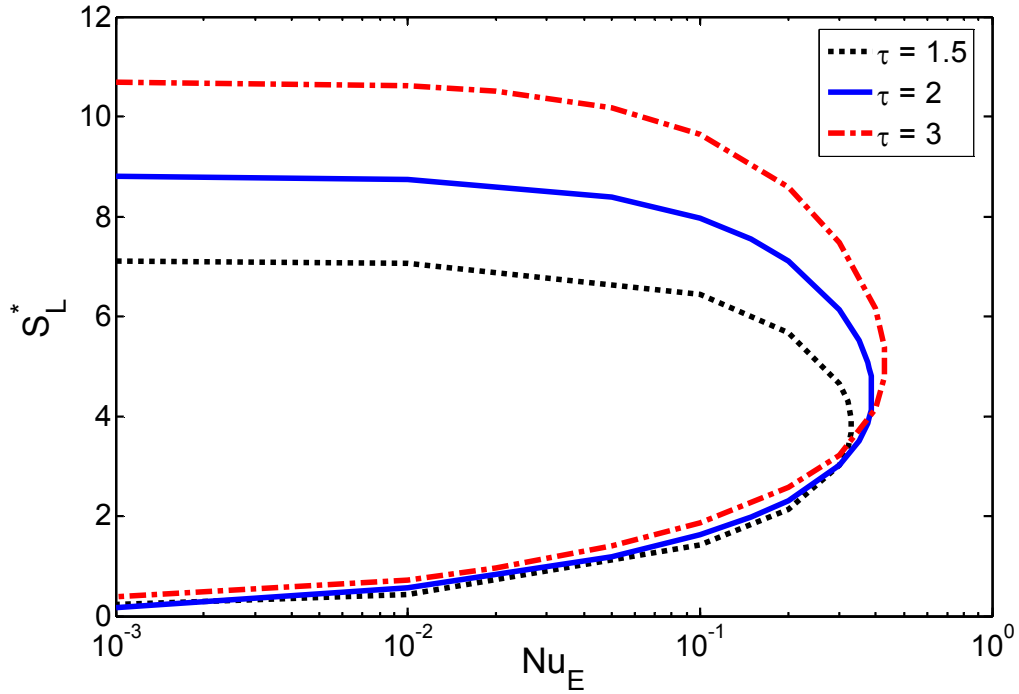


Figure 3-9: Burning velocity as a function of heat loss to the environment for three wall thickness ratios ($\kappa=10$).

Figure 3-9 is similar to fig. 3-8 except that the contours correspond to different wall thickness ratios. Increasing the wall thickness with respect to the flow passage height increases the burning velocity in both the high and low speed modes. It also increases the extinction Nusselt number. This is because increasing the wall thickness makes it more difficult for heat to be lost to the environment which enables more heat to be transferred upstream to the pre-flame.

3.3.3. Heat recirculation

The intersecting contours in figs. 3-8 and 3-9 show that the same flame speed can be achieved using a variety of different burner designs and suggests that κ and τ are only

important in terms of their effect on the net heat recirculation. To test this assertion, all of the points used to create figs. 3-8 and 3-9 are plotted against the associated non-dimensional heat recirculation in fig. 3-10. The fact that they appear to fall on a single curve regardless of whether the velocity profile is flat (plug) or fully developed (Poiseuille) and that the symbols corresponding to the intersections in figs. 3-8 and 3-9 overlap each other in fig. 3-10 suggests that heat recirculation is the primary parameter that determines the flame speed.

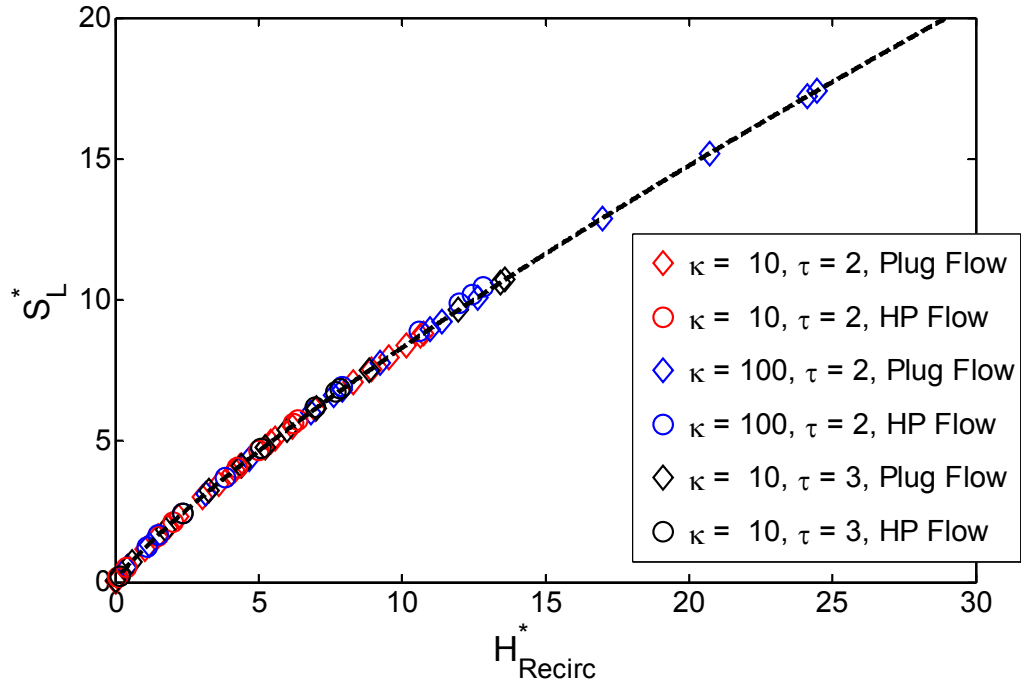


Figure 3-10: Burning velocity as a function of the non-dimensional total heat recirculation.

The primacy of heat recirculation can be proven more rigorously as follows: Begin by examining each term of the total heat recirculation (eq. 3-25)

$$H_{Recirc,gas}^* = \frac{1}{Pe_{free}} \int_0^1 \frac{\partial \theta_g(0^-, y^+)}{\partial x^+} dy^+ = \frac{1}{Pe_{free}} \int_0^1 \left(\int_{-\infty}^0 \frac{\partial^2 \theta_g(x^+, y^+)}{\partial x^{+2}} dx^+ \right) dy^+ \quad (3-26)$$

The inner integral can be computed directly and the boundary conditions can be applied to show that eq. 3-26 holds. Similarly, we can show that:

$$H_{Recirc, structure}^* = \frac{1}{Pe_{free}} \int_{-\infty}^0 \frac{\partial \theta_g(x^+, 1)}{\partial y^+} dx^+ = \frac{1}{Pe_{free}} \int_{-\infty}^0 \left(\int_0^1 \frac{\partial^2 \theta_g(x^+, y^+)}{\partial y^{+2}} dy^+ \right) dx^+ \quad (3-27)$$

The temperature functions for the gas are continuous and differentiable to the second order in the pre-flame region (the only discontinuity occurs at the flame itself or the gas-wall interface). Therefore, the order of integration in eq. 3-27 can be changed and rewritten in terms of the total heat recirculation as:

$$H_{Recirc}^* = \frac{1}{Pe_{free}} \int_0^1 \left(\int_{-\infty}^0 \left\{ \frac{\partial^2 \theta_g(x^+, y^+)}{\partial x^{+2}} + \frac{\partial^2 \theta_g(x^+, y^+)}{\partial y^{+2}} \right\} dx^+ \right) dy^+ \quad (3-28)$$

Replacing the term in braces using eq. 3-2 gives:

$$H_{Recirc}^* = \frac{1}{Pe_{free}} \int_0^1 \left(\int_{-\infty}^0 \left\{ Pe_{free} S_L^* f(y^+) \frac{\partial \theta_g}{\partial x^+} - \omega \delta(x^+) \right\} dx^+ \right) dy^+ \quad (3-29)$$

The inner integral can be computed directly. The second term in the integral is zero from the definition of the Dirac delta function. Applying eq. 3-22 gives:

$$H_{Recirc}^* = S_L^* \int_0^1 (f(y^+) \theta_g) dy^+ = S_L^* \theta_F \quad (3-30)$$

Since S_L^* is a function of θ_F (see end of §3.2), the converse is also true and therefore we have proven that H_{Recirc}^* only depends on S_L^* . In the case of plug flow, eq. 3-21 can be used to express θ_F as a function of S_L^* directly to get an analytical expression relating H_{Recirc}^* and S_L^* from eq. 3-30. This is the dashed curve in figure 3-10.

Therefore, the total heat recirculation appears to be the universal governing parameter that sets flame speed. This finding is quite helpful because it can be used to provide

practical guidance for initial micro-combustor designs. This illustrates why analytical models - though not as accurate as CFD based numerical models - can still be very useful tools for identifying and understanding the essential underlying physical processes.

3.4. Practical Applications of the Model:

The model developed here can be used in practical systems to identify the range of operation and to make preliminary estimates of potential improvement of thrust-to-weight ratio over conventional sized thrusters. The model can also be used to develop new non-intrusive diagnostic techniques. These applications are described next.

3.4.1. Identifying Design Ranges:

We start by re-writing Eq. 3-25 as:

$$H_{Recirc}^* = \frac{1}{Pe_{free}} \left(\int_0^1 \frac{\partial \theta_g(0^-, y^+)}{\partial x^+} dy^+ + \kappa \int_{-\infty}^0 \frac{\partial \theta_s(x^+, 1)}{\partial y^+} dx^+ \right) \quad (3-31)$$

Or:

$$\begin{aligned} H_{Recirc}^* &= \frac{1}{Pe_{free}} \left\{ \int_0^1 \frac{\partial \theta_g(0^-, y^+)}{\partial x^+} dy^+ - \int_{-\infty}^0 \left(\int_1^\tau \left\{ \kappa \frac{\partial^2 \theta_s(x^+, y^+)}{\partial y^{+2}} \right\} dy^+ + \kappa \frac{\partial \theta_s(x^+, \tau)}{\partial y^+} \right) dx^+ \right\} \\ &= \frac{1}{Pe_{free}} \left\{ \int_0^1 \frac{\partial \theta_g(0^-, y^+)}{\partial x^+} dy^+ + \int_1^\tau \int_{-\infty}^0 \left(\kappa \frac{\partial^2 \theta_s(x^+, y^+)}{\partial x^{+2}} \right) dy^+ - \int_{-\infty}^0 Nu_E \theta_s(x^+, \tau) dx^+ \right\} \end{aligned} \quad (3-32)$$

After performing the inner integral of the second term and some more algebraic rearranging it can be shown that:

$$H_{Recirc}^* = \frac{1}{Pe_{free}} \left(\int_0^1 \frac{\partial \theta_g(0^-, y^+)}{\partial x^+} dy^+ + \kappa \int_1^\tau \frac{\partial \theta_s(0^-, y^+)}{\partial x^+} dy^+ \right) - \frac{Nu_E}{Pe_{free}} \int_{-\infty}^0 \theta_s(x^+, \tau) dx^+ \quad (3-33)$$

The first term in parenthesis gives the total heat flux entering the pre-flame region through both the gas and structure. The second term gives the heat loss to the outer environment. It has already been shown that the left hand side (H_{Recirc}^*) depends only on S_L^* . Therefore, it is possible to choose values for S_L^* (range of operation) and one other design parameters and use eq. 3-33 to solve for the third. This would give very quick ‘first cut’ design guidance for estimating what materials or wall thicknesses might be used to achieve operation over a certain range of flame speeds.

3.4.2. Temperature Profile Guesses for Non-intrusive Diagnostics:

There might be diagnostic applications (like the one presented in Chapter 4) or other practical system applications that might require one to know the functional form of the temperature profiles a-priori. The solution presented for the conjugate heat transfer paper involves a Fourier series sum over infinite eigenvalues and involves complicated eigenfunctions (hypergeometric functions etc) and therefore we seek to represent these profiles by simpler polynomial profiles. Previous work [16], [76] demonstrated the feasibility of fitting 2nd and 4th order profiles to the temperature profile of a much simpler heat transfer model for flames in a channel.

$$\theta_g(y) = a_4 y^4 + b_4 y^3 + c_4 y^2 + d_4 y + e_4 \quad (3-34)$$

We take the same approach to the more sophisticated conjugate heat transfer flame model presented here and in particular for the Poiseuille flow velocity profile model which has an off center peak in the temperature profile. The idea is to see if these can be represented by a 4th order profile (as the off center peak cannot be captured with a 2nd order profile). Figs. 3-11 and 3-12 compare the exact solution to the 4th order polynomial

fit in the pre and post-flame regions of the flame ($x_{flame} = 0$). The temperature profile appears to be well approximated by the 4th order profiles as can be seen visually in both pre and post-flame regions.

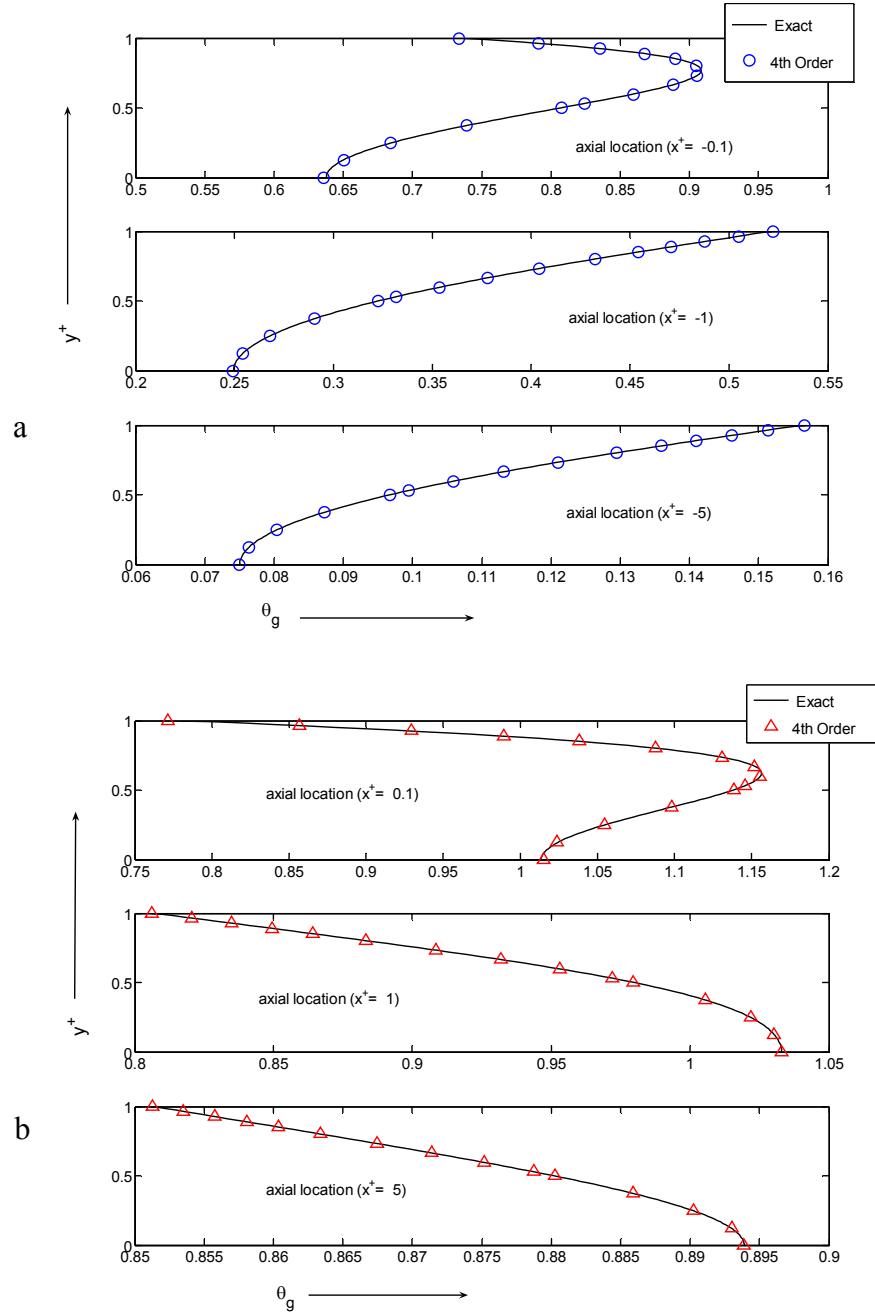


Figure 3-11: Comparison of transverse temperature profiles in the
a) Pre-flame and b) Post-flame, for Poiseuille flow ($\kappa = 10$, $\tau = 2$, $Nu_E = 0.0375$)

Table 3-1 shows the comparison between the model and the fit showing that the R^2 for the fit is either 1 or very close to 1 for all the profiles that were fit. Thus, this appears to justify the use of the 4th order fit to approximate the temperature profile. However, the slope at the wall from which heat fluxes would be estimated had a larger deviation in the near flame region (around 20%). This suggests that higher order profiles might be necessary to improve accuracy of heat recirculation estimates. Increasing the order of the profile poses new problems as it increases the number of unknowns (i.e., coefficients for the profile). This might not be good for experiments like the one described in the next chapter where finding unknown coefficients is already quite challenging and relatively few data points are available for fitting.⁴

Axial location (x^+)	$d\theta/dy^+ _{\text{wall}}$ (Model)	$d\theta/dy^+ _{\text{wall}}$ (4th order fit)	Difference in Slope (%)	R^2 (4th order fit)
-5	0.138583	0.14122	1.9043	1
-1	0.45493	0.46259	1.6831	1
-0.1	-1.41753	-1.72643	21.7914	0.9999
0.1	-2.06634	-2.47196	19.6299	0.9997
1	-0.39055	-0.37471	4.0558	1
5	-0.06098	-0.05962	2.2302	1

Table 3-1: Comparison between the analytical model and the 4th order temperature profile fit for Poiseuille flow ($\kappa = 10$, $\tau = 2$, $Nu_E = 0.0375$)

⁴ The number of wavelengths over which absorption is measured must equal or exceed the number of free parameters in the temperature profile in order for it to be possible to find a solution. In the experiment described in the next section, interferences and the spectral resolution of the instrument limit the number of wavelengths to 8. This means that the highest possible fit order would be 6. This will be discussed in greater detail in the next chapter.

3.3.4. Thrust Calculation

One of our main interests in developing microcombustors is as part of a chemical thruster for small satellites. Therefore, we would like to use the model presented above to make first order predictions of thruster performance. In §3.3.3 we have seen that wall conduction can significantly enhance the flame speed in micro/mesoscale combustors. The enhanced mass flow could mean that a microcombustor/nozzle combination could produce more thrust than a conventional device that cannot exploit structure thermal feedback.

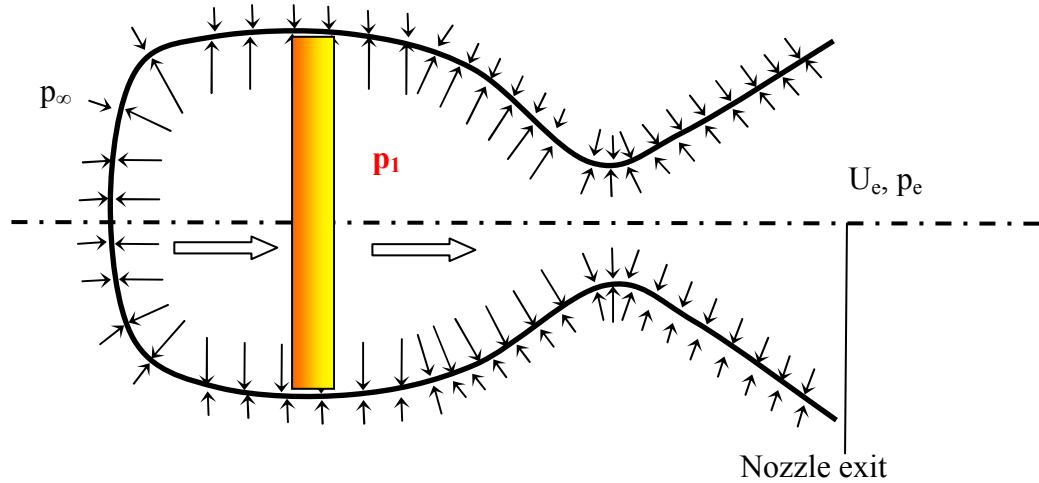


Figure 3-12: Schematic illustration of a combustor and nozzle unit.

As presented previously in §1.2.1 the thrust is computed using a simple momentum balance on the nozzle:

$$T_h = \dot{m}U_e + (p_e - p_\infty)A_e \quad (3-34)$$

In this expression, the subscript e denotes exit conditions. The main aim here is to establish how micro-thrusters perform in comparison to conventional sized thrusters. In order to do this we write eq. 3-34 for both conventional sized (using freely propagating

flame values) and micro-sized thrusters and take the ratio of their respective thrusts. Let us consider only a perfectly expanded nozzle (the pressure term in eq. 3-34 drops out) to achieve maximum thrust.

$$T_h^* = \frac{T_h}{T_{h,free}} = \frac{\rho S_L d U_e}{\rho S_{L,free} D U_{e,free}} = S_L^* \left(\frac{d}{D} \right) \left(\frac{U_e}{U_{e,free}} \right) \quad (3-35)$$

In this expression, d and D are the combustors width for the micro and conventional scale device respectively. If both combustors have the same total pressure and the nozzles are perfectly expanded we would get the exit velocities to be the same, i.e. $U_e = U_{e,free}$. Accounting for the dynamic pressure using the flame speed can be expected to change the total pressure in the combustor for microscale combustors where flame speeds can be 10-20 times as high as the freely propagating flame speed. However, the dynamic pressure component is still small compared to the static pressure (of even say 1 atm) and this effectively means we can assume that the static and total pressures in the thrust chamber are equal in both micro and conventional sized thrusters. Applying this to eq. 3-35 gives

$$T_h^* = S_L^* \left(\frac{d}{D} \right) \quad (3-36)$$

The ratio d/D can be calculated if we assume the wall thickness to be d in both cases and do a stress analysis based on the hoop stress for the conventional sized device. The hoop stress for the combustors wall is

$$\sigma_{cr} = \frac{2}{3} p_1 \left(\frac{D}{d} \right) \quad (3-37)$$

Where, σ_{cr} is the critical stress. The usual practice is to add a factor of safety (f_s) to the critical stress value to allow for a safety margin. Using this we get d/D as.

$$\left(\frac{d}{D}\right) = \frac{2}{3} \frac{p_1}{f_s \sigma_{cr}} \quad (3-38)$$

If we are interested in obtaining the thrust ratio scaling (eq. 3-36), we can use eq. 3-38 to represent the ratio of widths in eq. 3-36. However we are interested in the scaling of the thrust to weight ratio and since we are preserving the shape of the thruster shape as we scale down, it can be shown that the weight scales as the combustors width. Therefore we get the weight ratio between conventional scale and microscale thruster to be D/d . Using this in eq. 3-36 gives

$$(T_h^* / Wt^*) = S_L^* \quad (3-39)$$

Thus, for a perfectly expanded nozzle the thrust to weight ratio scales directly with the enhancement in flame speed. In fig. 3-10 it was seen that it is possible to get non-dimensional flame speeds of 10 – 20 for practical choices of combustor material and thickness. Thus, equation 3-39 indicates that we should expect increased thrust to weight by a similar factor.

Chapter 4: Experiment: Theory and Apparatus

4.1. Physics of Absorption:

The non-intrusive diagnostic technique developed in this work is based on absorption of infrared (IR) light by carbon dioxide (CO_2) molecules that are naturally produced in hydrocarbon-air combustion. To understand how we can infer important physical quantities such as temperature and concentrations of species from an absorption spectrum, we first need to understand the physics behind absorption of light by molecules. A lot of the details presented in this chapter may be found in [16] and [81]. However, they are presented here in a condensed form for completeness along with more recent enhancements to the technique that were made after the above references were published.

4.1.1. Qualitative Description of Absorption:

The total internal energy in a molecule is quantized or stored in discrete bundles that are associated with various vibrational, rotational, electronic, and nuclear quantum mechanical states. The highest energies are associated with nuclear states followed by electronic, vibrational and rotational states. Electronic states refer to the configuration of the outer electron shell, vibrational states refer to the various vibrations between constituent atomic nuclei, and rotational states refer to rotations that the nuclei make with respect to each-other. The overall quantum mechanical state (and hence total energy) of a particular molecule is described by its nuclear, electronic, vibrational and rotational quantum numbers (N, E, V, and J).

When a photon strikes a molecule, it will only be absorbed if the photon's energy matches the energy associated with an allowed transition to a higher nuclear, electronic, rotational, and vibrational state. Figure 4-1a is a schematic illustration of the potential wells associated with the ground and first excited electronic state for a typical diatomic molecule. The blue horizontal lines in each well mark the vibrational energies associated with different vibrational quantum numbers and the vertical arrows illustrate two possible transitions. Energies associated with rotational states are not shown to make the figure clearer and because they are usually much smaller than the vibrational energies. Figure 4-1b shows the energies and wavelengths associated with various types of transitions.

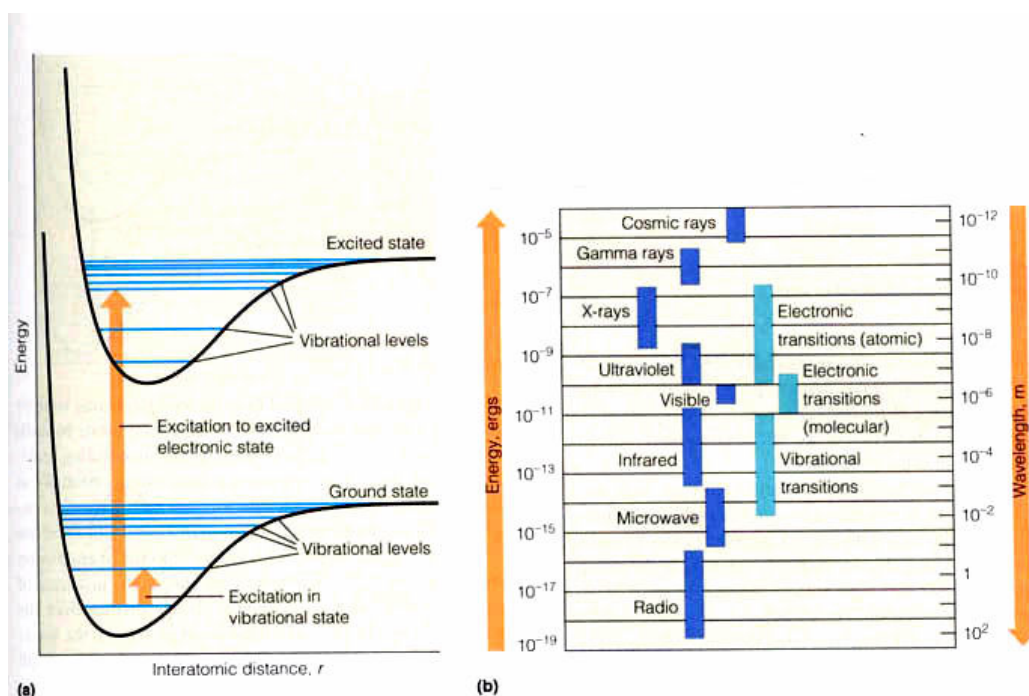


Figure 4-1: a) Vibrational and electronic transitions for a diatomic molecule b) Electromagnetic Spectrum and corresponding transitions [83]

Since molecules only absorb energy in discrete 'quanta' of energy that depends on the molecular structure, each molecule has a unique absorption signature. Therefore, it is possible to determine a sample's chemical composition by measuring its absorption

spectrum. IR light being “low energy” (or longer wavelength) light primarily excites vibrational and rotational transitions owing to their low energy states (see Fig. 4-1b). Absorption of higher energy photons in the ultraviolet region is usually associated with electronic in addition to vibrational and rotational transitions.

The strength and shape of a molecule’s absorption spectrum is related to its concentration and temperature. The concentration sets the number of molecules available to absorb. The temperature sets the distribution of initial energy states through the Boltzmann distribution ($\frac{N_J}{N_0} = (2J+1)e^{\frac{-BJ(J+1)}{k_B T}}$, see [84] pp. 445-449 for more details).

Figure 4-2 shows that raising the gas temperature raises the average rotational quantum number. This means that samples at higher temperatures will have more molecules in higher energy states.

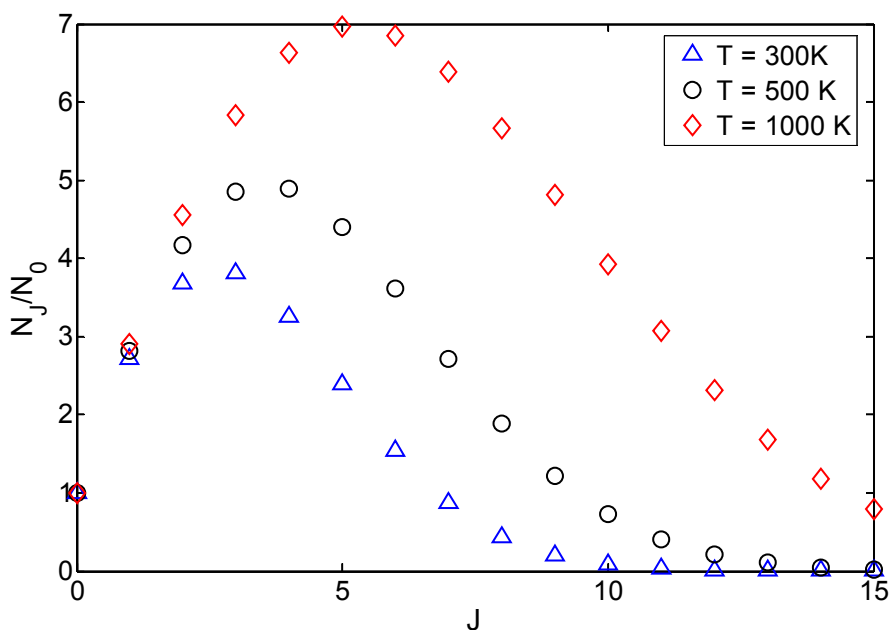


Figure 4-2: Relative populations of the rotational levels of HCl(g) at three different temperatures. (Adapted from [84])

Since the absorption spectrum depends on the distribution of energy states in the gas, it is a direct indicator of temperature. Therefore, measuring the absorption spectrum provides information on both temperature and concentration. A more detailed description of the absorption physics can be found in [84].

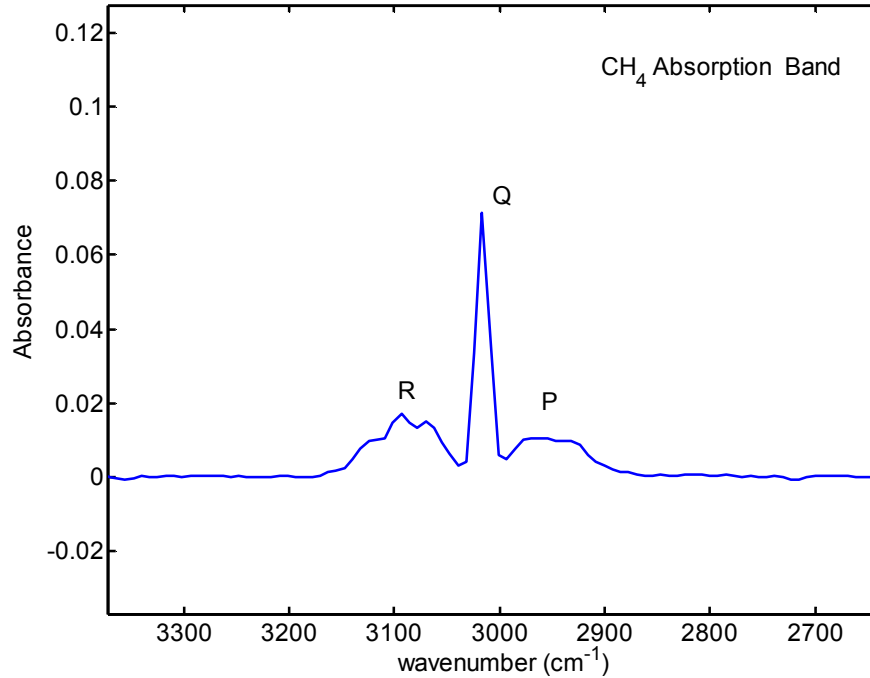


Figure 4-3: Rotational bands in CH₄ spectrum.

Fig. 4-3 shows the absorption spectrum of CH₄. The spectral resolution of the plot is low which means only the outer envelope of the vibrational band ‘head’ (which is composed of individual rotational lines) is visible. The rotational lines correspond to transitions [84] and [85] with $\Delta J = -1, 0$ and 1 respectively where J is the rotational quantum number. These are called respectively the P, Q, and R branches.

In this work, we are primarily concerned with the infrared spectrum of the CO₂ molecule which arises from the four vibrational modes illustrated in figure 4-4. CO₂ is a

linear molecule with two stretching (symmetric and asymmetric) and two bending (degenerate) modes. The symmetric stretching mode is excited by photons at 2350 cm^{-1} .

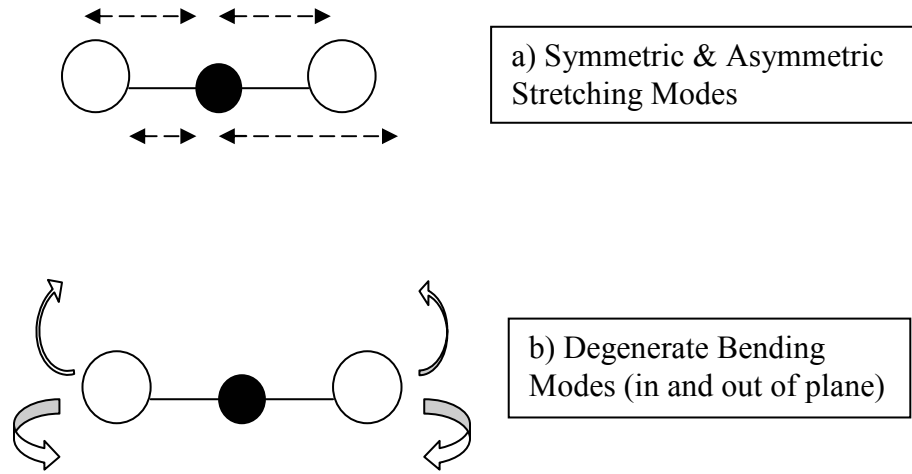


Figure 4-4: Illustration of CO₂ stretching and bending modes.

4.1.2. Review of Absorption Spectroscopy:

The Beer-Lambert law [86] relates the change in intensity of a beam of light passing through a gas column of length dx to the concentration C of the absorbing gas molecules in moles/liter:

$$\frac{dI(\bar{\nu})}{I(\bar{\nu})} = -k(\bar{\nu})Cdx \quad (4-1)$$

In this equation, I is the initial light intensity; dI is the change in transmitted intensity due to absorption by the sample along the optical path of length dx , $\bar{\nu}$ is the optical frequency (typically in cm^{-1} for infrared measurements) and $k(\bar{\nu})$ is an absorption coefficient that depends on the optical frequency. Integrating over the total length of the optical path L and converting natural logarithms to base 10 leads to the definition of the molecular absorbance $A(\bar{\nu})$:

$$\log_{10} \frac{I_0(\bar{\nu})}{I(\bar{\nu})} = A(\bar{\nu}) = \varepsilon(\bar{\nu})CL \quad (4-2)$$

In this expression, the absorption coefficient (k) has been replaced with the molar absorptivity ε ($\varepsilon(\bar{\nu}) = 2.306k(\bar{\nu})$) which is also a function of optical frequency. The fact that the absorbance is proportional to the path length L presents a challenge at the micro-scale where path lengths are reduced to a few millimeters or less. This is offset, however, by the fact that many of the species of interest in this work (CO, CO₂, H₂O, and CH₄) are present in relatively large concentrations.

While Eq. (4-2) could be used to infer concentration from an absorption measurement made at a single wavelength associated with a single ro-vibrational transition, more reliable results are obtained if measurements of absorption over many transitions are considered. As a result, concentration measurements are usually made by measuring the integrated absorbance \bar{A}_{band} , which is simply the integral of the absorbance over the entire absorption band:

$$\bar{A}_{band} = \int_{band} \varepsilon(\bar{\nu})CL d\bar{\nu} = \bar{\varepsilon}CL \quad (4-3)$$

Raising the gas temperature broadens the Boltzmann distribution of energies in the gas (ie., a wider range of energy levels are significantly populated) but the area under the distribution remains constant because total number of molecules is fixed. Therefore, the total area under the spectrum (\bar{A}_{band}) is insensitive to temperature because it is a function of the number of molecules present or the concentration but the shape of the absorption band ($A(\bar{\nu})$) changes appreciably with temperature because the shape of the Boltzmann distribution changes appreciably with temperature. This work exploits the fact that the

shape of the absorption band is a known function of temperature to infer the gas temperature from the absorption spectrum.

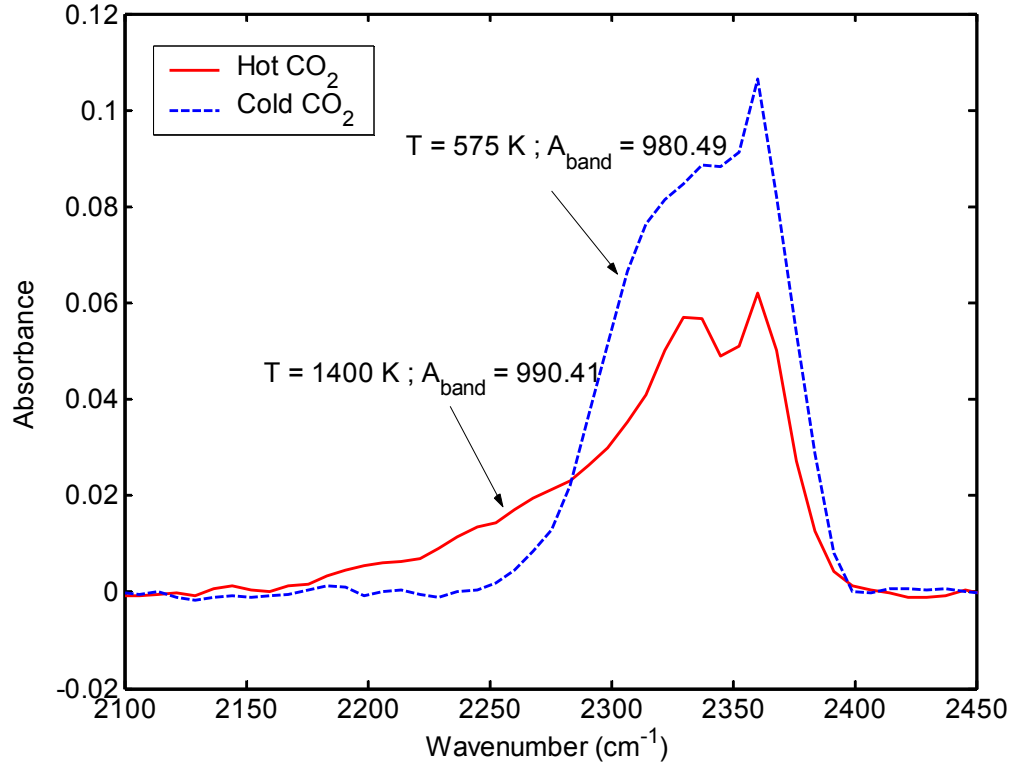


Figure 4-5: Sample hot versus cold CO₂ spectra, measured at 16 cm⁻¹ resolution

There are two approaches to modeling the temperature dependence of the absorption spectrum. High resolution models like HITRAN [68] and HITEMP [69] provide data for the location and temperature dependence of individual spectral lines associated with particular ro-vibronic transitions. These individual lines, when added together and viewed at relatively coarse resolution ($\Delta\bar{\nu} \sim 16 \text{ cm}^{-1}$), form the bands as shown in Fig. 4-4. In contrast, low resolution models like EM2C [71] describe the temperature dependence of the overall band shape. While high resolution models provide much more spectral detail, they require detailed knowledge of the temperature dependence of individual spectral lines. Unfortunately, reliable data is not available for most lines at temperatures greater

than about 1200K. Recent work [67] has shown that narrow band models are more reliable for inferring temperature from infrared spectra in combustion flows, and so that is the approach taken here.

The narrow band model is implemented using EM2C, a FORTRAN program with associated spectral databases developed by EM2C laboratories to compute the radiative intensity and transmissivity of a non-isothermal, non-homogeneous gas column consisting of mixtures of gases like H₂O, CO₂, CO etc. These calculations are accomplished by discretizing the optical path into n homogeneous isothermal elements using the Malkmus [87] statistical narrow band model and the Curtis-Godson approximation at a spectral resolution of 25 cm⁻¹. The temperature fitting procedure is described in detail later.

The Malkmus model assumes Lorentz line shapes averaged over a wide spectral interval and that the individual column elements are homogenous and isothermal. For a given column length L (cm), total pressure p (atm), and mole fraction X of absorbing gas, the transmissivity $\bar{\tau}^{\Delta\bar{\nu}}$ over the spectral interval $\Delta\bar{\nu}$ (in this case 25 cm⁻¹) is given by:

$$\bar{\tau}^{\Delta\bar{\nu}} = \exp \left[-2 \frac{\gamma}{\delta} \left(\left(1 + X p L k \frac{\delta}{\gamma} \right)^{1/2} - 1 \right) \right] \quad (4-4)$$

In this expression, k (cm⁻¹ atm⁻¹), δ (cm⁻¹) and γ (cm⁻¹) are the model parameters for the particular molecular species under consideration. The Curtis-Godson approximation involves replacing k and γ/δ in eq. 4-1 with average values of these parameters over the particular spectral interval being considered. The input parameters for the EM2C model come from the HITRAN database and supplementary data for k , $1/\delta$, and γ obtained by

EM2C laboratories. In the work reported here, we focus on absorption by CO₂ since it is naturally produced in the flame and gives a relatively strong signal.

4.1.3. Gas Temperature Measurement Principle:

Gas temperature measurements are made by fitting $A(\bar{\nu})$ for CO₂ predicted by the EM2C code to $A(\bar{\nu})$ measured from the experiments. This is accomplished in MATLAB using a Newton-Gauss algorithm and a least squares fitting routine 'lsqcurvefit'. The Newton-Gauss algorithm calls the EM2C FORTRAN program with initial guesses for the gas temperature profile and CO₂ concentration. The residual is computed based on the difference between the experimental spectrum and the model prediction. The routine perturbs the values slightly to find the largest gradient for the input parameters of temperature and concentration, and uses the direction of the gradient to iterate forward to find the values of concentration and temperature that best fit the experimental spectrum. The temperature corresponding to the best fit is taken to be the gas temperature. The resolution of the measurements is 16 cm⁻¹ while the resolution of the EM2C model is only 25 cm⁻¹. As a result, the output of the EM2C model must be interpolated onto the experimental data before the residual is computed.

4.2. Experimental Setup:

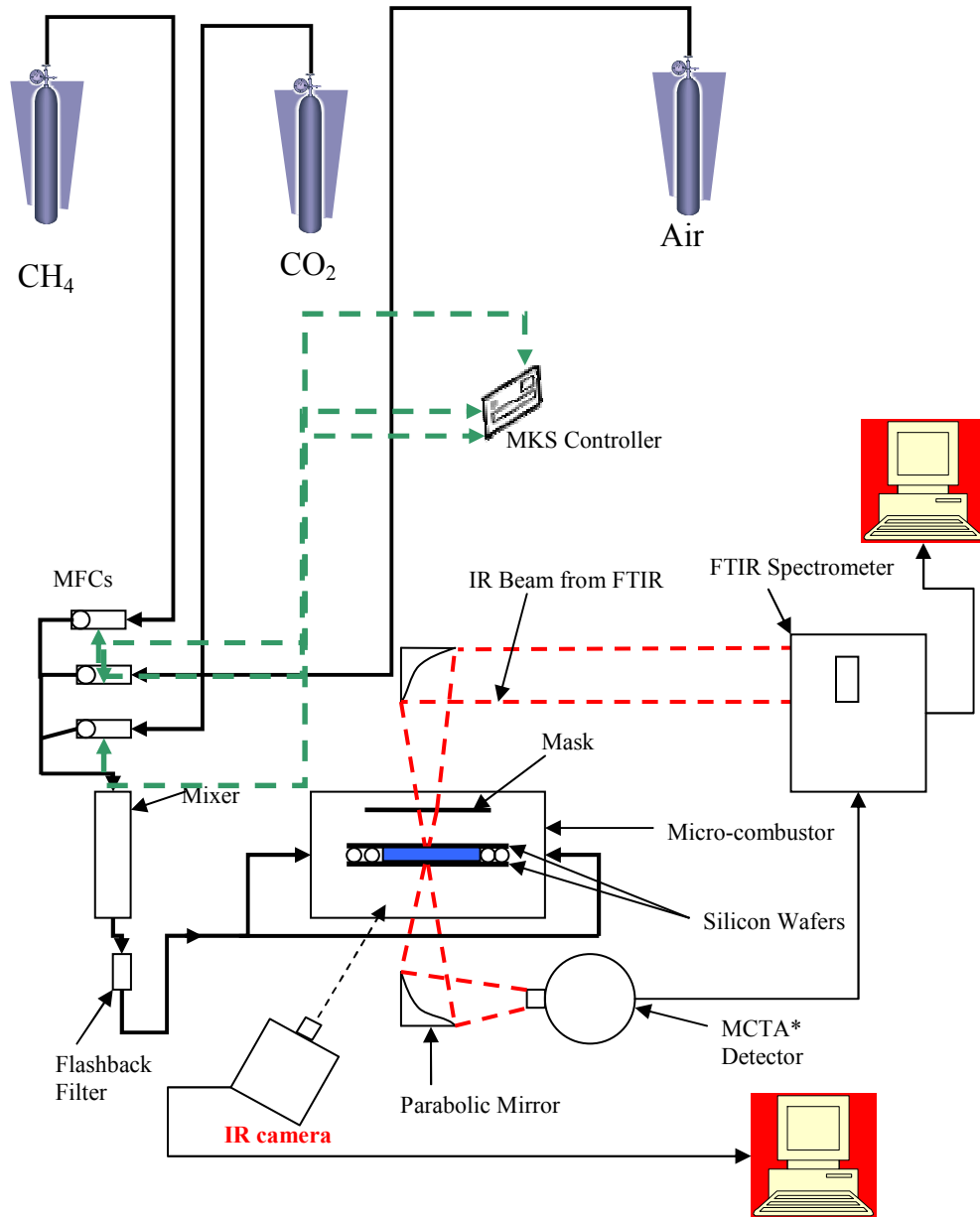


Figure 4-6: Schematic diagram of experiment.

The experimental set up consists of 1) a simulated microcombustor 2) an external optical setup for non-intrusive diagnostics and 3) mass flow controllers to control flow rates and inlet gas composition. The entire set up has been described in detail elsewhere ([16] and [82]) and is presented very briefly here. Fig. 4-6 is a schematic diagram of the

overall experiment. Two UFC-3000A mass flow controllers (MFCs) from Unit Instruments control the flow of fuel (methane) and oxidizer (air) into a mixing chamber consisting of a 1-1/4 inch diameter steel pipe filled with steel wool. The gas mixture exiting the chamber passes through a 15 μm millipore filter that serves as a flash arrestor before it enters the burner plenum. The MFCs are calibrated during each run using a Drycal DC-Lite positive displacement flow meter.

4.2.1. Simulated Microcombustor:

The burner (Fig. 4-7) itself consists of two silicon plates attached to movable supports which allow the gap between the plates to be varied from 500 μm to 50 mm.

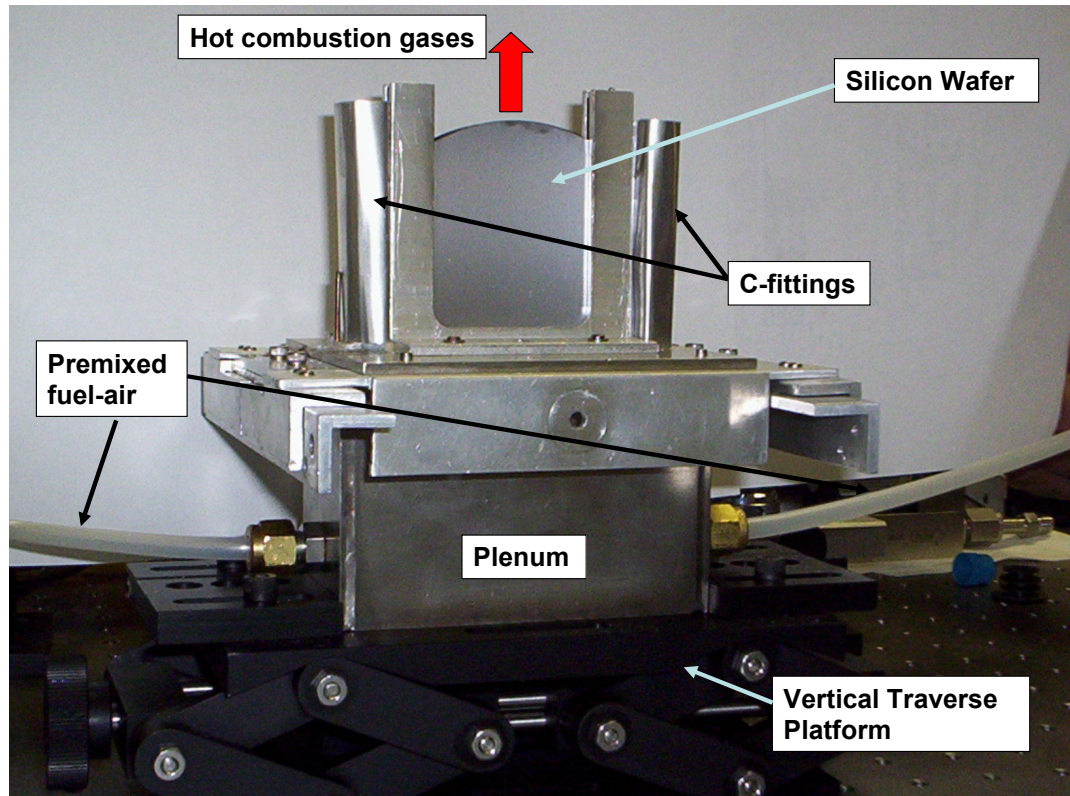


Figure 4-7: Simulated micro-combustor mounted on a vertical traverse.

Two vertical guides support the plates on the outside and a set of 4 vertically-oriented stainless-steel tubes (two at each wafer edge) support the wafers from the inside. The diameter of the internal stainless-steel tubes (2 mm in this work) fixes the minimum wafer spacing. Compliant packings of glass wool are held in place along the outside edges of the plates by loose-fitting ‘C’ shaped metal retainers (see Fig. 4-7). Together, the stainless steel tubing and the glass wool insulation provide an effective barrier to leakage and/or entrainment from the edges of the plate as the flow passes vertically upward between them. The silicon plates are constructed from ordinary silicon wafers used for MEMS micro fabrication. Hence, we refer to the burner as a “simulated” microcombustor as it has many of the important characteristics of a MEMS type combustor (material, passage dimension) but is made using conventional fabrication processes. Two types of wafers are used in this experiment: a p-type wafer doped with boron that has both sides polished, and an n-type wafer doped with phosphorous with only a single side polished. Both wafer types are described as ‘lightly’ doped by the manufacturer but the specific level of doping is unknown. The wafer electrical resistivity is 10-100 Ω -cm for both types of wafers, the thickness is 500 μ m, and the crystallographic orientation is 100.

4.2.2. External Optical System:

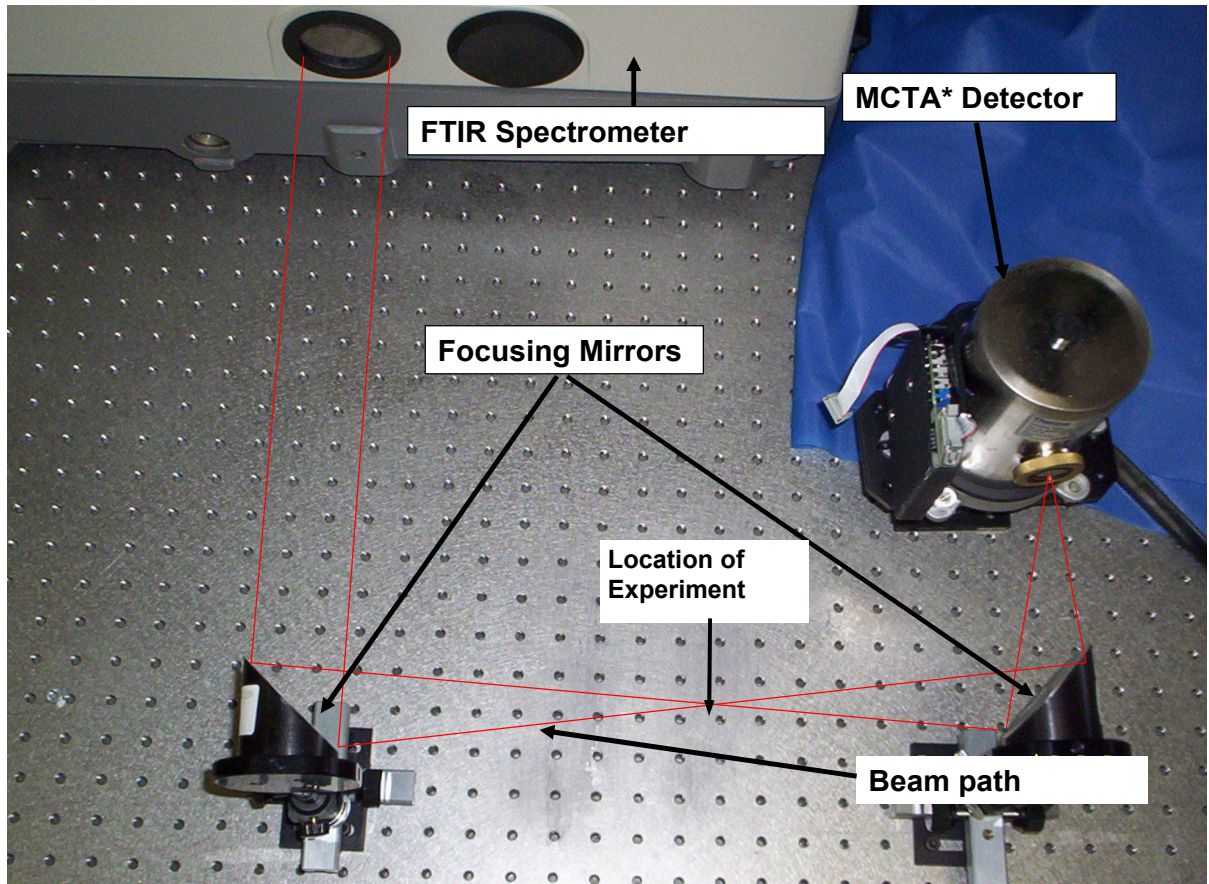


Figure 4-8: External optical arrangement (IR beam path in red).

As illustrated in Fig. 4-6, the beam from a Thermo Nicolet Nexus 870 Fourier transform infrared spectrometer (FTIR) is brought to a focus inside the simulated microcombustor using a 190 mm focal length off-axis parabolic mirror. The off-axis mirror reduces the beam diameter from approximately 38 mm to 10 mm. Fig. 4-8 is a photograph of the external optical system. The IR beam from the FTIR spectrometer is illustrated in red. This beam passes through the simulated microcombustor, is collected by a parabolic mirror with a focal length of 50.8 mm, and is focused onto the FTIR's Mercury Cadmium Telluride (MCTA*) detector that has been removed from the instrument cabinet and attached to the optical bench. The theory of operation of the

spectrometer is described in detail elsewhere [82]. It suffices here to say that the FTIR spectrometer uses a Michelson arrangement to create an optical path difference between the two light beams which are then recombined. The optical path difference in the recombined beams creates an interference pattern (interferogram) whose resolution is controlled by the speed of the moving mirror. The entire recombined beam is passed through the sample (in this case the microcombustor) which absorbs light at different wavelengths according to the type, concentration, and temperature of the species present. The total radiant flux that over all wavelengths that makes it through the sample is collected by a detector that records the intensity as a function of time. This time series is transformed to frequency (or wavenumber) space by performing a numerical Fourier transform.

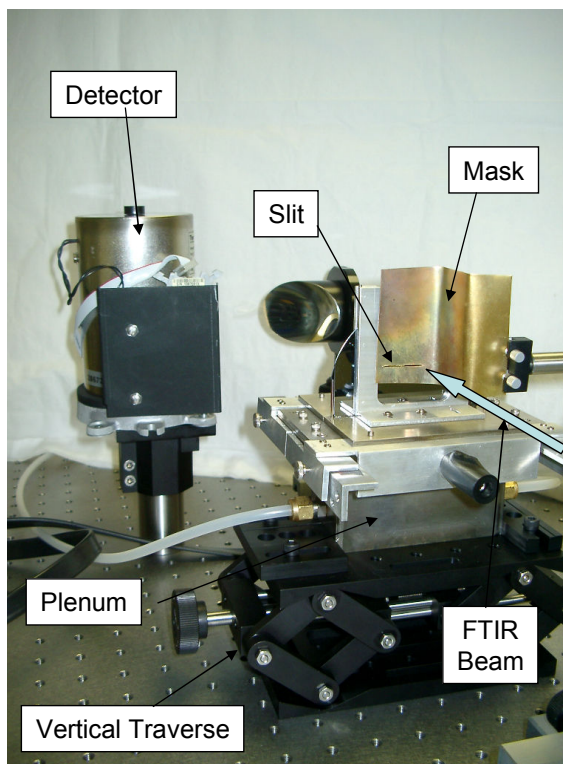


Figure 4-9: Side view of optical system.

As mentioned previously, the IR beam emerging from the spectrometer is focused down to a beam of about 10 mm diameter by the first focusing mirror. However, better spatial resolution is necessary to resolve temperature gradients in the streamwise direction. Spatial resolution is improved in this experiment using a spatial filter (mask with a 1mm slit) as shown in Fig. 4-9. This reduces the size of the beam so that it only extends 1 mm in the flow direction and 5 cm in the spanwise direction. The microcombustor is mounted on a vertical jack that enables different streamwise locations in the burner to be probed without adjusting the external optics.

4.2.3. Flow Control System:

Fig. 4-10 shows the flow control apparatus. As discussed earlier, it consists of an MKS digital controller which controls the MFC's which in turn are calibrated using DryCal DC-Lite flow meters.

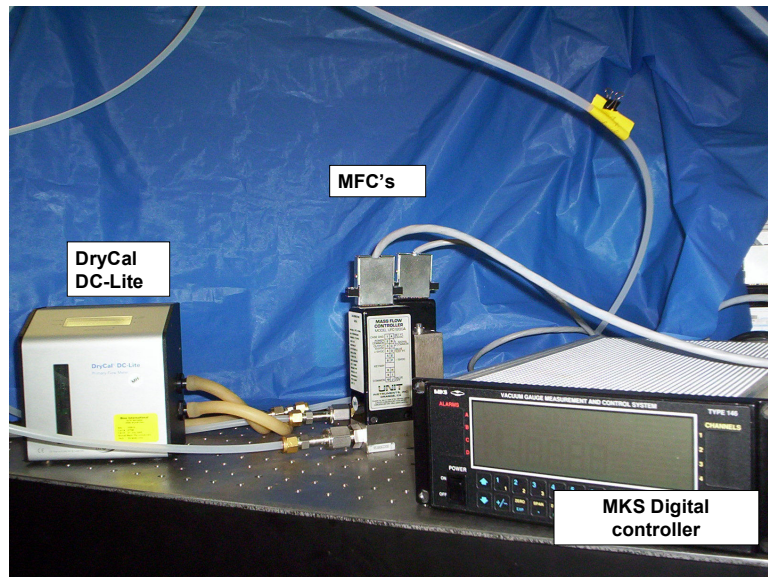


Figure 4-10: Flow Control System

The flow control apparatus enables control of the mixture composition (or equivalence ratio) and volumetric flow rate (or velocity). When the flame is stabilized inside the burner, the flame speed is equal to the velocity of the reactants.

4.3. Experimental Procedure:

The flow control system (MKS unit) is started after opening the fuel cylinder valve and air supply (drawn from an external tank). Initially, only air flows into the burner and the fuel control unit is set to zero. The MCT A* detector (connected externally to the spectrometer) is cooled by filling its dewar with liquid N₂. The FT-IR spectrometer is switched on and the external optical system is adjusted to yield maximum signal strength. A background scan is obtained and stored. Then, the flow is seeded with a trace quantity of CO₂ (1-2 %) and spectra are collected to verify that the CO₂ spectrum is distinctly visible. This trace quantity of CO₂ aids in collection of good spectra in the pre-flame regions where CO₂ concentrations are fairly low. The CO₂ flow is maintained throughout the experiment for reasons that will be discussed in the next section.

The fuel flow rate is set to the value associated with the desired equivalence ratio and the premixed fuel/air (either methane or propane) mixture enters the plenum below the plates. The equivalence ratio and the velocity of the flow are maintained by the fuel and air flow controllers. A stainless steel screen stretched across the discharge slot of the plenum flattens the velocity profile of the flow entering the plate gap and serves as a flashback arrestor. The mixture is ignited with the silicon plates at the desired spacing (~2mm). The flame typically stabilizes on the outer lip of the burner at the start up owing to the burner being at room temperature. The silicon plates get heated by conduction from the flame and sometimes are also heated externally by a flame lighter or an external heat

gun which raises the temperature of the plates and allows the flame to stabilize inside the channel. The external heating is then stopped and the combustor is allowed to equilibrate to its final state with a flame standing inside the channel between the two silicon plates.

Once the combustor reaches equilibrium (about 20 minutes after the external heating is stopped) the FT-IR spectrometer begins collecting absorption spectra (using the previously stored background scan as the baseline) at various vertical positions in the burner i.e. in the pre-flame, flame, and post-flame regions. Typically, 200 scans are collected per position which takes about 2 minutes.

An Omega 0.01" diameter k-type ungrounded thermocouple with a stainless steel sheath measures the outer surface temperature of the silicon plates at a single point through direct contact. This is used to calibrate measurements of the surface temperature distribution across the plates made using a FLIR Systems SC3000 infrared camera. The IR camera collects an image of emitted intensity in the 8-12um range from the silicon wafer. The wafer surface temperature distribution can be obtained from this image using the Stefan-Boltzmann equation for radiation [80]

$$\dot{q}'' = \sigma \varepsilon (T_s^4 - T_\infty^4) \quad (4-5)$$

In this expression, \dot{q}'' is the incident radiation flux per unit area, σ is the Stefan-Boltzmann constant and ε is the emissivity. The above equation is embedded in the software that interfaces the IR camera to the computer, however, the software has a built in starting guess for the emissivity which will not be accurate for all operating conditions. The single point, direct contact measurement made with the thermocouple is used to correct for this by recalculating the emissivity (using in built functions in the software).

Applying the emissivity correction to the IR camera image gives the final surface temperature distribution.

4.4. Temperature Measurement in the Microburner:

The optical path between the two silicon wafers is split into n equal cells. Each of the n cells is assigned a temperature based on the kind of profile we choose to fit (2nd or 4th order profiles) for the temperature between the two wafers.

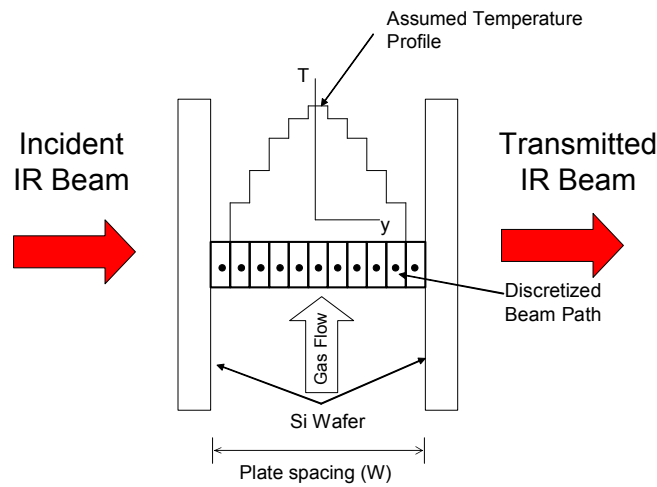


Figure 4-11: Illustration of discretized beam path with an assumed temperature distribution.

Figure 4-11 illustrates the optical path for absorption between the two silicon wafers along with a cartoon of the assumed temperature profile. Previous work [82], [76] showed that both 2nd and 4th order profiles represent the temperature profile with adequate accuracy. The temperature gradient at the wall was captured to within 1% by the 4th order profile and somewhat less accurately by the 2nd order profile. However, this conclusion was based on less sophisticated modeling that assumed plug flow in the

channel. Subsequent modeling efforts (as seen in chapter 3) have shown that under some conditions, the temperature actually peaks off the channel centerline. Capturing this behavior requires a 4th order profile at a minimum and hence this is what we use here.

The 4th order temperature profile is given by

$$T(y) = a_4 y^4 + b_4 y^3 + c_4 y^2 + d_4 y + e_4 \quad (4-6)$$

In this expression, y varies from zero to $2d$, the passage width, which in the current experiment is around 2.10mm. The temperature profile is forced to be symmetric about the channel centerline by requiring that:

$$T(0) = T(2d) \quad (4-7)$$

$$\left. \frac{dT}{dy} \right|_{y=d} = 0 \quad (4-8)$$

$$\left. \frac{dT}{dy} \right|_{y=0} = - \left. \frac{dT}{dy} \right|_{y=2d} \quad (4-9)$$

Subjecting eq. 4-6 to these conditions gives

$$b_4 = -4d a_4 \quad \text{and} \quad d_4 = -2d c_4 + a_4 (2d)^3 \quad (4-10)$$

Eq. 4-10 relates two of the fitting parameters to the other three. Therefore, there are only three independent temperature fitting parameters (namely a_4 , c_4 and e_4) even though we fit for a 4th order profile.

4.5. Challenges in Implementation and Remedies:

4.5.1. Interference from Silicon and CO:

Fig. 4-12 compares absorption spectra of CO₂ and CH₄, with the transmission spectrum of silicon over the same range. It shows that the silicon wafer's transmissivity is approximately 60% except for a small region around the CO₂ band where it varies from 55% to 60%.

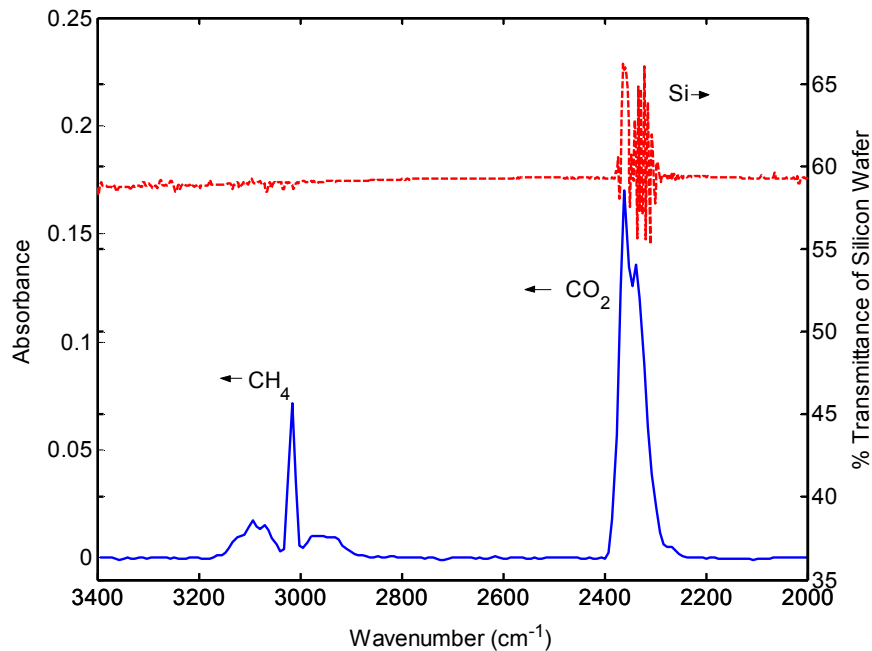


Figure 4-12: Comparison of CO₂, CH₄ (absorption) and Si (% transmittance) spectra.

This interference prevents capture of the strongest part of the CO₂ band in the 2300-2400 cm⁻¹ range. The complete nature of this interference is unclear but the 'dip' in the absorption spectrum of CO₂ near the peak appears to be related to spectral features of both silicon and CO₂. Silicon has an atomic absorption line [88] at ~2340 cm⁻¹ but

experimental measurements [89] of CO₂ absorbance that are not made with silicon in the optical path (see figures 4-4, 4-8 and 4-9 of ref. [89]) also show a ‘dip’ in this area - one that is not predicted by EM2C. Regardless, the interference is a function of temperature that is not easily subtracted out and it causes problems when trying to fit the CO₂ band.

The EM2C program which is used to fit the experimental data requires input of species concentrations of H₂O, CO and CO₂, the path length over which the absorption spectrum is to be calculated, and a guess for the gas temperature.

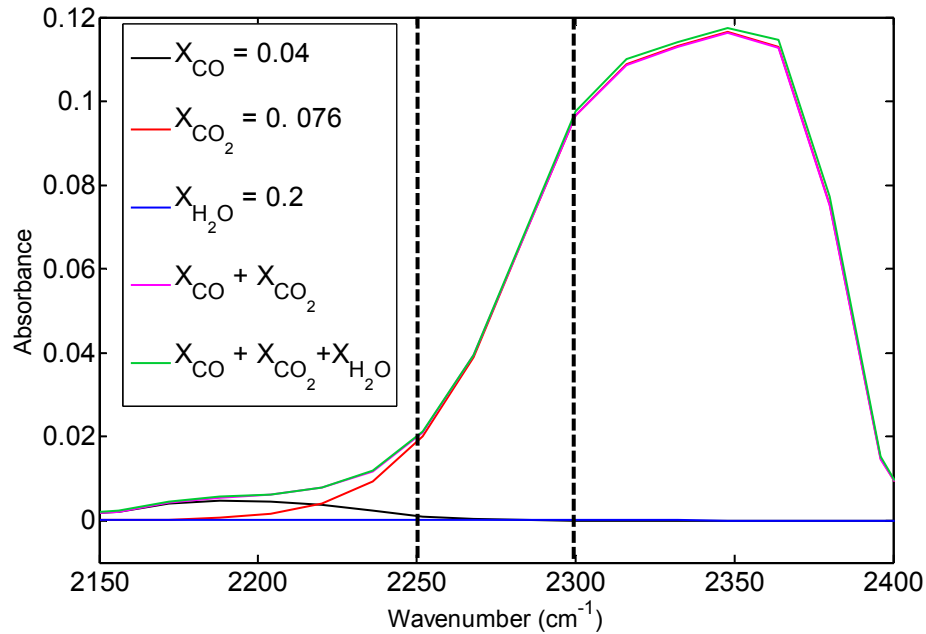


Figure 4-13: Absorbance spectra of CO₂ showing the relative influence of each species given as an input to the EM2C program in the spectral region of interest (T = 900 K, Optical Path Length (2 d) = 2.15 mm)

The spectral (wavenumber) region over which the absorption of CO₂ occurs without interference from other species can be predicted by the EM2C model. Fig 4-13 shows the relative absorbance of each of the species. The mole fraction values assumed for each species correspond to a CH₄/Air premixed flame burning at stoichiometric proportion

calculated using CHEMKIN. The figure indicates that we can expect interference from CO, which is likely to be present in hydrocarbon flames, in the wavenumber region of 2150-2250 cm^{-1} . Therefore, in order to avoid the region where this interference occurs, the experimental data is fitted in the range of 2250 – 2300 cm^{-1} wavenumbers. The solution implemented here is to fit only the region of the band (2250 – 2300 cm^{-1}) that is not affected by the interference from silicon and CO₂ and from CO on the other side of the band. This is illustrated in Fig. 4-14.

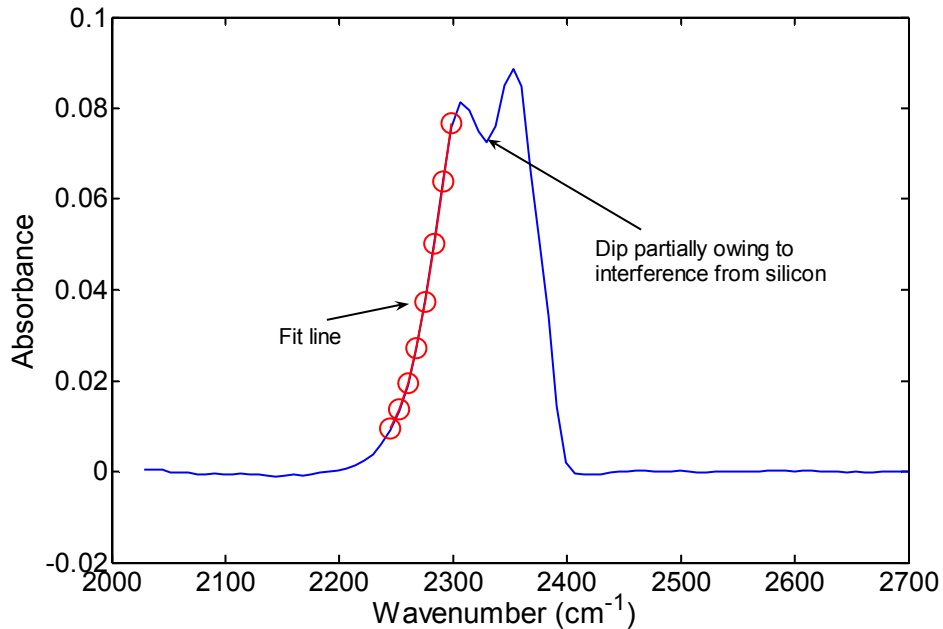


Figure 4-14: Fit of CO₂ spectra: $\phi = 0.85$, $U = 50$ cm/s, 2.12 mm wafer spacing, 21 mm downstream from inlet

4.5.2. High Temperature Effects:

Apart from the interference in the CO₂ band by silicon, additional complications arise because the IR transmissivity of silicon is also a relatively strong function of temperature [90]. This necessitates making measurements of the temperature dependence of the

transmissivity of the silicon plates. This was accomplished by heating the plates with a heat gun, recording the plate temperature with a sheathed k type thermocouple, and recording the absorbance measured by the FTIR.

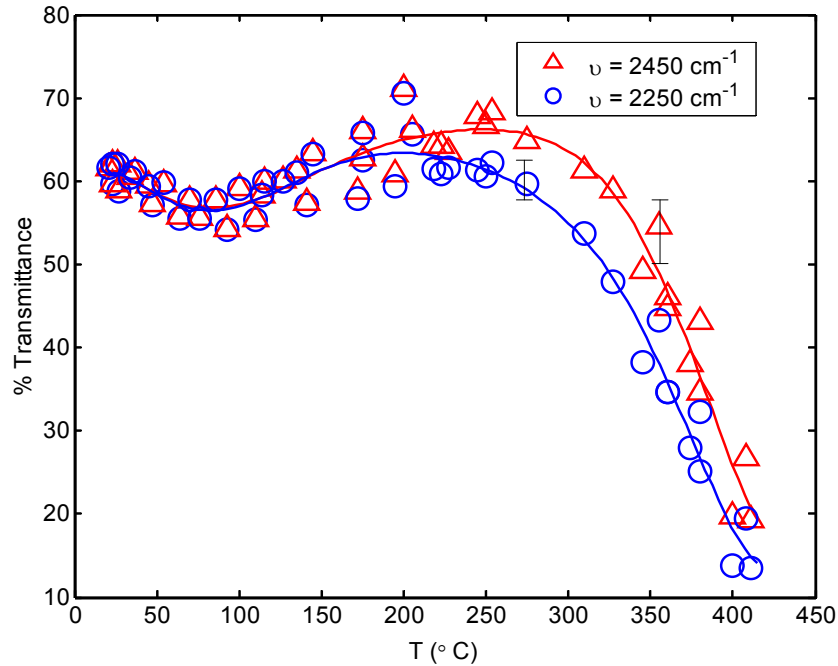


Figure 4-15: Percent transmittance of double side polished Si wafer vs. temperature at different wave numbers around the CO₂ regime (2250 – 2450 cm⁻¹).

The measured transmittance of Si as a function of temperature at 2250 cm⁻¹ and 2450 cm⁻¹ is shown in Fig. 4-15. Transmittance in the spectral region around the CH₄ band varied in a similar manner. The significant scatter in this data arises primarily from inconsistencies in the thermal contact between the thermocouple and the silicon plates as the thermocouple was repeatedly pressed against the plate surface. The line drawn through the data points in this figure is a best fit polynomial. The data show that the transmittance of the silicon wafers drops dramatically with increasing plate temperature. Alone, this does not pose a problem for the diagnostic technique because a baseline shift

and scaling is performed on every spectrum before it is co-added. However, the decrease in transmitted signal decreases the signal/noise ratio of the transmitted intensity measurement and therefore increases the uncertainty in concentration and temperature measurements. As a result, uncertainties in concentration and temperature increase with operating temperature because of the increasing opacity of silicon

In the results presented in Chapter 5, the peak temperature of the silicon plate reaches over 350 °C when operating at/close to stoichiometric conditions. This causes a dramatic drop in the transmissivity, a decrease in signal to noise ratio and hence very poor quality data. Therefore, we are only able to obtain good data in leaner ($\phi \leq 0.9$) and richer flames ($\phi > 1.15$), where the silicon wall temperature stays below 350 °C. Nevertheless, we would like to be able to make measurements over the entire flammability range including stoichiometric compositions.

A fix was attempted by replacing the silicon wafers with sapphire plates of the same thicknesses. Sapphire has thermal and material properties similar to silicon but has much higher IR transmissivity than silicon so we were hopeful that this would solve the problem. However, the sapphire wafers turned out to be much more sensitive to thermal gradients than silicon as they crack almost immediately when they come in contact with a flame. This could not be circumvented even by increasing the plate thickness. The failure of the sapphire windows forced a return to silicon. Therefore, a means of limiting the flame temperature is required. This could be accomplished by diluting the flow with excess N₂ and is discussed in more detail in the future work (Chapter 6).

4.5.3. Lack of CO₂ in pre-flame region

The temperature measurement technique relies on the presence of CO₂ in the absorption path.

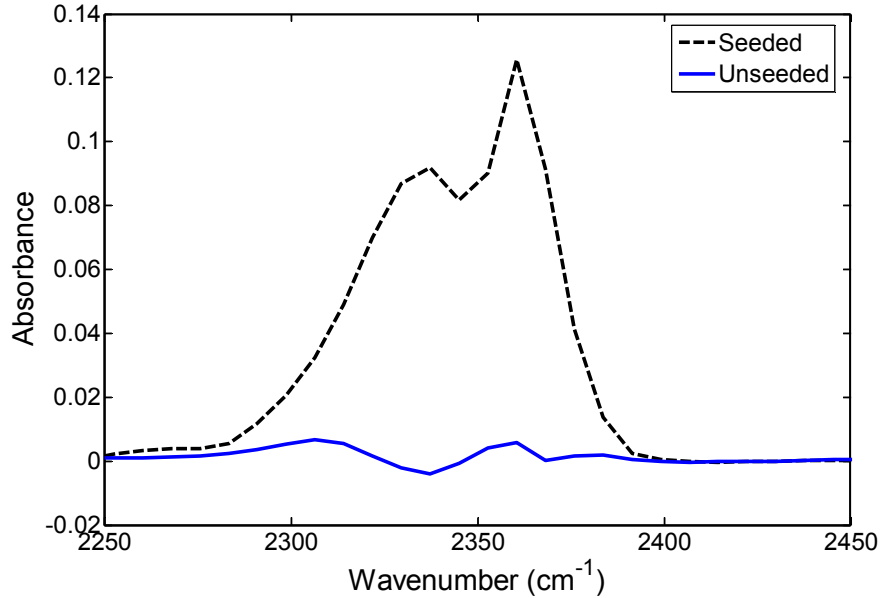


Figure 4-16: Comparison of CO₂ absorbance spectrum at the same location for seeded and unseeded flows in the pre-flame. $\phi = 0.8$, $U = 50$ cm/s, $z = 12$ mm.

Near the flame and in the post-flame regions, there is a sufficient concentration of CO₂ owing to the production of CO₂ in the reaction zone. However, in the pre-flame region only background quantities (384 ppm) of CO₂ are present. This reduces signal/noise and significantly affects the quality of the data. Fig 4-16 shows the pre-flame absorption spectrum in the CO₂ absorption region for the two cases (unseeded and seeded). The equivalence ratio (ϕ) is 0.8 and the flow velocity is 50 cm/s at a pre-flame location of $z = 12$ mm from the slot. As can be seen from the figure, in the absence of seeding (solid line) the absorption spectrum in the pre-flame region is not differentiable from the noise. Attempting to fit this using the EM2C program will result in large error

bars and an effectively meaningless gas temperature. Seeding the flow with a trace quantity (1-2%) of CO₂ by volume (dashed line) improves signal strength dramatically allowing us to make quantitative absorption measurements in the pre-flame. A few sample calculations were made in CHEMKIN for pre-mixed flames with a 2% addition of CO₂ to the reactant mixture and the variance in flame speed (from unseeded) was found to be less than 5%.

4.6. Gas Temperature Uncertainty:

Several factors (instrumental errors, temperature fitting errors etc.) contribute to the final uncertainty of the gas temperature inferred using the diagnostic technique developed here. In order to make meaningful measurements, it is very important to quantify the various sources of uncertainty and to understand how each contributes to the final uncertainty of the temperature measurement. A rigorous analysis of the uncertainty in the predicted temperature is presented elsewhere [16] so the focus here will be on what is new: incorporating the uncertainty introduced by the choice of the functional form of the temperature profile. However, a brief review of our previous work will be useful. The standard error is given by:

$$R_{sq} = \sum_{i=1}^N \left(A_{ex,i} - A_{fit,i} \right)^2 \quad (4-11)$$

In this expression, R_{sq} is the square of the residual from the fitting procedure, $A_{ex,i}$ is the i^{th} point of the experimentally measured absorbance spectrum, $A_{fit,i}$ is the i^{th} point of the best fit to the absorbance spectrum, and N is the total number of points defining the spectrum. The basic premise of the uncertainty analysis is to express the absorbance observed by

the instrument as the sum of the ‘real’ absorbance $A_{real,i}$ (ie. the absorbance that one would measure in the absence of instrument error) and σ_{rms} , the error introduced by the instrument:

$$A_{ex,i} = A_{real,i} \pm \sigma_{rms} \quad (4-12)$$

A similar approach is taken with the absorbance spectrum fitting procedure:

$$A_{fit,i} = A_{perfect\ fit,i} \pm \left[\left. \frac{\partial f_i}{\partial T} \right|_{X_{CO_2}} \delta T + \left. \frac{\partial f_i}{\partial X_{CO_2}} \right|_T \delta X_{CO_2} \right] \quad (4-13)$$

In this expression, $A_{perfect\ fit,i}$ is the absorbance at point i in the absence of fitting, measurement, *and* instrument errors while the second term represents the errors that arise from uncertainties in the inputs to the fitting procedure. In this latter term, f is the EM2C function used to compute the absorbance as a function of gas temperature and concentration and δX_{CO_2} is the uncertainty in the gas mole fraction. The latter is treated as a known uncertainty in this analysis. Substituting eqs. 4-12 and 4-13 into 4-11 leads to:

$$R_{sq} = \sum_{i=1}^N \left\{ \pm \sigma_{rms} \mp \left[\left. \frac{\partial f_i}{\partial T} \right|_{X_{CO_2}} \delta T + \left. \frac{\partial f_i}{\partial X_{CO_2}} \right|_T \delta X_{CO_2} \right] \right\}^2 \quad (4-14)$$

The solution, derived from solving Eq. (4-14) [7], is:

$$\delta T = \frac{\sum_{i=1}^N \alpha_i \beta_i \pm \left\{ \left(\sum_{i=1}^N \alpha_i \beta_i \right)^2 - \left(\sum_{i=1}^N \beta_i^2 \right) \left(\sum_{i=1}^N \alpha_i^2 - R_{sq} \right) \right\}^{1/2}}{\sum_{i=1}^N \beta_i^2} \quad (4-15)$$

In this expression, α and β are constants that can be computed using δ_{rms} , f , and δX_{CO_2} :

$$\alpha_i = \sigma_{rms} - \left. \frac{\partial f_i}{\partial X_{CO_2}} \right|_T \delta X_{CO_2} \quad (4-16)$$

$$\beta_{i,j} = \left. \frac{\partial f_i}{\partial T_j} \right|_{X_{CO_2}} \quad (4-17)$$

There are two solutions to Eq. 4-11 and the larger is taken as the uncertainty in the temperature. The effect of the temperature profile choice is incorporated as follows: A fourth order temperature profile is represented as:

$$T(y_j) = a_4 y_j^4 + b_4 y_j^3 + c_4 y_j^2 + d_4 y_j + e_4 \quad (4-18)$$

where, y_j is the mid-point of each of the n cells and the plate spacing is $2d$.

$$(j = 1:n); \quad y_j = \frac{2d(j - 1/2)}{n} \quad (4-19)$$

The EM2C function depends on the coefficients of the temperature profile and the CO₂ concentration

$$f = f(a_4, c_4, e_4, X_{CO_2}) \quad (4-20)$$

Now, looking back at Eq. 4-17, we can express $\beta_{i,j}$ as

$$\beta_{i,j} = \left. \frac{\partial f_i}{\partial T_j} \right|_{X_{CO_2}} = \left. \frac{\partial f_i}{\partial a_4} \right|_{X_{CO_2}} \frac{\partial a_4}{\partial T_j} + \left. \frac{\partial f_i}{\partial c_4} \right|_{X_{CO_2}} \frac{\partial c_4}{\partial T_j} + \left. \frac{\partial f_i}{\partial e_4} \right|_{X_{CO_2}} \frac{\partial e_4}{\partial T_j} \quad (4-21)$$

The index i represents the wavenumber space over which the absorbance spectrum is collected and the index j represents the location in the channel between the two plates at which the uncertainty is being computed. Direct differentiation of eq. 4-18 gives:

$$\frac{\partial T_j}{\partial a_4} = (y_j^4 - 4d y_j^3 + 8d^3) \quad (4-22)$$

$$\frac{\partial T_j}{\partial c_4} = (y_j^3 - 2d y_j) \quad (4-23)$$

$$\frac{\partial T_j}{\partial e_4} = 1 \quad (4-24)$$

Substituting eqs. 4-22, 4-23 and 4-24 in eq. 4-21 and then into eq. 4-15 gives the uncertainty in temperature at different locations in the channel while accounting for the choice of the fitted temperature profile.

4.7. Fundamental limitations:

The basic diagnostic technique described above was developed and verified experimentally in earlier work [16]. The principal contributions of this thesis in diagnostics area lie in the incorporation of the temperature profile along a line of sight. While it has been found experimentally that the approach described in §4.4 works quite well – i.e. it produces measurements that are consistent with conservation of energy and other observations of overall flame behavior – some important fundamental limitations have also been discovered.

In order to understand their significance, how they arise, and how they can be dealt with, it is useful to briefly step back and review the basic physics of the problem: The degree of light attenuation by absorption is given by Beer's law:

$$\frac{I}{I_0}(\lambda) = e^{-\varepsilon(\lambda, T)CL} \quad (4-25)$$

In this expression, I_0 is the incident flux, I is the transmitted flux, ε is the molar absorptivity of the absorbing species, λ is the wavelength, T is the temperature, C is the concentration of the absorbing species and L is the optical path length. Absorption measurements at two different wavelengths are required to determine both concentration and temperature of a mixture of known gases. Equation 4-25 assumes that the composition and temperature are uniform across the line of sight but this may not be the case in practical systems. To account for this, one can break the absorbing path into a series of adjacent cells each with its own temperature and concentration. The overall absorbance of a series of N such cells, is given by:

$$\frac{I}{I_0}(\lambda) = \prod_{i=1}^N e^{-\varepsilon(\lambda, T_i) C_i \frac{L}{N}} \quad (4-26)$$

At a minimum, measurements of I/I_0 at $2N$ wavelengths are required to solve this system.

The system is given by:

$$\begin{bmatrix} \frac{I}{I_0}(\lambda_1) \\ \frac{I}{I_0}(\lambda_2) \\ \vdots \\ \frac{I}{I_0}(\lambda_{2N}) \end{bmatrix} = \begin{bmatrix} \prod_{i=1}^N e^{-\varepsilon(\lambda_1, T_i) C_i \frac{L}{N}} \\ \prod_{i=1}^N e^{-\varepsilon(\lambda_2, T_i) C_i \frac{L}{N}} \\ \vdots \\ \prod_{i=1}^N e^{-\varepsilon(\lambda_{2N}, T_i) C_i \frac{L}{N}} \end{bmatrix} \quad (4-27)$$

There are a number of factors that complicate attempts to solve eq. 4-27 for T_i and C_i – the temperature and concentration distributions along the line of sight:

1. Since the absorbances appear as a product, T_i and C_i can appear in any order in the product without changing the total observed absorbance. This means that spatial information is lost when solving eq. 4-27 for T_i and C_i directly and individual cells

can be shuffled and arranged in any order to give the same intensity ratio (or absorbance)

2. The $2N$ wavelengths required to solve the system need to be spaced far enough apart so that the values of I/I_0 are substantially different. In the current experiment, interferences from silicon and CO combined with the spectral resolution of the FTIR limit the resolution of CO₂'s band head to only 8 points. This means that the temperature profile across the channel can only be represented using 4 points – a rather coarse profile.
3. Increasing the spectral resolution of the measurement so as to increase the number of $I/I_0(\lambda_i)$ available to the fitting routine may actually make things worse. The reason is that increasing the resolution of the measurement would mean that the rotational lines will start to emerge in the measured spectra. These features are not part of the EM2C model which is only for the rotational band envelope and the presence of these fluctuations presence would actually make it more difficult to match the model to the measurement.
4. The absorbance is a highly non-linear function of wavelength, temperature, and concentration. This makes it challenging to solve eq. 4-27 for T_i and C_i .
 - a. The most common approach to this problem – the least-squares method – is not suitable for solving eq. 4-27 for T_i and C_i . The reason is that the least-squares method seeks T_i and C_i that minimize the difference between the predicted and target function over a user-defined fitting interval. This has the effect of biasing the fitting procedure toward absorbance at wavelengths with

larger absorbance when matching at wavelengths with smaller absorbances is equally important. What is required is a technique in which a fitting tolerance can be specified for each $I/I_0(\lambda_i)$ point.

- b. Most non-linear systems have multiple solutions. Methodologies for identifying the physical meaningful solution have not been developed.

It turns out that our knowledge of the functional form of the temperature profile – established earlier from the modeling efforts – is the key to mitigating many of these problems. Instead of solving for T_i and C_i explicitly at every point, we assume that the concentration is approximately uniform across the channel and that the general shape of the temperature profile is well represented using a polynomial (something shown earlier). This has several effects:

1. It provides a mechanism for retaining the shape of the temperature profile across the channel
2. It reduces the number of unknowns in the problem thereby making it much easier to solve the system. In this experiment with absorbance measurements at 8 discrete wavelengths, representing the temperature distribution using a symmetric 4th order polynomial reduces the number of unknowns from 8 to 4. This greatly increases computational efficiency.
3. It provides a mechanism for excluding at least some physically meaningless solutions.

This approach is tested in the next section by performing the least-squares fitting procedure using a variety of initial guesses for the temperature profiles in different places in the combustor. It is found that in most cases, the resulting temperature profile is insensitive to the initial guess *provided a sensible initial guess is made*. For example, guessing that the temperature profile far upstream of the flame peaks at the center of the channel as opposed to the wall is not physically reasonable and will produce a solution with a similar non-physical character.

4.8. Initial Guess for T fitting parameters:

As discussed earlier in § 4.4 the optical path between the two silicon wafers is discretized into n cells for the purpose of computing the integrated, “line of sight” absorbance using the EM2C model. A 4th order profile is ‘guessed’ for the temperature between the two wafers based on the results of the analytical modeling. The parameters of the profile along with a concentration guess for CO₂ are given as inputs to the EM2C program to compute the absorbance as a function of the wavenumber and fit the experimental data. The implementation of the actual fitting is as follows: First, a matlab function was developed that takes the starting guess for the temperature fit parameters (namely: a_4 , c_4 and e_4 for eq. 4-6) and a guess for the CO₂ mole fraction as input variables and modifies the input files used by the EM2C program. It then invokes the EM2C program to compute the corresponding absorption spectrum. Second, a matlab script was created which loads the experimental data files onto the workspace and then calls the above developed matlab function via an internal optimization routine (‘lsqcurvefit’) based on non-linear least squares fitting and optimizes the fit parameters to give a best fit.

The critical requirement is to be able to provide a good starting guess for the fit parameters.

In order to check this, we try fitting several different temperature profiles to experimental data ($\phi = 1.15$, $U = 50$ cm/s). The initial profiles along with the initial guesses for their defining parameters are summarized in table 4-1. Both the type and magnitude of the profiles are varied.

Set No	Profile type	a_4 (cm ⁻⁴ -K)	c_4 (cm ⁻² -K)	e_4 (K)
1	Flat	0	0	500
2	Flat	0	0	1000
3	Flat	0	0	1500
4	C shape	2e4	2e3	500
5	C shape	2e4	9e3	500
6	C shape	2e5	2e4	800
7	C shape	2e5	5e4	800
8	Inverted C shape	2e4	0	500
9	Inverted C shape	5e5	2e3	800
10	Inverted C shape	7e5	1e3	800

Table 4-1: Initial guess choices for 4th order T profile

4.8.1. Profile Comparisons

i) Flat Temperature Profile: The first temperature profile fitted is a flat profile. We take eq. 4-6, set a_4 and c_4 to zero, and guess three different values for e_4 (500, 1000, 1500 K see table above). We would expect the solutions to converge as the profiles guessed are qualitatively the same and only have different starting values. The centerline gas temperatures returned for the converged solutions in each case are plotted in figure 4-17. The figure shows that the solution is independent of profile choice for all but one point in the pre-flame. Since the discrepancy is within the errorbar for the temperature, it is not

significant. The R^2 , which is a measure of the goodness of the fit, was greater than 0.99 for all these points⁵.

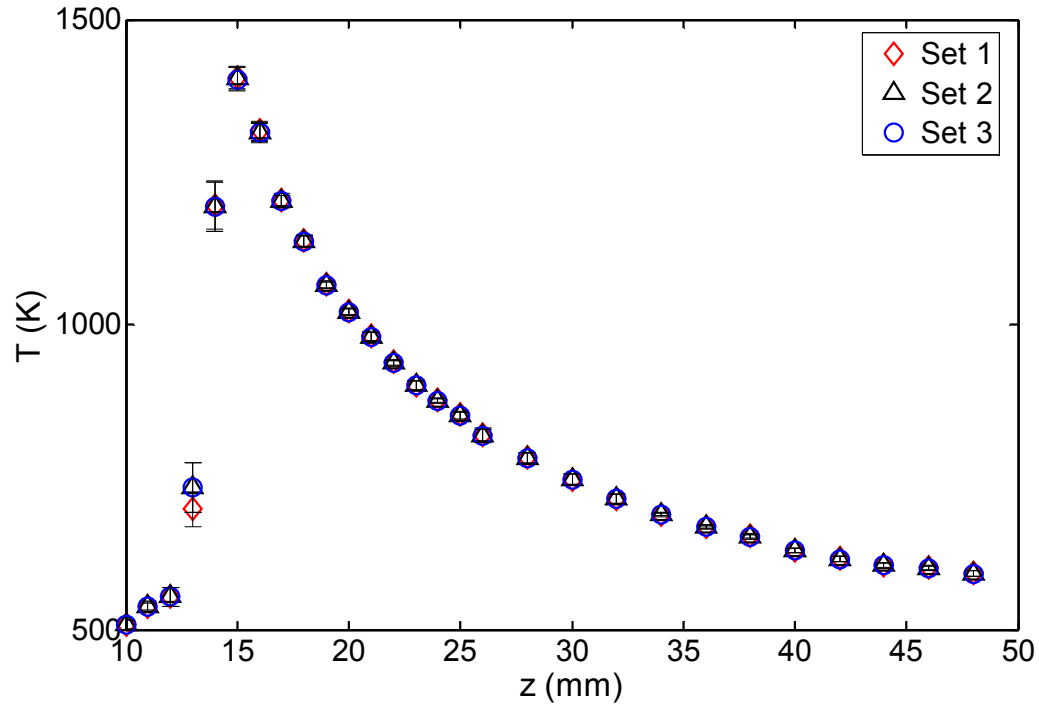


Figure 4-17: Plot of centerline temperature as a function of axial distance for three different initial guess values for a flat temperature profile ($\phi = 1.15$, $U = 50$ cm/s)

Figure 4-18 shows the corresponding transverse profiles for a few select axial locations. The axial locations chosen are as follows: one in the pre-flame, one at the flame, one in the post-flame close to the flame, and one far downstream from the flame. By visual inspection of the spectra (the disappearance of CH_4) the flame location was ascertained to be 14 mm downstream of the inlet slot.

The figure shows that the profiles deviate very little from the starting guess shape. As with the centerline measurements, the different starting guesses converge to the same final solution. What this means is that choosing an initially flat temperature profile causes

⁵ R^2 value of 1 implies perfect fit.

the EM2C program to treat the optical pathway as one block instead of n discretized blocks and the temperature returned is effectively the average gas temperature between the two wafers.

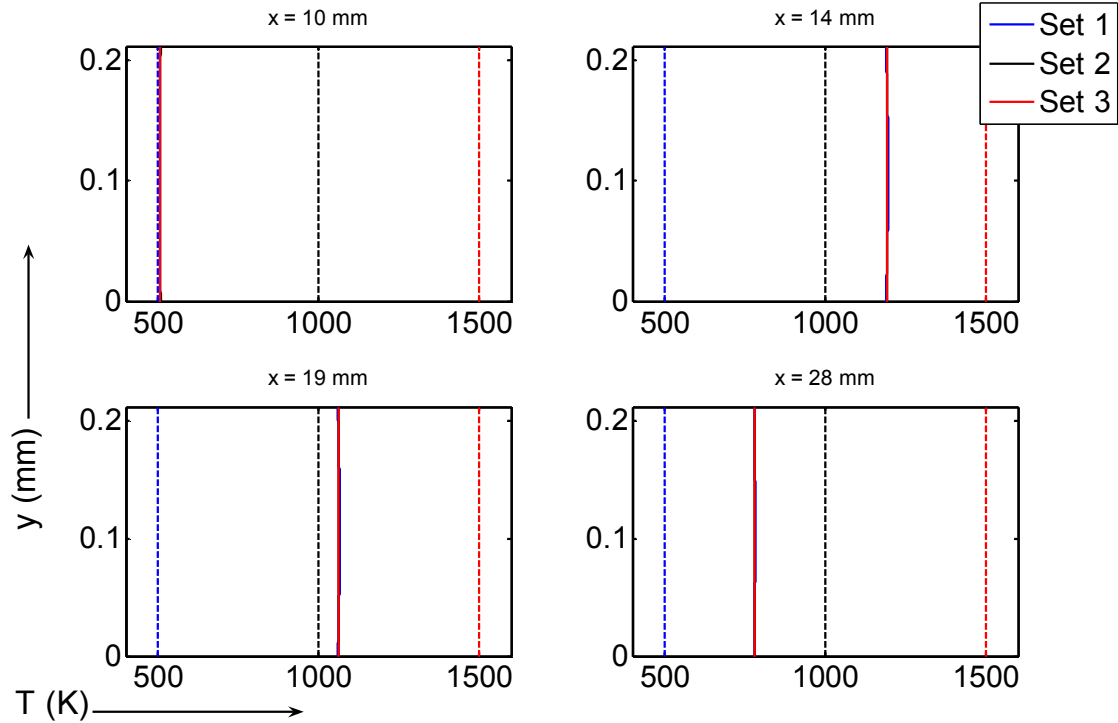


Figure 4-18: Plot of temperature as a function of transverse coordinate at four axial locations for four different initial “C” shaped guesses ($\phi = 1.15$, $U = 50$ cm/s)

ii) **“C” shaped profile:** The next profile we consider is a “C” shaped profile, in which the wall is hotter than the centerline of the flow as might be the case in the pre-flame. We consider the four initial guesses outlined in table 4-1. Figure 4-19 shows the corresponding centerline and wall temperatures. Unlike the flat temperature profiles, they do not converge nicely to the same solution at all axial locations. There are a few features to note in these plots. First, the wall temperature is always higher than the centerline at all axial locations (mimicking the starting shape). Second, initial guess sets 5 and 6 overlap the most. From the shapes of the temperature profiles evidenced in Chapter 3, it is clear

that this initial profile shape is a good guess for the pre-flame region and not a likely shape for the post-flame region. Accordingly it is seen that three of the sets (4, 5 and 6) converge to the same solution in the pre-flame.

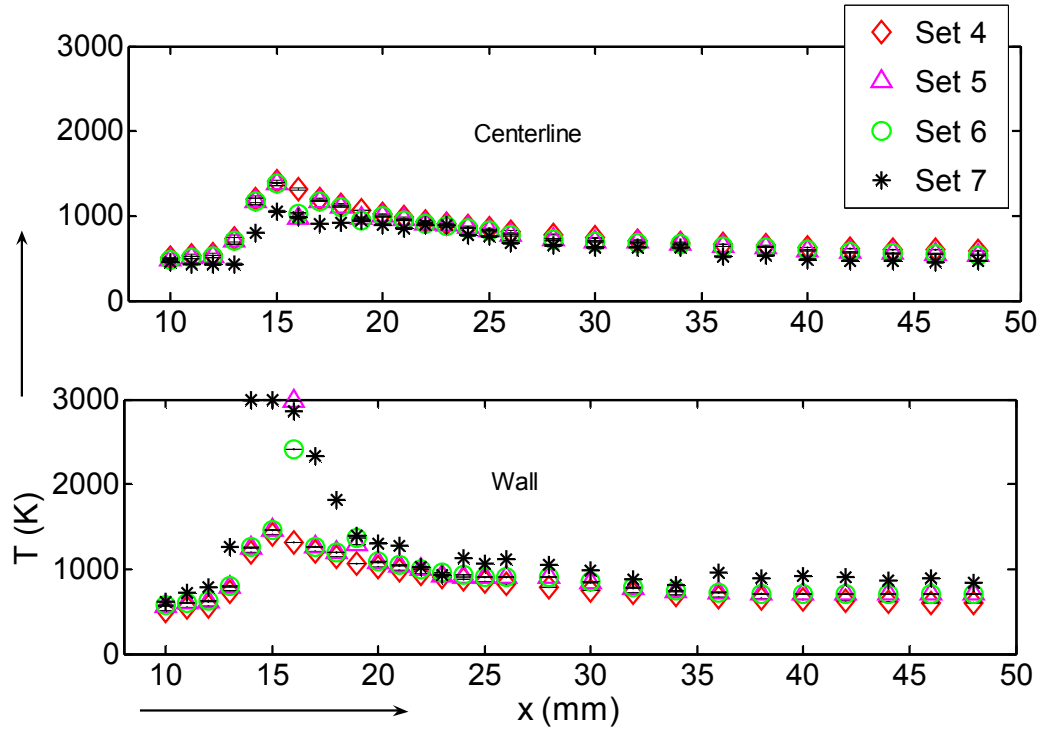


Figure 4-19: Plot of centerline and wall temperatures as a function of axial distance for four different initial guess values for a “C” shaped temperature profile ($\phi = 1.15$, $U = 50$ cm/s)

The very high wall temperatures seen at some points (near the flame) is probably a result of the shuffling problem identified earlier coupled with the fact that near the flame, the concave upward temperature profile is no longer appropriate.. A plot of the transverse profiles across the channel gives more insight. Figure 4-20 shows transverse profiles at the four axial locations selected previously for the flat profile case.

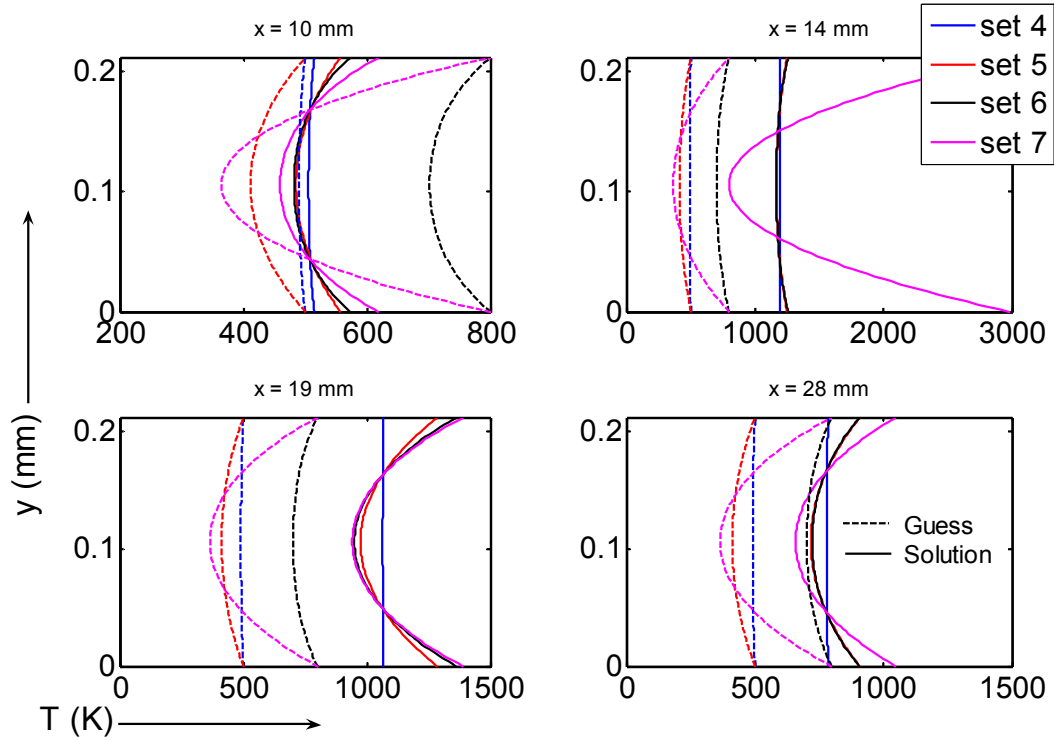


Figure 4-20: Plot of temperature as a function of transverse coordinate at four axial locations for four different initial “C” shaped guesses ($\phi = 1.15$, $U = 50$ cm/s). The dashed lines show the guesses and the solid lines show the converged solutions.

The figure shows that the shape of all converged solutions matches that of the starting guess. Guess set 4 has a very slight curvature and the solutions (blue lines) corresponding to this guess also converges with a slight curvature almost like the flat profile guess. Initial guess set 5 (red lines) starts with the same wall temperature (500 K, see table 4-1) as set 4 but has more curvature (about 100 K between wall and centerline). Guess sets 5 and 6 have the same curvature but start with different wall temperatures (500 K and 800 K). Guess sets 6 and 7 start at the same wall temperature (800 K) but with set 7 having a strong curvature.

The main point where they deviate is at the flame. The reason for this could be that the choice of fitting using a least squares approach cannot guarantee a close fit over all

spectral wavelengths. In the lower absorbance regions (around wavelengths of 2250 cm^{-1}) when the least squares approach tries to minimize the sum of the squares of the residual, the residual would be lower than at a higher wavelength primarily owing to the low value of the absorbance there. A plot of the fits (Figure 4-21) at the corresponding axial locations shows that the least squares may not be the best approach as seen from the fit at $x = 14\text{ mm}$.

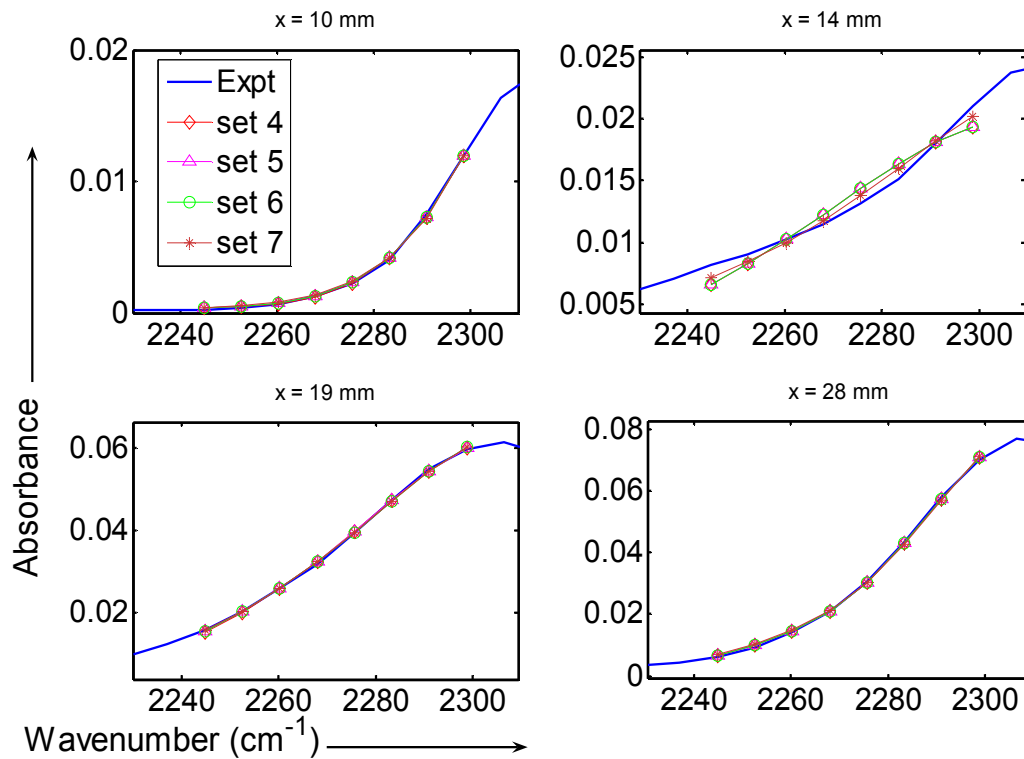


Figure 4-21: Plot of EM2C fit to the experimental absorbance as a function of wavenumber at four axial locations for four different initial “C” shaped guesses ($\phi = 1.15$, $U = 50\text{ cm/s}$)

Since R^2 is greater than 0.99 for all of these points, it would be prudent not to use R^2 as the only measure of fit quality. Rather, a convergence criterion should be imposed at each point of the fit to ensure a good fit.

iii) **Inverted “C” shape:** Finally we test an inverted “C” profile in which the centerline is hotter than the wall as might be the case in the post-flame. Again, we get nicely converged solutions with R^2 greater than 0.99 at every axial point. Again, the solutions follow the pattern of the starting guess and hence the centerline is always hotter than the wall (Fig. 4-22).

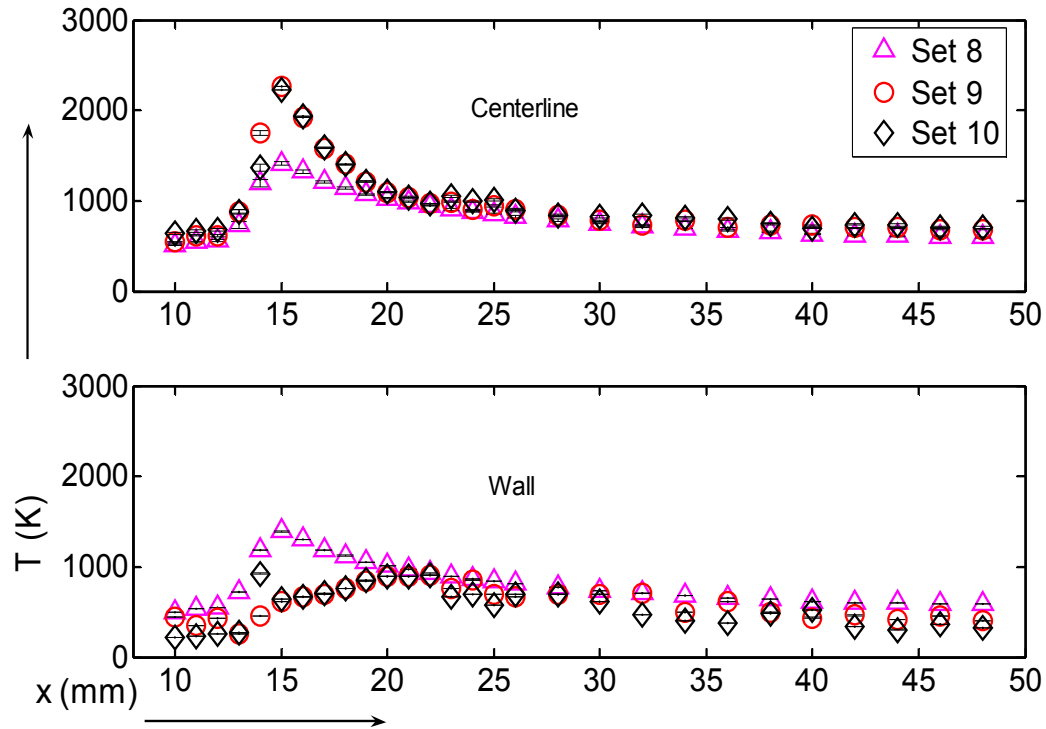


Figure 4-22: Plot of centerline and wall temperatures as a function of axial distance for four different initial guess values for a “C” shaped temperature profile ($\phi = 1.15$, $U = 50$ cm/s)

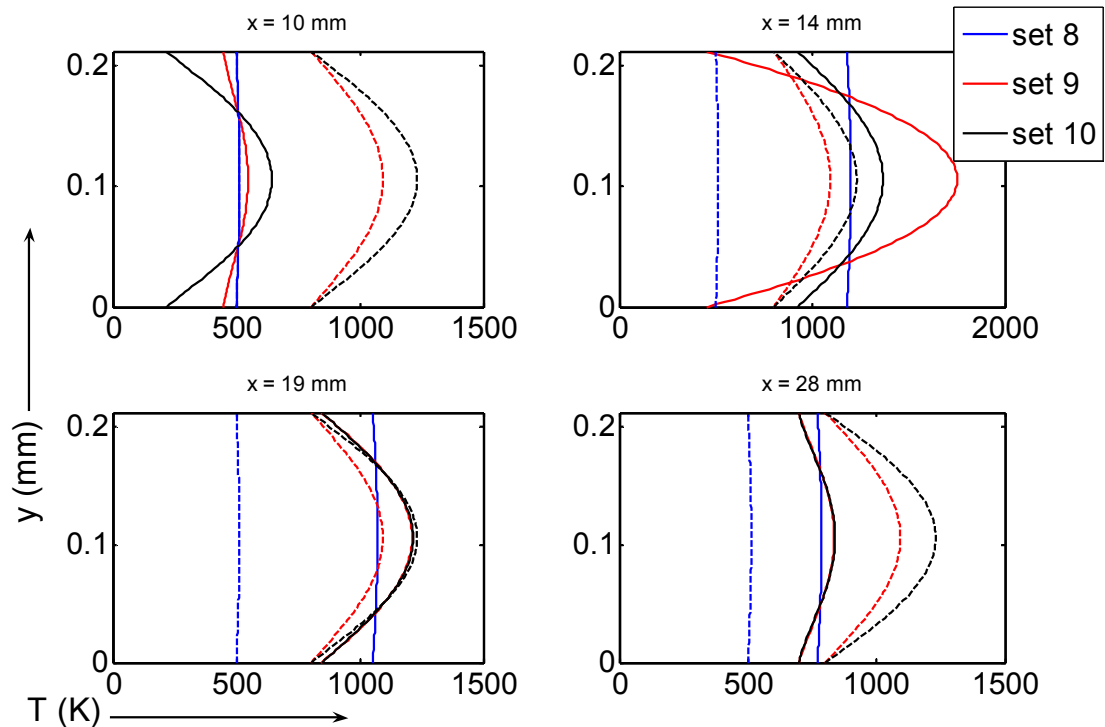


Figure 4-23: Plot of temperature as a function of transverse coordinate at four axial locations for four different initial “C” shaped guesses ($\phi = 1.15$, $U = 50$ cm/s). The dashed lines show the guesses and the solid lines show the converged solutions.

A plot of the transverse profiles (Fig. 4-23) at the four axial locations shows that two of the guess sets (9 and 10) that have a pronounced curvature in the starting shape converge to the same solution in the post-flame regions ($x = 19$ and 28 mm). The guesses do not converge at the pre-flame point ($x = 10$ mm) probably owing to the fact that this shape is a bad guess for the pre-flame. A plot of the spectral fits (Fig. 4-24) at these axial locations reveals that all sets fit well in the post-flame. At the flame ($x = 14$ mm), convergence using the least square’s method does not seem to be the best approach. Set 9 (red circles) has the best fit at the flame, and the corresponding transverse temperature profile is the closest to that predicted by the analytical model in Chapter 3.

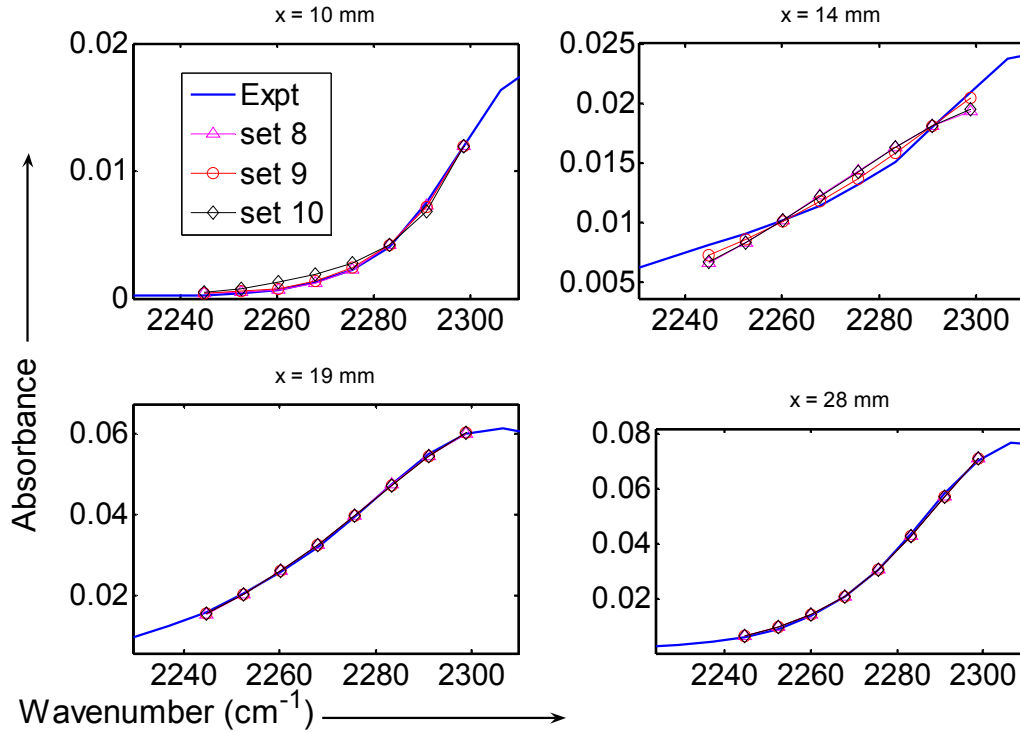


Figure 4-24: Plot of EM2C fit to the experimental absorbance as a function of wavenumber at four axial locations for four different initial “C” shaped guesses ($\phi = 1.15$, $U = 50$ cm/s)

4.8.2. Initial guesses based on analytical model:

The preceding subsection has demonstrated the need to have good guesses for the shapes and the amplitudes of the temperature profile in order to produce realistic fits. Care has to also taken to visually inspect the fits or develop a criterion for each point in the fit to ensure a good fit instead of the least squares fit (especially in and around the flame) criterion of R^2 . To accomplish this, the previously developed 2-D analytical model for the temperature (Chapter 3) can be used as a basis for the initial guesses of the temperature profile shapes. Recall that the model was developed for two different

velocity profiles: Plug flow and fully developed Poiseuille flow. Schlichting [ref] gives the entrance length (l_e), for the development of the velocity profile, as

$$\frac{l_e}{d} = 0.16 Re_d \quad (4-28)$$

where, Re_d is the Reynolds number based on channel half height. The Reynolds number in our burner ranges between 16 and 40 depending on the choice of the average temperature (at 300 K and 1000 K) for evaluating fluid properties like viscosity, density etc. Using this value for Re_d in Eq. 4-28 gives us $2.5 < l_e/d < 6.5$. In comparison, the interrogation region for our burner starts at 10 mm or $l/d \sim 10$. Therefore, we expect the flow to be hydrodynamically fully developed in the region where optical measurements are made. Hence, the Poiseuille flow solution is selected.

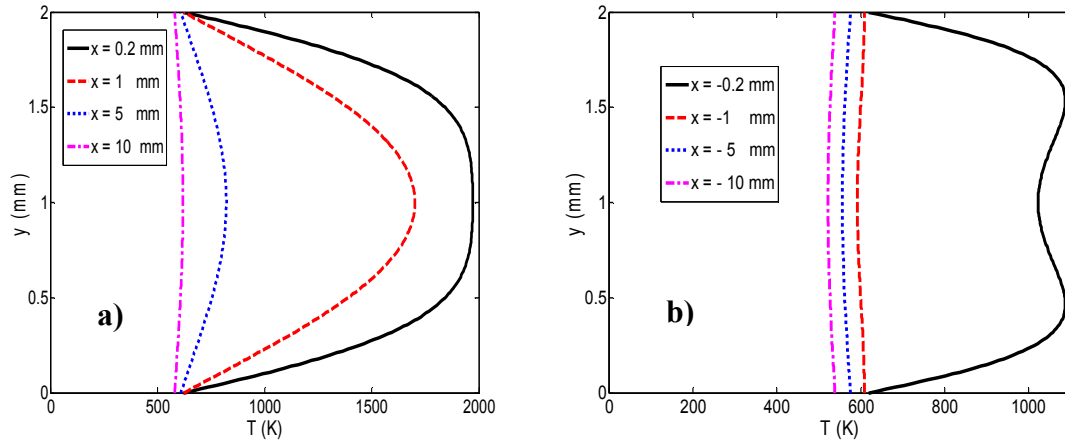


Figure 4-25: Transverse temperature profiles in the channel predicted by the analytical model using the Poiseuille flow solution. a) Pre-flame, b) Post-flame.

Figure 4-25 shows the temperature profiles predicted by the analytical model for fully developed flow in the burner. The figure shows that the pre-flame profiles are generally “C” shaped curves with a slight curvature except near the flame where a double peak shape is present. These off-center peaks are the result of the velocity profile as discussed

in the modeling section. The post-flame profiles at the same axial distances from the flame (Fig. 4-25 b) reveals that the profiles are mostly inverted “C” shapes except very near the flame where there is a bit of flattening of the curvature of the “C”.

These starting shapes are used as initial guesses for the temperature profiles in the pre and post-flame regions. Special attention is paid to the convergence between EM2C and measured absorbance at the individual points (i.e., at the different wavenumbers) of the fit -especially in the near flame region. While the accuracy of the profiles predicted by the analytical model developed in Chapter 3 is limited by the assumptions made in the model (i.e., flame sheet, flat flame, constant fluid properties with temperature etc), the shapes of the temperature profiles from the model still give a better starting point for the guesses than arbitrarily attempting to fit the profiles.

Chapter 5: Experimental Results

In this chapter the absorbance data collected from operating the burner over a range of equivalence ratios and mixture velocities is processed using the EM2C fitting procedure outlined in the previous chapter to obtain temperature profiles. The main aim of the experiment is to measure temperature profiles in the streamwise (along the flow) and the transverse (along line of sight between the two plates) directions and from these determine the gas-wall heat transfer and then infer the net heat recirculation to the pre-flame. The measured heat recirculation will be compared with the predictions of the analytical model developed in Chapter 3.

5.1. Model Based Temperature Fit:

In chapter 4 it was shown that the fitting routine needs a good starting guess in order to get temperature profiles that make physical sense (i.e., the wall being hotter than the gas in the pre-flame and vice-versa in the post-flame). It was also shown that knowledge of the functional form of the temperature profile was necessary in order to avoid the loss of spatial information when fitting for “integrated” absorbance. Table 5-1 summarizes the initial guesses for the temperature profiles in different parts of the burner with reference to the flame location (x_f).

S. No	a4 (K/cm ⁴)	c4 (K/cm ²)	e4 (K)	x_{location} (mm)
1	2.8e4	1e2	520	$x < x_f - 3$
2	-13e4	-6e3	579	$x_f - 3 \leq x \leq x_f$
3	-7e6	-5e5	650	$x_f \leq x \leq x_f + 1$
4	2e6	1e4	600	$x_f + 1 \leq x < x_f + 5$
5	5e5	1e4	550	$x_f + 5 \leq x$

Table 5-1: Initial guess for parameters to be supplied to the fitting routine

Figure 5-1 shows typical centerline and wall temperatures for one particular operating condition ($\phi = 1.15$, $U = 50$ cm/s).

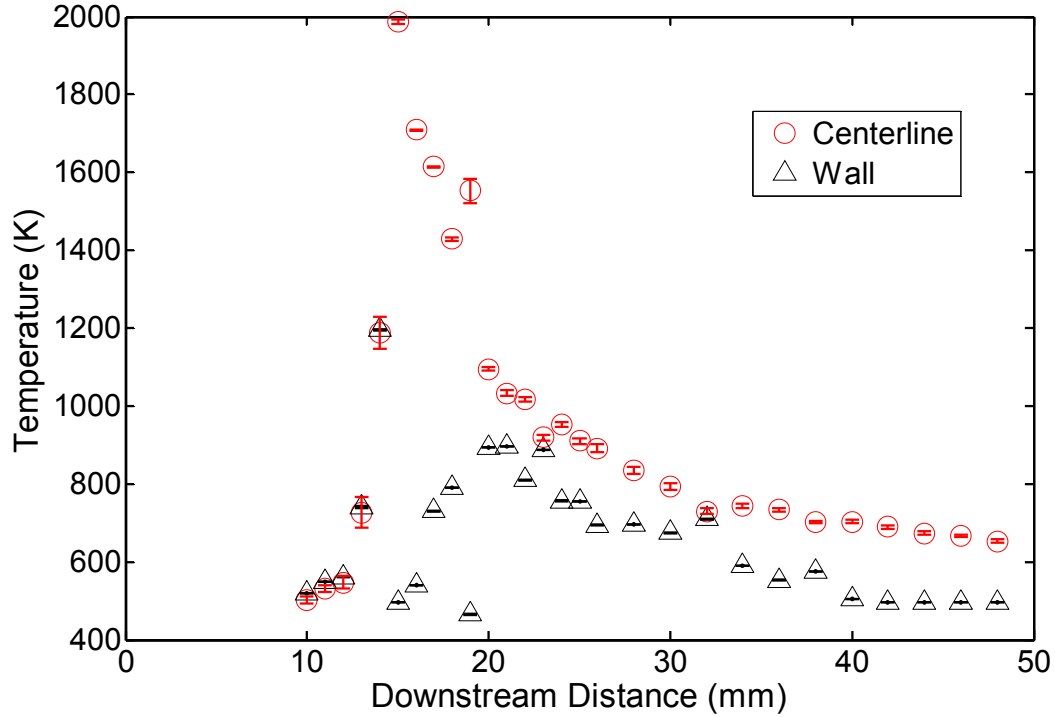


Figure 5-1: Centerline and wall temperatures as a function of downstream distance (CH₄/Air, $\phi = 1.15$, $U = 50$ cm/s)

Figure 5-2 shows transverse temperature profiles for a few axial locations. The flame location (x_f) is 15 mm downstream from the entrance slot. The peak gas temperature of about 2000 K occurs near the centerline of the passage at the flame location.

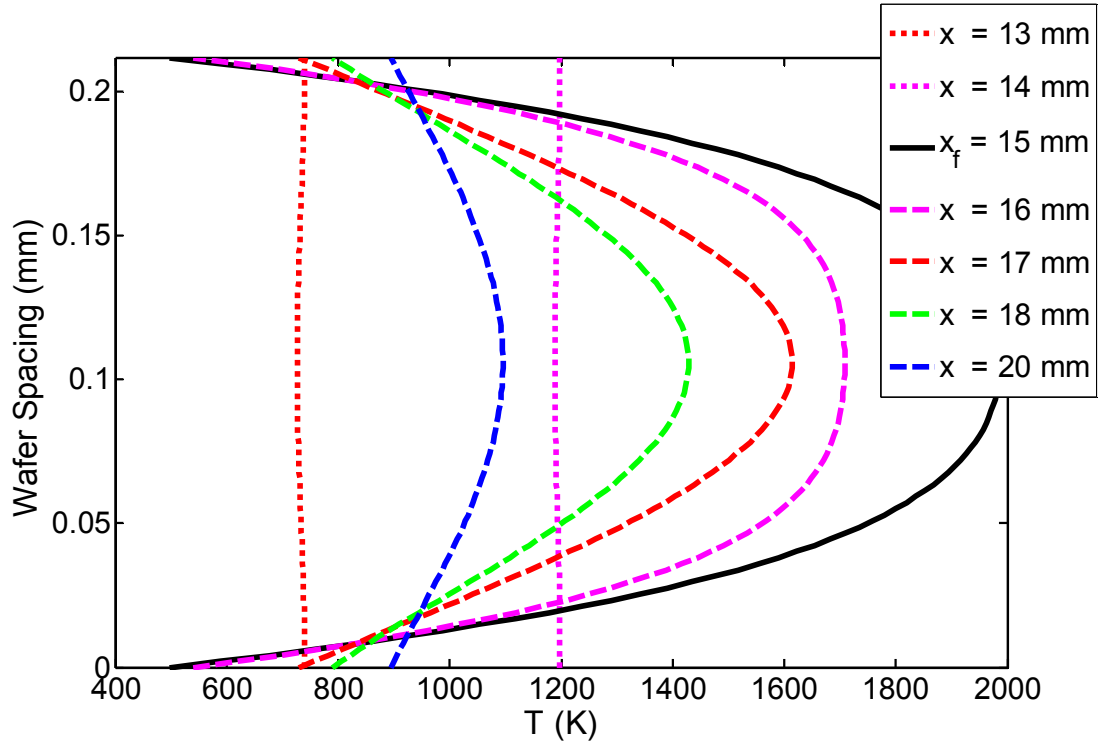


Figure 5-2: Transverse temperature profiles across the channel at select downstream locations (Flame location $x_f = 15$ mm)

Comparing Figs. 5-1 and 5-2, it can be seen that near the flame, where the wafer is the hottest, the fit based on the model fails to give solutions that are physically meaningful. The reason this particular profile is suspect is that the wall temperature is lower than the preceding point in the pre-flame. This cannot be correct and the reason can be inferred from figure 5-3 which shows an IR camera image of the burner operating at the same condition as Figs. 5-1 and 5-2. The solid vertical rectangle shows the zone of interrogation. We are able to make measurements starting only at about 10 mm from the entrance slot (base) of the burner.

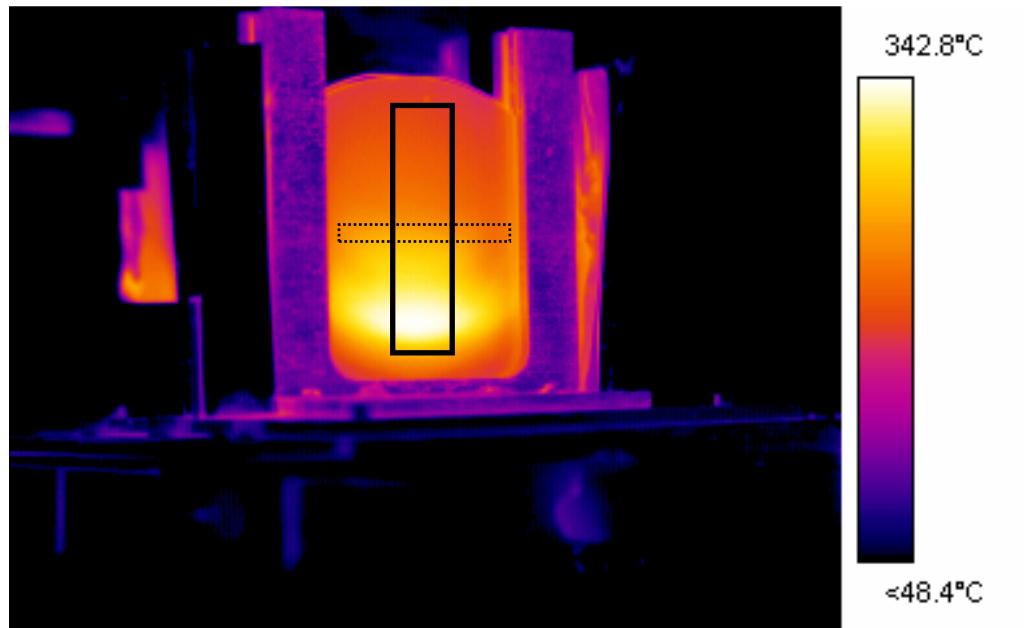


Figure 5-3: IR camera image of the burner with the flame stabilized inside (CH₄/Air, $\phi = 1.15$, $U = 50$ cm/s).

Returning to the reason for poor fitting near the flame, the IR image shows that the hottest spot (near the flame) is nearly 340 °C. Recall from Fig. 4-13 (in chapter 4) that as the wafer temperature approaches 350 °C and higher there is a dramatic reduction in the transmissivity (loss of 50% and higher as compared to room temperature). Therefore it is logical to conclude that the poor fitting near the flame probably occurs due to 1) loss in transmissivity of the wafer and 2) the inability of the least squares to converge uniformly at all wavelengths. However, away from the flame in the pre and post-flame regions, the fitting procedure seems to work well and we get physically reasonable solutions. Figure 5-4 shows the fits at a few select axial locations to illustrate how the least squares approach does not give good solutions near the flame. An attempt to fix this was made by constructing a starting guess from adjacent solutions but this still resulted in poor

matches to the absorption spectra. A possible solution to this problem is proposed in Future Work (Chapter 6).

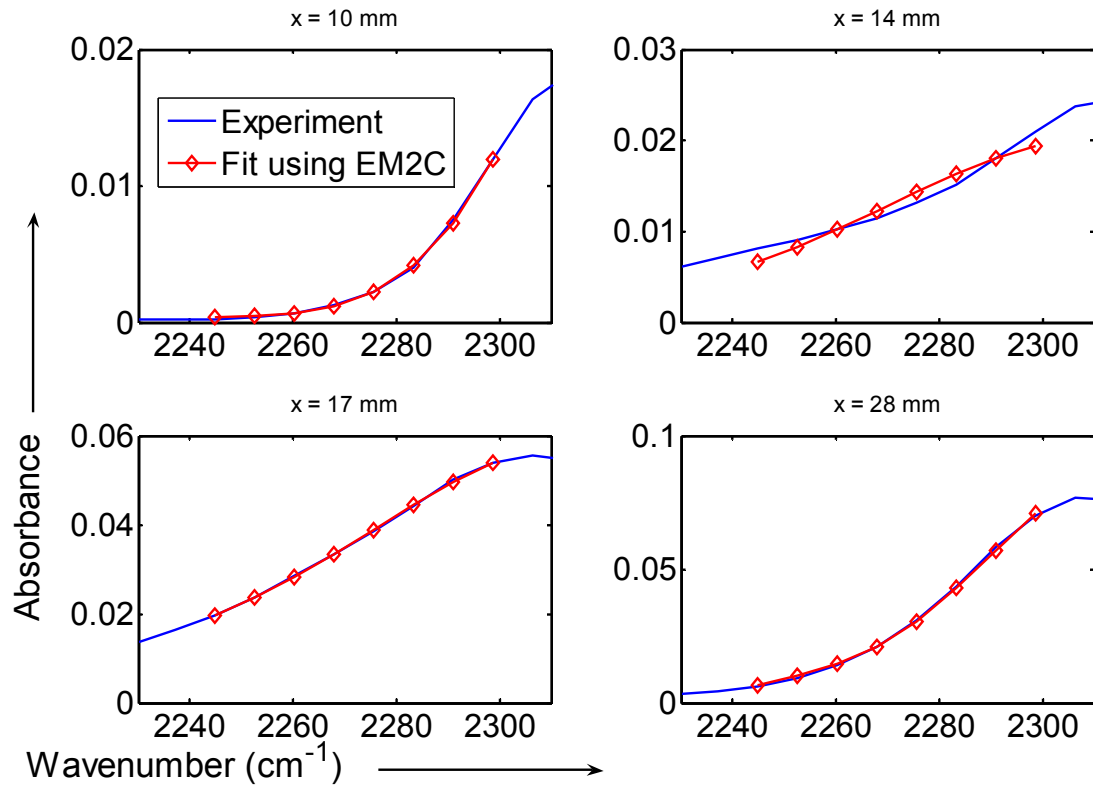


Figure 5-4: Comparison of the fit to the experimental data at different axial locations

The problem with high wafer temperature reducing transmissivity becomes more pronounced in near-stoichiometric flames ($\phi \sim 1$). To see this, consider IR images (Fig. 5-5) of the combustor operating at $\phi = 1$.

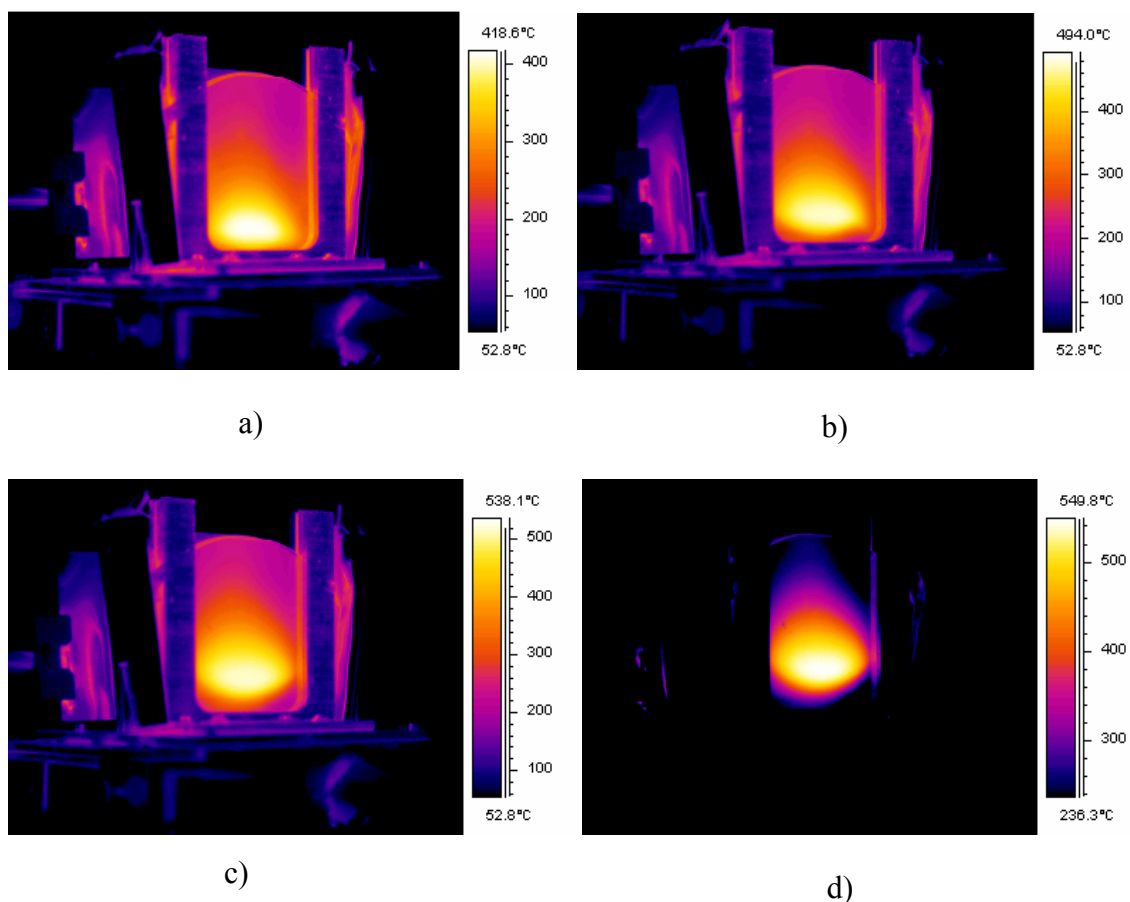


Figure 5-5: IR images of the burner at $\phi = 1.0$ for four different burning velocities:

a) $U = 55$ cm/s; b) $U = 60$ cm/s; c) $U = 65$ cm/s and d) $U = 70$ cm/s

The figure shows that the wafer temperature exceeds 400 °C over an appreciable portion of the interrogation region. To verify that transmission is indeed poor in this region, absorbance is plotted as a function of wavenumber in Figure 5-6 along with an attempted fit made using EM2C. In the figure, $\phi = 1$ at $U = 60$ cm/s. It is clear that the CO₂ band head is completely suppressed leaving only noise. As a corollary, the plot also illustrates that using poor quality data results in a failure of the EM2C function to be able to fit the absorbance data.

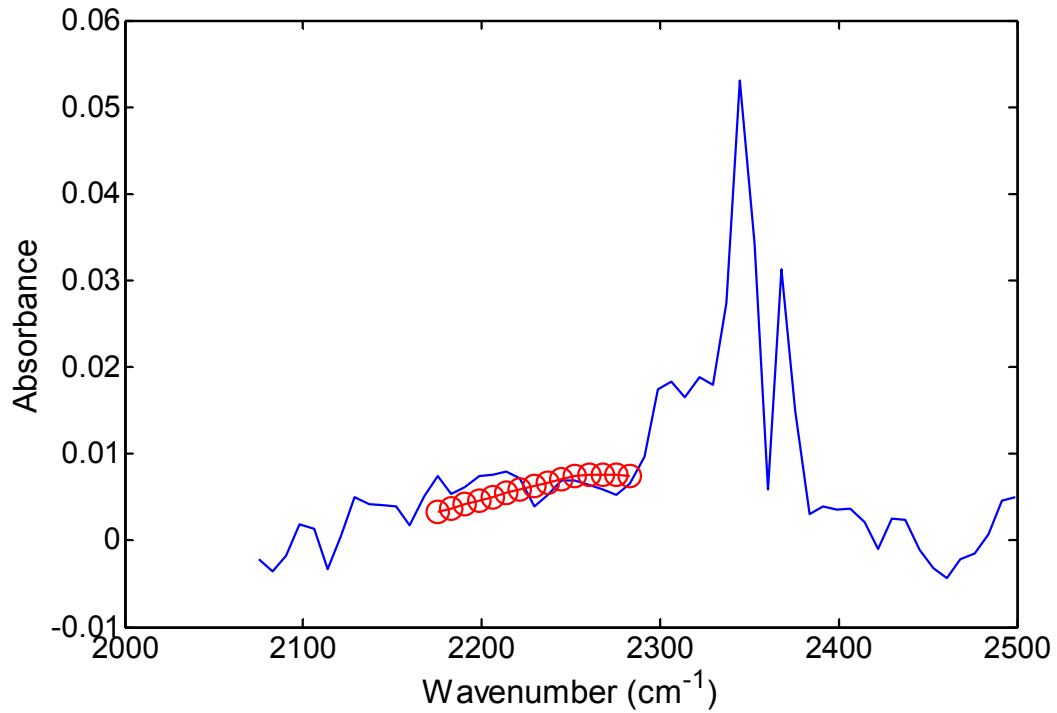


Figure 5-6: Absorbance vs Wavenumber ($\phi = 1.0$, $U = 60$ cm/s)

While the relative opacity of Silicon at high temperatures in the $2200\text{--}2300\text{ cm}^{-1}$ range makes it difficult to get accurate line of sight profiles in the near flame (and some post-flame) points, the diagnostic technique can still be used to make some first order estimates of heat recirculation (as will be described later in §5.2) based on the average temperature (which is a function of the integrated line of sight absorbance only) of the gas in the channel and the pre-flame profiles which have converged correctly.

Figure 5-7 shows a 2-D temperature distribution in the pre-flame and post-flame regions. The power of the technique despite some of its short comings is that enables measurement of temperature in both axial and transverse directions in a very small volume.

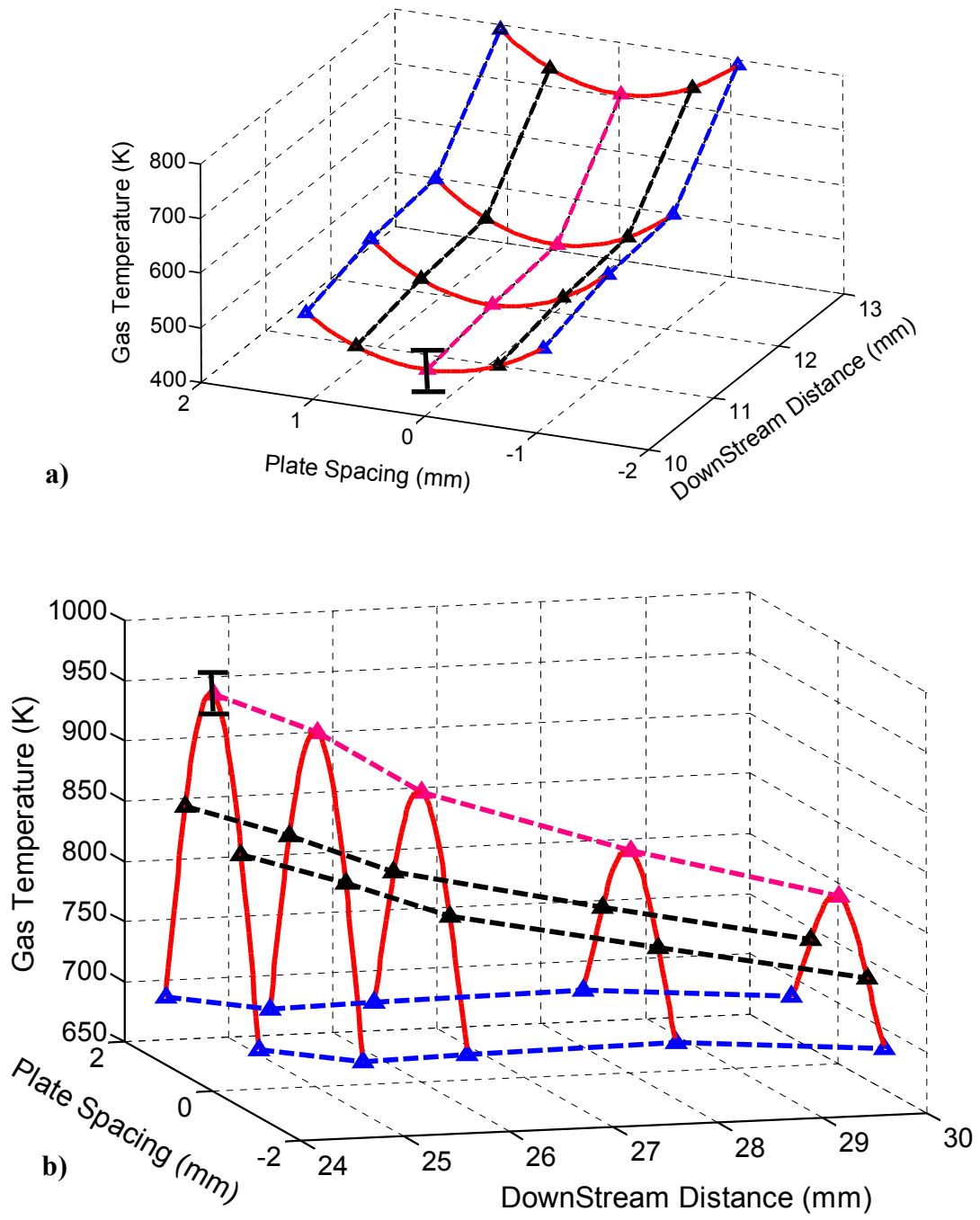


Figure 5-7: 2D temperature distribution in the channel ($\phi = 1.15$, $U = 50$ cm/s)

a) pre-flame region; b) Post-flame region

5.2. Comparisons of Temperature Profiles:

The burner was operated over a range of equivalence ratios and burning velocities for Methane/Air mixtures and a fewer number of Propane/Air mixtures. Table 5-2 shows the matrix of the operating conditions explored.

S. No.	Fuel/Air	Eq. Ratio (ϕ)	U (cm/s)
1	Methane	0.80	40
2	Methane	0.80	45
3	Methane	0.80	50
5	Methane	0.85	40
6	Methane	0.85	45
7	Methane	0.85	50
8	Methane	0.85	55
9	Methane	0.90	55
10	Methane	0.90	60
11	Methane	0.90	65
12	Methane	0.90	70
13	Methane	1.0	60
14	Methane	1.15	50
15	Methane	1.15	55
16	Methane	1.15	60
17	Propane	0.80	50
18	Propane	0.80	55
19	Propane	0.85	55
20	Propane	0.85	60
21	Propane	0.90	65

Table 5-2: Operating conditions for data collection from the burner

Collection of reliable data was not feasible in case 13 for several reasons: 1) The high flow rates needed to push the flame into the zone of interrogation increase the heat

release rate driving the wall temperature above 350 °C as can be seen from Fig. 5-7 b-d. This causes a dramatic drop in transmissivity (refer Fig. 4-13) which drives the absorption signal into the noise. 2) At lower flow rates, (see Fig. 5-7 a) the flame is not far into the channel to make any reliable gas temperature measurements to estimate heat recirculation.

For the purposes of providing a simple comparison between operating conditions, we define the average gas temperature at a given axial location as

$$T_{avg}(x) = \int_0^{2d} U(y) T(x, y) dy \quad (5-1)$$

In this expression, d is the channel half height and $U(y)$ is the fully developed Poiseuille flow velocity profile given by

$$U(y) = \bar{U} \left(2 \frac{y}{d} - \left(\frac{y}{d} \right)^2 \right); \quad 0 \leq y \leq 2d \quad (5-2)$$

Earlier, in § 4.8, it was shown that the velocity profile will always be fully developed in this burner over the region of interrogation. Therefore the use of this velocity profile appears justified

5.2.1. Constant Equivalence Ratio ϕ

i) Methane Plots:

The first comparison we make is between different flow velocities at the same equivalence ratio.

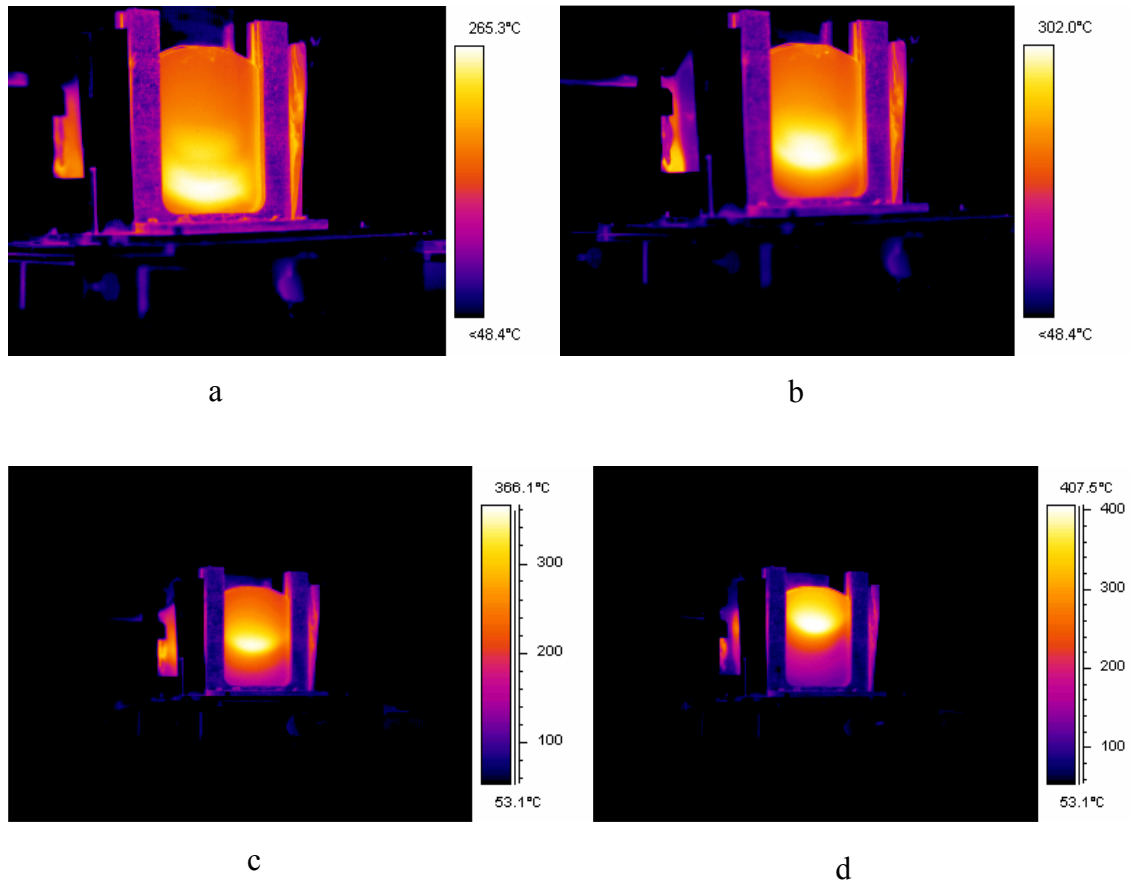


Figure 5-8: IR images of burner at four different flow velocities (CH_4/Air ; $\phi = 0.85$)

a) $U = 40$ cm/s; b) $U = 45$ cm/s; c) $U = 50$ cm/s and d) $U = 55$ cm/s

Figure 5-8 shows IR images of the burner at four different flow velocities at the same equivalence ratio ($\phi = 0.85$) for methane/air. As the flow velocity increases, the outer wafer temperature increases and the flame gets pushed further up into the channel. Notice also that increasing the flow rate increases the fraction of the total wafer area that exceeds 350°C (beyond which we have poor transmissivity). This is because increasing the flow rate increases the total heat release. Figure 5-9 shows the span-averaged gas temperature and outer surface temperature as a function of axial position in the burner for two velocities ($U = 40$ cm/s and $U = 50$ cm/s). As expected, the surface and gas temperatures increase as the flow rate increases. Increasing the flow rate also causes the flame to move

farther downstream. This is because more physical space is required to preheat the mixture to the ignition temperature.

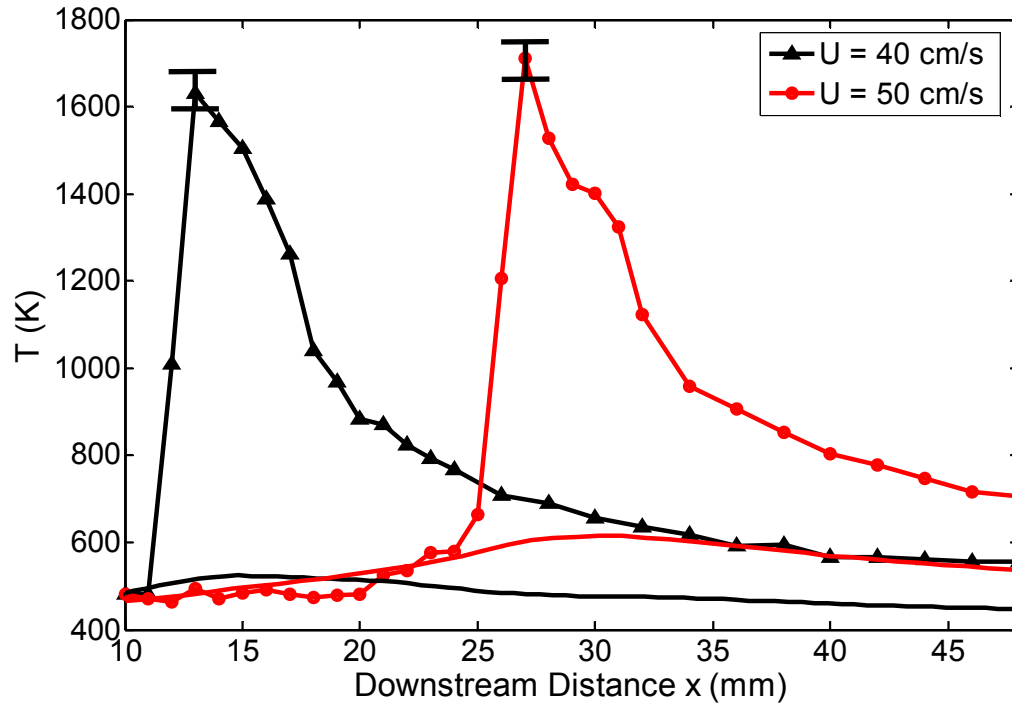


Figure 5-9: Average gas and surface temperatures as a function of x for two different velocities for CH_4/Air flame; $\phi = 0.85$

ii) Propane Plots:

We make comparisons of propane flames at the same equivalence ratio ($\phi = 0.85$) for two flow velocities of 55 and 60 cm/s. Fig 5-10 shows the IR images of the burner operating at the two velocities. Propane flames are more stable than methane flames of the same ϕ and U . This can be seen by comparing the relative distance between the flame and the entrance of the channel in Figs. 5-8 d and 5-10 a. The consequence of this is that as we increase the flow rate, the propane the flames get even hotter than methane (as seen in Fig. 5-10 b) and again we get poor data. This limits the range of exploration for propane flames more severely than for methane flames.

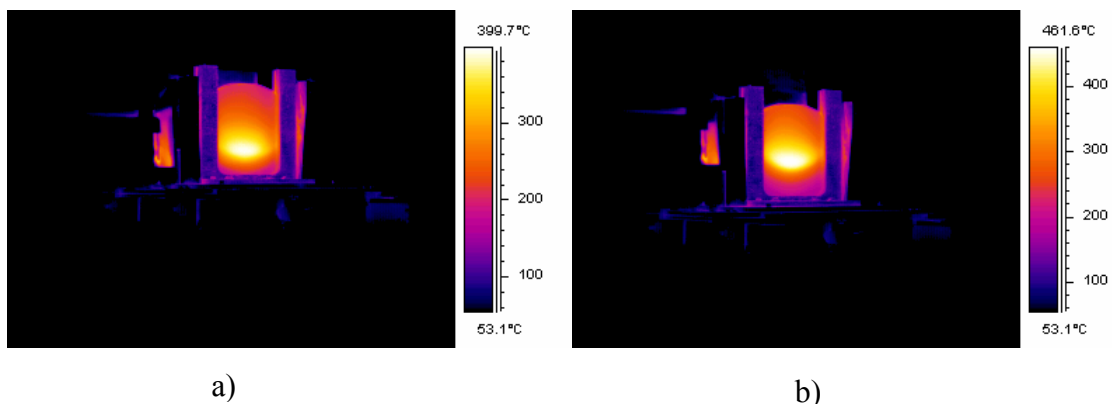


Figure 5-10: IR images of burner at two different burning velocities ($\text{C}_3\text{H}_8/\text{Air}$; $\phi = 0.85$) a) $U = 55 \text{ cm/s}$; b) $U = 60 \text{ cm/s}$

A plot of the average and outer wall temperature reveals trends similar to methane/air flames. As the flow rate increases, the gas and wall temperatures increase and the temperatures rise in the post-flame region. The pre-flame points also have poorer convergence and this leads to some ‘wrinkles’ in the axial temperature profile in the pre-flame. This is primarily because of the higher overall wafer temperatures with propane flames. Absorbance measurements in the pre-flame, where the CO_2 concentrations are much lower than the post-flame ($\sim 1\%$ vs. 6%), are impacted to a greater extent by the loss in transmissivity.

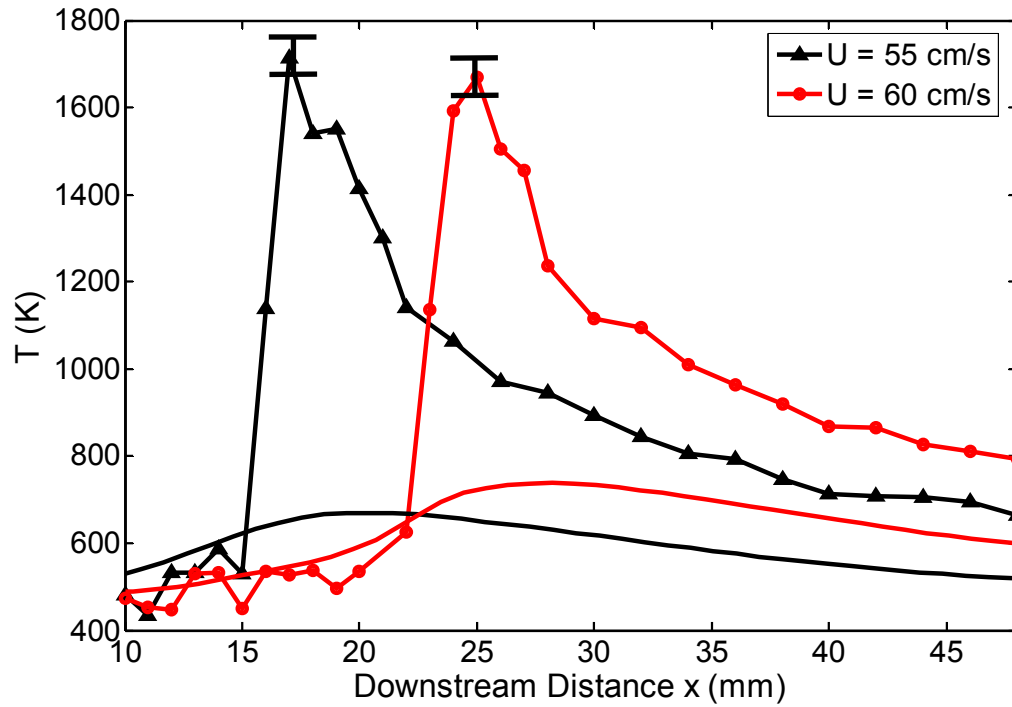


Figure 5-11: Average gas and surface temperatures as a function of x for two different velocities for $\text{C}_3\text{H}_8/\text{Air}$ flame; $\phi = 0.85$

5.3. Heat Recirculation and Flame Speed:

The main aim of the temperature measurements is to use the profiles to estimate the total heat recirculation that occurs in this burner. Fig 5-12 is a sketch of the axial temperature profile showing the zone of optical interrogation and the heat fluxes that we are interested in. It shows that our optical technique does not span the entire space over which heat recirculation occurs although it does span most of it. While the temperature at the start of the zone of interrogation (T_{in}) is already higher than that of the environment, it is still possible to make estimates of the heat recirculation based on what is measured.

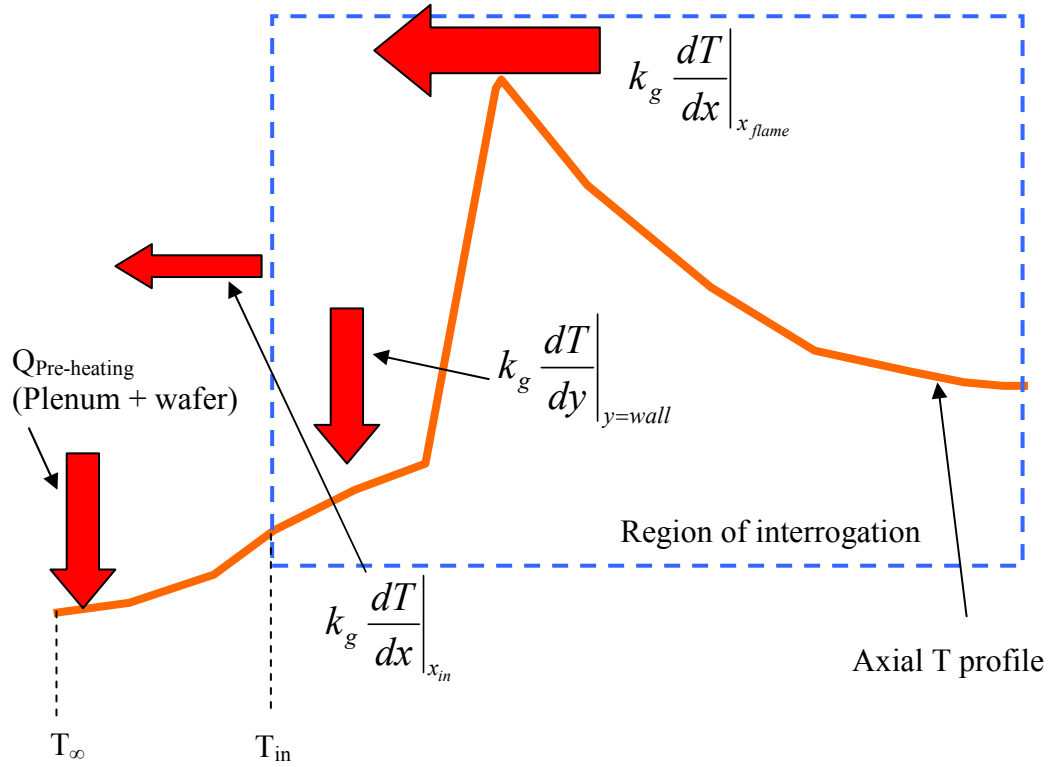


Figure 5-12: Cartoon sketch of heat fluxes used in calculation of heat recirculation in the burner

This is accomplished as follows: An an energy balance on the flow before it reaches the region of interrogation gives:

$$Q_{pre-heating} + k_g A_{channel} \left. \frac{dT}{dx} \right|_{x_{in}} = \dot{m} Cp (T_{in} - T_{\infty}) \quad (5-3)$$

In this expression, T_{in} is the temperature as the flow enters the optical measurement region and T_{∞} is the temperature of the gases entering the apparatus (standard conditions, $T_{\infty} = 298$ K). We get the second term on the left side of Eq. 5-3 and the right side of Eq. 5-3 from the measured temperature profiles. Therefore, the pre-heating can be calculated. From Chapter 3, we recall that total heat recirculation is defined as the sum of

the heat recirculation occurring via gas and wall respectively. The heat recirculation via the wall for our burner is given by:

$$H_{\text{Recirc},\text{wall}} = Q_{\text{pre-heating}} + \int_{x_{\text{in}}}^{x_{\text{flame}}} k_g \left. \frac{dT}{dy} \right|_{\text{wall}} dx \quad (5-4)$$

And, the heat recirculation via the gas is given by:

$$H_{\text{Recirc},\text{wall}} = k_g A_{\text{channel}} \left. \frac{d\bar{T}}{dx} \right|_{x=x_{\text{flame}}} \quad (5-5)$$

From equations 5-4 and 5-5, the total heat recirculation becomes:

$$H_{\text{Recirc},\text{total}} = H_{\text{Recirc},\text{wall}} + H_{\text{Recirc},\text{gas}} \quad (5-6)$$

The total heat recirculation is calculated for each operating condition of the methane/air flames and plotted below in figure 5-13. The red hashed region is the region where data could not be obtained owing to excessive heating of the wafer and subsequent loss of transmitted signal.

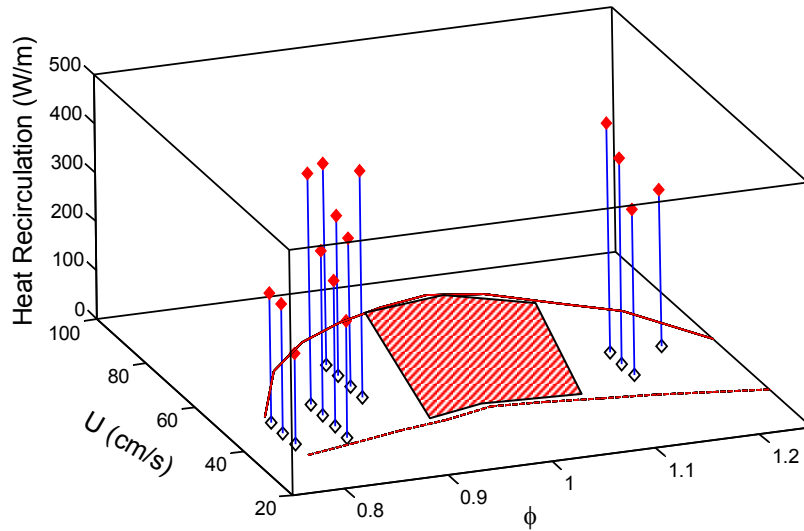


Figure 5-13: Heat Recirculation as a function of ϕ and U for CH_4/Air

The solid curve on the floor of the plot marks the burner's blow-off limit and the dashed marks the flash-back limit. We non-dimensionalize the total heat recirculation by the heat recirculation that would occur in a freely propagating flame (like in Chapter 3) via conduction through the gas. This is given by:

$$H_{Recirc}^* = \frac{H_{Recirc,total}}{\rho S_{L,free} Cp(T_{ad} - T_{\infty})d} \quad (5-7)$$

This definition enables us to plot the non-dimensional heat recirculation as a function of the non-dimensional flame speed for the experiment and compare to the predictions of the analytical model. In order to do this, however, recall that the analytical model contains Pe_{free} that needs to be selected in order to make the comparison. Pe_{free} depends upon the freely propagating flame speed and a characteristic gas temperature (which sets the density, thermal conductivity, etc.). The flame speed and the characteristic gas temperature should be functions of equivalence ratio. Table 5-3 gives $S_{L,free}$, the corresponding adiabatic flame temperature (calculated using CHEMKIN) and Pe_{free} for freely propagating flames for several characteristic gas temperatures over the range of equivalence ratios used for data collection in the burner.

S. No	ϕ	$S_{L,free}$ (cm/s)	T_{ad} (K)	$P_{e,free}$ (T = 300 K)	$P_{e,free}$ (T = 1200 K)	$P_{e,free}$ (T = 1500 K)
1	0.8	29.33	1863	12.63	4.00	3.49
2	0.85	33.53	1917	14.44	4.58	3.99
3	0.9	35.64	1955	15.35	4.87	4.25
4	1.15	40.71	2021	17.54	5.56	4.85
5	1.2	38.84	2011	16.73	5.30	4.63

Table 5-3: Parameters for freely propagating conditions

The table shows that Pe_{free} depends more strongly on the temperature used to evaluate it than the equivalence ratio.

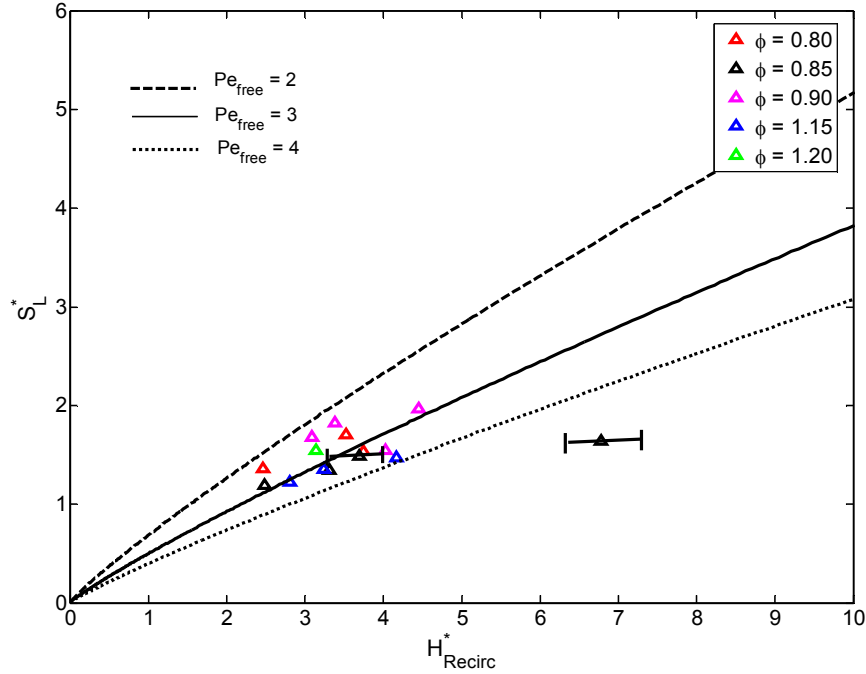


Figure 5-14: Comparison between model and experiments of non-D heat recirculation as a function of S_L^*

Figure 5-14 compares the non-dimensional flame speed and heat recirculation measured in the burner to the model predictions for a few Pe_{free} values. The figure experimental data are clustered together in a small range of non-dimensional flame speeds between 1 and 2 which makes it somewhat difficult to draw broad conclusions but it appears that a Pe_{free} of around 3 correlates most of the points within the experimental uncertainty. While the experimental uncertainty is relatively large, the measurements confirm the fundamental prediction of the model which is that flame speed is proportional to the degree of heat recirculation.

Chapter 6: Findings and Future Work

6.1. Key Contributions:

This dissertation has investigated the influence of structural heat conduction on flame speed and stabilization in microscale combustors. First, analytical models were developed for the heat transfer problem of a laminar flame stabilized in a channel with increasing degrees of complexity that started with a constant temperature wall, added conjugate heat transfer, and finally added the species transport equations to the conjugate heat transfer model. In this last step, the flame speed became an eigenvalue controlled by the design parameters of the combustor. Second, a non-intrusive diagnostic technique based on FT-IR spectroscopy was improved to enable measurement of temperature profiles along line of sight. This new tool was used to obtain 2-D gas temperature profiles inside a simulated microcombustor that, in turn, were used to validate the model's predictions. The key findings and contributions that have resulted from combined analytical and experimental approach are summarized below.

1. Three new analytical models of increasing complexity were developed for the stabilization of a flame in a micro-channel. In all cases, the flame was represented as an infinitesimal sheet of heat release and both plug and Poiseuille flows were considered. The models in increasing order of complexity are:
 - a. Constant wall temperature, no species equation
 - b. Conjugate heat transfer and heat loss to environment, no species equation
 - c. Conjugate heat transfer, heat loss to environment, and species equation.

2. The analytical models confirmed several aspects of micro-scale combustion that were known already. First, heat recirculation from the post-flame to the pre-flame through the structure increases burning velocity beyond the freely propagating flame speed and enhances flame stabilization. Second, the flame will quench if too much heat is lost to the environment. Third, multiple flame speeds are possible but only the solutions corresponding to enhanced flame speeds are stable.
3. The model has extended our understanding of micro-scale combustion in several important ways. First, the three principal design parameters governing flame stabilization in micro-combustors are identified: The structure to gas thermal conductivity ratio (κ), the flow passage half height to wall thickness ratio (τ), and the Nusselt number for heat loss to the environment (Nu_e). Second, the net heat recirculation from the post-flame to the pre-flame is the main physical process responsible for flame stabilization. Changes in the three design parameters and even the fuel are important only to the extent that they alter the net heat recirculation. Changing the design in a way that increases heat recirculation increases flame speed. Third, the model shows that the velocity profile influences the shape of the temperature distribution across the channel. Near the flame, the competition between the convective and diffusive terms causes the peak temperature to occur on either side of the passage center line. While previous work attributes these off-center peaks in temperature to flow straining, the models developed here indicate that their origin is at least partly thermal.
4. The analytical model was used to show that heat recirculation enables micro-scale chemical thrusters to achieve higher thrust/weight than conventional thrusters.

5. Transverse temperature profiles in micro-combustors are well represented using power laws.
6. Key improvements were made to a novel non-intrusive diagnostic technique for measuring temperature and chemical composition in micro-combustors. The technique was extended to permit measurement of temperature along a line of sight and a comprehensive uncertainty analysis was presented.
7. The key limitations of this non-intrusive technique were also identified. These include the need for a good initial estimate of the temperature profile and the unsuitability of the least-squares approach to spectral fitting.
8. The diagnostic technique was used to measure net heat recirculation in a simulated micro-combustor. These measurements confirm the model prediction that the flame speed is a linear function of heat recirculation.

6.2. Future Work:

This dissertation has advanced the understanding of the main processes responsible for flame stabilization in narrow channels and has successfully shown the impact of heat recirculation through the wall of the combustor on the flame speed. However, much more work is needed to suitably model and make measurements of the combustion process in small scale combustors.

First, the current analytical model applies to an infinitely long channel whereas, real combustors have finite lengths. Therefore, a new model incorporating finite length effects would be more capable of predicting the flame speeds more accurately. The temperature profiles from the model could also serve as a guide for fitting routines that make line of sight measurements.

Second, the techniques used to fit the spectra have been shown to be deficient. A new fitting procedure based on a genetic algorithm that would fit each and every wavenumber point may reduce or eliminate these problems.

Third, the one-step reaction model in the current work could be replaced with a multi-step model. While it would result in more computational expense, it would give more detailed information on the combustion process in the narrow channels and could serve as a tool to verify the accuracy of using one step models.

Fourth and finally, the utility of the diagnostic technique would be greatly improved by replacing the current system of mirrors and masks with optical fibers.

Appendix A: Solution and Eigenequation

The solution procedure involves separating variables in the two coordinate directions x^+ and y^+ . Thus,

$$\theta_{g,s}(x^+, y^+) = X_{g,s}(x^+) Y_{g,s}(y^+) \quad (\text{A-1})$$

Inserting this into the energy equation for the gas leads to

$$\frac{-(X_g'' - Pe U^+(y^+) X_g')}{X_g} = \frac{Y_g''}{Y_g} \quad (\text{A-2})$$

At first glance it appears that separation of variables has not worked! However, taking note of the fact that most combustion/heat transfer problems in pipe or channel flows have an exponential solution for the x^+ variable, we make the following substitution:

$$\frac{X_g'}{X_g} = \pm \alpha \quad (\text{A-3})$$

The choice of the plus or minus is based on whether we are interested in pre-flame or post-flame solutions. In all cases the non-dimensional temperature must become zero at the extremities. Substituting eq. A-3 into eq. A-2 and rewriting gives

$$Y_g'' + (\alpha^2 \mp \alpha Pe U^+(y^+)) Y_g = 0 \quad (\text{A-4})$$

Eq. A-4 is an ODE that can be solved after a transformation of variables. It has a general solution of the form

$$Y_g(\alpha, y^+) = (C Y_{g,1}(\alpha, y^+) + D Y_{g,2}(\alpha, y^+)) \quad (\text{A-5})$$

where

$$Y_{g,1}(y^+) = \text{Hypergeometric1F1}(\alpha, y^+) e^{p y^{+2}} \text{ or } \text{Cos}(\alpha, y^+) \quad (\text{A-6a})$$

$$Y_{g,2}(y^+) = \text{HermiteH}(\alpha, y^+) e^{p y^{+2}} \text{ or } \text{Sin}(\alpha, y^+) \quad (\text{A-6b})$$

The choice of the solution depends on whether we solve for the case of *Hagen-Poiseuille* flow or slug flow.

Next, we consider the boundary and interface conditions along the transverse (y^+) direction in order to relate the gas and structure solutions. Applying eq. 2-6b (symmetry condition) to eq. A-1 gives:

$$Y'_g(0) = 0 \quad (\text{A-10})$$

This gives

$$Y'_g(0) = (C Y'_{g,1}(\alpha, y^+) + D Y'_{g,2}(\alpha, y^+)) = 0 \quad (\text{A-11})$$

and leads to

$$D Y'_{g,2}(\alpha, 0) = 0 \quad \text{or} \quad D = 0 \quad (\text{A-12})$$

since

$$Y'_{g,1}(\alpha, 0) = 0 \quad \text{and} \quad Y'_{g,2}(\alpha, 0) \neq 0 \quad (\text{A-13})$$

The $Y_{g,2}$ function, fails to satisfy eq. A-10 and hence it is not admissible as a solution. This is a property of that particular function in itself namely the *Sine* or the *HermiteH* function. Therefore, the $Y_{g,1}$ (which satisfies eq. A-10) is the only solution, either the *Hypergeometric* or Cosine function. At this point we do not know what these eigenvalues (α 's) are but we explain how these are obtained shortly.

Isothermal Wall (Constant Wall Temperature):

For the case of constant wall temperature demanding that the Y_1 function satisfy eq. 2-11c (the other boundary condition at the wall) allows us to obtain the eigenvalues α_n i.e.

$$Y_1(\alpha_n, 1) = 0 \quad (\text{A-14})$$

Obtaining the eigenvalues (α_n) in the case of Plug flow is easier as the roots of the *Cosine* function are well known. However, in the case of Hagen-Poiseuille flow the eigenvalues (α_n) have to be determined numerically because the roots of the *Hypergeometric1F1* function do not have a closed form.

Conducting Walls (Conjugate Heat Transfer):

For the case of conjugate heat transfer, we cannot obtain the eigenvalues at the gas-wall interface as we allow for heat transfer through the wall. Before, we attempt to solve for the energy equation of the wall we would like to assert that the $X(x^+)$ functions for the gas and structure solutions are linearly dependent on each other. This is necessary to match structure temperature and heat flux at the wall. Therefore for simplicity (and without loss of generality) we assume that the $X(x^+)$ is the same for both gas and structure i.e.

$$X_g(x^+) = X_s(x^+) \quad (\text{A-15})$$

Hence, when we separate variables for the structure's energy equation we write it as

$$\frac{X_s''}{X_s} + \frac{Y_s''}{Y_s} = 0 \quad \text{or} \quad Y_s'' + \alpha^2 Y_s = 0 \quad (\text{A-16})$$

Eq. A-16 has solutions of the form

$$Y_s(\alpha, y^+) = E Y_{s,1}(\alpha, y^+) + F Y_{s,2}(\alpha, y^+) \quad (\text{A-17 a})$$

where

$$Y_{s,1} = \cos(\alpha y^+) \quad (\text{A-17 b})$$

$$Y_{s,2} = \sin(\alpha y^+) \quad (\text{A-17 c})$$

The temperature and heat flux match at the gas-structure interface gives (keeping eq. A-15 in mind):

$$Y_g(\alpha, 1) = Y_s(\alpha, 1) \quad (\text{A-18 a})$$

or

$$C Y_{g,1}(\alpha, 1) = E Y_{s,1}(\alpha, 1) + F Y_{s,2}(\alpha, 1) \quad (\text{A-18 b})$$

and

$$Y'_g(\alpha, 1) = \kappa Y'_s(\alpha, 1) \quad (\text{A-18 c})$$

or

$$C Y'_{g,1}(\alpha, 1) = \kappa (E Y'_{s,1}(\alpha, 1) + F Y'_{s,2}(\alpha, 1)) \quad (\text{A-18 d})$$

Solving eqs. A-18 b and d as a system of linear equation relates the constants E and F to C . The link between the temperature fields in the structure and gas arises through the relationship of E and F to C and also because the $X(x^+)$ functions are matched. Finally, we invoke the last boundary condition (eq. 2-28d) for the heat loss to the environment from the outer surface of the wall. The resulting equation is termed the “eigenvalue equation”

$$-Y'_s(\alpha, \tau) = \frac{Nu_E Y_s(\alpha, \tau)}{\kappa} \quad (\text{A-19})$$

The only unknown in eq. A-19 is the eigenvalue (α). The linear relationship between the constants E and F in the structure's solution to the constant C of the gas phase solution ensures that the above equation (after rearrangement) is a multiple of a function of α and C . The eigenvalues of the problem are all values of α that satisfy eq. A-19 and do not correspond to $C=0$, (the trivial solution to the PDE where the temperature is zero everywhere). Each eigenvalue has a corresponding eigenfunction (Y) each of which satisfies the ODE. Consequently, the linear combination of all these functions is the final solution to the PDE.

Appendix B: Orthogonality Condition

In order to obtain an orthogonality condition we go back to the ODE eqn for Y and write it out for two different eigenvalues as follows.

$$Y''_{g,m} + (\alpha_m^2 \mp \alpha_m Pe U^+(y^+)) Y_{g,m} = 0 \quad (\text{B-1 a})$$

$$Y''_{g,n} + (\alpha_n^2 \mp \alpha_n Pe U^+(y^+)) Y_{g,n} = 0 \quad (\text{B-1 b})$$

multiply the first equation by Y_n and second equation by Y_m and subtract one from the

other and integrate between 0 and 1 to obtain, i.e. $\int_0^1 eq.B-l a \times Y_{g,n} - eq.B-l b \times Y_{g,m} dy^+$

$$\int_0^1 (Y''_{g,m} Y_{g,n} - Y''_{g,n} Y_{g,m}) dy^+ + \int_0^1 (\alpha_m^2 - \alpha_n^2 \mp (\alpha_m - \alpha_n) Pe U^+(y^+)) Y_{g,m} Y_{g,n} dy^+ = 0 \quad (\text{B-2})$$

The first integral can be integrated by parts. This gives

$$(Y'_{g,m} Y_{g,n} - Y'_{g,n} Y_{g,m}) \Big|_0^1 + (\alpha_m - \alpha_n) \int_0^1 (\alpha_m + \alpha_n \mp Pe U^+(y^+)) Y_{g,m} Y_{g,n} dy^+ = 0 \quad (\text{B-3})$$

Now we can invoke the boundary condition at the centerline (eq. A-10) to further simplify eq. B-3 as

$$(Y'_{g,m} Y_{g,n} - Y'_{g,n} Y_{g,m}) \Big|_1 + (\alpha_m - \alpha_n) \int_0^1 (\alpha_m + \alpha_n \mp Pe U^+(y^+)) Y_{g,m} Y_{g,n} dy^+ = 0 \quad (\text{B-4})$$

Isothermal Wall (Constant Wall Temperature)

In the simple case of a constant wall temperature the first term in eq. B-4 vanishes owing to the boundary condition (eq. A-14 in Appendix A). This gives the orthogonality condition as

$$\int_0^1 (\alpha_m + \alpha_n \mp Pe U^+(y^+)) Y_{g,m} Y_{g,n} dy^+ = 0 \quad (B-5)$$

Conjugate Heat Transfer:

Revisiting eq. B-4, we can use the relationship between the Y functions of the structure and gas owing to the interface conditions eqs. A-18 a and c and rewrite eq. B-4 as

$$\kappa (Y'_{s,m} Y_{s,n} - Y'_{s,n} Y_{s,m}) \Big|_1 + (\alpha_m - \alpha_n) \int_0^1 (\alpha_m + \alpha_n \mp Pe U^+(y^+)) Y_{g,m} Y_{g,n} dy^+ = 0 \quad (B-6)$$

In order to replace the first term in the equation eq B-6 with an integral we look at the ODE for the structure (eq. A-16) and write it out for two different eigenvalues.

$$Y''_{s,m} + \alpha_m^2 Y_{s,m} = 0 \quad (B-7 \text{ a})$$

$$Y''_{s,n} + \alpha_n^2 Y_{s,n} = 0 \quad (B-7 \text{ b})$$

Applying similar manipulations to the above two equations as done earlier we can get

$$\int_1^\tau (Y''_{s,m} Y_{s,n} - Y''_{s,n} Y_{s,m}) dy^+ + \int_1^\tau (\alpha_m^2 - \alpha_n^2) Y_{s,m} Y_{s,n} dy^+ = 0 \quad (B-8)$$

Again the first term may be integrated by parts to give

$$\begin{aligned} & (Y'_{s,m} Y_{s,n} - Y'_{s,n} Y_{s,m}) \Big|_1^\tau + \int_1^\tau (\alpha_m^2 - \alpha_n^2) Y_{s,m} Y_{s,n} dy^+ \\ &= - (Y'_{s,m} Y_{s,n} - Y'_{s,n} Y_{s,m}) \Big|_1 + \int_1^\tau (\alpha_m^2 - \alpha_n^2) Y_{s,m} Y_{s,n} dy^+ = 0 \end{aligned} \quad (B-9)$$

Where we have made use of the outer wall boundary condition (eq. A-19) and simplified.

Using the result from eq. B-9 in eq. B-5 gives rise to the final orthogonality equation as

$$\int_0^1 (\alpha_m + \alpha_n \mp Pe U^+(y^+)) Y_{g,m} Y_{g,n} dy^+ + \kappa \int_1^\tau (\alpha_m + \alpha_n) Y_{s,m} Y_{s,n} dy^+ = 0 \quad (B-10)$$

Note that this orthogonality condition is different from a typical Sturm-Liouville type orthogonality. This is because the ODE's for the Y equations have the eigenvalues mixed up in a non-linear fashion and does not follow the Sturm-Liouville pattern. It is useful to also note that the form of eq. B-10 suggests what we are attempting in these problems. The integration first occurs in the gas phase in the domain of operation of the gas temperature solution (between 0 and 1) links up with the structure's solution at the interface ($y^+ = 1$) and integrates from there on to the outer wall. We also see the presence of the ratio of wall thermal conductivities (κ) multiplying the structure's part. Thus, we can see how the thermal coupling phenomenon is expressing itself mathematically in these equations and leads to the physical implications seen in the results section.

Appendix C: Evaluation of Coefficients

Isothermal Wall:

Substituting eq. 2-13 (see Chapter 2) into the *jump conditions* (eqs. 2-6 a and 2-6 c) evaluated at the flame ($x^+=0$) leads to:

$$\sum_{m=1}^{\infty} B_m \psi_m = \sum_{m=1}^{\infty} A_m \phi_m \quad (\text{C-1})$$

$$\sum_{m=1}^{\infty} A_m \lambda_m \phi_m + \sum_{m=1}^{\infty} B_m \beta_m \psi_m = 1 \quad (\text{C-2})$$

The derivation for the closed form expression for the coefficients starts with performing the following manipulations in order to isolate A_n :

$$\int_0^1 (eq.C - 2) \times (-PeU^+(y^+) + \lambda_n) \phi_n dy^+ \quad (\text{C-3})$$

This leads to:

$$\begin{aligned} & \int_0^1 \sum_{m=1}^{\infty} B_m (-PeU^+(y^+) + \lambda_n) \phi_n \psi_m dy^+ \\ &= A_n \int_0^1 (-PeU^+(y^+) + \lambda_n) \phi_n^2 dy^+ + \sum_{\substack{m=1 \\ m \neq n}}^{\infty} \int_0^1 A_m (-PeU^+(y^+) + \lambda_n) \phi_n \phi_m dy^+ \end{aligned} \quad (\text{C-4})$$

The second term on the right hand side can easily be identified as being part of the orthogonality condition (for the pre-flame). Therefore, we can use eq. B-5 to rewrite eq. C-4 as follows:

$$\begin{aligned} & \int_0^1 \sum_{m=1}^{\infty} B_m (-PeU^+(y^+) + \lambda_n) \phi_n \psi_m dy^+ \\ &= A_n \int_0^1 (-PeU^+(y^+) + \lambda_n) \phi_n^2 dy^+ + \int_0^1 \sum_{\substack{m=1 \\ m \neq n}}^{\infty} (-A_m \lambda_m \phi_n \phi_m) dy^+ \end{aligned} \quad (\text{C-5})$$

Simplifying the sum on the RHS gives:

$$\begin{aligned} & \int_0^1 \sum_{m=1}^{\infty} B_m \left(-PeU^+(y^+) + \lambda_n \right) \phi_n \psi_m dy^+ \\ &= A_n \int_0^1 \left(-PeU^+(y^+) + 2\lambda_n \right) \phi_n^2 dy^+ + \int_0^1 \sum_{m=1}^{\infty} \left(-A_m \lambda_m \phi_n \phi_m \right) dy^+ \end{aligned} \quad (C-6)$$

Now we use the second jump condition and do the following manipulation:

$$\int_0^1 (eq.C-1) \times \phi_n dy^+ \quad (C-7)$$

This gives:

$$\int_0^1 \sum_{m=1}^{\infty} A_m \lambda_m \phi_m \phi_n dy^+ = \int_0^1 \phi_n dy^+ - \int_0^1 \sum_{m=1}^{\infty} B_m \beta_m \psi_m \phi_n dy^+ \quad (C-8)$$

The fact that we have this naturally occurring “jump” condition in terms of the derivative of the temperature across the flame enables us to accommodate the non-linearity of the eigenvalue in the ODE for Y . Inserting eq. C-4 into eq. C-6 and rearranging gives:

$$\begin{aligned} & A_n \int_0^1 \left(-PeU^+(y^+) + 2\lambda_n \right) \phi_n^2 dy^+ \\ &= \int_0^1 \phi_n dy^+ + \sum_{m=1}^{\infty} B_m \int_0^1 \left(-PeU^+(y^+) + \lambda_n - \beta_m \right) \phi_n \psi_m dy^+ \end{aligned} \quad (C-9)$$

The term multiplying A_n on the left hand side of eq. C-9 can be evaluated as can the first term on the right hand side. The second term on the right hand side looks messy as it couples the eigenfunctions and eigenvalues from the pre and post flame regions in a complex fashion. However, if we consider the ODEs for the Y function in the pre and post-flame regions

$$\phi_n'' + (\lambda_n^2 - \lambda_n PeU^+(y^+)) \phi_n = 0 \quad (C-10)$$

$$\psi_m'' + (\beta_m^2 + \beta_m PeU^+(y^+)) \psi_m = 0 \quad (C-11)$$

Following the same approach used to derive the orthogonality condition, we compute the following

$$\int_0^l ((eq.C-10) \times \psi_m - (eq.C-11) \times \phi_n) dy^+ \quad (C-12)$$

This leads to:

$$\int_0^l (\phi_n'' \psi_m - \phi_n \psi_m'') dy^+ + (\lambda_n + \beta_m) \int_0^l (-PeU^+(y^+) + \lambda_n - \beta_m) \phi_n \psi_m dy^+ = 0 \quad (C-13)$$

Again because of the boundary conditions (eq. 2-10 and 2-11), the first integral (after integration by parts) can be easily shown to be zero. This means the second integral is also zero (as both λ and β are positive numbers). Using this result in eq. C-9 we obtain A_n (eq. 2-14 in Chapter 2). B_n is obtained by similar algebraic manipulations.

Conjugate Heat Transfer:

The “jump conditions” (eqs. 2-31 a, b and 2-32 a, b from the main text) and the orthogonality condition developed in the previous section are used to get analytical closed form expressions for the coefficients A_n and B_n . Substituting eqs. 2-33 and 2-34 into eqs. 2-31 a, b and 2-32 a, b leads to

$$\sum_{m=1}^{\infty} A_m \phi_{g,m} = \sum_{m=1}^{\infty} B_m \psi_{g,m} \quad (C-14 a)$$

$$\sum_{m=1}^{\infty} A_m \lambda_m \phi_{g,m} + \sum_{m=1}^{\infty} B_m \beta_m \psi_{g,m} = 1 \quad (C-14 b)$$

$$\sum_{m=1}^{\infty} A_m \phi_{s,m} = \sum_{m=1}^{\infty} B_m \psi_{s,m} \quad (C-15 a)$$

$$\sum_{m=1}^{\infty} A_m \lambda_m \phi_{s,m} + \sum_{m=1}^{\infty} B_m \beta_m \psi_{s,m} = 0 \quad (C-15 b)$$

Starting with $\int_0^l eq.C-14a \times (-PeU(y^+) + \lambda_n) \phi_{g,n} dy^+$ gives:

$$\begin{aligned}
& A_n \int_0^1 (-PeU^+(y^+) + \lambda_n) \phi_{g,n}^2 dy^+ + \int_0^1 \sum_{\substack{m=1 \\ m \neq n}}^{\infty} A_m (-PeU^+(y^+) + \lambda_n) \phi_{g,m} \phi_{g,n} dy^+ \\
& = \int_0^1 \sum_{m=1}^{\infty} B_m (-PeU(y^+) + \lambda_n) \psi_{g,m} \phi_{g,n} dy^+
\end{aligned} \tag{C-16}$$

Rewriting the second term on the left hand side using the orthogonality condition developed in the previous section (eq. B-10) and then adding the missing term in the summation transforms eq. C-16 to:

$$\begin{aligned}
& A_n \left(\int_0^1 (-PeU^+(y^+) + 2\lambda_n) \phi_{g,n}^2 dy^+ + 2\lambda_n \kappa \int_1^{\tau} \phi_{s,n}^2 dy^+ \right) \\
& - \int_0^1 \sum_{m=1}^{\infty} A_m \lambda_m \phi_{g,m} \phi_{g,n} dy^+ - \kappa \int_1^{\tau} \sum_{m=1}^{\infty} A_m (\lambda_m + \lambda_n) \phi_{s,m} \phi_{s,n} dy^+ \\
& = \int_0^1 \sum_{m=1}^{\infty} B_m (-PeU(y^+) + \lambda_n) \psi_{g,m} \phi_{g,n} dy^+
\end{aligned} \tag{C-17}$$

Once we have eq. C-17, the next set of algebraic steps becomes obvious: We need to rewrite the terms in the second line of the LHS. From a cursory inspection of the remaining “*jump conditions*” we can see that we need the following steps.

First $\int_0^1 eq.C - 14b \times \phi_{g,n} dy^+$ gives

$$\int_0^1 \sum_{m=1}^{\infty} A_m \lambda_m \phi_{g,m} \phi_{g,n} dy^+ = \int_0^1 \phi_{g,n} dy^+ - \int_0^1 \sum_{m=1}^{\infty} B_m \beta_m \psi_{g,m} \phi_{g,n} dy^+ \tag{C-18 a}$$

Then $\int_1^{\tau} eq.C - 15b \times \phi_{s,n} dy^+$ gives

$$\int_1^{\tau} \sum_{m=1}^{\infty} A_m \lambda_m \phi_{s,m} \phi_{s,n} dy^+ = - \int_1^{\tau} \sum_{m=1}^{\infty} B_m \beta_m \psi_{s,m} \phi_{s,n} dy^+ \tag{C-18 b}$$

and $\int_1^{\tau} eq.C - 15a \times \phi_{s,n} dy^+$ gives

$$\int_1^{\tau} \sum_{m=1}^{\infty} A_m \phi_{s,m} \phi_{s,n} dy^+ = \int_1^{\tau} \sum_{m=1}^{\infty} B_m \psi_{s,m} \phi_{s,n} dy^+ \quad (\text{C-18 c})$$

Using eqs. C-18 a-c in eq. C-17 and rearranging gives

$$\begin{aligned} & A_n \left(\int_0^1 (-PeU^+(y^+) + 2\lambda_n) \phi_{g,n}^2 dy^+ + \int_1^{\tau} 2\lambda_n \kappa \phi_{s,n}^2 dy^+ \right) - \int_0^1 \phi_{g,n} dy^+ \\ &= \int_0^1 \sum_{m=1}^{\infty} B_m (-PeU(y^+) + \lambda_n - \beta_m) \psi_{g,m} \phi_{g,n} dy^+ - \kappa \left(\int_1^{\tau} \sum_{m=1}^{\infty} B_m (\beta_m - \lambda_n) \psi_{s,m} \phi_{s,n} dy^+ \right) \end{aligned} \quad (\text{C-19})$$

Inspecting eq. C-19 we find that we can evaluate all the integrals on the LHS once we know the eigenvalues and eigenfunctions. Therefore, if we are able to simplify the RHS to known quantities we will be able to express the coefficient A_n in terms of known quantities. Before embarking on the manipulations it is useful to note that the term on the RHS has a form similar to the orthogonality condition developed in the previous section except that in the orthogonality condition we were either in the pre-flame and post-flame region only (as decided by the minus or plus in the equation) whereas here the pre-flame and post-flame functions and eigenvalues are mixed together. We look for the simplification of the term on the RHS by doing the following: Start by writing the ODEs for the gas phase in y^+ for the post-flame and pre-flame regions:

$$\psi_{g,m}'' + (\beta_m^2 + \beta_m PeU^+(y^+)) \psi_{g,m} = 0 \quad (\text{C-20 a})$$

$$\phi_{g,n}'' + (\lambda_n^2 - \lambda_n PeU^+(y^+)) \phi_{g,n} = 0 \quad (\text{C-21 b})$$

Then, take $\int_0^1 (eq. C-20a \times \phi_{g,n} - eq. C-21b \times \psi_{g,m}) dy^+$ to get

$$\int_0^1 (\psi_{g,m}'' \phi_{g,n} - \phi_{g,n}'' \psi_{g,m}) dy^+ + \int_0^1 (\beta_m^2 - \lambda_n^2 + (\beta_m + \lambda_n) PeU^+(y^+)) \psi_{g,m} \phi_{g,n} dy^+ = 0 \quad (\text{C-22})$$

This can be further written, after integrating the first term by parts, applying the boundary condition at the centerline on the eigenfunctions, and using the gas-structure interface conditions, as

$$-\kappa(\psi'_{s,m}\phi_{s,n} - \phi'_{s,n}\psi_{s,m})\Big|_{y^+=1} + (\beta_m + \lambda_n) \int_0^1 ((\lambda_n - \beta_m) - PeU^+(y^+)) \psi_{g,m}\phi_{g,n} dy^+ = 0 \quad (C-23)$$

Writing out the structure's ODE in a similar fashion

$$\psi''_{s,m} + \beta_m^2 \psi_{s,m} = 0 \quad (C-24 \text{ a})$$

$$\phi''_{s,n} + \lambda_n^2 \phi_{s,n} = 0 \quad (C-24 \text{ b})$$

and performing similar manipulations, (i.e. $\int_1^\tau (eq.C - 24a \times \phi_{s,n} - eq.C - 24b \times \psi_{s,m}) dy^+$,

integrating first term by parts and applying outer wall boundary condition) gives:

$$-(\psi'_{s,m}\phi_{s,n} - \phi'_{s,n}\psi_{s,m})\Big|_{y^+=1} + \int_1^\tau (\beta_m^2 - \lambda_n^2) \psi_{s,m}\phi_{s,n} dy^+ = 0 \quad (C-25)$$

Together eqs. C-23 and C-25 give

$$-\kappa \int_1^\tau (\beta_m - \lambda_n) \psi_{s,m}\phi_{s,n} dy^+ + \int_0^1 ((\lambda_n - \beta_m) - PeU^+(y^+)) \psi_{g,m}\phi_{g,n} dy^+ = 0 \quad (C-26)$$

Using eq. C-26 in eq. C-19 and rearranging finally gives the expression for A_n (eq. 2-37 in the main text). B_n can also be obtained by performing similar algebraic manipulations.

Appendix D: Table of Maximum Temperatures

Pe	k	t	NuE	Theta_Max	Flow type
0.1	10	2	10	0.4182	Plug
1	10	2	10	0.3938	Plug
5	10	2	10	0.1951	Plug
10	10	2	10	0.1018	Plug
5	0.1	2	10	0.2001	Plug
5	1	2	10	0.1999	Plug
5	100	2	10	0.1924	Plug
5	10	1.5	10	0.1926	Plug
5	10	3	10	0.1997	Plug
5	10	2	0.01	0.2696	Plug
5	10	2	0.1	0.2576	Plug
5	10	2	1	0.2181	Plug
5	10	2	100	0.1911	Plug
0.1	10	2	10	0.418	HP
1	10	2	10	0.3786	HP
5	10	2	10	0.1662	HP
10	10	2	10	0.1435	HP
5	0.1	2	10	0.264	HP
5	1	2	10	0.2097	HP
5	100	2	10	0.158	HP
5	10	1.5	10	0.1634	HP
5	10	3	10	0.1708	HP
5	10	2	0.01	0.2654	HP
5	10	2	0.1	0.2489	HP
5	10	2	1	0.1979	HP
5	10	2	100	0.1606	HP

Table of θ_{\max} for heat transfer solutions at various design cases

References

1. M. M. Micci and A. D. Ketsdever, “Micropropulsion for small spacecraft”, 2000, **187**, Progress in Astronautics and Aeronautics, AIAA, Chapters 1-3.
2. G. A. Risha, R.A. Yetter, V. Yang, and D.A. Fedorezyk, “Fundamental Studies on Electrolytic Ignition of Advanced HAN-Based Liquid Propellants for Space Propulsion Systems,” Joint 54th JANNAF Propulsion Meeting and 2nd Spacecraft Propulsion Meeting, Chemical Propulsion Information Agency, Johns Hopkins University, May 2007.
3. G. P. Sutton and O. Biblarz, “Rocket Propulsion Elements”, 7th ed. 2001, John Wiley and Sons, New York.
4. D. Manski, C. Goertz, H. D. Saßnick, J. R. Hulka, B. D. Goracke and D. J. H. Levack, “Cycles for Earth-to-Orbit Propulsion”, *Journal of Propulsion and Power*, 1998, **14** (5), pp. 588 – 604.
5. S. P. Burke and T. E. W. Schumann, “Diffusion Flames”, *Proceedings of the Combustion Institute*, 1937, **1**, pp. 2 – 11.
6. V. Yang and W. E. Anderson, “Liquid rocket engine combustion instability”, 1995, AIAA, Chapter 8.
7. Y. J. Choo and B. S. Kang, “The velocity distribution of the liquid sheet formed by two low-speed impinging jets”, *Physics of Fluids*, 2002, **14** (2), pp. 622 – 627.
8. L. C. Liou, “Combustion-wave ignition for rocket engines”, JANNAF Propulsion Meeting, 1992, **1**, pp. 295 – 311.

9. W. O. H. Mayer, B. Ivancic, A. Schik, and U. Hornung, "Propellant Atomization and Ignition Phenomena in Liquid Oxygen/Gaseous Hydrogen Rocket Combustors", *Journal of Propulsion and Power*, 2001, **17** (4), pp. 794 – 799.
10. K. J. Kacynski and J. D. Hoffman, "The prediction of nozzle performance and heat transfer in hydrogen/oxygen rocket engines with transpiration cooling, film cooling and high area ratios", 1994, Joint Propulsion Conference, AIAA- 1994-2757.
11. B. Lewis and G. Von Elbe, "Combustion, Flames and Explosion of Gases", 1951, Academic Press, Inc., New York.
12. D. A. Nield, A.V. Kuznetsov and Ming Xiong, "Thermally developing forced convection in a porous medium: parallel plate channel with walls at uniform temperature, with axial conduction and viscous dissipation effects", *International Journal of Heat and Mass Transfer*, 2003, **46**, pp. 643-651.
13. W. J. Minkowycz, A. Haji-Sheikh, "Heat transfer in parallel plates and circular porous passages with axial conduction", *International Journal of Heat and Mass Transfer*, 2006, **49**, pp. 2381 – 2390.
14. A. Mehra, X. Zhang, A. A. Ayon, I. A. Waitz, M. A. Schmidt, and C. M. Spadaccini, "A Six-Wafer Combustion System for a Silicon Micro Gas Turbine Engine", *Journal of MicroElectroMechanical Systems*, 2000, **9**(4), pp. 517 – 527.
15. J. Ahn, C. Eastwood, L. Sitzki and P. D. Ronney, "Gas-phase and catalytic combustion in heat-recirculating burners", *Proceedings of the Combustion Institute*, 2005, **30**, pp. 2463-2472.

16. S. Heatwole, A. Veeraragavan, S. Buckley and C. Cadou, "In-situ Species and Temperature Measurements in a Micro-combustor", *Journal of Nanoscale and Microscale Thermophysical Engineering*, 2009, **13** (1), pp. 54-76.
17. Y. Ju, B. Xu, "Effects of channel width and Lewis number on the multiple flame regimes and propagation limits in mesoscale", 2006, **178** (10), pp. 1723-1753.
18. Graetz L., "Über die Wärmeleitfähigkeit von Flüssigkeiten", *Annalen der Physik und Chemie.*, 1883, **18**, pp. 79-94.
19. J. R. Sellars, M. Tribus, J. S. Klein, "Heat Transfer to Laminar Flow in a Round Tube or Flat Conduit- The Graetz Problem Extended ", *Transactions of the ASME*, Feb 1956, pp. 441-448.
20. M. A. Ebadian and H. Y. Zhang, "An exact solution of extended Graetz problem with axial heat conduction", *International Journal of Heat and Mass Transfer*, 1989, **32** (9), pp. 1709-1717.
21. M. L. Michelsen and J. Villadsen, "The Graetz Problem with Axial Heat Conduction", *International Journal of Heat and Mass Transfer*, 1974, **17**, pp. 1391-1402.
22. A. S. Telles , E.M. Queiroz and G. Elmoã r Filho, "Solutions of the extended Graetz problem", *International Journal of Heat and Mass Transfer*, 2001, **44**, pp. 471-483.
23. J. Lahjomri and A. Oubarra, "Analytical Solution of the Graetz Problem with Axial Conduction", *Transactions of the ASME*, 1999, **121**, pp.1078-1083.
24. S. Kakac and Y.Yener, "Convective Heat Transfer", 2nd ed. 1995, CRC Press, pp. 132-180.

25. J. Jarosinski, "Heat transfer between hot combustion gases and a cold wall in narrow channels for limit flames", *International Journal of Heat and Mass Transfer*, Technical Notes, 1984, **27** (7), pp. 1113-1116.
26. X. Yin and H. H. Bau, "The conjugate Graetz problem with axial conduction", *Transactions of the ASME*, 1996, **118**, pp. 482-484.
27. G. Maranzana, I. Perry, D. Maillet, "Mini- and micro-channels: influence of axial conduction in the walls", *International Journal of Heat and Mass Transfer*, 2004, **47**, pp. 3993- 4004.
28. C. Hsu, "An Exact Analysis of Low Peclet Number Thermal Entry Region Heat Transfer in Transversely Nonuniform Velocity Fields", *American Institute of Chemical Engineers Journal*, 1971, **17** (3), pp. 732- 740.
29. J. B. Campos Silva, R. M. Cotta, J. B. Aparecido. , "Analytical Solutions to simultaneously developing laminar flow inside parallel-plate channels", *International Journal of Heat and Mass Transfer*, 1992, **35** (4), pp. 887-895.
30. Mallard, E., and LeChatelier, H. L., "Thermal Model for Flame Propagation", *Ann.Mines*, Vol. 4, No. 18, 1883, pp. 379.
31. Ya. B Zeldovich, "Theory of Limit of Quiet Flame Propagation", *Zh.Prikl. Mekh. Tekh. Fiz.*, 1941, **11** (1), pp. 159-169.
32. D. B. Spalding, "A Theory of Inflammability Limits and Flame-Quenching", *Proc. Royal Soc. A*, 1957, **240** (1220), pp. 83-100.
33. T. Takeno and K. Sato, "Excess Enthalpy Flame Theory", *Combustion Science and Technology*, 1979, **20**, pp. 73-84.

34. T. Takeno, K. Sato and K. Hase, "A Theoretical Study on an Excess Enthalpy Flame", *Proceedings of the Combustion Institute*, 1981, **18**, pp. 465-471.
35. F. Weinberg, "Advanced Combustion Methods", 1986, Orlando: Academic Press, Chapter 3.
36. J. Daou and M. Matalon, "Influence of Conductive Heat-Losses on the Propagation of Premixed Flames in Channels", *Combustion and Flame*, 2002, **128**, pp. 321- 339.
37. P. D. Ronney, "Analysis of non-adiabatic heat-recirculating combustors", *Combustion and Flame*, 2003, **135**, pp. 421-439.
38. Y. Ju and C. W. Choi, "An analysis of sub-limit flame dynamics using opposite propagating flames in mesoscale channels", *Combustion and Flame*, 2003, **133**, pp. 483-493.
39. C. Cui, M. Matalon, J. Daou and J. Dold, "Effects of differential diffusion on thin and thick flames propagating in channels", *Combustion Theory and Modeling*, 2004, **8**, pp. 41-64.
40. T. Leach, C. Cadou, G. Jackson, "Effect of structural conduction and heat loss on combustion in micro-channels", *Combustion Theory and Modelling*, 2006, **10** (1), pp. 85-103.
41. D. G. Norton and D. G. Vlachos, *Combust. Flame*, "A CFD study of propane/air microflame stability", 2004, **138**, pp. 97-107.
42. T. Leach and C. P. Cadou, "The Role of Structural Heat Exchange and Heat Loss in the Design of Efficient Silicon Micro-combustors", *Proceedings of the Combustion Institute*, 2004, **30**, pp. 2437-2444.

43. I. Shoegl and J. Ellzey, "Superadiabatic combustion in conducting tubes and heat exchangers of finite length," *Combustion and Flame*, 2007, **151**, pp. 142-159.
44. E. Barrios, J. C. Prince and C. Trevin, "The role of duct thickness on the quenching process of premixed flame propagation", *Combustion Theory and Modeling*, 2008, **12** (1), pp. 115–133.
45. N. Kim, "Effect of an inlet temperature disturbance on the propagation of methane-air premixed flames in small tubes", *Combustion and Flame*, 2009, **156**, pp. 1332-1338.
46. Y. Kotani and T. Takeno, "An Experimental Study on Stability and Combustion Characteristics of an Excess Enthalpy Flame", *Proceedings of the Combustion Institute*, 1982, **19**, pp. 1503-1509.
47. S. Churchill, "Thermally Stabilized Combustion", *Chemical Engineering Technology*, 1989, **12** (1), pp. 249 – 254.
48. P. D. Ronney, F. J. Weinberg, D. M. Rowe, and G. Min, "On Thermoelectric Power Conversion from Heat Recirculating Combustion Systems", *Proceedings of the Combustion Institute*, 2002, **29**, pp. 941-947.
49. P. D. Ronney, K. Takeda, K. Maruta, L. Sitzki, and K. Borer, "Catalytic Combustion in Microchannel for MEMS Power Generation", *The Third Asia-Pacific Conference on Combustion*, 2001.
50. A. Scarpa, R. Pirone, G. Russo, D.G. Vlachos, "Effect of heat recirculation on the self-sustained catalytic combustion of propane/air mixtures in a quartz reactor", *Combustion and Flame*, 2009, **156**, pp. 947-953.

51. E. Rudnyi, T. Bechtold, J. Korvink, C. Rossi, "Solid Propellant Theory of Operation and Modelling Strategy", AIAA-2002-5755, NanoTech 2002 – "At the Edge of Revolution", Houston, Texas, Sep. 9-12, 2002.
52. J. Kujawa, D.L. Hitt and G. Cretu, "Numerical Simulation of Supersonic Flow in Realistic MEMS Nozzle Geometries with Heat Loss", AIAA 2003-3585, 33rd AIAA Fluid Dynamics Conference and Exhibit, 23-26 June 2003, Orlando, Florida.
53. W.F. Louissos and D.L. Hitt, "Heat Transfer & Viscous Effects in 2D & 3D Micro-Nozzles", AIAA 2007-3987 37th AIAA Fluid Dynamics Conference, June 25-28, 2007, Miami, Florida.
54. K. Yang, I. Chen, B. Shew and C. Wang, "Investigation of the flow characteristics within a micronozzle/diffuser", *Journal of Micromechanical Microengineering*, 2004, **14**, pp. 26–31.
55. A. P. London, "Development and Test of a Microfabricated Bipropellant Rocket Engine", PhD dissertation, Massachusetts Institute of Technology, June 2000.
56. A. Fernandez-Pello, "Micropower Generation Using Combustion: Issues and Approaches", *Proceedings of the Combustion Institute*, 2002, **29**, pp. 883-899.
57. H. T. Aichlmayr, D. B. Kittelson, and M. R. Zachariah, "Miniature free-piston homogeneous charge compression ignition engine-compressor concept- Part I: performance estimation and design considerations unique to small dimensions", *Chemical Engineering Science*, 2002, **57**, pp. 4161-4171.
58. H. T. Aichlmayr, D.B. Kittelson, and M.R. Zachariah, "Micro-HCCI combustion: experimental characterization and development of a detailed chemical kinetic model with coupled piston motion", *Combustion and Flame*, 2003, **135**, pp. 227-248.

59. W. J. A. Dahm, J. Ni, K. Mijit, J. R. Mayor, G. Qiao, S. W. Dyer, A. G. Benjamin, Y. Gu, Y. Lei, M. L. Papke, "Micro Internal Combustion Swing Engine (MICSE) for Portable Power Generation Systems". AIAA Paper 2002-0722, AIAA, Reno, NV (2002).
60. C. R. Shaddix, "Correcting Thermocouple Measurements for Radiation Loss: A Critical Review", Proceedings of the 33rd National Heat Transfer Conference, HTD99-282, August 15-17, 1999, Albuquerque, New Mexico.
61. S. T. Wereley and L. Gui, "Advanced algorithms for microscale particle image velocimetry", *AIAA Journal*, 2002, **40**, pp. 1047-1055.
62. W. P. Shih, J. G. Lee and D. A. Santavicca, "Stability and Emission Characteristics of a Lean Premixed Gas Turbine Combustor", *Proceedings of the Combustion Institute*, 1996, **26**, pp. 2771-2778.
63. O. Jacquot and P. Herve, "Determination of temperature fields in exhaust gases by infrared spectroscopy", *Proceedings of SPIE*, 1998, **3493**, pp. 71-78.
64. D. Bailly, C. Camy-Peyret, and R. Lanquetin, "Temperature Measurements in Flames through CO₂ and CO Emission: New Highly Excited Levels of CO₂", *Journal of Molecular Spectroscopy*, 1997, **182**, pp. 10-17.
65. J. S. Lindner, Z. Hansheng, and R. L. Cook, "Non-intrusive Determination of Combustion Efficiency Using FTIR Spectroscopy", *Proceedings of SPIE*, 1995, **2365**, pp. 285-301.
66. C. P. Koshland, D. Lucas, B. S. Higgins, and R. F. Sawyer, "Detection of Chlorinated Hydrocarbons in Combustion Using In-Situ FTIR Spectroscopy", *Proceedings of the Combustion Institute*, 1992, **24**, pp. 1597-1604.

67. M. F. Modest and S. P. Bharadwaj, "Medium Resolution Transmission Measurements of CO₂ at High Temperature", *Journal of Quantitative Spectroscopy and Radiative Transfer*, 2002, **73** (2-5), pp.329-338.
68. L. S. Rothman, and et al., "The HITRAN Molecular Spectroscopic Database and HAWKS (HITRAN Atmospheric Workstation)", 1996 Edition.
69. J. Heland, K. Schafer, and R. Haus, *Investigations of Hot Exhaust Gases with Passive FTIR Emission Spectroscopy*. Proceedings of SPIE, 1998. **3493**: p. 2-10.
70. W. Grosshandler, "RADCAL: A Narrow-Band Model for Radiation Calculations in Combustion Environment", NIST Technical Note 1402, 1993.
71. A. Soufani and J. Taine, "High Temperature Gas Radiative Property Parameters of Statistical Narrow-Band Model for H₂O, CO₂ and CO and Correlated K-model for H₂O", *International Journal of Heat and Mass Transfer*, 1997, **40** (4), pp. 987-991.
72. X. Zhang, A. Mehra, A. A. Ayon, and I. A. Waitz, "Igniters and temperature sensors for a micro-scale combustion system", *Sensor and Actuators*, 2003, **103**, pp. 253-262.
73. K. Breuer, J. Bird, G. Han, A. Westin, K. Johan and Z. Cao, "Infrared Diagnostics for Measuring Fluid and Solid Motion Inside Silicon Microdevices", *Microscale Thermophysical Engineering*, 2004, **8**(2), pp. 169-182.
74. S. Heatwole, C. P. Cadou, and S. G. Buckley, "In situ Infrared Diagnostics in a Silicon-Walled Microscale Combustion Reactor: Initial Measurements", *Combustion Science and Technology*, 2005, **177**, pp. 1449-1461.
75. S. E. Heatwole, "In Situ Infrared Diagnostics for a Micro-scale Combustion reactor", M. S. Thesis, 2004, University of Maryland.

76. A. Veeraragavan and C. Cadou, "Heat transfer in mini/micro channels with combustion: a simple analysis for application in non-intrusive IR diagnostics", *ASME Journal of Heat Transfer*, 2008, **130** (12), pp. 124504 – 1:5.
77. A. Veeraragavan, K. Dellimore and C. Cadou, "Heat transfer analysis for channel flames modeled as a heat source in 2D channels with constant wall temperature", *AIAA J. Thermophysics and Heat Transfer*, **23** (3), 2009, pp. 551-559.
78. ESI U.S. R&D, Inc., "CFD-ACE+ V2004 Modules Manual- Volume 1," ESI U.S. R&D, May 2004
79. Schlichting, H., "Boundary-Layer Theory", 7th Ed., McGraw-Hill, New York, 1979, pp.47-69.
80. A. Bejan, "Convection heat transfer", 3rd ed. 2004, Wiley, New Jersey, Chapters 3 and 4.
81. F. A. Williams, "Combustion Theory", 2nd ed. 1985, Addison-Wesley Publishing Company, California, page 273.
82. A. Veeraragavan, "Heat Transfer Analysis for Improved In-situ Infrared Temperature Diagnostics in Microcombustor", M. S. Thesis, 2006, University of Maryland.
83. Class Notes, Department of Chemistry and Biochemistry, Arizona State University, http://www.biochem.arizona.edu/classes/bioc462/462a/NOTES/Protein_Properties/protein_purification.htm.
84. D. A. McQuarrie, "Quantum Chemistry", 1983, University Science Books, California, Chapter 10.
85. J. S. Winn, "Physical Chemistry", 1995, Harper Collins College Publishers, New York, Chapters 18-20.

86. D. Harris, Exploring Chemical Analysis, 3rd edition, W.H. Freeman & Company, 2004.
87. W. Malkmus, “Random band Lorentz with exponential tailed 1/S line-intensity distribution function”, *Journal of the Optical Society of America*, 1967, **57**, pp. 323-329.
88. NIST Database for Atomic Spectra,
<http://physics.nist.gov/PhysRefData/ASD/index.html>
89. A. Pettersson, “Investigations of Infrared Chemiluminescence Emission from Laboratory Flames”, M.S. thesis, Lund Institute of Technology, Lund University, 2004.
90. W.R. Runyan, “Technology Semiconductor Silicon”, McGraw-Hill Book Company, 1996.
91. A. F. Bicen, D.G.N. Tse and J. H. Whitelaw, “Combustion characteristics of a model can type combustor”, *Combustion and Flame*, 1990, **80**, pp. 111-125.
92. K. Maruta, J. K. Parc, K. C. Oh, T. Fujimori, S. S. Minaev, and R. V. Fursenko, “Characteristics of Microscale Combustion in a Narrow Heated Channel”, *Combustion, Explosion and Shock Waves*, 2004, **40** (5), pp. 516-523.